Mechanisms of plastic deformation of magnesium matrix nanocomposites

Camila Mallmann

Communauté
UNIVERSITÉ Grenoble Alpes

THÈSE

Pour obtenir le grade de

DOCTEUR DE LA COMMUNAUTÉ UNIVERSITÉ GRENOBLE ALPES

Spécialité : **Science des matériaux**

Arrêté ministériel : 25 mai 2016

Présentée par

Camila MALLMANN

Thèse dirigée par **Marc FIVEL, Emilie FERRIE** et
codirigée par **Aude SIMAR, Erica LILLEODDEN**

préparée au sein du **Laboratoire SIMaP**
dans **l'École Doctorale I-MEP2**

Mechanisms of plastic deformation of magnesium matrix nanocomposites

Thèse soutenue publiquement le **18 Novembre 2016**
devant le jury composé de :

M., Jérôme CREPIN
Directeur de Recherche, Centre de Matériaux Mines-ParisTech, Président
M., Marc LEGROS
Directeur de Recherche CNRS, CEMES Toulouse, Rapporteur
M., Jean-Luc BECHADE
Directeur de Recherche, CEA-Saclay/SRMA, Rapporteur
M., Jon M. MOLINA-ALDAREGUIA
Chercheur Sénior, IMDEA Madrid, Examinateur
M., Marc FIVEL
Directeur de Recherche CNRS, Directeur de thèse
Mme., Emilie FERRIE
Maître de Conférences Université Grenoble Alpes, Encadrante
Mme., Erica LILLEODDEN
Professeur Helmholtz-Zentrum Geesthacht, Encadrante
Mme., Aude SIMAR
Professeur Assistante Université Catholique de Louvain, Encadrante

Contents

Acknowledgment

First of all, I would like to thank the members of the jury for having accepted to evaluate my Ph.D. work and for their comments and fruitful discussions during the defense: Mr. Jérôme CREPIN, Mr. Marc LEGROS, Mr. Jean-Luc BECHADE and Mr. Jon MOLINA-ALDAREGUIA.

I would like to express my gratitude to my supervisors Marc, Emilie, Erica and Aude for their support, encouragement and discussions over these three years. Besides, a special thanks to Aude who has contributed significantly to the success of the project, even though she joined the team halfway through my Ph.D. It has been a great pleasure to work with four researchers who taught me so much. Thank you for the incredible opportunity to work in multicultural environments in different countries (France, Belgium and Germany).

The work that I have accomplished during this three years would not be possible without the support and collaboration of so many persons in the different groups that I had the chance to work with: SIMaP, HZG and UCL.

Thanks to all my colleagues from SIMaP laboratory, especially Charles, Xavier, Sebastian and Harry, who have experienced the pressure and stress of writing a thesis. I cannot forget to thank Matthieu, who has gently give me his office and with whom I shared a few "mates". To all my colleagues from the blue room (Charles, Xavier, Shrey, Thibaut, Bruno and Étienne) for their daily support and encouragement (especially during the last months). To Claire, Claude and Elisabeth for taking care of all the paper work and making my life so much easier.

In addition, I would like to express my gratitude to my colleagues from HZG who have always received me so well. An especial thanks to my colleagues from WME (Paula, Max, Henry, Kaixiong, Julian, Leyung, Jingsi and Julia) that have welcomed me with a

smile even when I had the microscope booked for more than a month. Thanks also to the people from MagIC, especially Hajo Dieringa, who provided me with the first samples used in this work and Gert Wiese, who introduced me the pleasant task of polishing magnesium samples for hours. To Nadiia, Jingsi, Henry and Paula, who have shared their offices with me.

For the fruitful collaboration with UCL, I would like to thank all who worked with me in the preparation of the samples using FSP, and Florent for the analysis and discussions on the tomography results. To Hosni Idrissi, for the discussions and the tests performed using *in situ* TEM.

The extended characterization of my samples would not be possible without the help, advice and discussion with Rachel and Frédéric (MEB), Stéphane (DRX), Florence (EBSD), Gilles, Patricia and Edgar (TEM), Pierre, Rémi, Luc and Alessandra (tomography), Christèle (sample preparation), Thierry (EDM), Jürgen and Nadiia (compression test), Charles (testing machine), Xavier and Franck (everything)... Also special thanks to the METSA network, CEMES laboratory and Frédéric Mompiou for making it possible to do the *in situ* TEM experiments.

I cannot forget the ones who, even though not directly related with the Ph.D., have been so important in acomplishing this work: Marie, Anna, Pierre, Thomas, Thomas (Lucile), Lucile, Pedro, Katia, Marine, Benjamin, Xaxá, Salma, Mohamed... Thank you all for your friendship and support.

I am also thankful to my parents and brother who, even from far away, have always supported me and my choices, granting me the strength to overcome any obstacle. Béa, Cricri, Marine and la Mamie who have also encouraged me and Alexandre for his financial support.

Last, but not least, I would like to express my deepest gratitude to Arnaud. His love, support, encouragement and patience have been essential in accomplishing this work.

French summary - Résumé étendu en français

Ces dernières années, les nanocomposites à base magnésium ont été l'objet de nombreuses études. Avec une densité de 1,74 g.cm^{-3}, le magnésium est le plus léger des métaux utilisés pour des applications structurales. Ainsi, lui et ses nanocomposites représentent une solution prometteuse pour des applications dans lesquelles l'allégement de structures, l'économie d'énergie et la réduction des émissions à effet de serre sont requises. Pour autant, sa résistance mécanique est très faible, et doit donc être augmentée afin de rivaliser avec d'autres métaux légers tels que l'aluminium et le titane. Une solution consiste à renforcer le magnésium et ses alliages en introduisant des nanoparticules d'oxydes.

L'utilisation des nanocomposites à base magnésium en tant que matériaux de structure requiert une étude fondamentale des mécanismes de déformation plastique. De par sa structure cristalline hexagonale compacte, le magnésium présente des propriétés plastiques complexes telles qu'une très forte anisotropie plastique et une prédisposition au maclage. La Figure 1 montre les cinq modes de déformation les plus courants dans le magnésium, à savoir: glissement basal, prismatique, pyramidal $\pi 1$ et pyramidal $\pi 2$, ainsi que le système de maclage de traction.

En ce qui concerne le glissement, celui-ci a lieu seulement lorsque la contrainte de cisaillement résolue dans le plan de glissement pour une certaine direction atteint une valeur critique (CRSS). Expérimentalement, il a été observé que le glissement basal est le mode de déformation prédominant à température ambiante. Ceci est dû à une faible valeur de la CRSS pour le glissement basal dans le magnésium (0,5 MPa), inférieure à celles observées dans d'autres systèmes de glissement. Cependant, le glissement basal permet seulement d'accommoder la déformation dans la direction $< a >$. Dans la direction $< c >$, la déformation peut être accommodée soit par le système pyramidal $\pi 2$, soit par le maclage. A température ambiante, le maclage de traction $\{1\,0\,\bar{1}\,2\}$ est le plus couram-

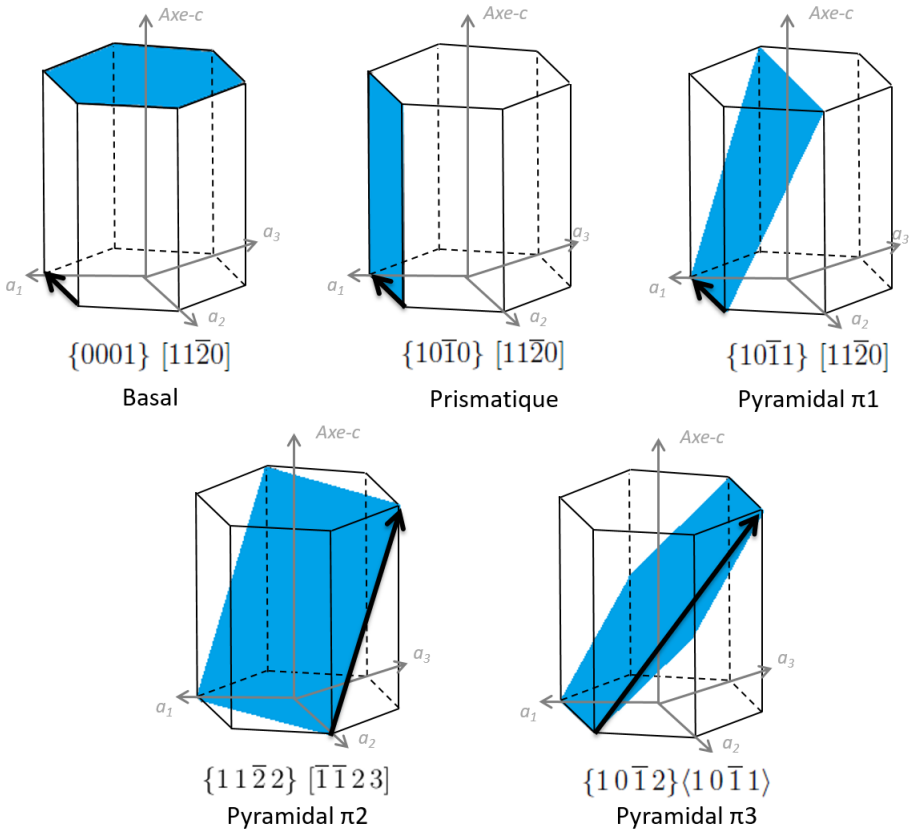

Figure 1 – Les modes de déformation les plus courament observés pour le magnésium et ses vecteurs de Burgers respectifs (flèches noires).

ment observé. Celui-ci a lieu lorsqu'une contrainte de traction est appliquée sur l'axe-c, entraînant une réorientation d'environ 86° de l'axe-c autour de l'axe [1 1 $\bar{2}$ 0] (Figure 2). La CRSS pour l'activation de la macle de traction dans le magnésium est également basse, avec une valeur entre 2 et 3 MPa.

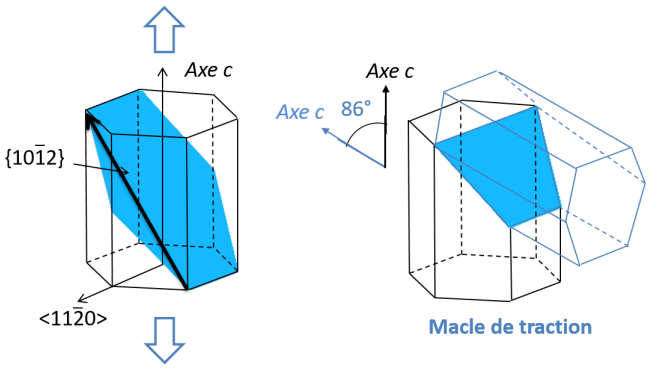

Figure 2 – Schéma de la réorientation du cristal dans la région maclée lors du maclage de traction {1 0 $\bar{1}$ 2}.

Cette étude vise à l'élaboration d'un nanocomposite "modèle" de magnésium pur renforcé par des particules d'oxydes ainsi qu'à sa caractérisation microstructurale et mécanique. Une attention particulière sera portée sur l'effet des particules sur les mécanismes de renfort. Le comportement mécanique sera alors étudié en utilisant le nanocomposite "modèle" polycristallin afin de confirmer le renforcement macroscopique induit par les particules. Une étude du comportement plastique à l'échelle du monocrystal suivra. Ces travaux seront basés sur des études précédemment réalisés par E. Lilleodden [1] et G. S. Kim [2] sur les mécanismes de déformation plastique de micropiliers monocristalins de magnésium. Leurs études ont montré que les mécanismes de déformation du magnésium sont fortement influencés par l'orientation cristalline initiale et la taille du micropilier. Des essais macroscopiques et de microcompression seront également réalisés sur des échantillons de magnésium pur, élaborés en utilisant des conditions similaires.

Fabrication et choix du nanocomposite "modèle"

Avant de pouvoir réaliser l'étude des mécanismes de déformation, il est nécessaire d'élaborer le nanocomposite "modèle". Un effet de renfort des nanocomposites par des particules requiert qu'elles soient dispersées de manière homogène, ce qui pose de réels problèmes lors de l'élaboration. Les nanoparticules ayant en général une très faible mouillabilité par le métal liquide et une forte tendance à s'agglomérer, cela peut entraîner une mauvaise dispersion des particules. Dans ces travaux, différentes techniques ont été testées et comparées pour l'élaboration des nanocomposites:

- **Solidification assistée aux ultrasons**

  Des nanocomposites renforcés avec trois types de particules d'oxydes (Al_2O_3, MgO et Y_2O_3) ont été fabriqués par solidification assistée aux ultrasons. Ces nanocomposites ont été élaborés dans le cadre du projet européen Exomet (FP7-NMP-2011-LARGE-4) dans le centre de recherche Helmholtz Zentrum Geesthacht (HZG), en Allemagne. Les particules d'Al_2O_3, MgO et Y_2O_3 ont respectivement un diamètre moyen de 36 nm, 300 nm et 500 nm. Lors de la fabrication, les particules sont ajoutées au magnésium fondu (Figure 3 (a)) puis, un mélangeur à haute vitesse et une sonotrode (Figure 3 (b)) assurent leur dispersion et la fragmentation des agglomérats. Une fois le mélangeur et le sonotrode enlevés, le moule descend dans un bain d'eau placé sous le four (Figure 3 (c)).

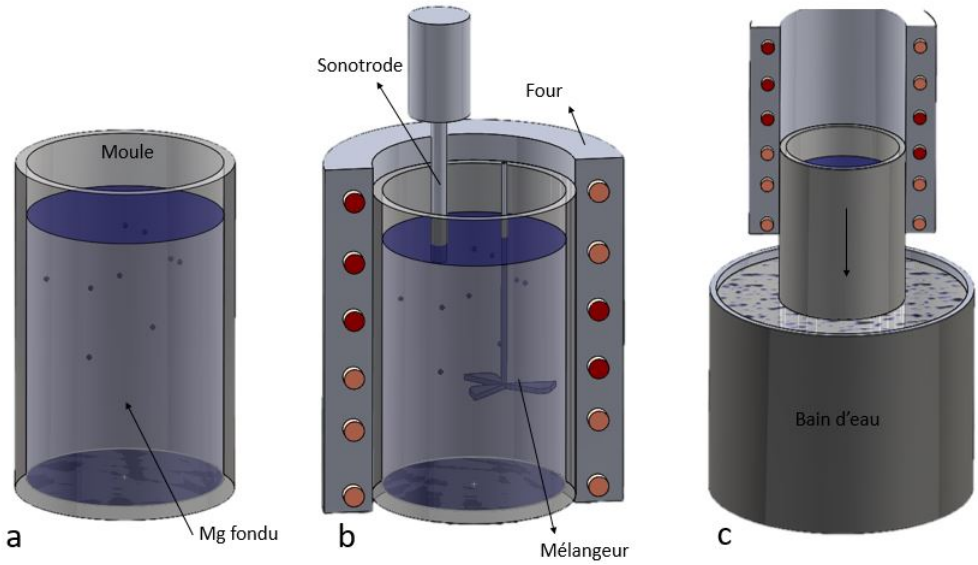

Figure 3 – Schéma du procédé de solidification assistée aux ultrasons.

- **Procédé de friction malaxage (FSP)**

  Ce procédé a été utilisé pour fabriquer des nanocomposites renforcés par des particules d'Y_2O_3. C'est une technique d'élaboration à l'état solide où un outil tournant pénètre dans le matériau grâce à la chaleur générée par sa rotation qui rend le matériau malléable. Un mélange "mécanique" entre les particules de renfort et le magnésium est ainsi obtenu. Le schéma de l'élaboration par ce procédé est présenté dans la Figure 4. Une rainure est usinée dans l'axe central d'une plaque de magnésium de 3 mm et remplie avec des particules d'Y_2O_3. Une deuxième plaque de magnésium plus fine (0,5 mm) couvre la rainure afin d'éviter la perte de particules lors du procédé. L'outil FSP avance tout au long de l'axe central où se trouve la rainure. La zone de FSP correspond à la zone qui contient le nanocomposite dans laquelle le magnésium et l'Y_2O_3 sont déjà mélangés. Différents paramètres d'élaboration ont été testés: la vitesse d'avance de l'outil, qui varie entre 300 et 500 mm/min, et la vitesse de rotation, qui varie de 1000 à 1500 rpm.

Le nanocomposite "modèle" choisi pour l'étude approfondie des mécanismes de déformation, doit présenter une dispersion de particules homogène. De plus, pour mener l'étude du monocristal, il sera nécessaire que le composite "modèle" possède des grains de taille suffisante afin de pouvoir fabriquer des micropiliers à l'intérieur d'un grain unique en utilisant un faisceau d'ions focalisés (FIB). L'orientation cristalline du grain choisi pour la fabrication du micropilier est connue seulement en surface (par EBSD) et la présence de gros grains permet d'augmenter la probabilité que tout le micropilier soit usiné dans

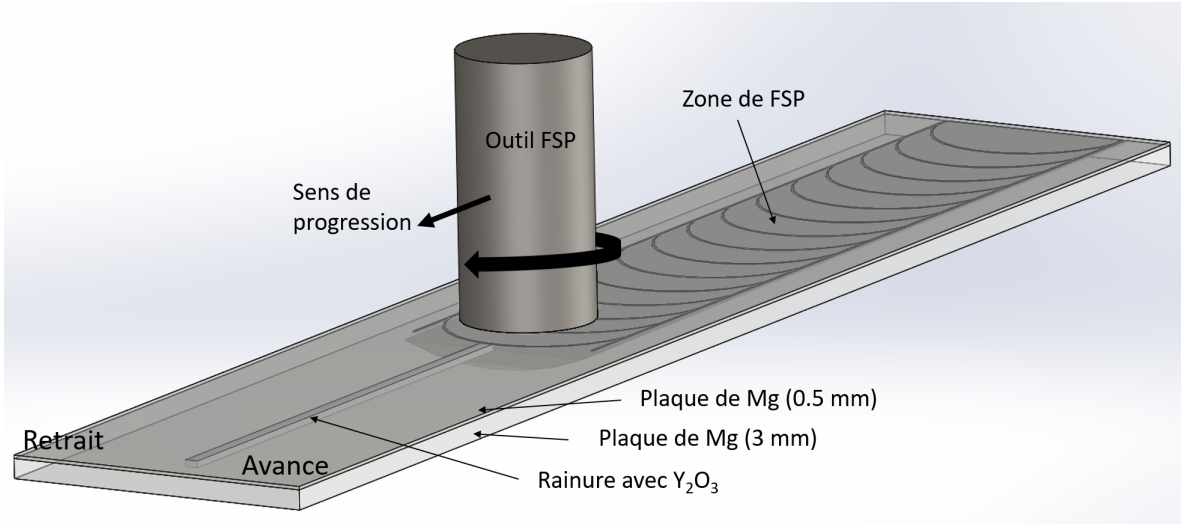

Figure 4 – Schéma de l'élaboration par procédé de friction malaxage. Le côté d'avance correspond au côté où le mouvement de rotation de l'outil FSP va dans la même direction du sens de progression, tandis que le côté de retrait correspond au côté opposé.

un même grain. L'addition de particules de renfort a une forte tendance à réduire la taille des grains et complique l'obtention de piliers monocristallins. De plus, une bonne stabilité chimique entre le magnésium et les particules (y compris à chaud lors de l'élaboration) est nécessaire afin d'éviter l'apparition de phases indésirables. En résumé, le nanocomposite "modèle" doit avoir une dispersion de particules homogène, une microstructure grossière et les particules doivent être stables.

La microstructure des nanocomposites a été caractérisée par microscopie optique, microscopie électronique à balayage (MEB), microscopie électronique en transmission (MET) ainsi que par microtomographie aux rayons-X (synchrotron et laboratoire). Ces caractérisations ont permis de définir le nanocomposite "modèle" fabriqué par procédé de friction malaxage avec une vitesse d'avance de 500 mm/min et une vitesse de rotation de l'outil de 1500 rpm. Ces paramètres ont permis d'obtenir le nanocomposite "modèle" avec les meilleures caractéristiques.

Une caractérisation microstructurale plus poussée du nanocomposite "modèle" par nanoholotomographie aux rayons-X synchrotron et MET, a permis d'accéder à la dispersion en 3 dimensions des particules ainsi qu'à leur morphologie. La reconstruction 3-D d'une région du nanocomposite "modèle" est présentée en Figure 5. Cette analyse plus poussée a permis d'identifier une légère agglomération des particules de diamètre supérieur à 500 nm. D'autre part elle montre que le FSP entraîne la fragmentation des particules d'Y_2O_3: les particules ont leur taille réduite, passant d'un diamètre initial de

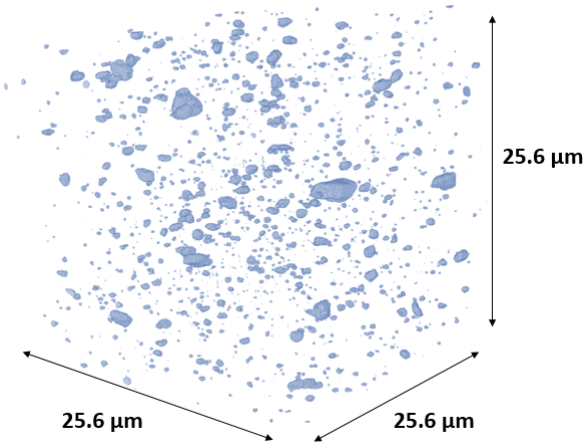

Figure 5 – Reconstruction 3-D de la nanoholotomographie aux rayons-X synchrotron fait sur le nanocomposite “modèle” en utilisant un taille de voxel de 25 nm.

3,5 μm à quelques centaines de nanomètres dans certains cas. Il a été observé que 90 % des particules d'Y_2O_3 ont un diamètre inférieur à 400 nm. Les caractéristiques du nanocomposite “modèle” sont détaillées dans le Tableau 1.

Tableau 1 – Caractéristiques du nanocomposite “modèle”.

Diamètre moyen des particules		430 nm
Fraction volumique moyenne	Globale f_v^{global}	0,33 %
	Particules agglomérées f_v^{aggl}	0.47 %
	Particules isolées f_v^{isol}	0.11 %
Fraction volumique de particules d'Y_2O_3	Agglomérées	61 %
	Isolées	39 %
Volume moyen d'un agglomérat		(3,93 μm)^3
Taille moyenne d'un agglomérat		8,03 particules
Distance moyenne entre particules		1,3 μm

Renfort par des particules

Essais de traction

Afin de confirmer un effet de renfort de la part des particules d'Y_2O_3 dans le nanocomposite “modèle”, des essais de traction ont été réalisés sur les échantillons polycristallins. Des éprouvettes de traction ont été prélevées dans la zone de FSP selon le

processus décrit sur la Figure 6. Des échantillons de magnésium pur, fabriqués en utilisant

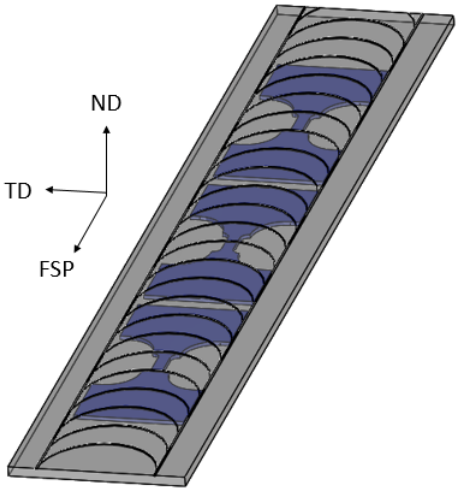

Figure 6 – Schéma du prélevement des éprouvettes de traction dans la zone de FSP.

les mêmes paramètres que ceux utilisés pour le nanocomposite "modèle", ainsi que des nanocomposites ayant une fraction volumique d'Y_2O_3 supérieure (1,64 et 2,11 %) ont été comparés au nanocomposite "modèle". La Figure 7 compare la courbe contrainte vraie-déformation vraie des échantillons de magnésium pur (FSP Mg) avec des échantillons de magnésium renforcés par des particules d'Y_2O_3 et le Tableau 2 présente les propriétés mécaniques extraites du graphique pour chaque échantillon.

Tableau 2 – Propriétés mécaniques des échantillons présentés en Figure 7.

Échantillon	**0.2 % Limite d'élasticité (MPa)**	**Limite à la rupture (MPa)**	**Ductilité (%)**	**Coefficient de durcissement (MPa)**
Mg	52.4±2.5	115,2±1,1	28,8±1,9	279,5±41
Mg+Y_2O_3(0,3%)	68,7±1,8	142,1±8,6	28,3±0,1	425,8±43
Mg+Y_2O_3(1,64%)	72,4±5,5	159,2±5,2	28,5±1,8	382,5±36
Mg+Y_2O_3(2,11%)	71,4±4,5	156,1±0,1	27,9±2,2	425,4±20,5

Une amélioration de la limite à la rupture et de la limite d'élasticité a été observée lors de l'addition de particules d'Y_2O_3, sans pour autant influencer la ductilité du matériau. De plus, confirmant à la littérature [3, 4], le coefficient d'écrouissage des échantillons contenant des particules augmente. L'augmentation de la limite à la rupture est en lien direct avec l'écrouissage plus important observé pour les nanocomposites. Cet écrouissage est confirmé par le coefficient d'écrouissage, décrivant le taux de stockage de

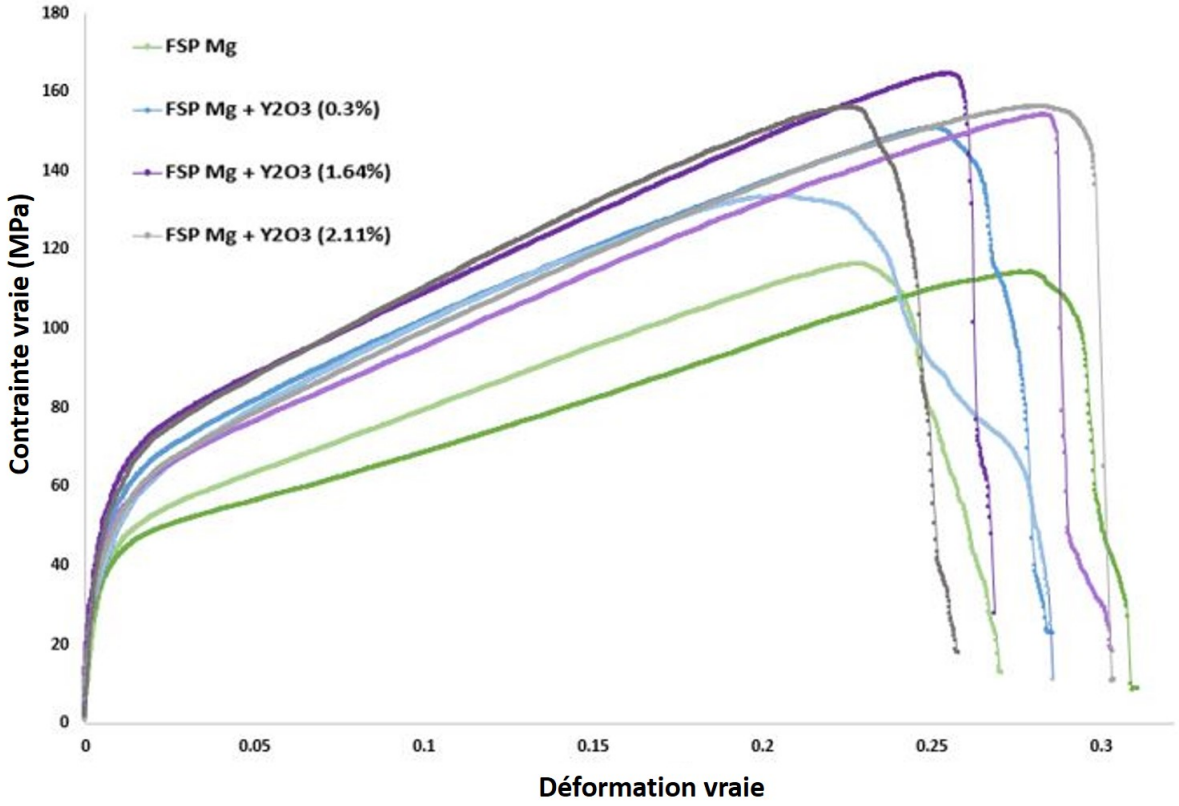

Figure 7 – Comparaison de la déformation vraie vs. contrainte vraie entre le magnésium pur et le magnésium renforcé par différentes fractions volumiques de particules d'Y_2O_3.

dislocations. Les différentes fractions volumiques de particules d'Y_2O_3 semblent avoir peu d'influence sur les propriétés mécaniques.

Concernant les mécanismes de durcissement des nanocomposites, il faut considérer l'effet Hall-Petch qui rend compte de l'influence de la taille de grain. En effet, la présence de joints de grains bloque le mouvement des dislocations: la forte désorientation cristalline observée entre deux grains rend la transmission des dislocations d'un grain à l'autre trop énergétique. Ainsi, plus les grains sont petits, plus cet effet est important. La taille de grain des échantillons FSP Mg et FSP Mg+Y_2O_3 (0,3 %) est présenté dans la Figure 8. La taille moyenne de grains des échantillons FSP Mg et FSP Mg+Y_2O_3 (0,3 %) est respectivement de 7,8±0,66 μm et 11,7±1,23 μm. Comme la taille de grain est supérieure dans le cas de l'échantillon FSP Mg+Y_2O_3 (0,3 %), l'effet Hall-Petch n'est pas responsable de l'augmentation de la limite d'élasticité observée dans les essais de traction.

La forte anisotropie du magnésium se traduit par la formation d'une texture

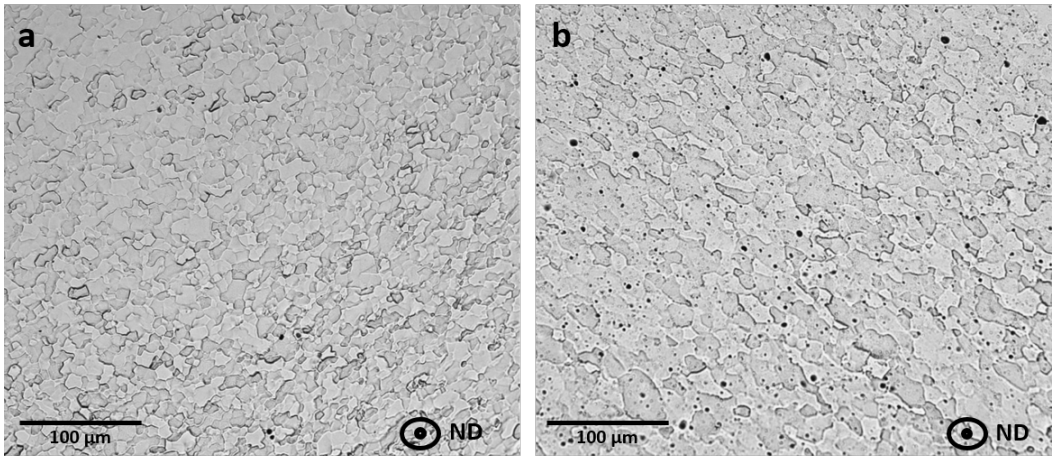

Figure 8 – Taille de grain mesurée dans la surface (ND) des échantillons de traction FSP Mg (a) et FSP Mg + Y_2O_3 (0,3 %) (b).

très marquée qui peut elle aussi avoir une forte influence sur la réponse mécanique. La Figure 9 montre les figures de pôle (0 0 0 2) et (1 0 $\bar{1}$ 1) incomplètes (la limite supérieure de l'angle χ est 75° et non 90°) obtenues par diffraction aux rayons X des échantillons FSP Mg et FSP Mg + Y_2O_3 (0,3, 1,64 and 2,11 %) avant et après essai de traction. La présence des particules d'Y_2O_3 semblent avoir très peu d'influence sur la texture, quelque soit la fraction volumique ajoutée.

En conclusion, les particules d'Y_2O_3 semblent avoir un effet direct dans le renfort du nanocomposite. Des mécanismes comme l'effet de transfert de charge, l'effet Orowan et l'effet du coefficient de dilatation thermique peuvent expliquer ce renfort. L'effet de transfert de charge est responsable du transfert des efforts de la matrice à la phase plus dure (particules céramiques) lorsqu'un composite est soumis à un chargement externe. L'effet Orowan considère, lui, que les particules de renforts agissent comme des obstacles pour le mouvement des dislocations; lorsqu'un segment de dislocation doit se courber pour contourner des particules. Si la dislocation continue son mouvement, elle franchira la particule en laissant une boucle de dislocation autour de celle-ci. Enfin, la différence entre les coefficients de dilatation thermique de la matrice et des particules génère des incompatibilités de déformation lors de refroidissements partant des températures élevées. Ces incompatibilités de déformation sont relaxées par l'émission des dislocations géométriquement nécessaires (GND). Des essais de microcompression et du MET *in situ* seront réalisés afin d'identifier les mécanismes responsables du durcissement observé lors des essais de traction.

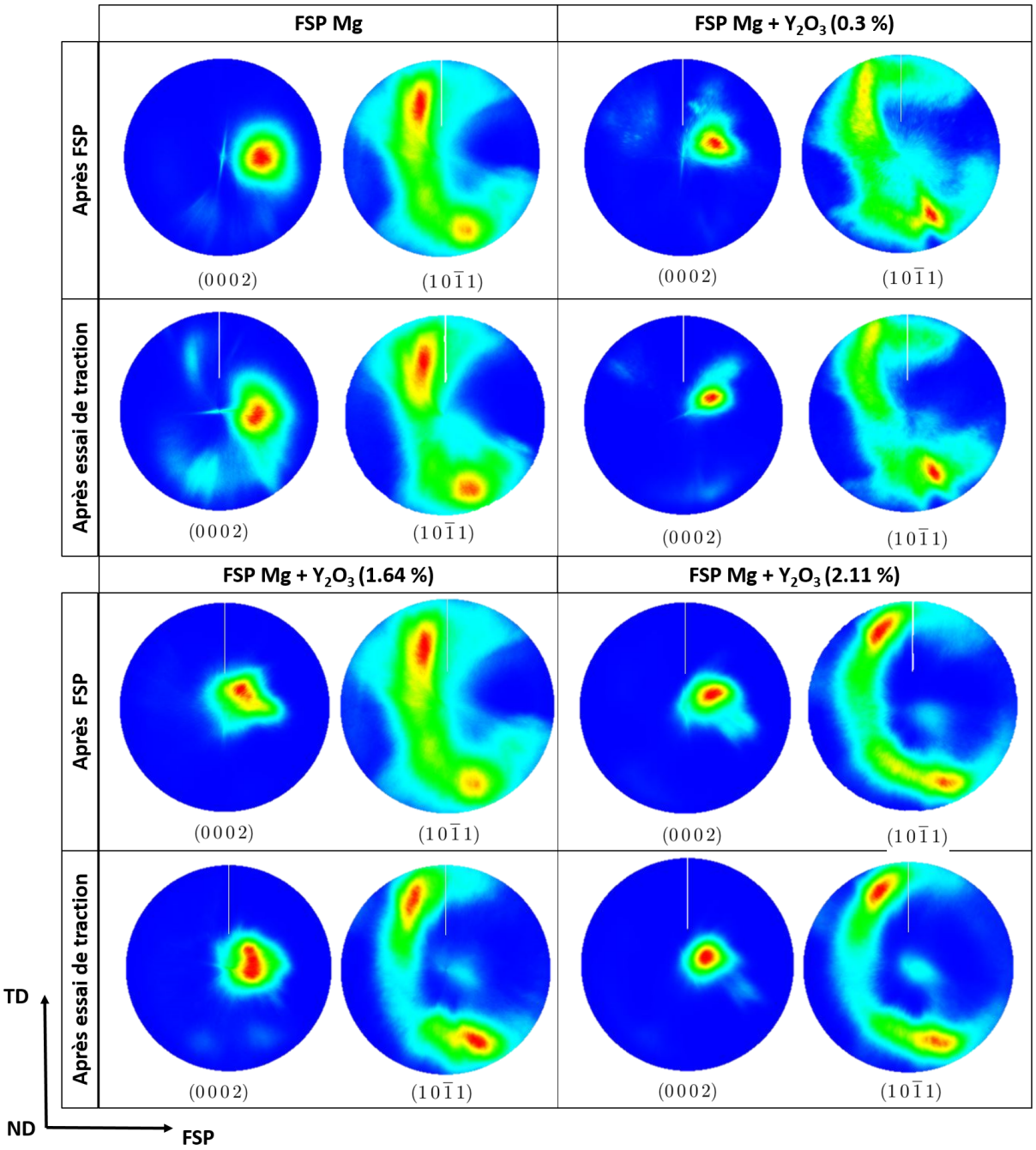

Figure 9 – Figures de pôle (0 0 0 2) et (1 0 $\bar{1}$ 1) incomplètes ($0° < \chi < 75°$) obtenues par diffraction aux rayons X des échantillons FSP Mg et FSP Mg + Y_2O_3 (0,3, 1,64 and 2,11 %) avant et après essai de traction. La direction de FSP est parallèle à la direction de chargement.

Essais de microcompression

Le comportement mécanique monocristallin du nanocomposite "modèle" (FSP Mg + Y_2O_3) sera comparé à celui du magnésium pur (FSP Mg) par des essais de mi-

crocompression. Comme décrit précédemment, des micropiliers monocristallins sont fabriqués dans un seul grain en utilisant un faisceau d'ions focalisés puis testés dans un nanoindenteur pour lequel l'indenteur a été remplacé par un embout plat. Ainsi, l'essai de nanoindentation est similaire à un essai de compression uniaxial à température ambiante. Des illustrations de l'essai de microcompression et d'un micropilier typique sont présentées sur la Figure 10 (a) et (b), respectivement.

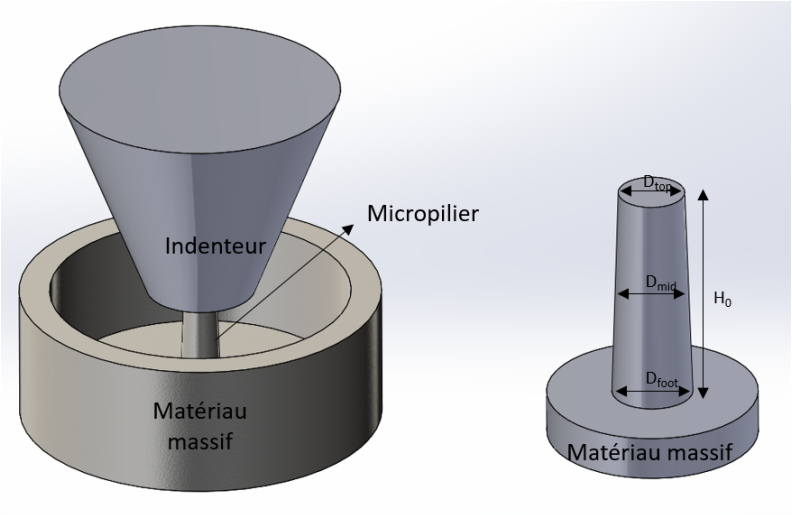

Figure 10 – Illustractions de l'essai de microcompression et d'un micropilier typique. $H_\circ$ correspond à la hauteur initiale du micropilier et D_{top}, D_{mid} et D_{foot} correspondent aux diamètres respectifs en haut, au millieu et en bas du micropilier.

Le principal objectif des essais de microcompression est de comprendre l'influence des particules d'Y_2O_3 sur les mécanismes de déformation plastique du magnésium, tant pour les mécanismes dépendants de l'orientation que ceux dépendant de l'effet de taille. Le comportement mécanique des micropiliers présentant une orientation favorisant le glissement basal ou bien le maclage de traction seront comparés, dans la mesure où ce sont les deux modes de déformation préférentiels à température ambiante. Différentes tailles de micropiliers seront également comparés: 2, 5, 10 et 15 μm (diamètre à mi hauteur).

Micropiliers favorablement orientés pour un glissement basal

Le comportement mécanique des micropiliers de 5 μm (diamètre à mi hauteur) favorables au glissement basal est présenté en Figure 11. Il est possible d'observer une augmentation de la contrainte jusqu'à une valeur critique à partir de laquelle une déformation plastique massive de la déformation (massive strain burst) se produit. Cette

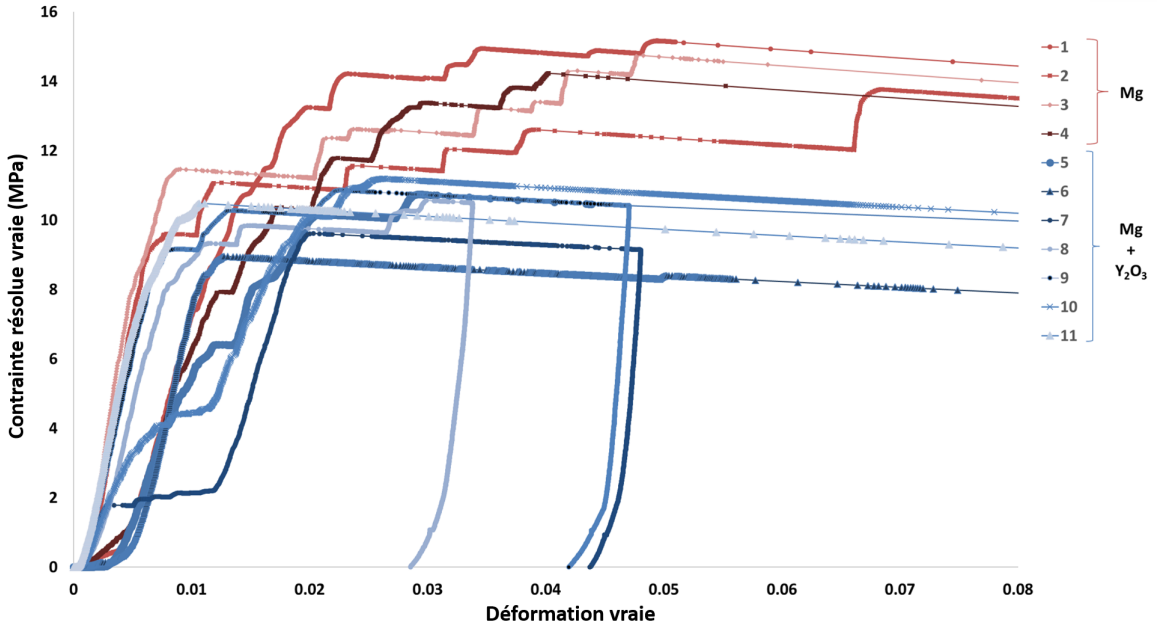

Figure 11 – Déformation vraie vs. contrainte résolue vraie pour les micropiliers de 5 μm favorables au glissement basal.

déformation massive est causée par le glissement basal comme l'illustre la Figure 12.

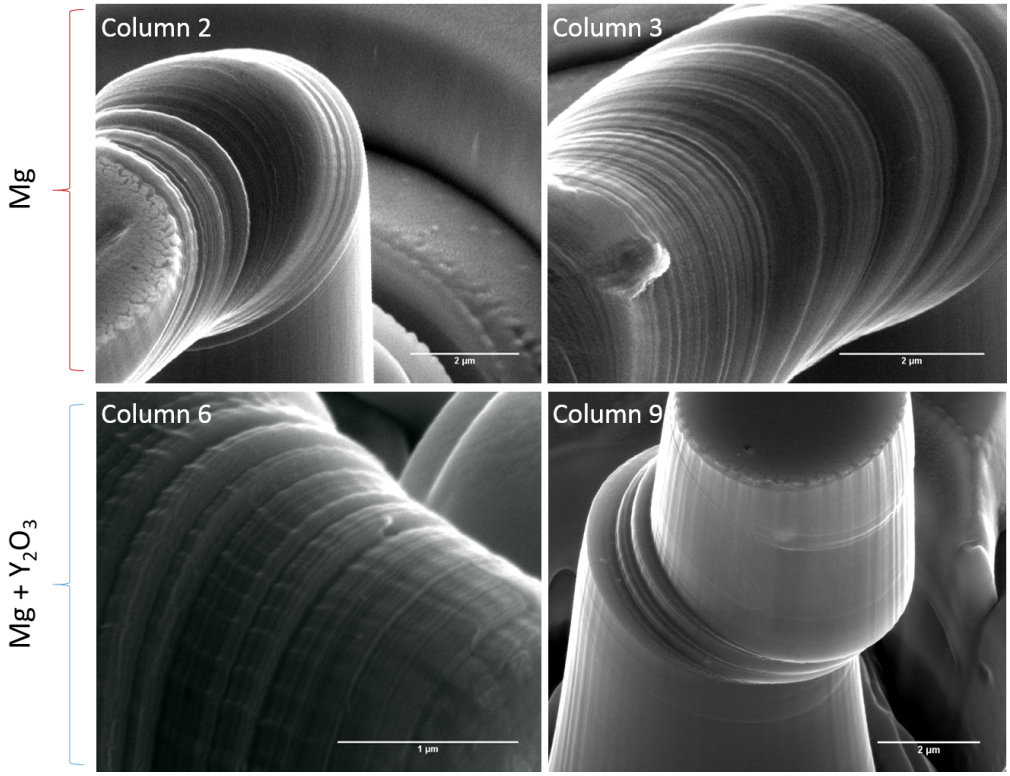

Figure 12 – Micrographies MEB des micropiliers déformés après déformation plastique massive de la déformation pour les micropiliers de 5 μm. Les micropiliers 2 et 3 correspondent au FSP Mg, tandis que les micropiliers 6 et 9 correspondent au FSP Mg + Y_2O_3 (Figure 11).

La contrainte critique pour l'activation de ce glissement basal massif est supérieur pour le FSP Mg que pour le FSP Mg + Y_2O_3. La densité de dislocations potentiellement mobiles, supérieure dans le cas du FSP Mg + Y_2O_3, est responsable de cette diminution. En effet, comme expliqué auparavant, la différence entre le coefficient de dilatation thermique du magnésium et celui de Y_2O_3 induit la génération de dislocations géométriquement nécessaires (GND) à l'interface entre les particules et la matrice lors du refroidissement. Les micrographies MET confirment une importante densité de dislocations à l'interface entre le magnésium et Y_2O_3 (Figure 13). Cette densité de dislocations supérieure devrait avoir un effet de renfort si on considère une augmentation de la contrainte nécessaire pour surmonter l'effet de forêt de dislocations. Néanmoins, dans le cas du magnésium, les dislocations sont majoritairement confinées dans des plans basaux parallèles entre eux. Ainsi, l'effet forêt est négligeable et la contrainte critique pour l'activation du glissement basal dépend seulement de la densité initiale de dislocations potentiellement mobiles: plus la densité est forte, plus le glissement plastique se déclenchera facilement.

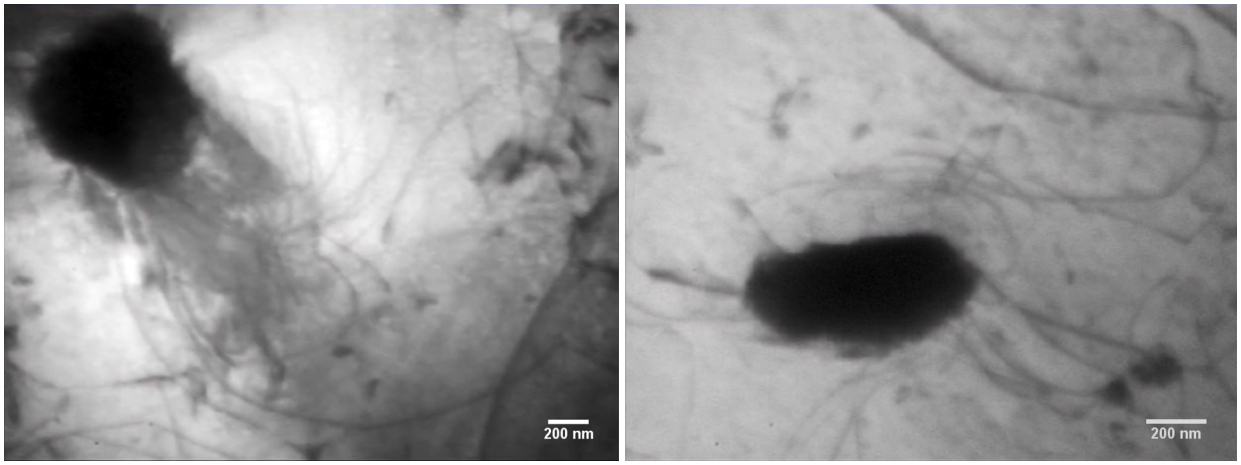

Figure 13 – Micrographies MET du nanocomposite "modèle" montrant une importante densité de dislocations à l'interface avec les particules d'Y_2O_3 (MET LaB_6 Jeol JEM-2010 à 130 kV).

La présence des particules d'Y_2O_3 a également un impact sur l'effet de taille. La Figure 14 montre que l'addition de particules d'Y_2O_3 atténue considérablement l'effet de taille observé dans le magnésium pur.

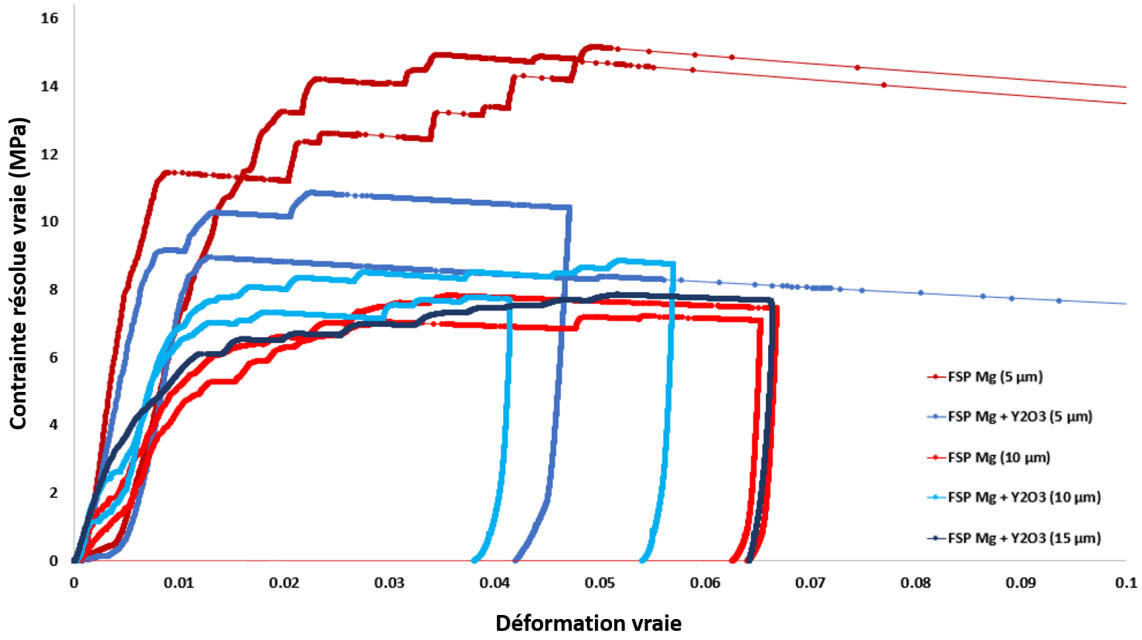

Figure 14 – Effet de taille observé sur la courbe déformation vraie vs. contrainte résolue vraie pour les micropiliers favorables au glissement basal. Un effet de taille très marqué est observé pour le magnésium pur, tandis que l'addition des particules d'Y_2O_3 atténue cet effet dans le FSP Mg + Y_2O_3.

Micropiliers orientés favorablement au maclage de traction

Les essais de microcompression réalisés sur des micropiliers orientés favorablement au maclage de traction montrent que la présence des particules d'Y_2O_3 diminue la contrainte nécessaire pour la propagation instable de la macle.

Les analyses EBSD des sections transverses des micropiliers de magnésium pur après les essais de microcompression montrent que la nucléation des macles a lieu dans la partie supérieure des micropiliers. Ceci s'explique par la concentration de contrainte à l'interface entre l'indenteur et le micropilier. Un maximum de deux macles a été observé dans les micropiliers de FSP Mg analysés. Au contraire, dans le cas du FSP Mg + Y_2O_3, de multiples macles semblent avoir nuclées à l'interface avec les particules d'Y_2O_3, comme le montre la Figure 15. De la même manière que pour les micropiliers favorables au glissement basal, l'addition des particules d'Y_2O_3 atténue l'effet de taille pour le maclage.

Comme exposé précédemment, le maclage de traction conduit a une réorientation cristalline de 86° par rapport à l'orientation initiale du cristal. Dans la zone maclée, l'axe c est pratiquement parallèle à l'axe de chargement. Cette nouvelle orientation n'est

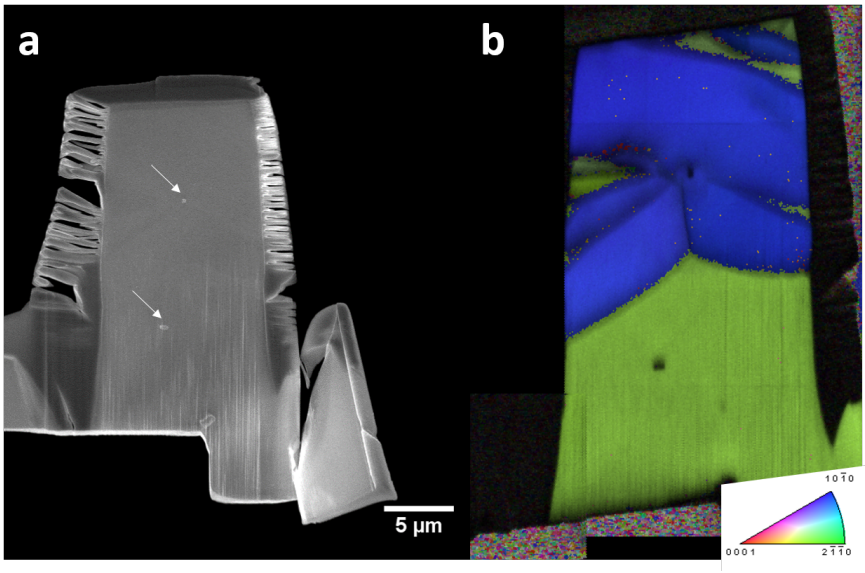

Figure 15 – De multiples macles, qui semblent avoir nuclées à l'interface des particules d'Y_2O_3 (flèches blanches) sont observées. En (a) une micrographie MEB et en (b) la cartographie EBSD de la même région.

pas favorable ni au glissement basal ni au maclage de traction. La déformation est accommodée par les six systèmes pyramidaux $\pi 2$ équivalents, qui ont un vecteur de Burgers $< c + a >$. L'activation et la multiplication de ses dislocations $< c + a >$ entraînent un écrouissage causé par l'interaction entre les dislocations (effet forêt). Après cette étape d'écrouissage, un effet de taille est observé dans le cas du FSP Mg + Y_2O_3, tandis qu'il était atténué par la présence de particules lors du maclage (Figure 16).

Essais *in situ* au MET

Pour étudier les mécanismes de renfort des particules, des essais *in situ* de cyclage thermique et de traction dans un MET ont également été réalisés sur le nanocomposite "modèle". Le premier mécanisme étudié est celui d'Orowan. La Figure 17 montre les différentes étapes au cours du cyclage thermique (échauffement jusqu'à 350°C), où deux dislocations sont mises en évidence par les flèches bleue et rouge. Dans un premier temps (de (a) à (f)), la dislocation 1 se courbe autour d'une particule d'Y_2O_3 jusqu'à la formation d'un jog (g). Ce jog persiste une fois que la dislocation a contourné la particule d'Y_2O_3 (h). Après avoir contourné cette particule d'Y_2O_3, la dislocation 1 rencontre une autre particule et le processus se répète. Dès que la dislocation 1 a contourné la première particule, la dislocation 2 commence a se courber autour de cette même particule ((i) à

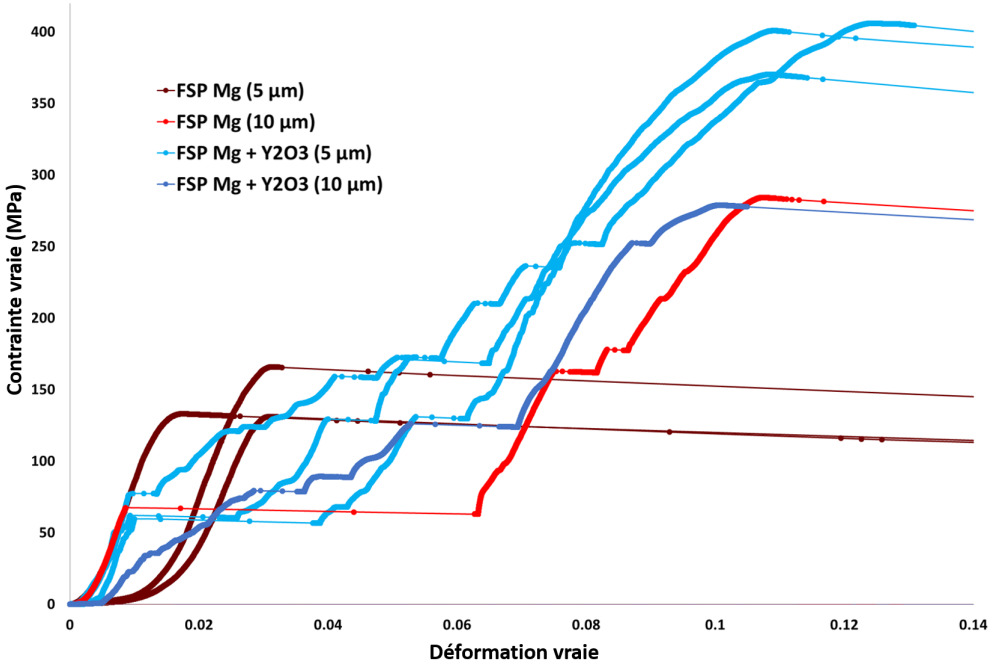

Figure 16 – Effet de taille observé sur la courbe déformation vraie vs. contrainte résolue vraie pour les micropiliers favorables au maclage de traction. Un effet de taille est observé après l'écrouissage du FSP Mg + Y_2O_3, tandis qu'il était atténué par la présence de particules lors du maclage.

(l)).

La Figure 17 montre que les dislocations se courbent autour des particules d'Y_2O_3 comme le prévoit l'effet Orowan. Une fois la dislocation passée, il n'est pas possible d'observer la présence d'une boucle de dislocation autour de la particule, mais un jog s'est formé. Ceci indique qu'il ne s'agit pas du mécanisme d'Orowan. Le mécanisme observé dans la Figure 17 peut plutôt être expliqué par le glissement des dislocations entre les différents plans présents dans les matériaux de structure cristalline hexagonal compacte. La Figure 18 schématise la formation d'un jog lorsque deux dislocations coin s'interceptent. Dans les matériaux de structure hexagonale compacte, si P_{AB} correspond au plan basal, le plan P_{XY} peut par exemple correspondre au plan pyramidal $\pi 2$. Comme les dislocations glissent beaucoup plus facilement dans le plan basal que dans le plan pyramidal $\pi 2$, le fléchissement de segments de dislocations est seulement dû à la difficulté de glissement des dislocations dans les plans non-basaux.

Le dernier mécanisme étudié est celui de génération de GNDs causé par la différence de coefficient de dilatation thermique. Il a déjà été discuté lors de l'étude des micropiliers favorables au glissement basal. La Figure19 confirme l'émission de GNDs à

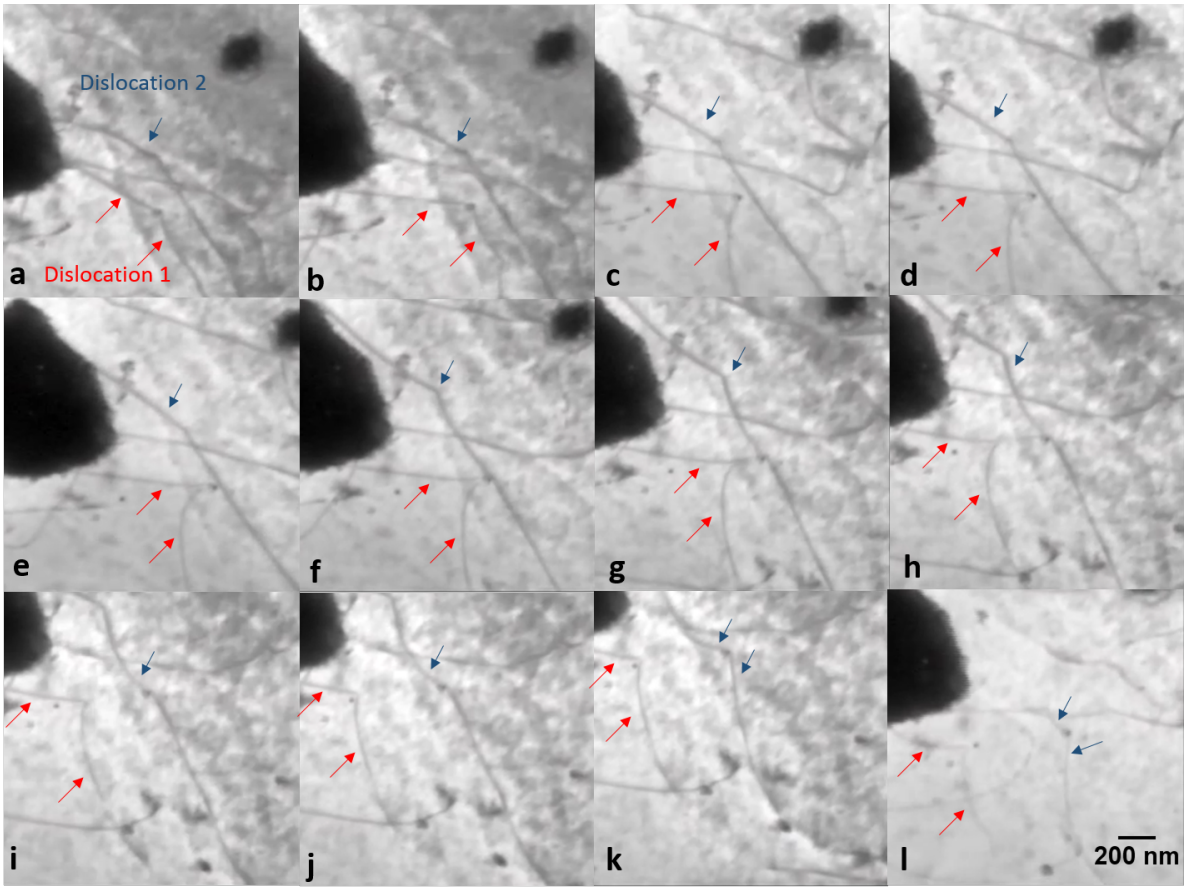

Figure 17 – Micrographies MET montrant les différentes étapes au cours d'un cyclage thermique (échauffement jusqu'à 350°C). Les dislocations se courbent lors qu'elles rencontrent des particules. De (a) à (f), la dislocation 1 se courbe autour d'une particule d'Y_2O_3 jusqu'à la formation d'un jog (g). Celui-ci persiste même après que la dislocation ait contourné la particule d'Y_2O_3 (h). Dès que la dislocation 1 a contourné la particule d'Y_2O_3, la dislocation 2 rencontre la même particule et se courbe autour d'elle ((i) à (l)).

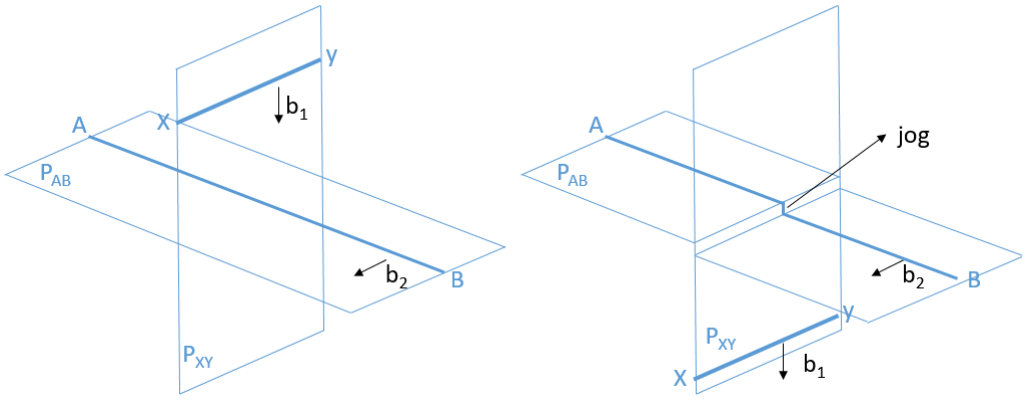

Figure 18 – Schéma de la formation d'un jog lorsque deux dislocations coin s'interceptent (d'après [5]).

l'interface avec des particules d'Y_2O_3 au cours d'un cyclage thermique entre la température ambiante et 350°C.

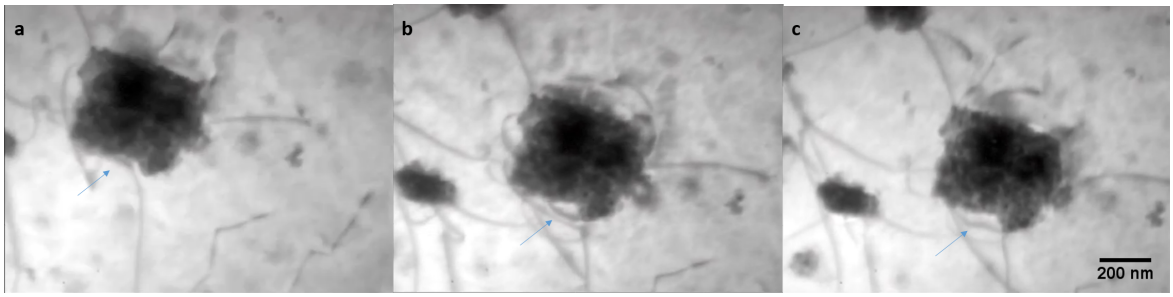

Figure 19 – Micrographies MET montrant différentes étapes du cyclage thermique (jusqu'à 350°C). Les flèches indiquent la génération des dislocations à l'interface avec les particules d'Y_2O_3.

Conclusion

Ce travail de thèse est centré sur l'étude des mécanismes de déformation plastique dans les nanocomposites à base de magnésium. A cette fin, un nanocomposite "modèle", présentant une dispersion homogène de particules d'oxyde, une microstructure grossière et une bonne stabilité des particules dans la matrice de magnésium, a été élaboré. Différentes techniques d'élaboration et différentes particules de renfort ont été considérées. Les meilleurs résultats ont été obtenus pour un nanocomposite renforcé par des particules d'Y_2O_3 élaboré par FSP. Le nanocomposite "modèle" a été caractérisé en 2 et 3 dimensions par différentes techniques, dont la nanoholotomographie aux rayons-X synchrotron et le MET.

Une étude du comportement mécanique multi-échelle a été réalisée en utilisant des échantillons polycristallins et monocristallins. Des essais de traction sur des éprouvettes millimétriques ont mis en évidence un effet de renfort de la part des particules même en faible fraction volumique (0,3 %). Des caractérisations microstructurales (mesures de la texture et de la taille de grains) ont prouvé que ce renfort n'était dû ni à un effet de taille de grain ni à une modification de la texture, mais bien à un effet direct de la présence des particules. Une étude plus poussée à l'échelle du monocristal a alors été réalisée par des essais de microcompression de micropiliers usinés par FIB dans des grains d'orientation choisie. À température ambiante, le magnésium se déforme majoritairement par glissement basal ou par maclage de traction. Ses deux orientations ont été étudiées

afin de voir l'influence de la présence des particules.

Les essais sur les micropiliers favorables au glissement basal ont montré un faible effet de renfort de la part des particules. La présence de particules d'Y_2O_3 a cependant atténué l'effet de taille normalement observé pour le magnésium à cette échelle. Ce phénomène s'explique par la présence d'une densité de dislocations mobiles supérieure dans le nanocomposite.

Dans le cas du maclage de traction, la présence des particules d'Y_2O_3 semble faciliter la nucléation des macles dû à l'hétérogénéité de la microstructure qui génère des concentrations de contraintes autour des particules. Les particules d'Y_2O_3 modifient également les mécanismes de déformation plastique par la nucléation de multiples macles à l'intérieur d'un seul micropilier. Dans un micropiliers de magnésium pur, une seule (ou dans certains cas deux) macle est présente.

En complément des essais de microcompression, des essais *in situ* MET ont mis en évidence l'interaction des particules avec les dislocations. Ces observations participent à la compréhension du comportement polycristallin. Le renfort observé pour le nanocomposite "modèle" s'explique probablement par a un effet complémentaire de l'écrouissage et de durcissement structurel (interaction des particules d'Y_2O_3 avec des dislocations).

Introduction

Magnesium based composites have attracted much attention over the past few years as a promising solution to lightweighting, energy saving and emission reduction, especially for automotive and aerospace applications. With a specific weight as low as 1.74 g.cm^3, magnesium is the lightest of all structural metals. However, its strength needs to be improved in order to compete with other light metals such as aluminum and titanium alloys. In the past few years, several studies have focused on the reinforcement of magnesium and its alloys with oxide nanoparticles [6, 7, 8, 9, 10].

The use of magnesium nanocomposites as structural materials demands a fundamental study of their deformation mechanisms. Plasticity in magnesium, which has a hexagonal close packed crystal structure, is characterized by a very strong plastic anisotropy as well as a complex twinning activity. This strong plastic anisotropy is also responsible for the formation of a very strong texture in the case of wrought magnesium and magnesium alloys, which strongly modifies the macroscopic mechanical response. The development and proper understanding of magnesium and its alloys, as matrix for nanocomposites relies hence on the understanding of magnesium plasticity in the presence of nanoparticles.

The aim of the present study is the elaboration of a "*model*" particulate reinforced nanocomposite and its microstructural and mechanical characterization focusing on the effect of particles on the strengthening mechanism. In the present work, different processing techniques will be used and compared for the elaboration of this "*model*" material. A complete microstructural characterization of the obtained "*model*" nanocomposite, including the 3D distribution of the reinforcement and its morphology will be carried out in order to confirm a homogeneous dispersion of the particles.

The mechanical behavior will be investigated macroscopically using the polycristalline nanocomposite in order to confirm the strengthening induced by the particles

at macroscale. An investigation of the typical plastic behavior of the single crystalline nanocomposite will then took place. The choice of single crystalline specimens is motivated by the idea of eliminating the effects of grain boundaries and strain incompatibilities, isolating then the role of the particles and the crystal orientation in the strengthening mechanisms. This single crystal investigation will be based on previous studies performed by Lilleodden [1] and Kim [2] on the deformation mechanisms of magnesium single crystalline microcolumns. In these studies, it was shown that the deformation behavior is strongly affected by the initial crystallographic orientation and microcolumn size. Nevertheless, to the author's knowledge, there are no studies on the single crystalline deformation mechanisms of magnesium based nanocomposites reinforced with oxide particles. In this thesis, the plastic deformation of these nanocomposites will be studied by means of microcompression testing. Tensile and microcompression testing are performed on pure magnesium samples elaborated in the same conditions for comparison.

Outline

This PhD report is organized as follows:

- **Chapter 1** summarizes the theoretical background about magnesium and magnesium based nanocomposites. The deformation mechanisms in magnesium at room temperature, including dislocation slip and twinning are introduced. A short review about the processing techniques currently used for the elaboration of magnesium matrix nanocomposites is also presented. Theories regarding the strengthening mechanisms in metal matrix nanocomposites are discussed in the last section of this chapter.

- **Chapter 2** is dedicated to the description of the different characterization techniques used during this study. The microstructure of the nanocomposites was characterized using: optical microscopy, scanning electron microscopy, electron backscatter diffraction, transmission electron microscopy, tomography and X-ray diffraction.

- **Chapter 3** focuses on the two different processing techniques used for the elaboration of the "*model*" nanocomposite used during this study: ultrasound assisted casting (Section 3.1) and friction stir processing (Section 3.2). The processing conditions and parameters are described in details for each technique. A deep microstructural

characterization was performed for the nanocomposites obtained in order to select the most adequate one.

- **Chapter 4** presents the experimental mechanical investigations performed in the "*model*" nanocomposite selected in Chapter 3. It includes tensile tests of macroscopic samples, microcompression testing for different crystal orientations and *in situ* transmission electron microscopy mechanical testing (tensile testing and thermal cycling).

- Concluding remarks and perspectives are presented in the last chapter.

CHAPTER 1

State of the art

The current study focuses on the plastic behavior of magnesium based nanocomposites and the main purpose of this chapter is to review the theoretical background of magnesium and magnesium based composites. At first, the crystallography of magnesium and its deformation modes (slip and twinning) will be introduced. The procedure for the calculation of the Schmid factor in hexagonal close-packed crystals is also presented. The second part of this chapter introduces the magnesium based composites and nanocomposites along with the different recent processing routes. At last, a review about the main mechanisms responsible for the strengthening in composites and nanocomposites are discussed.

1.1 Magnesium

Magnesium is the lightest of all structural metals, with a density of only 1.74 $g.cm^{-3}$. It gives a huge potential to magnesium to compete with other light metals like aluminum and titanium whose densities are 2.7 $g.cm^{-3}$ and 4.1 $g.cm^{-3}$, respectively.

Magnesium has a hexagonal close-packed structure (hcp), as represented in Figure 1.1: the three axes a_1, a_2 and a_3 are 120° apart in the basal plane (in gray) while the vertical c-axis is normal to the basal plane. The planes and directions are indicated using the Miller-Bravais system with four indices ($hkil$). The lattice parameters c and a are, respectively, 5.21 Å and 3.21 Å.

The c/a ratio is an important parameter for hcp metals as it influences their plastic behavior (further details in Section 1.2.1). For an ideal hcp structure, the c/a ratio is 1.633. In the ideal hcp structure, the atoms are arranged in close packed layers stacked in the sequence ABAB. The atomic layer situated between two basal planes (Figure 1.1) is located in such a way that it covers one half of the valleys between the two basal planes. However, a deviation from the ideal c/a ratio is often noted. In the case of magnesium, the c/a ratio is equal to 1.623 [11], slightly lower than the ideal ratio. It means that the atoms are compressed along the c-axis.

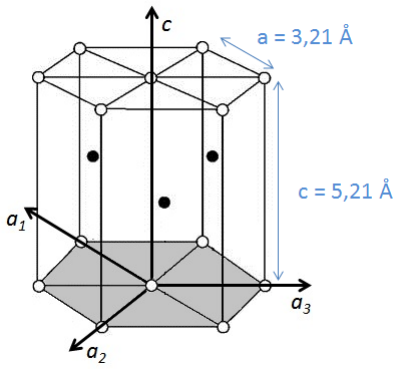

Figure 1.1 – Hexagonal close-packed structure of magnesium.

1.2 Deformation mechanisms in magnesium

The five more common deformation modes in magnesium (basal, prismatic, pyramidal $\pi 1$ and pyramidal $\pi 2$ slip systems and pyramidal $\pi 3$ tensile twin system) are presented in Figure 1.2. There are several equivalent slip and twinning systems, due to the symmetry of the hcp crystal, however, only one of each family is represented. Further explanation about the slip and twinning process are presented in sections 1.2.2 and 1.2.3, respectively. Table 1.1 summarizes the possible hexagonal close-packed slip systems.

At room temperature, only a limited number of slip systems can accommodate the plastic deformation. According to the Taylor/von Mises criterion [12, 13], at least five independent slip systems are theoretically needed in order to accommodate a given homogeneous deformation. The basal slip is the predominant slip mode in magnesium and it provides only two independent slip systems. The prismatic slip offers two additional independent slip systems. Basal, prismatic and pyramidal $\pi 1$ slip systems have a $< a >$ Burgers vector. As pyramidal $\pi 1$ slip produces a shape change equivalent to basal and

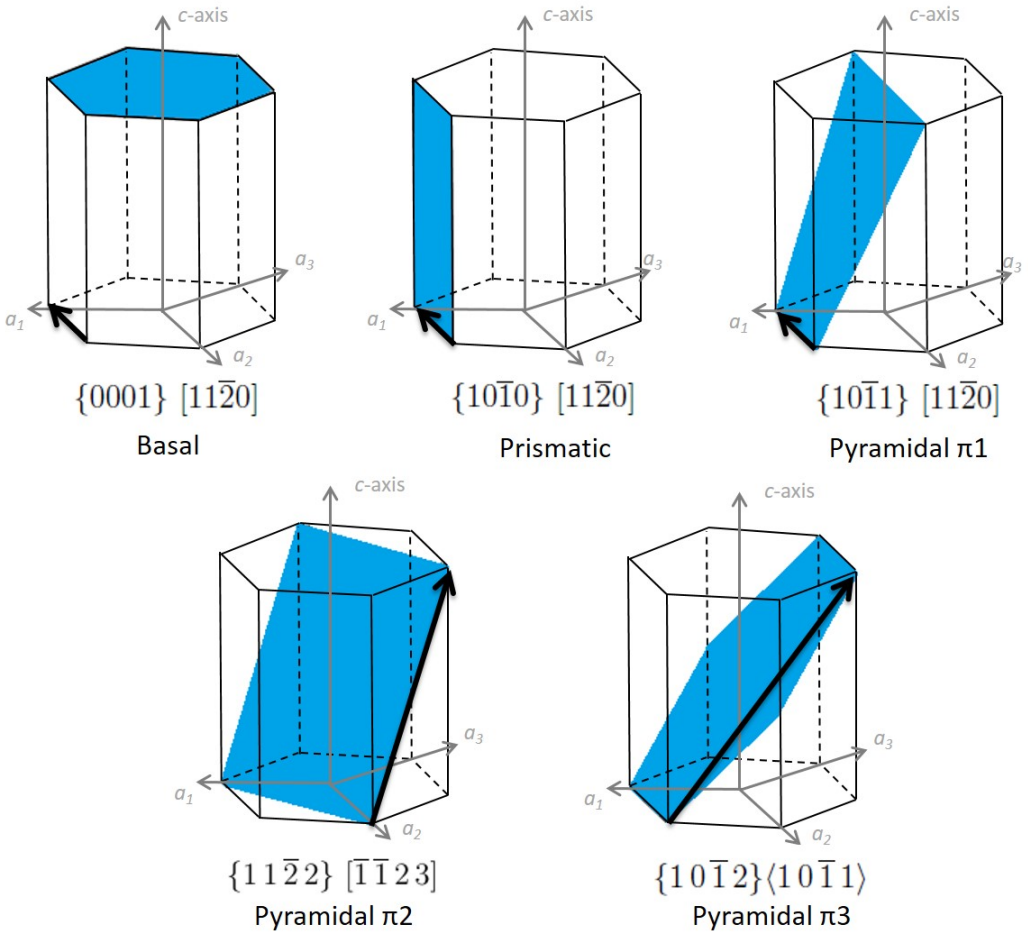

Figure 1.2 – Slip and twinning systems in magnesium with their respective Burgers vector (black arrow).

prismatic slip combined, basal, prismatic and pyramidal $\pi 1$ slip systems together represent only four independent slip systems and cannot fulfill the five independent slip systems.

According to Partridge [14], dislocations with a $< c >$ Burgers vector in magnesium are sessile. So, the deformation along the c-axis must be accommodated by either pyramidal $\pi 2$ slip or by mechanical twinning (also known as pyramidal $\pi 3$). The pyramidal $\pi 2$ slip mode provides hence five independent slip systems as mentioned in Table 1.1. With a Burgers vector of $< c+a >$, it allows a deformation part in the direction of the c-axis. However, the energy of the Burgers vector of the pyramidal $\pi 2$ slip system is greater than the one of other slip systems, so pyramidal $\pi 2$ slip is energetically less favorable [2]. The pyramidal $\pi 3$ mechanical twinning also helps to accommodate the strain along the $< c >$ direction (see Figure 1.6). However, the twinning shear can only accommodate a finite amount of strain. It provides then only 0.5 independent deformation modes [2]. In total, there are only 4.5 independent deformation modes in magnesium and the

Taylor/von Mises criterion is not satisfied.

Table 1.1 – Independent modes of deformation in hexagonal close-packed crystals.

Direction	**Plane**	**Cystallographic indices**	**Relative energy of dislocations**	**Number of independent mode**
$< a >$	Basal	$\{0\,0\,0\,1\}\ \langle 1\,1\,\bar{2}\,0\rangle$	$\|a\|^2$	2
	Prismatic	$\{1\,0\,\bar{1}\,0\}\ \langle 1\,1\,\bar{2}\,0\rangle$		2
	Pyramidal $\pi 1$	$\{1\,0\,\bar{1}\,1\}\ \langle 1\,1\,\bar{2}\,0\rangle$		4
$< c >$		$\{h\,k\,i\,0\}\ [0\,0\,0\,1]$	$3.67\ \|a\|^2$	
$< c+a >$	Pyramidal $\pi 2$	$\{1\,1\,\bar{2}\,2\}\ [\bar{1}\,\bar{1}\,2\,3]$	$2.63\ \|a\|^2$	5
Twinning	Pyramidal $\pi 3$	$\{1\,0\,\bar{1}\,2\}\langle 1\,0\,\bar{1}\,1\rangle$		0.5

1.2.1 Resolved Shear Stress

Slip only takes place once the resolved shear stress (RSS) on the slip plane in the slip direction reaches a critical value, called the critical resolved shear stress (CRSS). In order to calculate the resolved shear stress for a single crystal, it is necessary to know the direction of the applied force (F) with respect to the slip plane and the slip direction. Using the angles defined in Figure 1.3, the resolved shear stress is the ratio between the component of the stress along the slip direction (Fcosλ) and the area of the slip plane (A/cosϕ). Therefore, the resolved shear stress can be calculated by the following equation:

$$RSS = \sigma cos\phi cos\lambda \tag{1.1}$$

where the angle between the normal of the slip plane and the loading axis is ϕ and the angle between the slip direction and the loading axis is λ (Figure 1.3). The term $cos\phi cos\lambda$ is called Schmid factor (m). If the loading axis is normal (λ=90°) or parallel (ϕ=90°) to the slip plane, the Schmid factor is zero and no slip can occur. Reversely, if λ=ϕ=45°, the Schmid factor is maximum with m=0.5.

The c/a ratio affects the plastic behavior of a material. Typically, the CRSS for the activation of the pyramidal $\pi 2$ systems ($< c+a >$ Burgers vector) will change if the planes are more or less tilted in comparison with the c axis [15, 16].

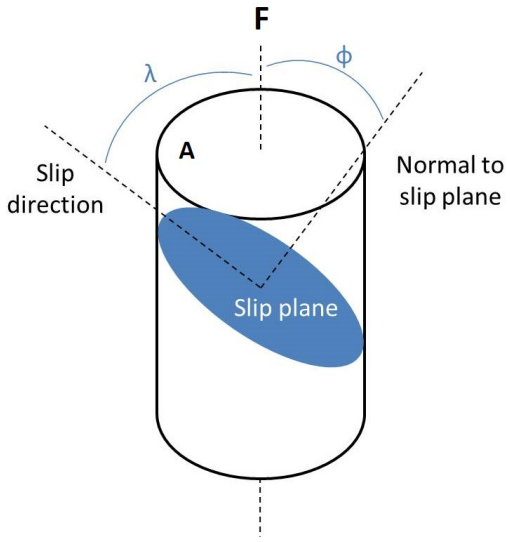

Figure 1.3 – Schematics for calculation of the resolved shear stress.

1.2.1.1 Schmid factor calculation for hcp materials

The Schmid factors for a specific loading axis will determine which deformation mode (slip or twinning system) will be more easily activated. It is hence very important in the investigation of slip and twinning in magnesium. The asymmetry of the c/a ratio and the use of the Miller-Bravais system with four indices make the calculation more difficult than for cubic metals. In the present work, the summarized equations for Schmid factor calculation in hcp materials are presented. Further details about the calculations can be found in Thomas *et al.*[17] and Kim [2].

In order to obtain the Schmid factor, it is necessary to calculate the inner product between the slip direction $[u_1v_1t_1w_1]$ and the loading axis $[u_2v_2t_2w_2]$ (angle λ) and between the loading axis $[u_2v_2t_2w_2]$ and the slip plane $(hkil)$ (angle ϕ). The Schmid factor can be calculated by multiplying equations 1.2 and 1.4.

$$cos\lambda = \frac{u_1u_2 + v_1v_2 + t_1t_2 + \theta^2w_1w_2}{(u_1^2 + v_1^2 + t_1^2 + \theta^2w_1^2)^{0.5}(u_2^2 + v_2^2 + t_2^2 + \theta^2w_2^2)^{0.5}} \tag{1.2}$$

where for magnesium,

$$\theta^2 = \frac{2}{3}(\frac{c}{a})^2 = 1.756 \tag{1.3}$$

$$cos\phi = \frac{u_2h + v_2k + t_2i + w_2l}{(u_2^2 + v_2^2 + t_2^2 + \theta^2 w_2^2)^{0.5}(h^2 + k^2 + i^2 + \theta^{-2}l^2)^{0.5}} \tag{1.4}$$

In the present work, the Schmid factor of the five main deformation modes in magnesium (basal, prismatic, pyramidal $\pi 1$ and pyramidal $\pi 2$ slip systems and pyramidal $\pi 3$ tensile twin) will be calculated for each grain orientation in order to predict which system will be activated first.

1.2.2 Deformation by slip

Slip occurs by the movement of dislocations in a certain slip plane. This movement leads to the formation of steps at the crystal's surface that can be visible with high resolution microscopes. The length of these steps is characterized by the Burgers vector. The orientation of the crystal remains the same after plastic slip. Figure 1.4 shows a schematics of the slip process.

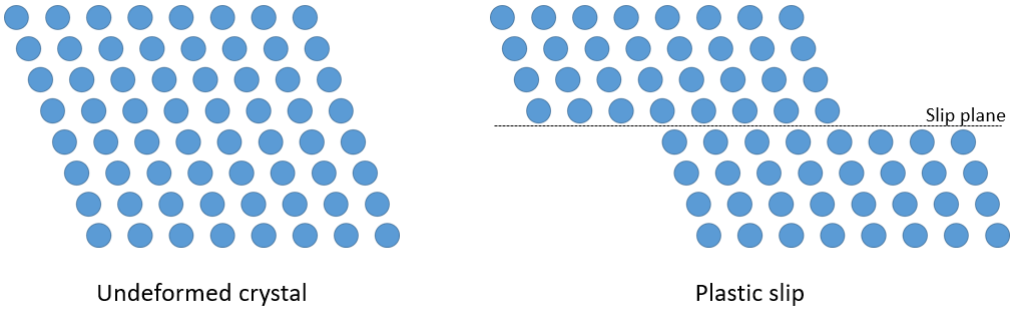

Figure 1.4 – Schematic of the plastic slip.

The slip systems that can be activated in magnesium have been presented in Figure 1.2. For a similar Schmid factor, if the CRSS of a certain slip system is lower than the others, this slip system will be activated first. It was observed experimentally that the predominant deformation mode for magnesium, at room temperature, is basal slip (plane $\{0\,0\,0\,1\}$) along direction $\overrightarrow{a_1}$, $\overrightarrow{a_2}$ or $\overrightarrow{a_3}$) [18]. It can be concluded that basal slip systems have the lowest CRSS. According to the literature [19, 20], the CRSS for activation of basal slip is 0.5 MPa. The CRSS for activation of the different slip systems in magnesium are presented in Table 1.2.

It has already been mentioned in Section 1.2, that only 4.5 independent slip

Table 1.2 – CRSS for activation of the different slip systems in magnesium at room temperature.

Slip system	**CRSS (MPa)**	**Reference**
Basal	0.5	[19, 20, 21]
	0.6	[22]
	0.76	[23]
	0.81	[24]
Prismatic	39.2	[25]
	50	[26]
	22	[27]
	23.7	[28]
Pyramidal $\pi 2$	102	[29]
	90-92	[28]

modes are available for magnesium: 2 for basal slip, 2 for prismatic slip and 0.5 for twinning. Since the Taylor/von Mises criterion is not satisfied, several studies have focused on the understanding of slip mechanisms in magnesium single crystals and especially the role of non basal slip systems. Reed-Hill *et al.* [25] and Yoshinaga *et al.* [18] have performed tensile tests on magnesium single crystals with a basal plane parallel to the loading direction in order to activate non-basal slip systems. These studies have proved that prismatic slip was the predominant deformation mode at room temperature under these conditions. At higher temperature, pyramidal $\pi 1$ slip also contributes to deformation [18], but is not an important mode of plastic deformation at room temperature [30]. Later, Tegart £*et al.* [31] have shown non-basal slip systems having a component in the *c*-axis operating in hcp crystals. Obara *et al.* [32] have proved the evidence of $< c+a >$ slip in single crystals at elevated temperatures. Recently, Wu and Curtin [33, 34] have shown using molecular dynamics simulations that $< c+a >$ dislocations undergo a thermally activated transition into basal-dissociated dislocations, which are sessile.

1.2.3 Deformation by twinning

The understanding of twinning has a key role in the study of the plastic deformation of magnesium: twinning is a major deformation mode, along with basal slip, at room temperature and can accommodate the deformation along the *c*-axis. Twinning takes place by the translation of atoms in order to accommodate the deformation. After

twinning, the twinned portion of the crystal is a mirror image of the parent crystal (see Figure 1.5). It is a directional mechanism that cannot be reversible, differently from dislocation slip which is reversible. This one-directional character allows the contribution with only 0.5 independent deformation mode (see Section 1.2). Another difference between slip and twinning is that slip occurs in multiples of the atomic spacing, while during twinning the atoms movements are inferior to interatomic distances [11].

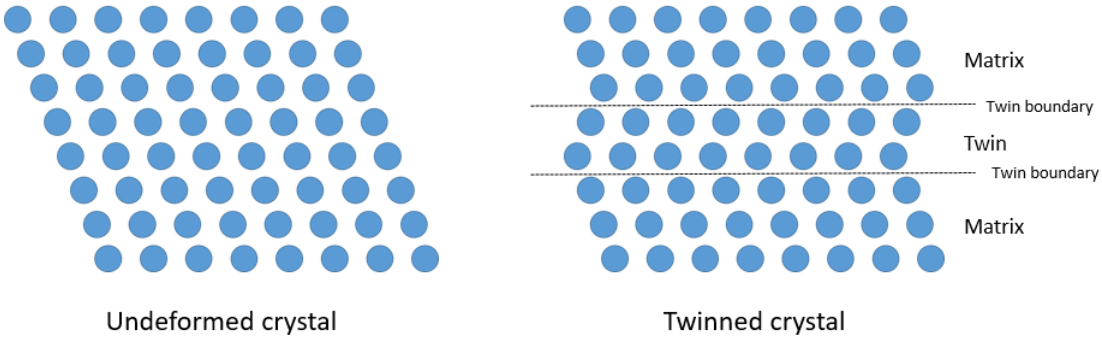

Figure 1.5 – Schematic of the twinning.

In magnesium, three twinning systems have been identified and are summarized in Table 1.3. The twins that can be activated are classified in two modes according to

Table 1.3 – Summary of the twins that can be activated in magnesium.

Stress	**Twin plane**	**Direction**	**Rotation axis**	**Re-orientation [35]**	**CRSS (MPa)**
Compression	$\{1\,0\,\bar{1}\,1\}$	$\langle 1\,0\,\bar{1}\,\bar{2}\rangle$	$[1\,1\,\bar{2}\,0]$	56°	114 [36]
Extension	$\{1\,0\,\bar{1}\,2\}$	$\langle 1\,0\,\bar{1}\,\bar{1}\rangle$	$[1\,1\,\bar{2}\,0]$	86°	2-3 [37]
Compression	$\{1\,0\,\bar{1}\,3\}$	$\langle 3\,0\,\bar{3}\,2\rangle$	$[1\,1\,\bar{2}\,0]$	64°	-

how the load (compression or tensile) is applied with respect to the c-axis. $\{1\,0\,\bar{1}\,2\}$ twins are expected when a tensile stress is applied along the c-axis, whereas $\{1\,0\,\bar{1}\,1\}$ and $\{1\,0\,\bar{1}\,3\}$ twins are expected when a compression stress is applied along the c-axis. The so-called extension twins (or tensile twins), $\{1\,0\,\bar{1}\,2\}$ twins, lead to an extension along the c-axis and a reorientation of the c-axis in the twin of about 86° around the $[1\,1\,\bar{2}\,0]$ axis. On the other hand, the compression twins lead to a contraction along the c-axis. The reorientation of twinned volume after $\{1\,0\,\bar{1}\,1\}$ and $\{1\,0\,\bar{1}\,3\}$ twins is, respectively, 56° and 64° around the $[1\,1\,\bar{2}\,0]$ axis. The $\{1\,0\,\bar{1}\,2\}$ twins are most commonly observed

in magnesium. A schematics of the re-orientation of the crystal in the twinned region in the case of $\{1\,0\,\bar{1}\,2\}$ extension twinning and $\{1\,0\,\bar{1}\,1\}$ compression twinning is presented in Figure 1.6. The twinning system more easily activated in magnesium is the $\{1\,0\,\bar{1}\,2\}$ $\langle 1\,0\,\bar{1}\,1\rangle$ (Figure 1.2).

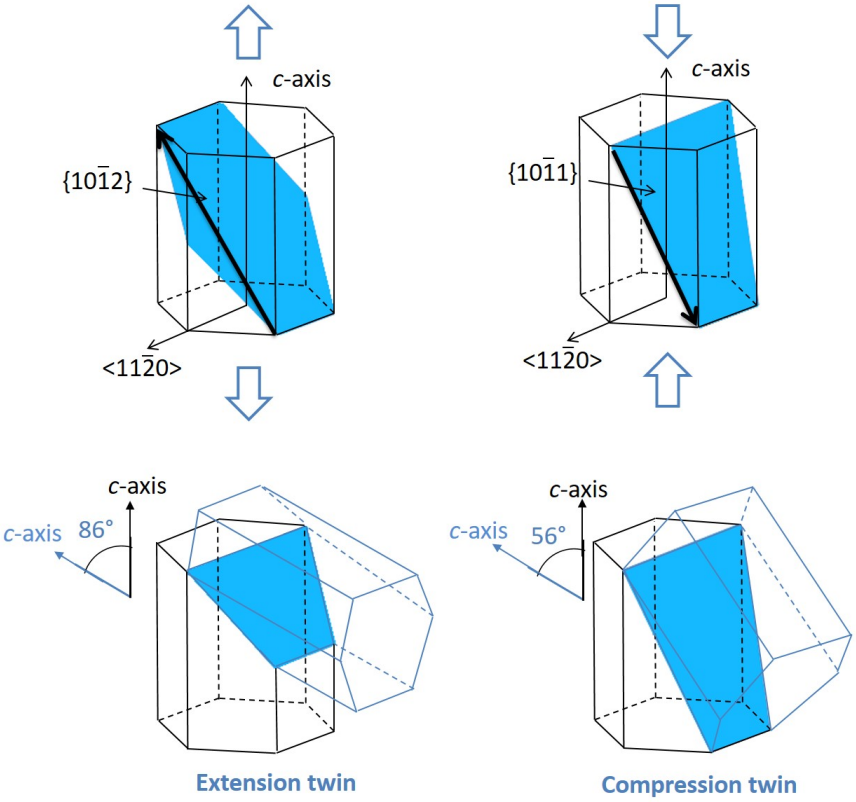

Figure 1.6 – Schematics of the re-orientation of the crystal in the twinned region during $\{1\,0\,\bar{1}\,2\}$ extension twin and $\{1\,0\,\bar{1}\,1\}$ compression twin.

In a polycrystal, twinning is described as a two (sometimes three) steps mechanism occurring inside a grain (nucleation, propagation and growth). Wu *et al.* [38] proposed a model that explains the twin nucleation, propagation and growth in magnesium polycrystals (Figure 1.7(a)). The twin nucleates at a stress concentration zone (like a grain boundary) and propagates until it reaches an obstacle (other side of the grain boundary, for example) to form a twin band that will grow by thickening. Figure 1.7(b) represents the twinning process as a function of twinning resistance ($\widehat{\tau}^{\alpha}$) and the volume fraction of the twin f^{α}. The stress ($\widehat{\tau}^{\alpha}$) must overcome a high resistance $\tau_{\circ}^{\alpha}$ for the twin to nucleate. Once the twin has nucleated, there is a stress relaxation in the propagation stage. The twin propagates spontaneously and form a twin band. Further work-hardening of the material in the twin leads to twin thickening.

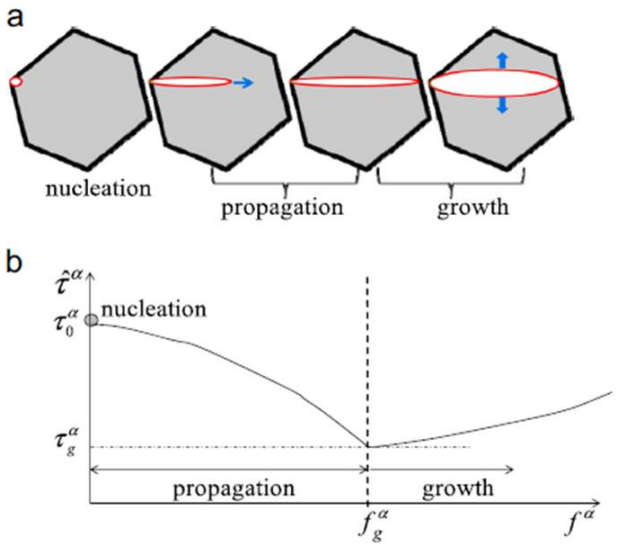

Figure 1.7 – Schematic representation of twin nucleation, propagation and growth (a). In (b), the stress relaxation process is represented in terms of twinning resistance $\widehat{\tau}^\alpha$ as a function of the twin volume fraction f^α [38].

As mentioned in Chapter 1.2, plastic slip develops in a given slip system when the resolved shear stress reaches the CRSS. There is still a debate in the literature whether twinning nucleation also depends on the CRSS or not. Some studies [39, 40] support the applicability of the CRSS and the Schmid's law. However, other studies [41, 42] disagree, debating that some potential twins subjected to a high resolved shear stress are not observed experimentally, while other twins, that are not favorable, are evidenced. Beyerlein *et al.* [43] have employed two different CRSS for twin nucleation and growth in hcp crystals: a larger CRSS for the twin to nucleate and a smaller one for the twinning growth.

Studies assuming a CRSS for twin activation show that the CRSS for the activation of $\{1\,0\,\bar{1}\,2\}$ extension twinning is much lower than the one required for activation of $\{1\,0\,\bar{1}\,1\}$ compression twinning: the CRSS for $\{1\,0\,\bar{1}\,2\}$ and $\{1\,0\,\bar{1}\,1\}$ twins are respectively, 2-3 MPa [37] and 114 MPa [36]. It explains why extension twins are more common in magnesium.

As it has already been mentioned that twinning contributes to the accommodation of the deformation in the $< c >$ direction, but it has another contribution to plastic deformation: twinning may enhance the ductility due to the changes in texture [44]. Since the crystallographic orientation of the twin is different from the parent crystal, additional slip systems can be activated in the twinned region and accommodate the subsequent de-

formation. The parent orientations undergo twinning, while the twinned regions undergo slip if further loading is applied. This contribution has an important influence especially in single crystals. Since no grain boundary (that could stop twin propagation) are present in single crystals, almost the whole volume can be twinned once the twin is nucleated.

In the previous section (Section 1.2.1), the c/a ratio was shown to affect the activation of a certain slip system. Additionally, the c/a ratio also affects the twinning behavior of magnesium. Yoo [45] has shown that the nucleation of a certain twinning system is affected by the c/a ratio. Figure 1.8 shows the relation between the twinning shear and c/a ratio for the six most common twinning systems in hcp materials.

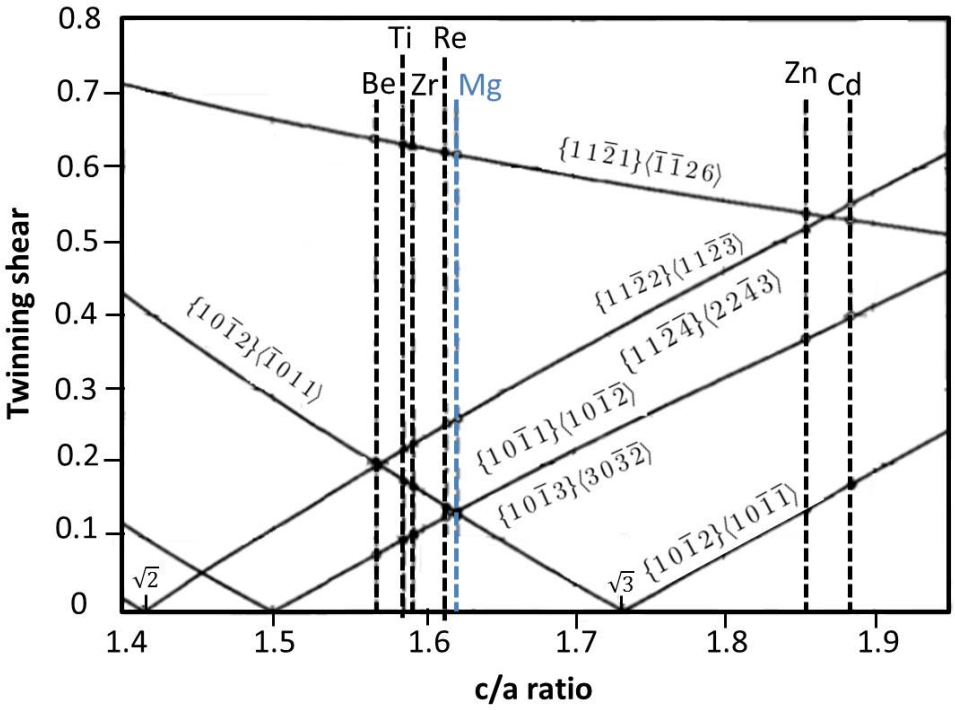

Figure 1.8 – Relation between the twinning shear and the c/a ratio for hcp materials, according to [45].

A positive slope in Figure 1.8 causes a contraction along the c-axis, while a negative slope causes an extension along the c-axis. The $\{1\,0\,\bar{1}\,2\}$ twin reverses its shear direction at a twinning shear of $\sqrt{3}$ and it acts as an extension twinning in the case of magnesium. Usually a higher occurrence of a certain twin mode is related to a lower value of twinning shear. In the case of magnesium, the extension twins are the more commonly observed and present a twinning shear of 0.129 [45].

1.3 Magnesium based nanocomposites

As it has already been mentioned in Section 1.1, magnesium is an excellent candidate to replace aluminum and titanium in applications that require lightweighting due to its low density. However, its low yield stress and ductility limit its use as a structural material. There are several alternatives to increase the mechanical properties of magnesium: alloying, microstructural modifications (decrease of the grain size, for example) and development of composites. In the past few years, attention has been focused on the use of reinforcements in both pure magnesium and magnesium alloys attempting to improve their mechanical properties. The reinforcements may consist of hard ceramic particles (like Al_2O_3, Y_2O_3, SiC, SiO_2), fibers, carbon nanotubes...

The first studies of magnesium based composites (1980s and 1990s) have used micro-sized reinforcements. Hack *et al.* [46] have successfully elaborated one of the first magnesium based composites using a commercially pure magnesium and long continuous Al_2O_3 fibers (diameter 20 μm). A high volume fraction of reinforcement (35 % and 55 %) have been employed. Later, Schröder *et al.* [47] have used liquid infiltration of fiber-particle preforms (mixture of fibers and particles) to elaborate magnesium matrix composites. SiC particles (6 μm diameter) and Al_2O_3 short fibers (3 μm diameter and 150-300 μm length) were used as reinforcement. A significant increase of the mechanical properties could be obtained: the yield strength of the composite was 40 % higher than the one of the unreinforced matrix.

Magnesium composites elaborated using AZ91 magnesium alloy and 20 % (volume fraction) of short Al_2O_3 fibers were studied by Purazrang *et al.* [48]. The cylindrical fibers were 150 μm long and had a diameter of 3 μm. This reinforcement phase have helped to increase the tensile strength of the AZ91 at room temperature. However, the resulting composites had a lower ductility. The reduction of the ductility is a common problem when using micrometer-sized reinforcements. The main reasons are the particle or fiber cracking, due to preexisting defects inside the reinforcement, or the presence of porosities at the reinforcement/matrix interface, which accelerate failure [49]. Furthermore, Purazrang study [48] has shown by fractographic examination that cracks can initiate at the interface between the matrix and the fibers. It supports the theory that probably the bonding between the fibers and the magnesium matrix was weak.

Vaidya *et al.* [50] have used 15 μm and 52 μm-sized SiC particles as reinforcement

for AZ91D magnesium alloy. The tested volume fractions of particles were 20% and 25%. The addition of SiC particles increases the strength and the elastic modulus of the alloy. This study also evidenced that the improvement of the strength using 15 μm-sized SiC was more significant when compared with the bigger particles. Thus, the reduction of the reinforcement size seems to have a beneficial effect on the mechanical properties.

Since 2000, most of the studies have been focusing on the addition of nanoparticles that have a beneficial effect on the improvement of the mechanical properties of magnesium without decreasing its ductility [51, 52]. Wong *et al.* [53] have studied the influence of the addition of micrometer- and nanometer-sized SiC reinforcement on the mechanical properties of pure magnesium. The composite reinforced with 50 nm-sized SiC had a higher yield strength and ultimate tensile strength when compared to the composite reinforced with 25 μm-sized SiC. Such improvement was reached using a volume fraction of only 1 % for the nanometer-sized SiC, ten times inferior than the one used for the micronmeter-sized SiC. At the same time, the ductility was five times superior when using the nano-sized SiC. Such an improvement is attributed to the ability of nanometric particles to activate non-basal slip systems [54]. Hence, the use of nanoreinforcements allows an improvement of the mechanical properties even for a low volume fraction of reinforcements.

Similarly, Hassan *et al.* [55] has shown that the addition of only 1.1 % (volume fraction) of Al_2O_3 particles could almost double the yield strength and the ductility of pure magnesium. Nanocomposites elaborated with magnesium and 0.22 vol.% of Y_2O_3 have reached an increase of the yield strength (+124 %) and ductility (+71 %) [56]. This increase is followed by a reduction of grain size from 50 μm for pure magnesium to 10 μm for the nanocomposite. The reduction of the grain size can explain the strengthening observed in this case. The strengthening mechanisms in nanocomposites will be further discussed in Section 1.4.

The evolution of the magnesium based composites since the 1980s is summarized in Table 1.4. It is possible to notice a strong reduction of the reinforcement size with the years, accompanied with a reduction of the volume fraction of reinforcement phase. The recent need of development of lighter materials is responsible for the incredible increase of scientific studies published in this area (the number of papers published has been estimated according to Google Scholar [57]).

Table 1.4 – Evolution of the research activity on magnesium based composites.

Period	Reinforcement size/shape	Volume fraction	Number of publications	References
1980-	Continuous fibers Preform[1]	10-80%	< 70	[58], [59] [60], [61]
1990-	Fibers (length>100 μm) Oxide particles (6-50 μm) Preform	10-50%	< 130	[50], [47], [62], [63], [48], [64]
2000-	Nanoparticles (<60 nm) Microparticles Short fibers Preform	0.5 - 2% (particles) <25% (fibers and preform)	< 450	[65], [56], [66], [67], [68], [69], [70]
2010-	Nanoparticles (< 50 nm) Nanotubes Whiskers	< 14%	> 800	[6], [7], [10], [4], [71], [72], [73], [74]

1.3.1 Processing of magnesium based nanocomposites

In order to achieve the desired mechanical properties in the nanocomposite, the reinforcement particles must be well dispersed in the metal matrix. However, an homogeneous dispersion of nanoparticles is difficult to achieve. The main issues of concern in the processing of magnesium based composites is the low wettability of the reinforcing phase (usually ceramic nanoparticles) by the molten metal and the dispersion of the particles. The particles tend to agglomerate and form clusters which are difficult to break, leading to an inhomogeneous distribution of particles within the matrix. The main reason is the high surface-to-volume ratio of the nano-sized particles. A strong bonding between the nanoparticles and the matrix is necessary to obtain an effective load-transfer mechanism (further details are given in Section 1.4).

Several processing routes to fabricate nanocomposites have been proposed and the most widely used are described below. Some examples of magnesium based nanocomposites elaborated by each technique are also described.

[1] Three dimensional fabric forms designed with a specific shape

1.3.1.1 Solid processes

Powder metallurgy

Powder metallurgy was one of the first methods developed for processing magnesium matrix nanocomposites due to the difficulty of wetting nanoparticles with the molten metal when using liquid processes. In powder metallurgy, magnesium and the reinforcement powders are first mixed to achieve the desired composition and uniform dispersion of the reinforcement. The mixture is then compacted, degased and sintered at a given temperature under controlled atmosphere or vacuum [75]. A schematic of the powder metallurgy process is presented in Figure 1.9. The most common techniques for powder compaction are hot isostatic pressing (HIP), hot pressing, cold isostatic pressing (CIP) or cold pressing [52]. The sintering can be performed using conventional resistance furnace, microwave-assisted rapid sintering and spark plasma sintering (SPS). The SPS method is effective in obtaining fully dense materials [76].

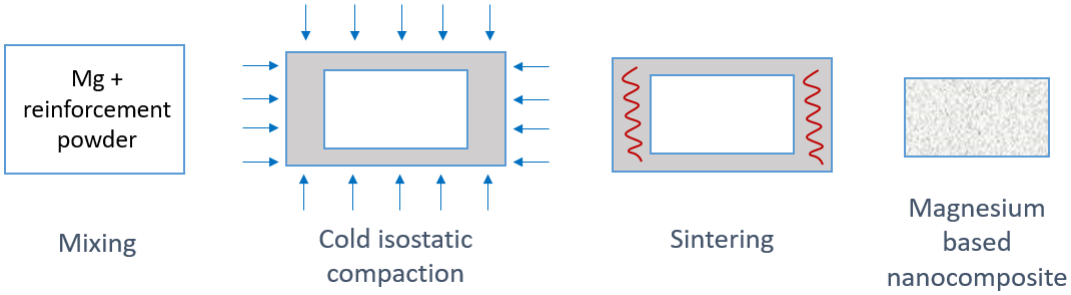

Figure 1.9 – Schematics of a typical powder metallurgy process in the case of CIP.

Eugene *et al.* [66] have used powder metallurgy to elaborate Mg-SiC (1 vol.%) nanocomposites. Conventional sintering and microwave sintering were compared. The nanocomposites have shown an improvement of 10% in the microhardness, 26% in the yield stress and 31% in the ductility. The microwave sintered composites present the best improvement of the mechanical properties. Powder metallurgy has however the disadvantage of being expensive and not ideal for large scale production. Another drawbacks are the oxidization of the powders and the presence of porosities.

Mechanical alloying

Mechanical alloying is a powder metallurgy technique which uses high energy ball milling. The raw powders undergo repeated cold welding, fracturing and re-welding until obtaining fine powders. This technique usually allows the achievement of a good

dispersion of the nanoparticles due to the breaking of the particle clusters during ball milling. Some solid state chemical reactions between oxyde and metallic powder may also occur, leading to the formation of alloys. After milling, the powders are compacted (the different techniques of compaction are the same as for powder metallurgy) and sintered. Liu *et al.* [77] have synthesized Mg-Al_2O_3 nanocomposites by mechanical alloying and the obtained nanocomposites show an uniform dispersion of reinforcement particles. Ferkel *et al.* [8] have reinforced magnesium with SiC nanoparticles and compared conventional mixing and ball milling. The largest flow stress and lowest creep rates were found in the nanocomposite ball milled.

Friction stir processing (FSP)

FSP is a solid-state processing technique derived from friction stir welding. During the process, a non-consumable rotating tool penetrates in the material and advances along the processing area (Figure 1.10). The heat generated by the friction of the tool turns the material malleable. The material flow follows the movement of the tool, from the front to the back of the tool and around the pin, where it cools down [78]. It leads to a mechanical mixing between the particles and the base material and creates a strong plastic deformation. Different methods can be used in order to insert the reinforcing phase prior

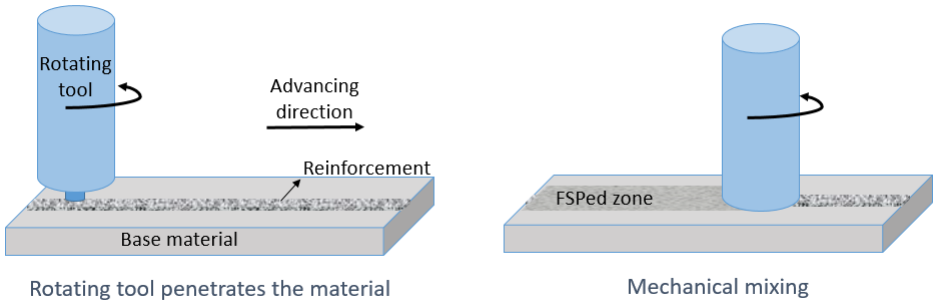

Figure 1.10 – Schematics of friction stir processing.

to FSP: particles or short fibers can be placed in grooves [79], holes [80], mixed with a solvent and then applied on the surface [81], deposited on the surface by thermal spraying [82] or woven into a fabric [72]. The different possibilities for disposal of reinforcements are schematically represented in Figure 1.11.

FSP has been employed to incorporate SiO_2 nanoparticles into an AZ61 magnesium alloy [83]. The SiO_2 particles lead to an improvement of the hardness and the wear property in the stirred zone (Figure 1.12). Faraji *et al.* [84] have incorporated 30 nm-sized Al_2O_3 particles. They have reported an improvement in the wear resistance

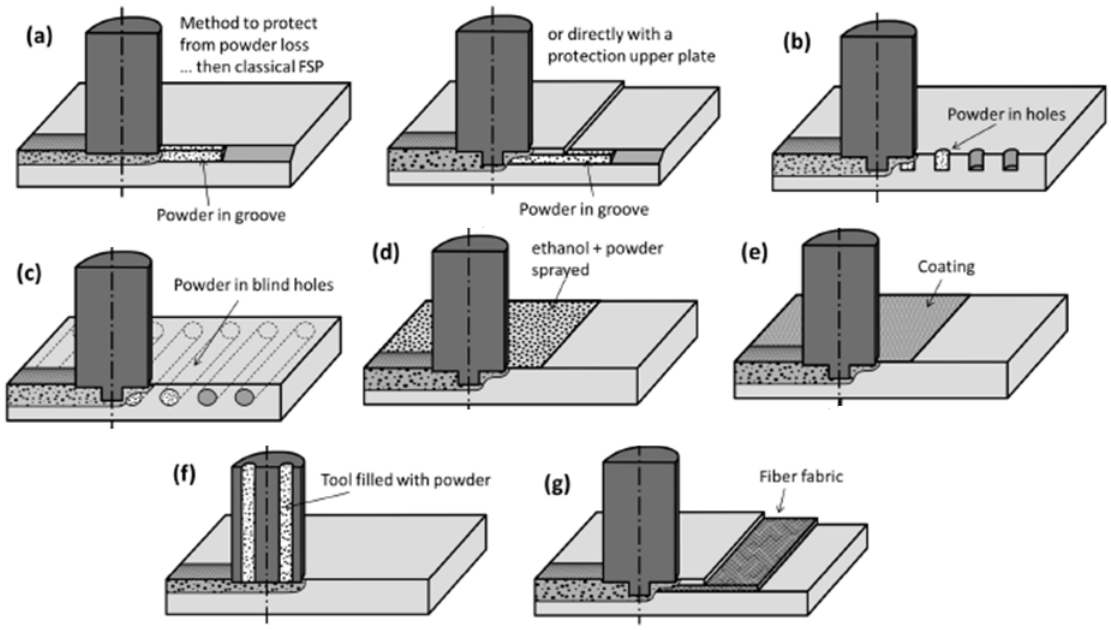

Figure 1.11 – Schematics of various reinforcement disposal methods: powder placed in grooves machined near the surface (a), powder placed in holes drilled near the surface (b), powder placed in blind holes (c), powder dispersed in ethanol and sprayed on the surface (d), coating prior to FSP (e), consumable composite pinless tool (f) and fabric stacked between two plates (g) [78].

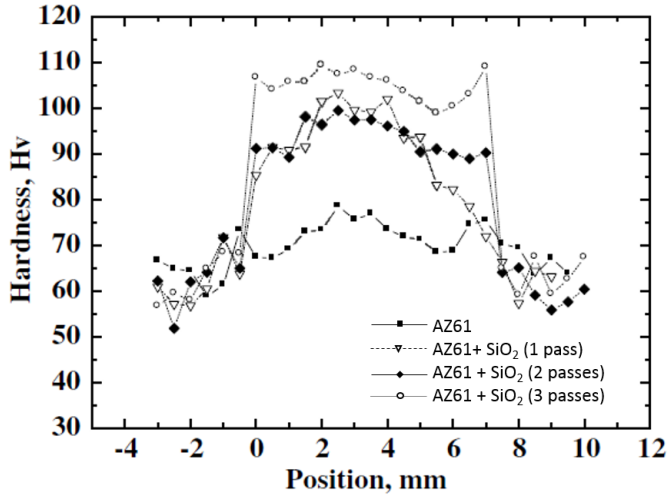

Figure 1.12 – Variation of the microhardness distribution in the base material (AZ61) and the composites (AZ61 + SiO_2) in the FSPed zone [83].

for the composite and shown the importance of the processing parameters for obtaining a better particle distribution. Short carbon fibers were incorporated in different magnesium alloys (AZ31B and AZ91D) using FSP [72]. The presence of the reinforcement reduces the grain size and increases the yield strength from 15 to 25%.

1.3.1.2 Liquid processes

Ultrasound assisted casting

Severe aggregation of nanoparticles frequently occurs for composites prepared by conventional liquid metallurgy [52]. In addition to the poor wettability, the nanoparticles tend to float on the top of the molten bath even if their density is superior to the density of the molten metal. One solution to ensure a better distribution of particles inside the molten metal is the use of a sonotrode. The high-intensity ultrasonic waves generate a strong cavitation and acoustic streaming [85]. It involves the formation, growth, pulsating and collapsing of micro-bubbles. This process generates short-time micro "*hotspots*" that reach high temperatures (around 5000°C) and high pressures (around 1000 atm). These "*hotspots*" will last for few microseconds, leading to high heating/cooling rates (10^{10} K/s) [86]. The transient cavitation produces also an implosive impact which is strong enough to break the particles clusters and disperse them more uniformly [85]. The implosive impact added to the local high temperatures enhance the wettability of the particles by the molten metal [87]. A schematic of the ultrasound assisted casting is shown in Figure 1.13.

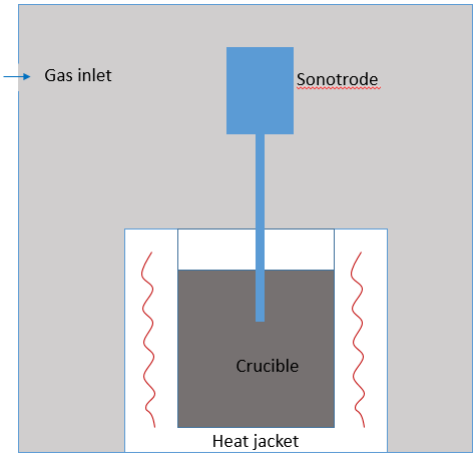

Figure 1.13 – Schematic of the ultrasound assisted casting (inspired from [52]).

Using this technique, Erman *et al.* [6] have successfully elaborated magnesium matrix composites reinforced with 1 wt% of SiC nanoparticles using ultrasound assisted casting. Such a small amount of nanoparticles allows an increase of 42 % in the yield strength. Wang *et al.* [88] have shown an improvement of the yield strength, ultimate tensile strength and ductility of AZ91D alloys reinforced by SiC at room temperature. AZ91D reinforced with 1 wt% of AlN nanoparticles have shown a great improvement of

tensile properties at high temperature [89]. Recently, Chen *et al.* [10] have successfully obtained a dense and uniform dispersion of SiC nanoparticles in a magnesium matrix. Mg_6Zn ingots with 1 vol.% of SiC obtained by ultrasound assisted casting were submitted to an evaporation process that favors the concentration of the SiC nanoparticles (evaporation of magnesium and increase of the volume fraction to 14%). The obtained nanocomposite presents a specific yield strength (yield strength/density) and a specific modulus (modulus/density) higher than almost all structural metals (see Figure 1.14).

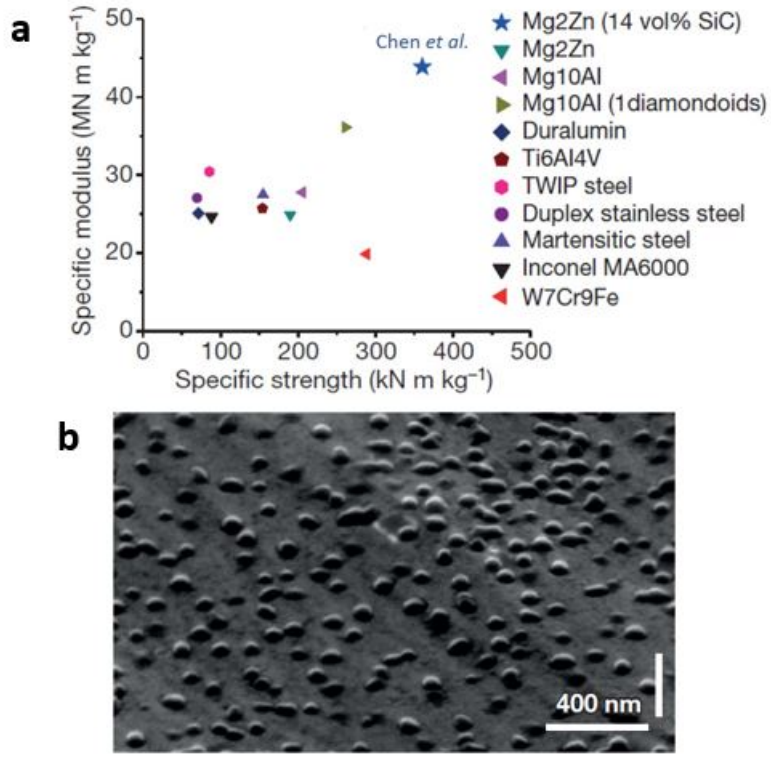

Figure 1.14 – Specific modulus versus specific yield strength of Mg_2Zn-SiC elaborated by ultrasound technique (14% volume fraction) (blue star) in comparison with the results obtained for other alloys by microcompression testing (a) and a SEM micrograph showing the homogeneous dispersion of SiC particles (b) [10].

Disintegrated melt deposition (DMD)

DMD process combines conventional casting and spray casting (see Figure 1.15). During DMD, the particles and the matrix metal are melted and stirred under a protective atmosphere. When poured, the melt is disintegrated using argon gas jets and deposited onto a metallic substrate. Ershadul *et al.* [9] and Chen *et al.* [73] have incorporated Al_2O_3 nanoparticles (1.5 % and 3 %, respectively) into different magnesium alloys using DMD. The nano-sized Al_2O_3 contributes to the improvement of the mechanical properties of the

base material, including microhardness (67 % in [9]), yield strength (20 % in [73]) and work of fracture (50 % in [9]).

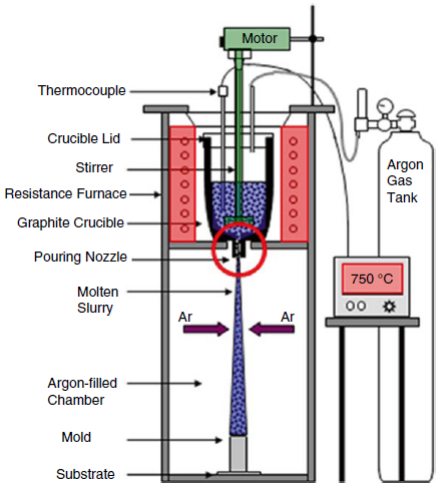

Figure 1.15 – Schematic of the disintegrated melt deposition process [90].

Squeeze casting

Squeeze casting (or preform infiltration) uses a preform that contains the reinforcement. The preform is placed in the casting mold and the molten metal is then poured into the mold. Solidification takes place under high pressure. A schematic of the process is shown in Figure 1.16. Zhang *et al.* [74] have used squeeze casting to elaborate carbon nanotubes reinforced magnesium matrix nanocomposites. A remarkable improvement of the mechanical properties was obtained with 1 wt% of carbon nanotubes.

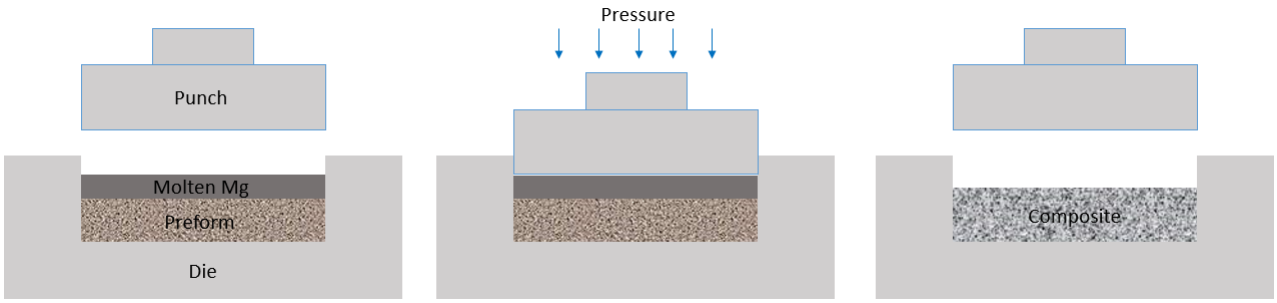

Figure 1.16 – Schematic of squeeze casting.

Table 1.5 describes the main advantages and drawbacks of each technique presented. This information will be taken into account for the choice of the processing technique that will be used for the processing of the "*model*" magnesium based nanocomposite

used in the present study.

Table 1.5 – Advantages and drawbacks of the main techniques used for the elaboration of magnesium based nanocomposites.

Processing technique	**Advantages**	**Drawbacks**
Ultrasound assisted casting	Relatively homogeneous dispersion of the reinforcement, low cost, possibility to elaborate large and complex parts	Large grain size and shrinkage porosity
DMD	Cost-effective method, fine grains, low porosity and homogeneous dispersion of reinforcements	Used mainly to elaborate ingots, requires secondary processing (usually extrusion)
Squeeze casting	Increase in the wettability (under vacuum), possibility of high volume fraction of particles, low porosity	Limited geometries, expensive
Powder metallurgy	Minimal wettability-related problems, possibility of high volume fraction of reinforcements, good dispersion, fine microstructure	Expensive, porosity, oxidization of powders and limited shapes
Mechanical alloying	Homogeneous dispersion of the particles, small grain size	Chemical reactions may occur, expensive
FSP	Small grain size, homogeneous dispersion of the reinforcement phase, local modification of the alloy with reinforcements	Surface technique

1.4 Strengthening mechanisms in metal matrix nanocomposites

Section 1.3 have presented some studies where the addition of reinforcement particles have increased the mechanical properties of magnesium and its alloys. The simplest way for predicting the mechanical behavior of a composite is given by the rule of mixtures. This rule assumes that there is no synergistic or interaction effect between the

constituents of the composites and calculates the properties of the composite based on the relative volume of each constituent. The strength of the composite can be calculated as

$$\sigma_{composite} = f_{reinforcement}\sigma_{reinforcement} + (1 - f_{reinforcement})\sigma_m \tag{1.5}$$

where $f_{reinforcement}$ is the volume fraction of reinforcement and $\sigma_{reinforcement}$ and σ_m are the strength of the reinforcement material and the matrix, respectively. The same equation can be used for the calculation of other properties such as elastic modulus, density, ultimate tensile strength... This linear approach is rather satisfactory for composites with high volume fractions of reinforcements, but fails to predict the behavior of nanocomposites for which the size of the reinforcement and the interaction with dislocations play a key role.

The improvement of the mechanical properties of metal matrix nanocomposites with respect to the properties of the matrix alone results from the contribution of different strengthening mechanisms: load transfer effect, Hall-Petch strengthening, Orowan strengthening and coefficient of thermal expansion (CTE) and elastic modulus (EM) mismatch [52, 91, 51]. Each one of these strengthening mechanisms will be explained individually followed by a discussion of the sum of the contributions.

1.4.1 Load transfer effect

When the composite is subjected to external loading, the load is transferred from the soft matrix to the hard reinforcement phase (usually ceramic particles). A good bonding at the interface between the reinforcement and the matrix is necessary to observe the load transfer effect. The general equation for the contribution of the load-transfer effect in strengthening is proposed by Nardone *et al.* [52]:

$$\Delta\sigma_{LT} = f_v\sigma_m \left[\frac{(l+t)(l/t)}{4l}\right] \tag{1.6}$$

where f_v is the volume fraction of particles, σ_m is the yield strength of the matrix, l is the size of the reinforcement parallel to the loading axis and t is the thickness.

In the case of spherical particles, Equation 1.6 reduces to [92]:

$$\Delta\sigma_{LT} = \frac{1}{2}f_v\sigma_m \tag{1.7}$$

1.4.2 Orowan strengthening

The reinforcement particles act as obstacles for the dislocation movement. When a dislocation line reaches non shearable particles Figure 1.17(I), its segment close to the particle will be pinned; however, the segment further away from the particle continues to move. The dislocation takes a bowed shape (Figure 1.17(II)). If the dislocation continues to move, it can bypass the particles and leave a dislocation loop around the particle, as shown in Figure 1.17(III). This is called Orowan looping.

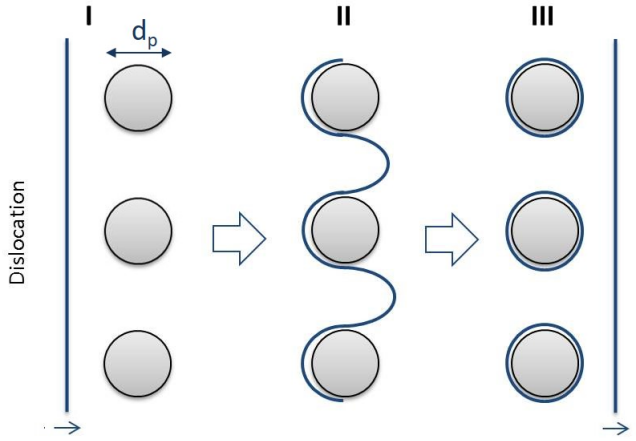

Figure 1.17 – Schematic of the Orowan strengthening mechanism.

The increase of the yield strength due to the Orowan looping effect can be estimated by the Orowan-Ashby equation [93]:

$$\Delta\sigma_{OR} = \frac{0.13 G_m b}{\lambda} ln \frac{d_p}{2b} \tag{1.8}$$

where b is the Burger's vector magnitude, G_m is the matrix shear modulus (for magnesium 16.5 GPa [92]), λ is the interparticle spacing and d_p is the particle size. A more recent variation of this expression has been proposed by Zhang and Chen [94]:

$$\Delta\sigma_{OR} = \frac{0.13 G_m b}{d_p \left(\sqrt[3]{\frac{1}{2f_v}} - 1 \right)} ln \left(\frac{d_p}{2b} \right) \tag{1.9}$$

As depicted by Equation 1.9, for a given volume fraction (f_v), the Orowan strengthening is more important when small particles are used (nanocomposites). As a consequence, the Orowan strengthening does not play a fundamental role in the case of micronmeter-sized reinforced composites because of the large interparticle spacing and the fact that

the particles are too large [95].

1.4.3 Coefficient of thermal expansion (CTE) and elastic modulus (EM) mismatch

The mismatch between the coefficient of thermal expansion of the metal matrix and the reinforcement phase generates misfit strains during cooling from elevated temperature (during processing or thermal treatment). The high misfit strains generated at the reinforcement/matrix interface are relaxed by the generation of geometrically necessary dislocations (GND) [96]. The difference between the elastic modulus of the matrix and the hard reinforcement phase can lead to the formation of additional GND during straining of the nanocomposites [97]. These later strains can be ignored since the thermal strains are one order of magnitude greater [98]. The GND density (ρ) due to CTE mismatch can be estimated by [99, 96]:

$$\rho_{CTE} = \frac{A\Delta\alpha\Delta T f_v}{b d_p (1 - f_v)} \tag{1.10}$$

where A is a geometric constant which is theoretically between 4 (for large aspect ratio reinforcements) and 12 (for spherical particles) [100], $\Delta\alpha$ is the difference between the CTE of matrix and reinforcements and ΔT is the difference between current temperature and the maximum temperature experienced during the process. The contribution of the CTE mismatch on the strengthening of the composite can be calculated by [96]:

$$\Delta\sigma_{CTE+EM} = \beta G_m b \sqrt{\rho_{CTE}} \tag{1.11}$$

where β is a constant in the order of 1.25 [92].

1.4.4 Hall-Petch strengthening

The reinforcement particles have a direct influence on the grain size of a composite, acting as pinning points that can prevent grain growth. The addition of more reinforcement (increase of f_v) and a reduction of the reinforcement size (d_p) lead to a finer microstructure as predicted by the Zener equation [92]:

$$d_{matrix} = \frac{4 d_p}{3 f_v} \tag{1.12}$$

The Hall-Petch strengthening comes from the fact that grain boundaries can block the dislocation movement. Due to the cristallographic disorientation between adjacent grains, the dislocation requires more energy to be transmitted to the neighbor grain. The grain boundary is also a region with high lattice disorder, which prevents the dislocation from moving in a continuous slip plane [101]. The smaller the grains, the stronger the back stress induced by the dislocations that pile up at the grain boundaries. The Hall-Petch equation [93] predicts the contribution of the grain size to the strengthening:

$$\Delta\sigma_{H-P} = \frac{k_y}{\sqrt{d_{matrix}}} \tag{1.13}$$

where k_y is the strengthening coefficient, which is a constant that depends on the material (0.28 MPa $m^{0.5}$ for magnesium [102]), and d_{matrix} is the average grain size.

1.4.5 Sum of contributions

The different mechanisms mentioned previously can act in synergy so that the final strength of the nanocomposite is difficult to be estimated. Several studies have proposed different models to calculate the yield strength of the composite. The summing method [103] is the most simple. It estimates the final strength of the composite by summing the contributions of the different strengthening mechanism to the original yield strength of the matrix (σ_m). The yield strength of the composite (σ_c) can be calculated by:

$$\sigma_c = \sigma_m + (\Delta\sigma_{Load-Transfer} + \Delta\sigma_{CTE} + \Delta\sigma_{Orowan} + \Delta\sigma_{Hall-Petch}) \tag{1.14}$$

This method however usually overestimates the yield strength because it does not take into account the interactions between the different mechanisms.

Other studies use the quadrature method, that also considers a superposition of all the effects. The final strength of the composite is estimate with the following equation:

$$\sigma_c = \sigma_m + \sqrt{(\Delta\sigma_{Load-Transfer})^2 + (\Delta\sigma_{CTE})^2 + (\Delta\sigma_{Orowan})^2 + (\Delta\sigma_{Hall-Petch})^2} \tag{1.15}$$

This method provides results similar to experimental data [104, 105].

Ramakrishnan method [91] considers only the contribution of the load transfer

effect and the dislocation strengthening due to CTE mismatch:

$$\sigma_c = \sigma_m(1 + f_1 + f_d + f_1 f_d) \tag{1.16}$$

$$f_1 = 0.5 f_v \tag{1.17}$$

$$f_d = \frac{k G_m b \sqrt{\rho_{CTE}}}{\sigma_m} \tag{1.18}$$

where k is a constant (approximately 1.25). f_d and f_1 are improvement factors associated with the dislocation strengthening of the matrix and the load transfer effect of the reinforcement.

A more recent model developped by Zhang *et al.* [94, 106] predicts the yield strength of particulate-reinforced metal matrix nanocomposites. It does not take into account the grain size refinement, ignoring the effect of nanoparticle-induced grain refinement. The yield strength of the composite can be calculated by:

$$\sigma_c = (1 + 0.5 f_v)\left(\sigma_m + A + B + \frac{AB}{\sigma_m}\right) \tag{1.19}$$

$$A = 1.25 G_m b \sqrt{\frac{12 \Delta T \Delta \alpha f_v}{b d_p (1 - f_v)}} \tag{1.20}$$

$$B = \frac{0.13 G_m b}{d_p \left[\left(\frac{1}{2 f_v}\right)^{\frac{1}{3}} - 1\right]} ln \frac{d_p}{2b} \tag{1.21}$$

where A and B are the coefficients related to the CTE mismatch and the Orowan strengthening, respectively. B equals to the Equation 1.9.

Following these detailed contributions of each strengthening mechanisms, a comparison of their effects using the data available in the literature [3, 107, 108, 72] will be performed in the case of magnesium based nanocomposites considering different reinforcements: Al_2O_3, Y_2O_3 and SiC. Table 1.6 summarizes the properties and parameters of the different magnesium based composites. The compared composites have been elaborated using different processing routes: disintegrated melt deposition followed by extrusion [107], powder metallurgy followed by extrusion [3, 108] and friction stir processing [72]. The Burgers vector magnitude (b), shear modulus (G_m) and yield strength (σ_m) of the matrix

are, respectively, 0.32 nm, 16.5 GPa and 97 MPa. The contribution of each strengthening mechanisms was calculated using the previously presented equations (Equantions 1.7, 1.9, 1.11 and 1.13).

Table 1.6 – Properties and parameters of the different magnesium based composites used for the study of the contribution of the different strengthening mechanisms on the strength of the nanocomposites.

Composites (f_v)	**Grain size (μm)**	**Reinforcement diameter (nm)**	**Reinforcement length (μm)**	**ΔT (K)**	**$\Delta\alpha$ (x10^{-6} K)**
Mg [107]	49	-	-	225	18.83
Mg - 1.1% Al_2O_3	14	50	-	225	18.83
Mg [3]	60	-	-	225	16.93
Mg - 0.66% Y_2O_3	13	29	-	225	16.93
Mg [108]	20	-	-	325	16.93
Mg - 0.7% Y_2O_3	18	30-50	-	325	16.93
Mg [72]	16.4	-	-	375	24.2
Mg - 3.8% C	10	5800	15.5	375	24.2

Figure 1.18 shows the contribution of the different previously described mechanisms to the total strength of the composite. It can be noticed that the most important effect comes from the Hall-Petch strengthening. The Hall-Petch is related to the grain size, which can be reduced by the presence of particles. However, in most cases, the processing technique used for the elaboration has a stronger influence. In the case of Mg-0.7% Y_2O_3 composites [108] for example, the grain size does not vary much with the addition of the particles: the contribution of the Hall-Petch strengthening is similar with and without the addition of Y_2O_3 particles.

Considering then the Orowan strengthening, its contribution to the strength of the composite is higher in the case of smaller particles (reinforcement diameter smaller than 50 nm) and is inversely proportional to the reinforcement size. In the case of the magnesium reinforced with carbon fibers [72], the contribution of the Orowan strengthening is negligible due to the size of the particles. Another observation is that the contribution of the GND generation was more significant than the Orowan strengthening for all

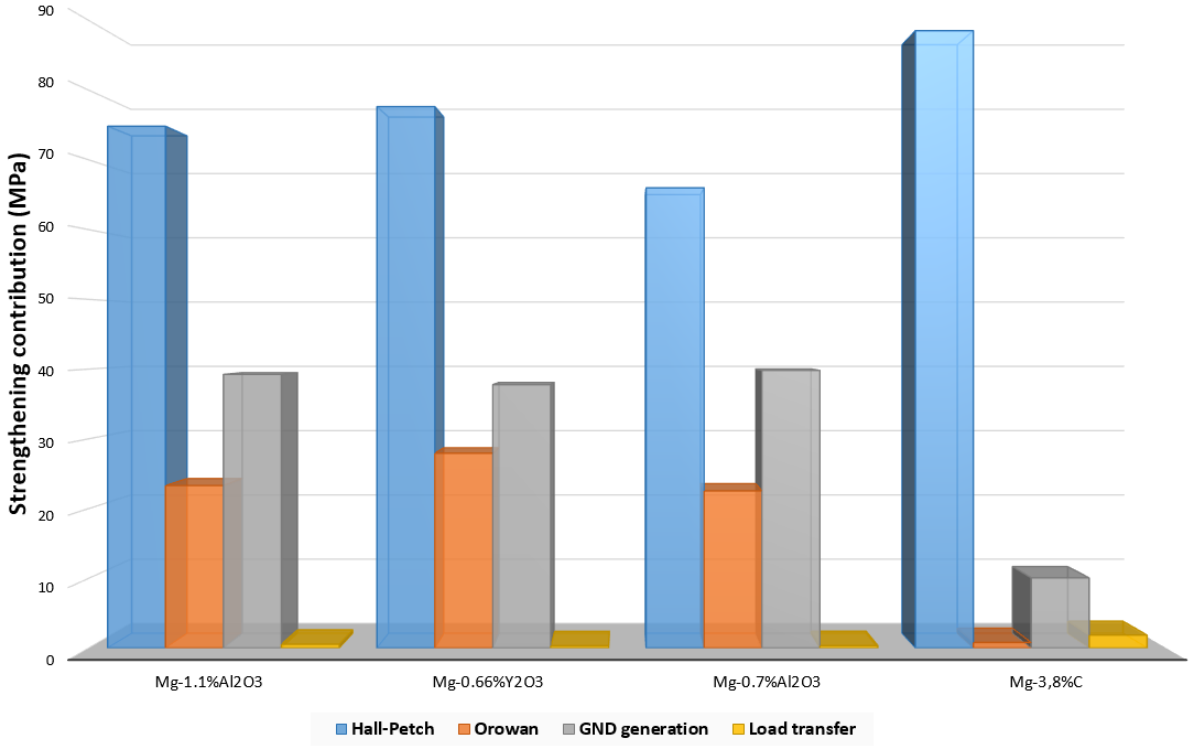

Figure 1.18 – Contribution of different strengthening mechanisms on the final strength of magnesium based composites [3, 107, 108, 72].

the compared composites. The reason for the reduced Orowan effect is the dislocation annihilation at high temperature due to atomic diffusion [92]. Similarly, the load transfer effect is negligible for all the analyzed composites due to the low volume fraction of reinforcements.

One can conclude from this literature survey that it is important to take into account several parameters when elaborating a composite: the choices of the processing route and reinforcement (phase, size and volume fraction) can strongly affect the major mechanisms responsible for the strengthening of the composite. The microstructure (grain size) depends on the processing route, but it can be altered by the addition of reinforcements. In a more moderate way, the choice of the reinforcement can also change the coefficient of thermal expansion mismatch ($\Delta\alpha$), which has a direct influence on the GND generation strengthening, as shown in Equation 1.10. Load transfer effect and Orowan strengthening mechanisms also compete between each other: larger reinforcements will increase the load transfer effect, while decreasing the Orowan strengthening. Since the aim of the present study is to investigate the typical plastic behavior of magnesium single crystals strengthened by oxide dispersed particles, this study will focus on the contribution of the Orowan strengthening, GND generation or load transfer.

Furthermore, the present comparison of the contribution of each mechanism on the strengthening is based on experimental results, however, it is still missing experimental studies that could distinguish the influences of each mechanism. In the study developed during this PhD, the investigation of the mechanical behavior at polycrystalline and single crystalline scales will help on the distinction between the different strengthening mechanisms: Hall-Petch and Orowan, GND generation and load transfer.

Key points of Chapter 1

1. Magnesium has a strong plastic anisotropy due to its hcp crystalline structure.
2. Basal, prismatic, pyramidal $\pi 1$ and pyramidal $\pi 2$ slip and twinning are the five more common deformation modes in magnesium. Basal, prismatic and pyramidal $\pi 1$ slip systems have an $< a >$ Burgers vector, while pyramidal $\pi 2$ and twinning can accommodate a deformation along the c-axis.
3. At room temperature, magnesium deforms mainly by basal slip and by $\{1\,0\,\bar{1}\,2\}$ extension twinning. This twinning deformation promotes a re-orientation of the basal plane in the twinned region of 86° and is activated when a tensile stress is applied along the c-axis or a compression stress perpendicular to the c-axis.
4. The number of studies using magnesium based nanocomposites has significantly increased over the past few years especially because magnesium is a good candidate for applications that require lightweighting. The reinforcement phase are usually hard ceramic particles (Al_2O_3, Y_2O_3, SiC, SiO_2), fibers, carbon nanotubes...
5. The processing routes to elaborate magnesium based nanocomposites include casting techniques (ultrasound assisted casting, disintegrated melt deposition and squeeze casting), powder metallurgy, mechanical alloying and friction stir processing. The main issues concerning the elaboration of magnesium based nanocomposites is the low wettability of ceramic particles and the achievement of a homogeneous 3D dispersion of the particles.
6. The improvement of the mechanical properties in nanocomposites results from the contribution of different strengthening mechanisms: load transfer effect, Orowan strengthening, Hall-Petch strengthening and GND generation due to the difference in the coefficient of thermal expansion.
7. To date, studies that investigate experimentally which are the predominant mechanisms are still missing.

CHAPTER 2

Characterization techniques

In the present chapter, the experimental methods employed during this study will be described and sample preparation for microstructural analysis using optical microscopy, scanning electron microscopy (SEM), transmission electron microscopy (TEM) and cross section electron backscattered diffraction (EBSD) will be detailed. The parameters used for conventional mechanical testing (tensile and compression) and microcompression testing will also be presented.

The small size of the reinforcement phase and the need to obtain information about the 3D dispersion of these reinforcements imply the use of high resolution techniques, such as TEM, microtomography and nanoholotomography, for the characterization of their morphology and 3D distribution.

2.1 Optical microscopy

2.1.1 Sample preparation

Magnesium and magnesium alloys are delicate metallic specimens to prepare for microstructural examination. The low hardness makes it easy to polish (the material is removed easily), however it also facilitates the apparition of scratches that are difficult to remove. In the case of composites, the material contains particles with a much higher hardness than the matrix. It makes it even more difficult to eliminate the scratches.

Mechanical twinning may also be created during cutting, grinding or even handling if the pressures are excessive. Finally, magnesium is also quite reactive and the use of water during polishing can contribute to the formation of an oxide layer. Thus, special care has been taken in order to avoid any damage or microsctructural modifications during sample preparation.

The cutting was performed carefully in order to reduce the damage introduced to the specimens. SiC abrasive papers from P1200 to P2400 (SiC grain size of 15.3 μm and 6.5 μm respectively) were used for the grinding. Water was used in order to minimize heating of the specimen (some oxidation is acceptable at this stage).

The polishing was performed manually using an alcohol based monocrystalline diamond suspension with grain sizes from 3 μm to 0.25 μm. The first step of polishing uses 3 μm size diamond suspension with ethanol as a lubricant and the second step a mixture of water free silica suspension (0.2 μm) and 1 μm size diamond suspension. Despite the careful polishing of the samples, the presence of some deformation twins seemed unavoidable.

2.1.2 Chemical Etching

A proper chemical etching is necessary to evidence microstructural features. Grain boundaries of pure magnesium samples can be revealed using Nital (5 mL of nitric acid and 95 mL of ethanol). Nital also helps to remove some of the damaged layer, generated during grinding and polishing. The same etchant cannot be used for the nanocomposites due to preferential etching at the interface between the particles and the matrix. Thus, the nanocomposites were chemically etched using acetic-picral (5 g of picric acid, 10 mL of acetic acid, 100 mL of ethanol and 10 mL of distilled water).

2.2 Scanning Electron Microscopy/Focused Ion Beam

Scanning Electron Microscopy (SEM) uses a focused beam of high-energy electrons to generate a variety of electron-sample interactions at the surface of the specimen in a volume often described as a pear of interaction. These electron-matter interactions include secondary electrons (SE), backscaterred electrons (BSE), diffracted backscaterred

electrons (EBSD), photons, visible light and heat. Each interaction reveals information about the sample. For example, SE shows the morphology and topography of the sample while the BSE gives qualitative information about the contrasts in composition in multiphase samples. The contrast is sensitive to the atomic number (Z) of the atoms.

Focused Ion Beam (FIB) operates similarly to the SEM. The main difference comes from the highly focused ion beam (usually gallium) instead of the electron beam (SEM). The FIB generally operates at low beam currents for imaging or high beam currents for milling. The ions of the beam collide with the surface atoms of the sample, transferring energy to the surface electrons. The effect is the sputtering of ionized atoms which lead to the substrate milling. The ion beam also produces secondary electrons which provide imaging. FIB milling allows the selection of different patterns in order to remove material within a specific pattern. However, special care must be taken when using the FIB: the sputtering of Ga^+ ions at the surface of the sample can lead to gallium implantation and thermal stress.

In the present study, FIB milling was applied to prepare the microcolumns for the microcompression testing, to do the cross sectioning of the microcolumns for EBSD analysis and to prepare TEM samples. The following actions were taken to prevent or reduce the damage of the samples:

- Despite the possibility of imaging with FIB in dualbeam systems, SEM was used in order to reduce the exposure to the Ga^+ beam.
- The two most commonly used FIB-based methods for fabrication of microcolumns are annular milling and lathe milling. In the lathe milling technique, the sample surface is tilted to a small angle relative to the ion beam and a series of small rectangular cuts and rotations are used to remove material in order to form the microcolumn [109]. Differently, in the annular milling technique, the surface of the sample remains perpendicular to the ion beam through the entire process. Among the two methods, annular milling was chosen against lathe milling due to the lower ion dose in the columns fabricated using this technique [109].
- FIB imaging is necessary for some very sensitive cuts (final thinning of TEM samples for example) or alignments once the sample is tilted. In these cases, single-frame images of the area were taken, minimizing the exposure time.

Despite these precautions, some FIB damage artifacts could still observed. Fig-

ure 2.1 shows straight lines, which are aligned in the same direction as the FIB beam during milling, at the surface of a TEM foil. These are called curtaining artifacts. Additionally, energy-dispersive X-ray spectroscopy (EDS) of some TEM foils have proven the presence of some gallium contamination in the TEM foils.

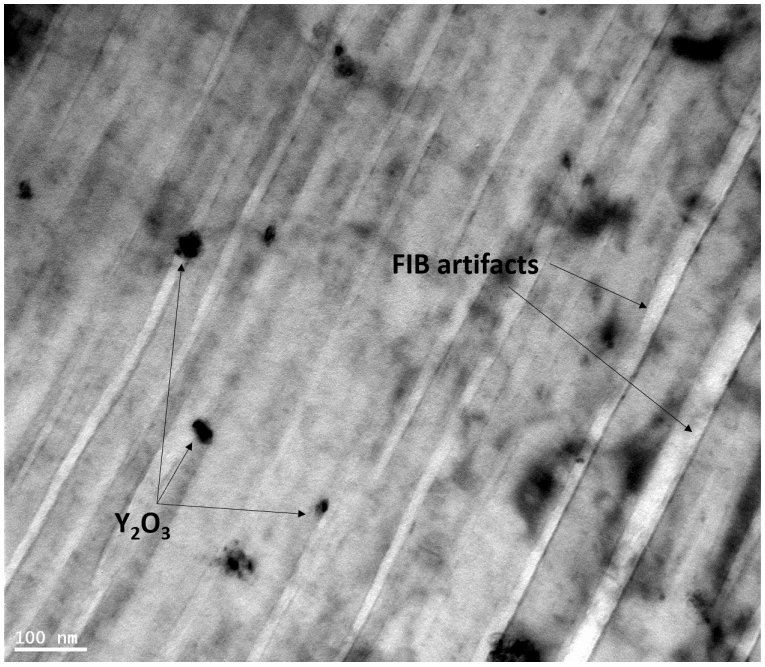

Figure 2.1 – Example of FIB artifacts in a TEM foil prepared using FIB milling: straight lines are visible in the same direction as the FIB beam.

In the present study, a FEI Nova Nanolab 200 Dualbeam Scanning Electron and Focused Ion Beam (FIB) microscope based at the Helmholtz-Zentrum Geesthacht was used. Figure 2.2 shows a schematics of the microscope, including the EBSD detector and the electron and ion beams.

2.3 Mechanical testing

The multi scale mechanical response of the magnesium based nanocomposites has been investigated in the present work. At macro scale, tensile and compression tests are performed in polycrystalline materials, while the single crystalline plastic behavior is studied using microcompression testing. Sections 2.3.1 and 2.3.2 explain in details the experimental methods employed for macro- and microscale mechanical testing.

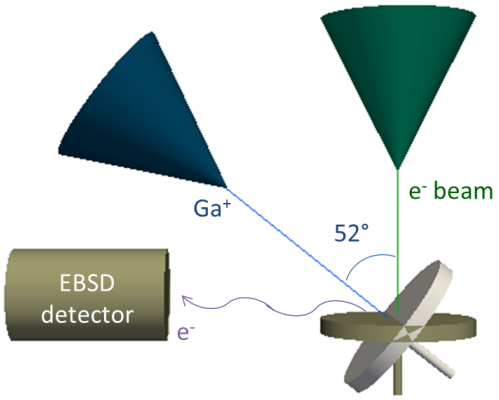

Figure 2.2 – Schematics of the FEI Nova Nanolab 200 Dualbeam Scanning Electron and Focused Ion Beam (FIB) microscope: the electron beam is aligned in the vertical axis, the ion beam is oriented 52° with respect to the electron beam and the EBSD detector is oriented at 70° with respect to the electron beam. When the sample is at 5 mm of the electron beam and tilted 52°, electron and ion beam focus the same point.

2.3.1 Macroscale mechanical testing

Magnesium based composites used during the present study were tested uniaxially under ambient conditions. Compression and tensile tests have been performed as follows:

- Compression experiments were performed in an universal mechanical testing machine Zwick Z010 TN. The initial engineering strain rate was 2.10^{-3} s^{-1}. Cylindrical compression specimens were elaborated using electrical discharge machining (EDM) with the following dimensions: 2 mm diameter and 6 mm height.

- Tensile tests were performed using two different tensile devices. The first is a Instron3360 test machine containing a advanced video extensometer (AVE2663-821), where a head velocity of 1 mm/min and an engineering strain of $6{,}4.10^{-4}$ s^{-1} were used. The tensile specimens used for this device have been prepared by milling machining with the dimensions presented in Figure 2.3(a). In addition, a Gatan Microtest MT2000EW tensile stage has been used *ex situ* with a cross head velocity of 0.072 mm/min and an engineering strain rate of 4.10^{-4} s^{-1}. These tensile specimens have been fabricated by EDM following the dimensions in Figure 2.3(b).

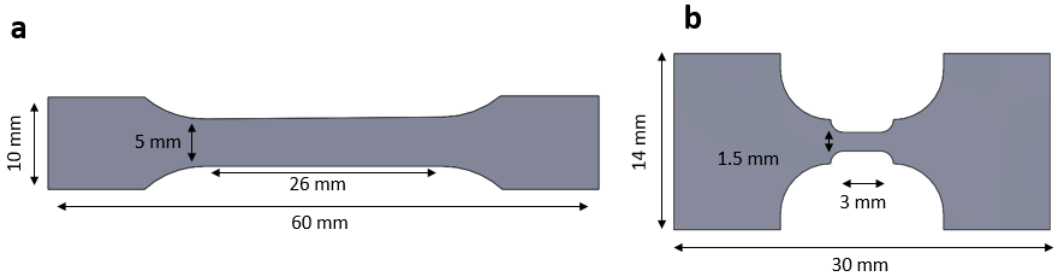

Figure 2.3 – Dimensions of the two different tensile specimens used in the study. The specimen thickness for (a) and (b) are 1 mm and 1.2 mm, respectively. Specimens (a) and (b) have been tested in the Instron test machine and Gatan Microtest tensile stage, respectively.

2.3.2 Microcompression/Nanoindentation

Instrumented nanoindentation is a mechanical testing method which provides a high resolution load and displacement measurements. During the test, an indenter tip is pressed on the surface of the material. The indentation load-displacement data can be used to determine the mechanical properties of the material, such as elastic modulus (E) and hardness [110]. The load-displacement data obtained during a typical nanoindentation test is shown in Figure 2.4: the deformation during loading is assumed to be both elastic and plastic. During unloading, the elastic displacement is recovered and it is generally assumed that there is no plastic deformation. The experimentally measured stiffness (S) can be calculated from the upper portion of the unloading portion using Equation 2.1, where P is the load and h is the displacement. The hardness (H) can be estimated using the peak indentation load (P_{max}) and the projected area of the indenter impression (A) using Equation 2.2. Knowing the stiffness, the hardness and the peak indentation load, the elastic modulus (E) can be calculated using Equation (2.3). Details about the calculations are presented in Oliver and Pharr [111].

$$S = \frac{dP}{dh} \tag{2.1}$$

$$H = \frac{P_{max}}{A} \tag{2.2}$$

$$E^2 = \frac{S^2 H \pi}{4 P_{max}} \tag{2.3}$$

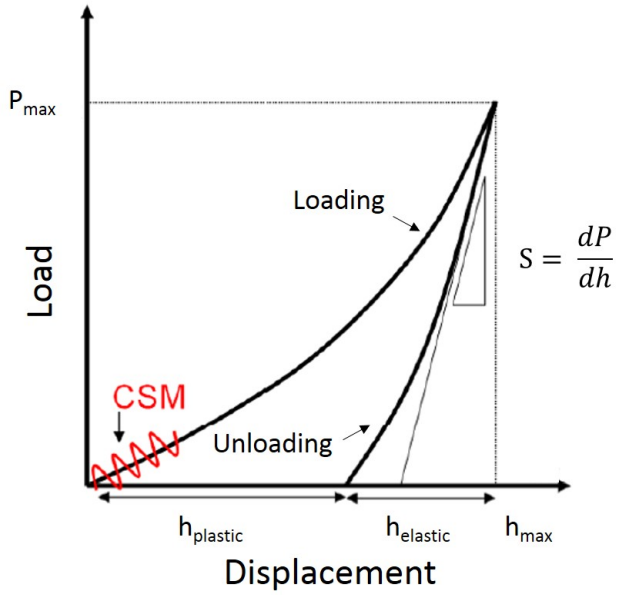

Figure 2.4 – Schematic illustration of the load-displacement data obtained during nanoindentation testing.

In the past few years, the development of the continuous stiffness method (CSM)[110, 111] allows the continuous measurement of the contact stiffness during the entire loading of the indenter. The principle of this method consists in the application of a small oscillation on the load or displacement and the measurement of the load or displacement response.

During this study, a Nanoindenter XP (from MTS Nano Instruments, now Agilent) based at the Helmholtz-Zentrum Geesthacht was used. The maximum depth is 500 μm with depth resolution inferior to 0.01 nm and the maximum load is 500 mN with a load resolution of 50 nN.

2.3.2.1 Microcompression testing

The microcompression testing technique was first developed by Uchic *et al.* [112]. Cylindrical compression specimens (microcolumns) are fabricated into the surface of the bulk material and tested using a conventional nanoindenter, whose indenter tip is replaced by a flat punch. The nanoindentation hence works as a conventional uniaxial compression test.

One major difference between nanoindentation and microcompression is related

to the data analysis. During the present study, the protocol proposed by Lilleodden has been followed to analyze the data. The details are described below:

Load

$$P_{sample} = P_{raw} - k_s h_{raw} \tag{2.4}$$

where P_{raw} is the raw applied load, k_s is the instrument spring constant and h_{raw} is the raw displacement.

Displacement

$$h_{sample} = h_{raw} - h_{surface} - h_{loadframe} - h_{substrate} \tag{2.5}$$

where $h_{surface}$ is the surface position, $h_{loadframe}$ is the load-frame displacement and $h_{substrate}$ is the substrate displacement.

The $h_{loadframe}$ is equivalent to

$$h_{loadframe} = \frac{P_{sample}}{S_{loadframe}} \tag{2.6}$$

where $S_{loadframe}$ is the load-frame stiffness whose value is considered 1.078 mN/nm.

The $h_{substrate}$ is equivalent to

$$h_{substrate} = \frac{1-\nu^2}{E}\frac{P_{sample}}{D_{foot}} \tag{2.7}$$

where ν is the Poisson's ratio, E is the Young's modulus, and D_{foot} is the diameter of the column foot (see Figure 2.5). The Poisson's ratio and the Young's modulus for magnesium are 0.34 and 45 GPa, respectively. This displacement profile correspond to the displacement of the material under the column.

Engineering stress

$$\sigma_{eng} = \frac{4P_{sample}}{\pi D_{mid}^2} \tag{2.8}$$

where D_{mid} is the initial mid-height diameter of the column.

Engineering strain

$$\varepsilon_{eng} = \frac{h_{sample}}{H_o} \tag{2.9}$$

where H_o is the initial sample height.

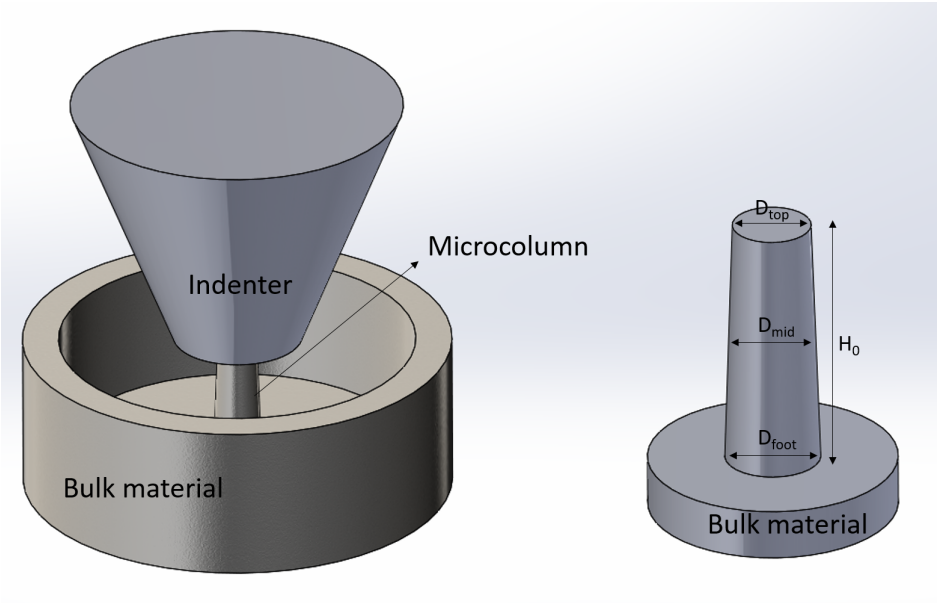

Figure 2.5 – Schematic illustration of the microcompression testing and the microcolumn.

The microcompression tests were conducted *ex situ* (outside the SEM) in a Nanoindenter XP (Agilent) equipped with a flat-ended conical indenter with a circular punch. The flat punch diameter must be larger than the columns but smaller than the perimeter of the surrounding bulk materials from which the columns were machined (see Figure 2.5). Columns with a maximum mid-height diameter of 10 μm were tested using a 15 μm circular punch and larger columns using a 50 μm circular punch. Special care was taken in order to ensure that the surface of the sample was parallel to the flat punch surface, such that the columns could be loaded uniaxially. To do so, indents have been performed on the surface of the sample using the flat punch indenter prior to microcompression testing. The perimeter of contact should be symmetric, indicating a good alignment between the surface normal and the loading axis. The microcompression experiments were run to varying maximum strain using a nominally constant strain rate of 10^{-3} s^{-1} (columns with 2 and 5 μm mid-height diameter), 2.10^{-4} s^{-1} (columns with 10 μm mid-height diameter) and 4.10^{-4} s^{-1} (columns with 5, 10 and 15 μm mid-height diameter). The instrument is an inherently load-controlled instrument, and thus the displacement rate was controlled *via* a feedback from the loading signal in order to achieve a specified strain rate. No additional attempt to control the displacement rate was made, and therefore physical instabilities related to the material behavior during the microcompression testing can lead to large displacements bursts. The size of the bursts is a coupled effect of material and instrument behavior [2].

2.3.2.2 Microcolumns fabrication

The microcolumns were machined at the surface of the bulk material using FIB milling. Prior to the fabrication of the microcolumns, EBSD scans (presented in Section 2.4) were performed in order to determine the local orientation of the sample surface and the existence of twins in the regions of interest. One of the major difficulties was to obtain single crystalline regions large enough and with a specific orientation from a polycrystalline material, where a single crystalline microcolumn could be machined.

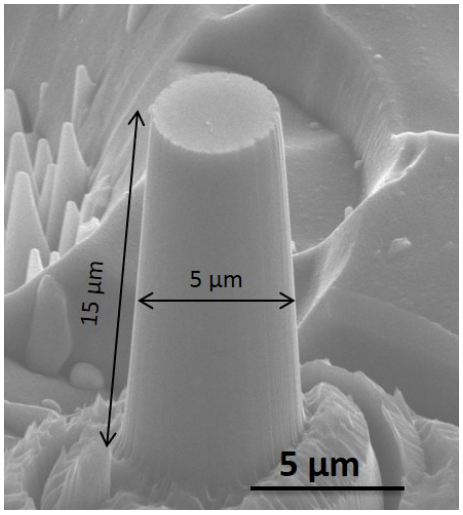

Figure 2.6 – SEM micrograph of a typical microcolumn fabricated by annular milling.

Annular milling technique (Section 2.2) was chosen for the microcolumns fabrication. A column is made of a series of successive circular cuts at varying diameters. The final geometry will depend on the milling parameters. The voltage of the ion beam was kept constant at 30 kV, but the probe currents varied. Attempt was made to ensure a 3:1 aspect ratio of height to mid-height diameter. In any case where the aspect ratio was greater than 4:1 or smaller than 2:1, the column was discarded. Due to the annular milling technique, the columns present a slightly larger diameter in the base of the columns than on the top. Although the column taper leads to some variation in the axial stress along the column, it helps to stabilize the columns when there is any misalignement between the microcolumn and the flat punch during the microcompression test. A SEM micrograph of a typical microcolumn fabricated by annular milling is presented in Figure 2.6.

Different columns sizes have been used during this study: 2, 5, 10 and 15 μm (the size is defined by the mid-height diameter). However, only a few larger columns (with a mid-height diameter of 10 and 15 μm) were fabricated due to practical issues, mainly

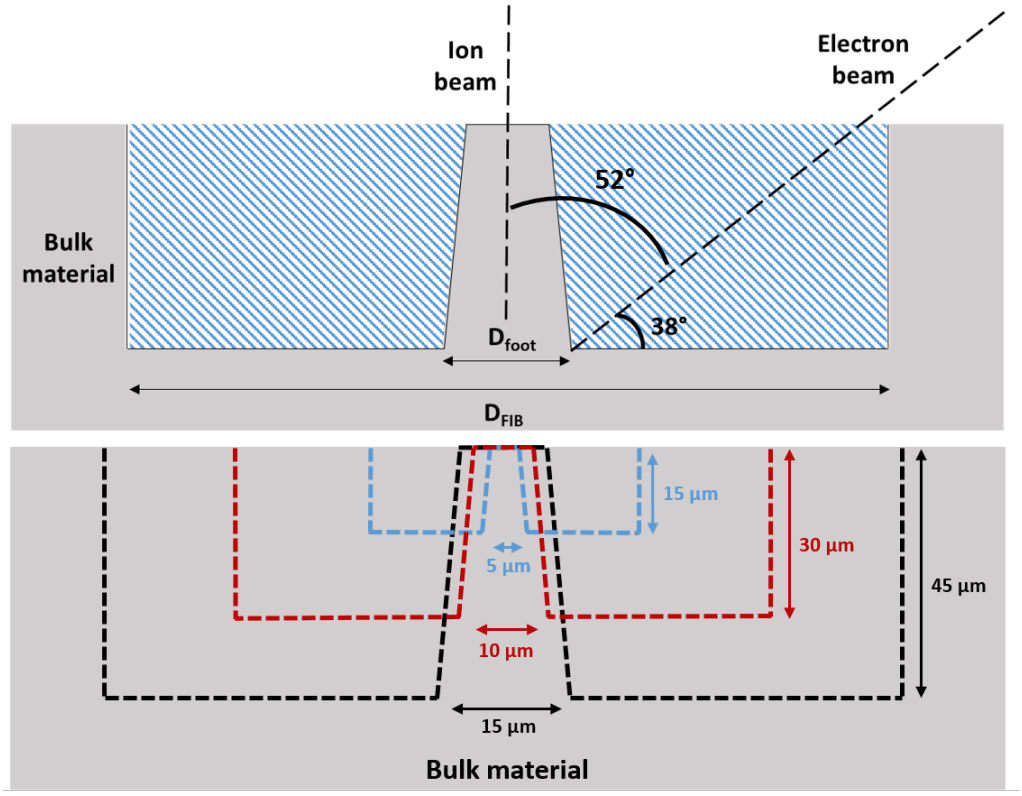

Figure 2.7 – Schematics of the process of FIB milling used for the fabrication of the microcolumns (a). The microcolumn is fabricated inside the bulk material (grey) and the dashed blue area represent the material that is removed during FIB milling. The schematics in (b) show that the larger the column, the larger the D_{FIB} in order to be able to observe the microcolumn foot.

concerning the milling time: the FIB milling time is indeed considerably high (several hours) for such columns when compared to 2 and 5 μm microcolumns (maximum 2 hours). The volume of material that must be removed for the fabrication of a microcolumn with a mid-height diameter of 10 μm is 8 times superior to the one removed for a 5 μm column. This difference goes to 27 for 15 μm columns. It is important to remember that the normal to the surface of the specimen has an angle of 52° with the electron beam during FIB milling (see Section 2.2). Thus, a huge amount of material needs to be removed for bigger columns in order to be able to image the column foot and know the exact height of the column (schematics in Figure 2.7). Another difficulty when working with larger columns is that the EBSD analysis performed prior to column machining only gives information about the orientation of the surface. Thus, it is preferable to use grains much larger than the column diameter so that the probability to have a single crystalline microcolumn will be higher.

After microcompression testing, the deformed columns were carefully observed in the SEM in order to investigate the deformation shape, slip traces and other potential features.

2.4 Electron Backscatter Diffraction

Electron Backscatter Diffraction (EBSD) is a useful technique for investigating crystal orientation. It enables the determination of individual grain orientations, local texture, point-to-point orientation and phase identification at the surface of crystalline bulk materials. This technique plays an important role in this study, since the micro-columns are machined inside a single crystalline volume with a well-known orientation: EBSD analysis allows the identification of the grains with the suitable orientation for the fabrication of microcolumns.

The EBSD detector is installed inside the SEM chamber (see Figure 2.2). During EBSD analysis, the normal to the sample surface will be tilted 70° with respect to the electron beam. The electrons emitted by the SEM (electron beam) will collide at the surface of the sample and as a result, backscatter electrons will be emitted. The electrons satisfying Bragg's law (Equation 2.10) will be detected on the phosphorous screen of the EBSD detector. The electrons diffracted from different planes form the diffraction pattern. The Hough transform (image processing algorithm) is then used to identify the Kikuchi bands from the diffraction pattern. Each Kikuchi line corresponds to the diffraction of a family of planes (Figure 2.8(a)). The Kikuchi pattern is indexed using Miller indices in order to determine the crystal orientation. Figure 2.8(b and c) show respectively the color coded map and the EBSD orientation map for a typical magnesium sample.

$$n\lambda = 2d_{hkl}sin\theta \tag{2.10}$$

In the present study, a voltage of 20 kV and a current of 2.4 nA have been used for the EBSD scans. The analysis of the EBSD data has been performed using OIM software.

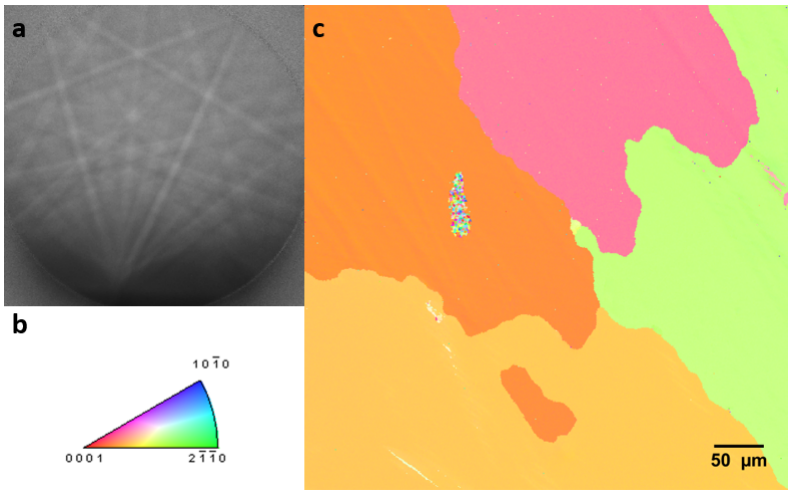

Figure 2.8 – Kikuchi pattern of magnesium (a). Color coded map type (b) and EBSD orientation mapping (c) for a magnesium sample.

2.4.1 Sample preparation for classical EBSD

The backscattered electrons used in EBSD are generated near the surface of the sample (few nanometers). The sample preparation is thus critical for achieving a good indexation. Sample preparation should remove any surface damage (scratches, relief...). The cutting and polishing procedure precised in Section 2.1.1 was applied. However, additional manual polishing with 0.25 μm diamond suspension and water free silica suspension (0.2 μm) is required. This step is crucial for EBSD and polishing one sample for more than 4 hours can be needed in order to remove the deformed surface layer.

2.4.2 Sample preparation for cross section EBSD

Thin lamellas were extracted from several microcolumns after microcompression testing using FIB milling in order to measure the misorientations associated with the deformation using EBSD. Cross section of the columns was performed because a smooth surface is necessary for EBSD. Figure 2.9 shows the procedure of cross sectioning of the microcolumns. It is important to use a thick lamella (thickness around 2 μm) for EBSD: if the sample is too thin it becomes electron transparent and transmission EBSD will be need. However, this technique was not available for this work. The procedure used is as follows:

(i) Platinum was first deposited on the top of the column and in an undeformed region.

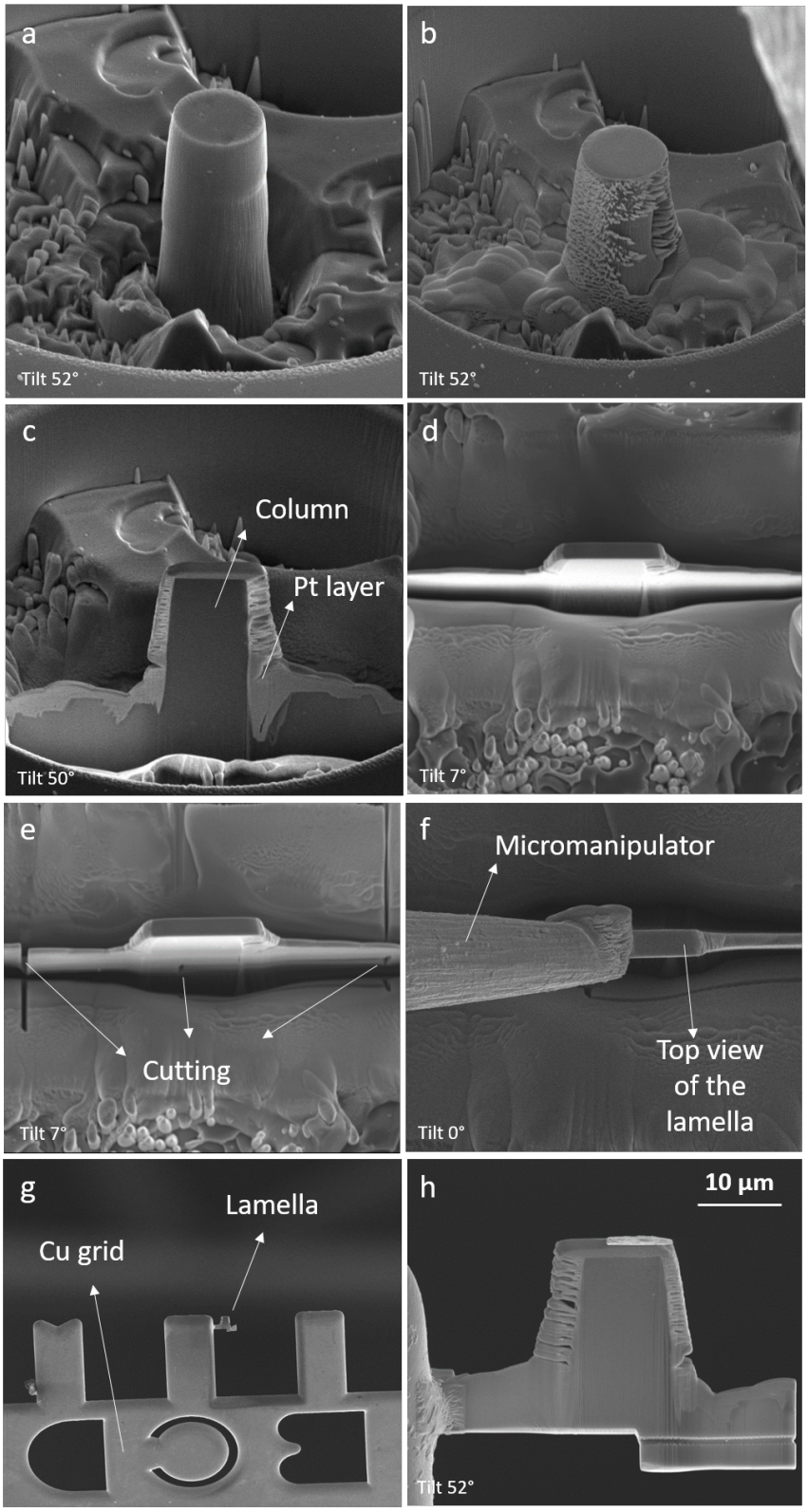

Figure 2.9 – Typical working procedure of TEM and EBSD sample preparation by FIB cross-sectioning. In *a* and *b*, a deformed microcolumn before and after platinum deposition, respectively. Side (*c*) and top (*d*) view after FIB cross-sectionning. A through-sectioning to free the lamella from the bulk material (*e*). The lamella was attached to the Omniprobe micromanipulator (*f*). The lamella was mounted on the copper grid in *g*. Final thinning of the lamella using cleaning cross section (*h*).

The platinum layer acts as as protective layer (Figure 2.9 a and b);

(ii) A FIB cross-sectioning was performed in the upper and bottom side (Figure 2.9 c and d). The thickness of the lamella at this point is around 2 to 2.5 μm;

(iii) Through-section cutting was performed to free the lamella from the bulk, leaving only one connecting section (Figure 2.9 e);

(iv) The lamella was lifted out using an Omniprobe micromanipulator. In Figure 2.9 f, platinum is used to attach the lamella to the Omniprobe;

(v) The lamella is mounted on the copper grid (Figure 2.9 g);

(vi) A slight thinning was performed using the "cleaning cross section" (Figure 2.9 h) in order to obtain a proper surface for EBSD analysis.

During cross section EBSD of the deformed microcolumns, special care was taken in order to avoid shadowing problems. Any surface topography or relief can compromise the analysis.

2.5 Transmission Electron Microscopy

In Transmission Electron Microscopy (TEM), a thin specimen is irradiated with an electron beam with an uniform current density [113]. The acceleration voltage used in such microscopes varies usually from 80 to 300 kV. High energy electrons emitted in the electron gun are accelerated towards a thin specimen. A series of electromagnetic lenses help to focus the electron beam (Figure 2.10). Condenser lenses placed between the sample and the electron gun allow the variation of the illumination aperture and of the area of the specimen illuminated. Objective lenses, on the other hand are responsible for the imaging system. A series of lenses placed below the sample (intermediate and projector lenses) are responsible for the imaging of the electron-intensity distribution onto a fluorescent screen. Figure 2.10 schematically represents a TEM. TEM samples should be thin enough to be electron transparent: thin enough to transmit sufficient electrons such that enough intensity arrives on the fluorescent screen [115]. Usually, sample thickness is inferior to 200 nm. Further details about the technique can be found in [113, 115, 114].

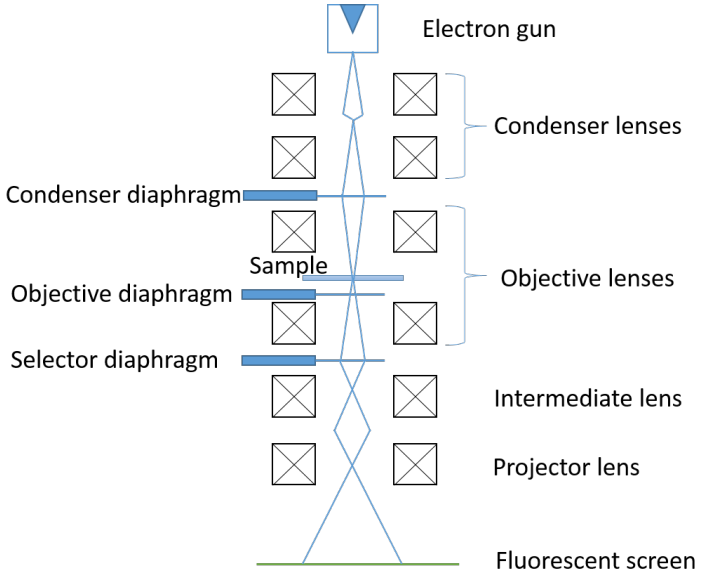

Figure 2.10 – Schematics of a transmission electron microscope (TEM) (inspired from [114]).

In the present study, bright-field (BF) images and diffraction patterns were obtained using TEM microscopy. In the bright-field mode, an aperture is placed in the back focal plane of the objective lens. It allows only the primary beam to pass. The imaging results from a weakening of the direct beam by its interaction with the samples. The contrast in the image is due to difference in the absorbance of thicker or denser areas of the sample. The diffraction patterns give information about the crystal structure and orientation. The scattered electrons are used to form the diffraction pattern. In the diffraction mode, the imaging lenses (between the sample and the fluorescent screen) are adjusted in a way that the back-focal plane of the objective lenses act as the object plane for the intermediate lens. Thus, a diffraction pattern is projected onto the fluorescent screen [115]. Figure 2.11 shows the operations of the TEM imaging system involved when using diffraction mode (projection of the diffraction pattern onto the screen) and image mode (projection of the image onto the screen).

Different transmission electron microscopes were used during this study:

- a MET LaB_6 Jeol 2010 with an accelerating voltage of 200 kV based at SIMaP,
- a MET FEG Jeol JEM2100 F with an accelerating voltage of 200 kV based at CMTC,
- a MET LaB_6 Jeol JEM-2010 microscope using an accelerating voltage of 130 kV used for *in situ* experiments (*in situ* tensile testing and thermal cycling). These

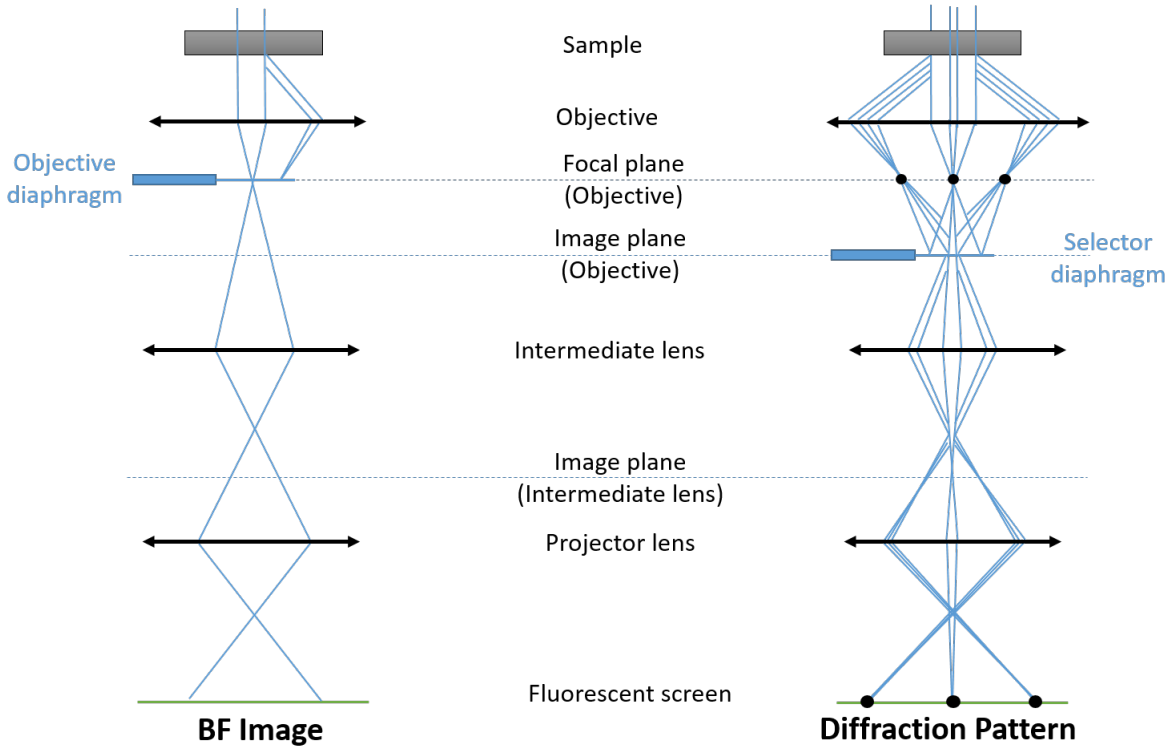

Figure 2.11 – Schematic representation of the TEM imaging system when using the image and the diffraction modes (inspired from [114, 116]).

tests were performed within CEMES laboratory (Toulouse - France) by Frédéric Mompiou. A Gatan room-temperature straining device was used for the *in situ* tensile testing.

2.5.1 Sample preparation for TEM

Two different techniques were used for TEM foils preparation: electropolishing and FIB.

- Electropolishing: lamellas sampled from the studied nanocomposites were first mechanically thinned until 100 μm and then electrochemically polished using a solution of perchloric acid (1 %) and ethanol. Electropolishing was performed in a TenuPol-5 from Struers. The polishing parameters were 50 V at -5°C.

- FIB: the beginning of the procedure applied for the preparation of the TEM foils by FIB is similar to the one for EBSD and is detailed in Section 2.4.2. An additional step was performed after EBSD (Figure 2.9): the lamella is thinned down to 200 nm

in order to reach the electron transparency. Then, a final cleaning was performed under a low voltage(5 keV) and low current (70 pA) at a glancing angle, minimizing the ion damage layer.

Prior to TEM analysis, a plasma cleaning of the foil with a mixture of argon and hydrogen was performed during 8 minutes.

2.5.2 Diffraction pattern interpretation

The diffraction pattern of hexagonal closed-packed crystals are usually difficult to index. The main reasons are the use of the four-index Miller Bravais notation and the fact that the patterns can be different for different hcp materials material, since the c/a ratio can differs with the materials [115]. The diffraction patterns obtained in the present study were interpretated using the ACOM (Automated Crystal Orientation Mapping) software [117, 118, 119]. The ACOM technique facilitates the interpretation of diffraction patterns, especially for random orientations (out of zone axis). ACOM uses only the spots of the diffraction pattern for orientation identification. However, there is also a possibility of manually using the Kikuchi lines for the interpretation.

ACOM associates the acquired diffraction pattern to a pre-calculated template using image correlation (Figure 2.12). The pre-calculated templates are generated using

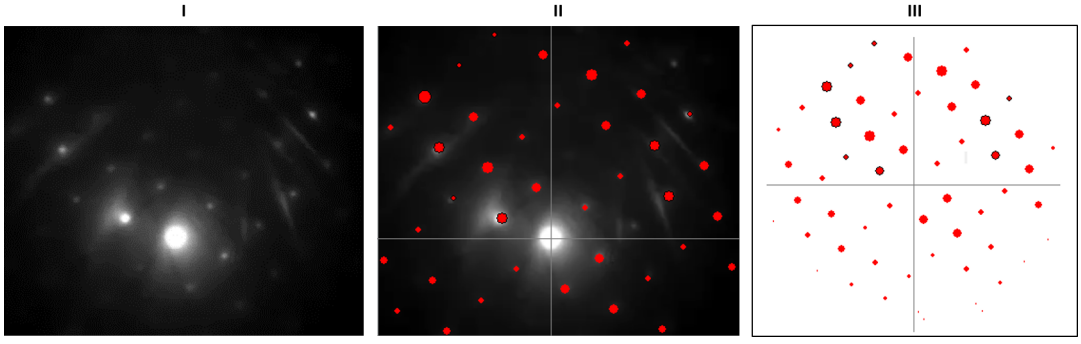

Figure 2.12 – Diffraction patterns indexing procedure. The ACOM software associated the acquired diffraction pattern (I) to pre-calculated templates (III) using image correlation. The best match indicates the orientation of the crystal (II).

the DiffGen (Diffractions generator) software. All possible simulated orientations (every 1°) within the fraction of the stereographic projection limited by the crystal symetry are calculated. The crystal informations used in the present work were extracted from the

Crystallography Open Database [120] (identification number: 4111965), corresponding to magnesium. The acceleration voltage was changed according to the acquisition parameters in order to obtain the pre calculated template. A match between the experimental pattern and the simulated pre-calculated template is given by a correlation index. The highest correlation index corresponds to the adequate orientation. Equation 2.11 defines the correlation index: the factor **P** is related to the pre-calculated templates and **T** to the acquired pattern [121].

$$Q(i) \sim \sum_{j=1}^{m} P(x_j, y_j) T_i(x_j, y_j) \tag{2.11}$$

where the pattern is represented by the intensity function P(x,y) while every template i is given by the function T_i(x,y) [117].

2.5.3 Dislocation indexation

Dislocations indexation was performed under the two beam condition or using the second most intense spot (Figure 2.13). Dislocations are visible or invisible depending on the magnitude of the scalar product between **g** (reciprocal lattice vector) and **b** (Burger's vector). When **g.b=0**, dislocations are invisible or show a weak contrast. Figure 2.14 illustrates the dislocation extinction condition.

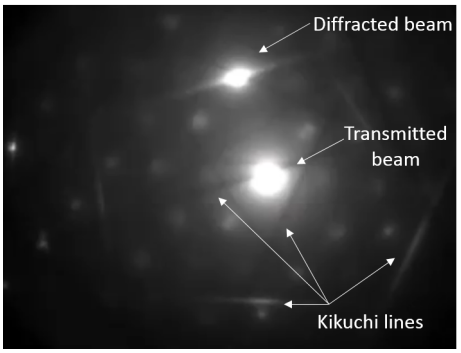

Figure 2.13 – Diffraction pattern in two beam condition for dislocation imaging. Highest intensity spot (after transmitted beam) is used for the determination of the **g** vector.

It is important to precise that dislocation imaging in magnesium requires working in specific conditions: the low atomic number of magnesium gives a low contrast. Additionally, magnesium is sensitive to electron irradiation damage. Irradiation damage in magnesium was observed when working at 160 kV and 200 kV and room temperature at the Jeol JEM-2010 microscope. Figure 2.15 shows the nucleation and growth of electron

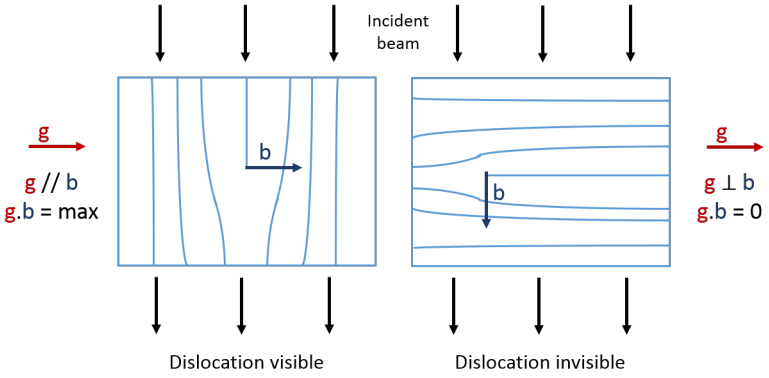

Figure 2.14 – Dislocation extinction condition.

irradiation induced dislocation loops when imaging a certain region of a magnesium-Y_2O_3 nanocomposite elaborated by FSP. TEM analysis performed at the Jeol 2010 (SIMaP) and Jeol JEM2100 F (CMTC) microscopes have used an accelerating voltage of 200 kV, but irradiation damage has not been observed.

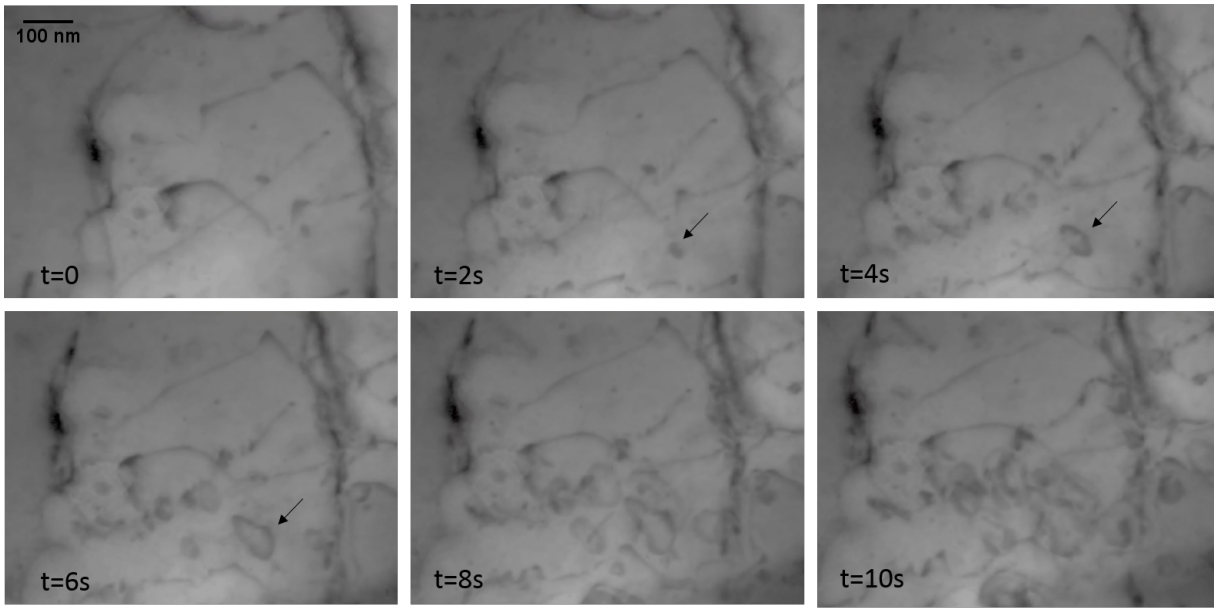

Figure 2.15 – *In situ* observations of loop growth of TEM induced irradiation damage in magnesium observed at 200 kV and room temperature (TEM LaB_6 Jeol JEM-2010).

2.6 X-ray tomography

X-ray tomography or computed tomography (CT) is a non-destructive technique that provides a three dimensional (3D) image of the analyzed material. In other words, a

3D map of the coefficient of linear absorption. It is physically based on the partial absorption and/or phase shift of an X-ray beam that passes through a sample. The transmitted beam hits a scintillator that converts the X-rays into visible light and a photodetector produces a digital image. This technique is sensitive to changes of the atomic number and the concentration, but not to crystal orientation or grain boundaries. The principle of X-ray tomography consists in the acquisition of several hundreds radiographs of the sample (2D projections) while it rotates. Depending on the incident beam geometry (parallel or conical), the radiographs or projections are acquired over a sample rotation of 180° or 360°. The 3D volume can be reconstructed from these projections using a specific algorithm [122, 123]. A schematic representation of the acquisition and reconstruction process can be found in Figure 2.16 [124].

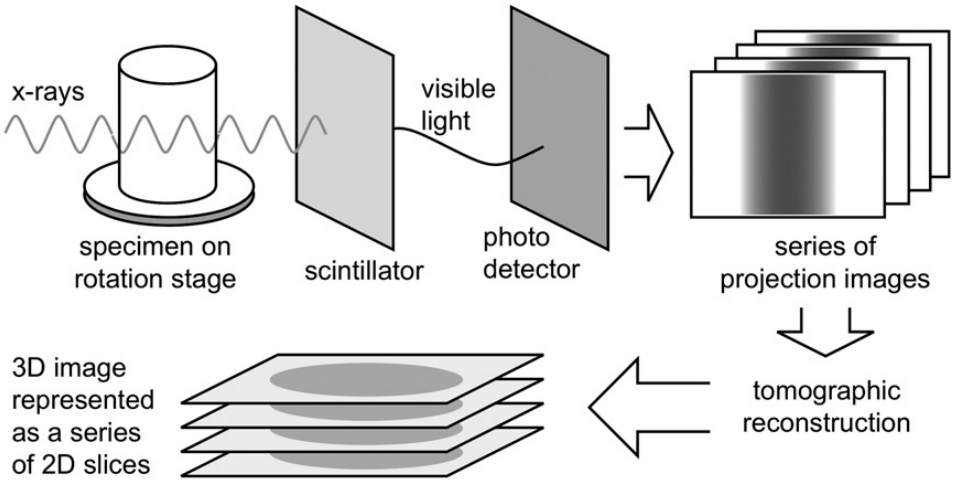

Figure 2.16 – Schematic representation of the tomography acquisition and reconstruction [124].

In the present study, conventional tomography and Synchrotron X-ray radiation tomography were applied for the three dimensional characterization of the composites. The main difference between a tomographic analysis performed in a laboratory tomograph and in a synchrotron facility is the X-ray source. Synchrotron radiation is characterized by a high X-ray flux as well as a coherent and monochromatic beam. The high flux is responsible for the reduced acquisition time and low noise. The monochromaticity of the beam is the basic assumption of the reconstruction algorithms. It allows then the resolution of very subtle variations in the absorptivity of different phases, increasing the contrast. Since the synchrotron beam is coherent, nearly parallel, there is no magnification of the image as in a laboratory tomograph, where the beam is conical [125]. The coherency of the beam is also responsible for the formation of interferences (phase contrast) that

allows the performance of nanotomography. Table 2.1 summarizes the main differences between a laboratory X-ray source and a Synchrotron radiation.

Table 2.1 – Differences of the X-ray source used in a conventional tomography and in a Synchrotron radiation tomography.

Laboratory X-ray source	Synchrotron radiation
Low flux	High flux
White beam	Monochromatic, pink beam or white beam
Conical beam	Parallel or conical (focalized) beam

Tomographic scans were carried out in order to identify the three dimensional spatial distribution of the reinforcement particles and the presence of porosities or defects generated during processing. Three different tomography facilities were used during the study in order to obtain a better resolution:

- A laboratory tomograph (Nanotom XL from RX Solution) with a Quadro 4320 detector and a nanofocus X-ray tube, based at SIMAP-GPM2. The accelerating voltage of the tube was 45 kV. The voxel size obtained during tomography analysis on this equipment was 0.5μm. About 920 images were recorded during the tomography scans, each using an exposure time of 2 s. The scans time vary from 60 to 90 minutes.

- Fast microtomography experiments were carried out on the ID19 beamline of the European Synchrotron Radiation Facility (ESRF). The sample was glued at the top of an aluminum rod fixed on a rotating stage. A dedicated optic system with a x10 (pixel size 1.1μm) or x20 (pixel size 0.55μm) optic and LuAG scintillator was placed in front of the camera. The camera is a PCO Dimax that allows fast acquisition imaging. The tomographic scans were performed with a pink beam of 17.6 keV and an exposure time of 2.10^{-3} s. The 3D volumes were reconstructed by applying back-projection algorithms to the recorded data.

- Synchrotron X-ray nanoholotomography scans performed at the ID16A (nano-imaging Beamline, at the ESRF) by Alexandra Pacureanu were part of the MA2584 proposal. One characteristic of the nanoholotomography is that radiographs were taken at four sample-source distances while keeping the detector position fixed. The distances

were modified in order to obtain the following pixel sizes and fields of view: 120 nm (243 μm) , 50 nm (95 μm) and 25 nm (45 μm). The field of view defines the area that will be visible in the tomography. Since the sample was significantly larger than the fields of view (sample diameter is 500 μm), local tomography was performed after selecting the relevant region of interest on a low resolution tomography scan. Further details about the imaging set-up can be found in [126].

Table 2.2 summarizes the main differences between the different tomography set ups used in this study. A higher resolution is obtained with the use of a smaller pixel size, however, it is associated with a reduction of the analyzed volume. The 3-D images (reconstructed tomography) were quantitatively analyzed (segmentation and particle quantification) using the ImageJ software and in-house plugins.

Table 2.2 – Characteristics of the different tomographic analysis performed during this study.

Parameter	Laboratory tomograph	ID19 (microtomography)	ID16A (nanotomography)
Pixel size	0.5μm	1.1μm, 0.55μm	120 nm, 50 nm, 25 nm
Duration	60-90 min	<10 s	≈10 h (for 3 pixel sizes)
Energy	45kV	17.6keV	17keV
Field of view	500μm	1.1mm	243μm, 95μm, 45μm
Analyzed volume	10.10^7 μm^3	1.10^9 μm^3	1.10^7, 7.10^5, 7.10^4 μm^3
Local tomography	No	No	Yes

2.7 X-ray diffraction

Pole figure is a mean of displaying the crystallographic texture. When a crystal is submitted to a monochromatic X-ray beam with a wavelength of λ, a given crystallographic plane family hkl, with an interplanar spacing d_{hkl}, will diffract if the normal to these hkl planes makes an angle $(\pi/2)$ - θ with the beam. This is the fundamental of X-ray diffraction which is governed by Bragg's law (Equation 2.10).

Pole figures are obtained by XRD measurements when the diffraction angle (2θ) is fixed and the diffracted intensity is collected by varying two geometrical parameters,

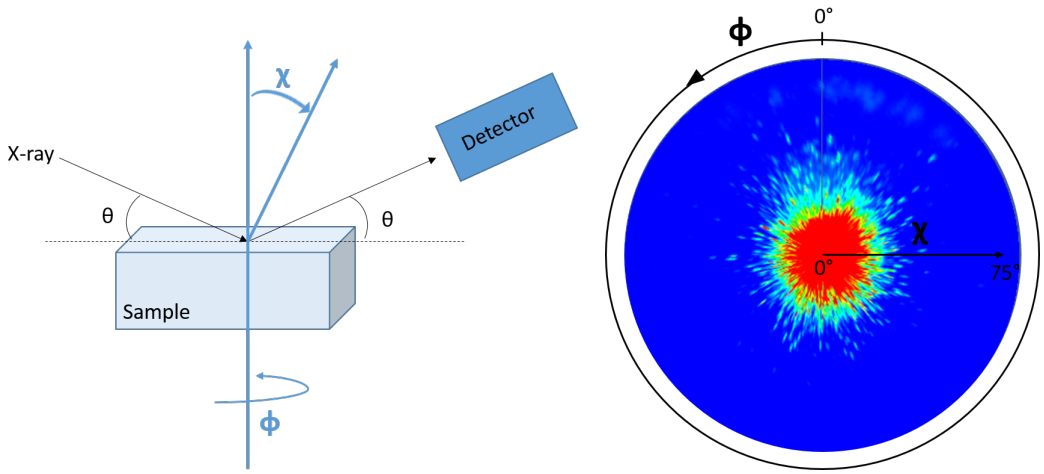

Figure 2.17 – Schematic representation of the XRD measurements and the (0 0 0 1) incomplete pole figure analysis.

which are the χ angle (tilt angle from the sample surface normal direction) and the ϕ angle (rotation angle around sample surface normal direction). The obtained diffracted intensity data is plotted as a function of χ and ϕ. In the present work, χ varies from 0° to 75° and ϕ varies from 0° to 360°. The pole figure is represented by the stereographic projection of the crystallographic planes. Figure 2.17 shows a schematic representation of the XRD measurement and a typical pole figure.

Key points of Chapter 2

1. Microstructural characterization of the nanocomposites has been performed using optical microscopy, SEM, EBSD, TEM and X-ray diffraction.
2. 3D characterization of the reinforcement dispersion and morphology in the nanocomposite has been performed using X-ray tomography (laboratory tomography, fast microtomography and nanoholotomography) with different resolutions.
3. Compression and tensile specimens have been sampled from polycrystalline nanocomposites.
4. Single crystalline microcolumns were machined into the surface of bulk nanocomposites using focused ion beam (FIB) milling. Microcolumns with varying mid-height diameters (2, 5, 10 and 15 μm) were machining, keeping an aspect ratio of 3. EBSD was employed to determine the grain orientation prior to the machining of the microcolumns.
5. Microcompression testing was performed *ex situ* using a conventional nanoindenter, whose indenter tip has been replaced by a flat punch.
6. The compressed columns were analyzed *post mortem* using SEM, EBSD and TEM. The twin and slip activities were investigated.
7. Cross-sectioning of the deformed columns using FIB milling was performed in order to prepare lamellas for EBSD and thin foils for TEM.

CHAPTER 3

Processing and characterization of magnesium matrix nanocomposites

The aim of this chapter is to discuss the processing of the "*model*" magnesium based nanocomposite whose mechanical properties will be characterized at the scale of the polycrystal and the single crystal in Chapter 4. One challenge is the processing of single crystalline samples with a homogeneous distribution of reinforcement particles and a controlled volume fraction. The mechanical behavior will then be investigated by microcompression testing of microcolumns fabricated in grains of a polycrystalline nanocomposite. A microcolumn machined inside a given grain can be considered as a single crystal. Several relevant orientations for magnesium will be tested by microcompression testing. The crystal orientation of the grains is obtained using EBSD analysis and since the microcolumns are machined inside a single grain, it is hence preferable to elaborate a polycrystalline nanocomposite with coarse grains. It increases the probability that the entire column will be inside a single grain. This is rather challenging as the addition of small reinforcement particles tends to reduce the grain size

Another important aspect is the homogeneity of the particles distribution in the nanocomposite. The volume of the microcolumns used during this study varies from 19 μm^3 for the 2 μm-diameter column to 176 μm^3 for the 15 μm-diameter column. Thus, it is important to have a homogeneous dispersion of the particles, in order to ensure the presence of particles even inside the smaller columns and to have a comparable volume fraction between microcolumns.

The choice of pure magnesium as a matrix for the nanocomposite instead of an

alloy comes from the fact that it allows to work with a simple system: pure magnesium and reinforcement phase. Additionally, the chemical stability between the magnesium matrix and the particles is also critical and the thermal instability of the particles during the elaboration process can also create undesirable phases. These aspects must be taken into consideration for the choice of the reinforcement and the elaboration processing.

Considering the aspects discussed above, the most important requirements for the nanocomposite used for the study of the mechanisms of plastic deformation are: coarse grains, a homogeneous particle distribution and chemical stability of the particles. A "*model*" nanocomposite presenting these characteristics needs then to be elaborated. The different elaboration methods more commonly used for the elaboration of magnesium based composites have been briefly presented in Section 1.3.1. Table 3.1 correlates these elaboration methods with the requirements for the "*model*" nanocomposite.

Table 3.1 – The requirements for the "*model*" nanocomposite are correlated with the processing techniques more commonly used for magnesium based nanocomposites.

Processing techniques	**Required characteristics**		
	Coarse grains	Particle distribution	Chemical stability
Ultrasound assisted casting	✓	✓	≈
Disintegrated melt deposition	✓	✓	≈
Squeeze casting	✓	✓	X
Powder metallurgy	X	✓	X
Mechanical alloying	X	✓	X
Friction stir processing	≈	✓	✓

Considering at first, the coarse microstructure required for the "*model*" nanocomposite, powder metallurgy and mechanical alloying were discarded due to the fine grain structure obtained for the nanocomposites fabricated using these techniques. Friction stir processing usually produces composites with a fine microstructure due to the dynamic recrystallization that takes place during the processing. However, some studies [127, 128, 129, 130] have shown that abnormal grain growth can occur during subsequent thermal treatment. Additionally, DMD and squeeze casting techniques were not available in the present study. Thus, ultrasound assisted casting and friction stir processing were

chosen as two candidates for the elaboration of the "*model*" nanocomposites used in this study.

Different oxide particles have been tested as reinforcements for magnesium: Al_2O_3, MgO and Y_2O_3. Section 3.1 and Section 3.2 detail the ultrasound assisted casting and the friction stir processing, respectively. The processing parameters, materials and volume fraction of reinforcement will be presented. Each section presents a complete microstructural characterization of the obtained nanocomposites, including synchrotron X-ray microtomography and nanoholotomography for determination of the 3 dimensional dispersion of the particles.

3.1 Ultrasound assisted casting

Ultrasound assisted casting has been the first option for the elaboration of the nanocomposites due to its low cost and the possibility to obtain a coarse microstructure. Magnesium based composites reinforced with three different oxide particles were elaborated using ultrasound assisted casting. Al_2O_3, MgO and Y_2O_3 oxide particles were used as reinforcements.

In the present section, the details about the elaboration process using ultrasound assisted casting will be presented, followed by a characterization of the nanocomposites. The microstructural characterization as well as the mechanical characterization will determine the viability to use these nanocomposites as "*model*" nanocomposite suitable for the study of the deformation mechanisms.

3.1.1 Materials

The nanocomposites were elaborated within the framework of the European project Exomet (7th Framework Programme of the European Commission - FP7-NMP-2011-LARGE-4) at the Helmholtz Zentrum Geesthacht (HZG), Germany. The matrix consists of high purity magnesium. Al_2O_3, MgO and Y_2O_3 particles with an average size of 36 nm, 300 nm and 500 nm, respectively, were used as reinforcement material. The reinforcement particles were provided by TOMSK, a partner of Exomet project. The micrographs of the oxide particles are shown in Figure 3.1.

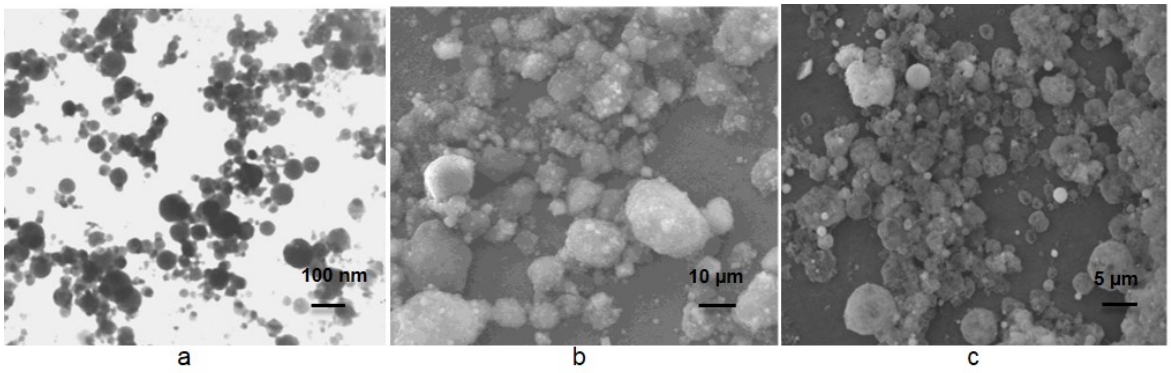

Figure 3.1 – TEM micrographs of the oxide particles provided by TOMSK: Al_2O_3 (a), MgO (b) and Y_2O_3 (c) (micrographs provided by Exomet project).

3.1.2 Processing parameters

Pure magnesium was melted and the temperature was kept constant at 720°C. The melt was poured into a cylindrical mould (preheated to 450°C) and placed into a three zones resistance furnace to maintain the temperature constant at 670°C. The reinforcement particles (1 weight %) were introduced in the molten magnesium (Figure 3.2(a)) and

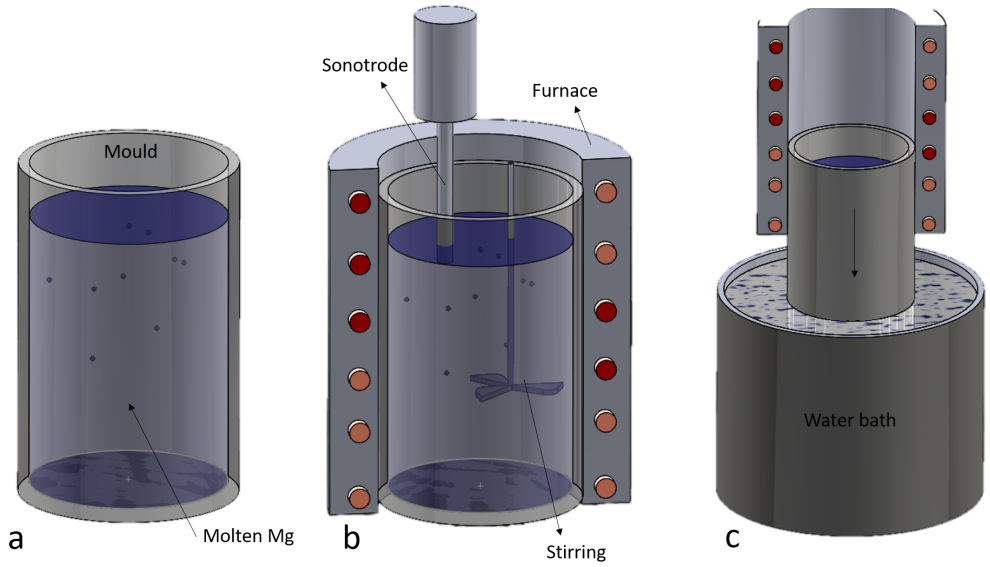

Figure 3.2 – Schematics of the ultrasound assisted casting. The reinforcement particles are introduced into the molten magnesium (a). A high speed stirring and a sonotrode (b) help to disperse the particles and to break the particles agglomerates. Once the stirrer and the sonotrode are removed, the mould moves down into a water bath (placed below the furnace) at a constant speed (c).

the homogenization was conducted during 5 minutes using a high speed stirring (200 rpm)

and a sonotrode (0.3 kW) (Figure 3.2(b)). The ultrasound generator used is a UIP1500HD from Hielscher. The ultrasonic waves help to break the particles agglomerates. The melt was quickly cooled down by lowering the mould into a water bath located beneath the ring furnace (Figure 3.2(c)). The mould descends into the water bath at a constant speed, thus, solidification starts at the bottom of the mould. The same process was used to elaborate four different samples: pure magnesium (reference sample), magnesium reinforced with Al_2O_3, MgO and Y_2O_3. Further details about this process can be found in [131, 132]. Table 3.2 summarizes the samples fabricated by ultrasound assisted casting.

Table 3.2 – Summary of the samples fabricated using ultrasound assisted casting.

Sample	**Particle shape**	**Particle size (nm)**	**Weight fraction (%)**	**Volume fraction (%)**
Mg	-	-	-	-
Mg+Al_2O_3	spherical	36	1	0.45
Mg+MgO	spherical	300	1	0.49
Mg+Y_2O_3	spherical	500	1	0.35

3.1.3 Microstructural characterization

A microstructural analysis of each sample has been performed using optical microscopy, scanning electron microscopy (SEM), transmission electron microscopy (TEM) and EBSD. Additionally, synchrotron X-ray microtomography has been performed in order to obtain the 3D dispersion of the reinforcement particles. During microtomography, 2016 images were recorded and the pixel size was 0.55 μm.

3.1.3.1 Grain size

All the samples elaborated by ultrasound assisted casting present coarse grains. It was not possible to measure the grain size since most of the grains were larger than 1 mm. To the author's knowledge, there is no efficient measurement technique for such large grains. EBSD (Figure 3.3) and polarized light optical microscopy (Figure 3.4) were used in order to confirm the grain size.

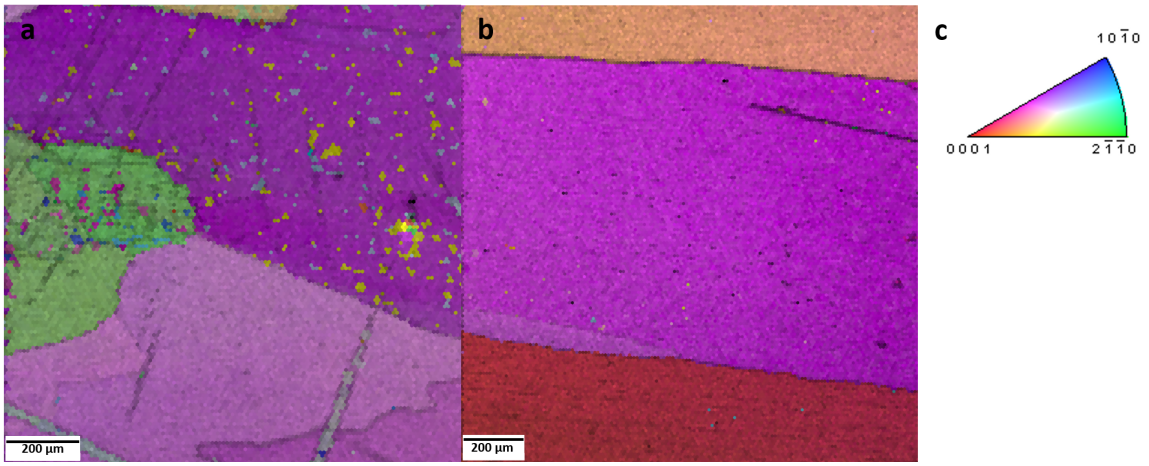

Figure 3.3 – EBSD orientation map of Mg (a) and Mg+Al_2O_3 (b) confirm the large grain size. The grayscale component is given by OIM software image quality index. The color coded map is shown in (c).

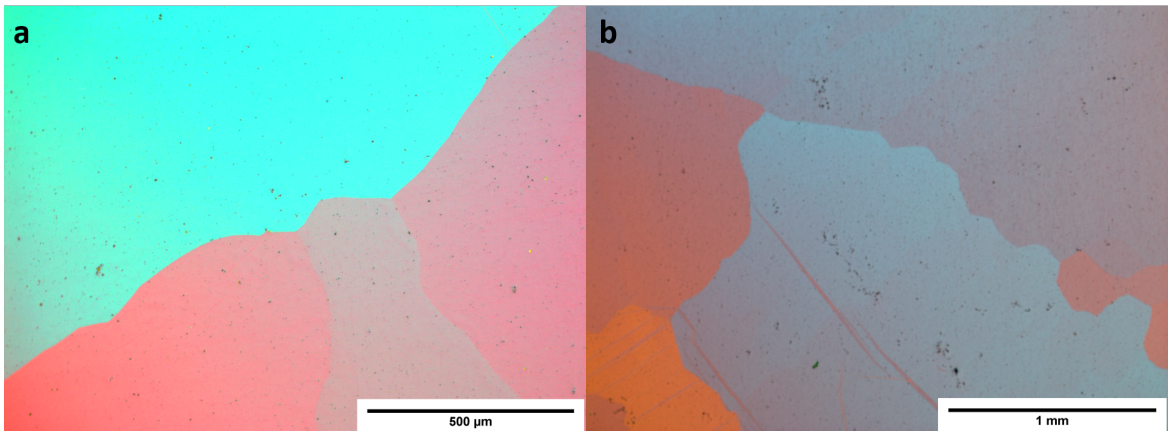

Figure 3.4 – Polarized light optical micrographs evidence the large grain size obtained for samples fabricated by ultrasound assisted casting without any chemical etching: Mg+MgO (a) and Mg+Y_2O_3 (b).

3.1.3.2 Reinforcement dispersion

The importance of a homogeneous dispersion of the reinforcement phase has already been mentioned in the requirements for the "*model*" nanocomposite. Scanning electron microscopy and synchrotron X-ray microtomography have been used in order to investigate the dispersion of the reinforcements in the magnesium matrix and to verify the presence of porosities. The results will be presented individually for each nanocomposite fabricated by ultrasound assisted casting.

- **Mg + Al_2O_3**

The heterogeneous dispersion of Al_2O_3 particles in the magnesium matrix can be observed in Figure 3.5(a). The initial size of the Al_2O_3 particles is 36 nm, however most of the particles are agglomerated in clusters larger than 5 μm as it can be seen in Figure 3.5 (b and c). The clustering can also be observed at small scale in the TEM micrographs (Figure 3.6). TEM micrographs evidence the presence of small Al_2O_3 (size close to 50 nm) inside the clusters.

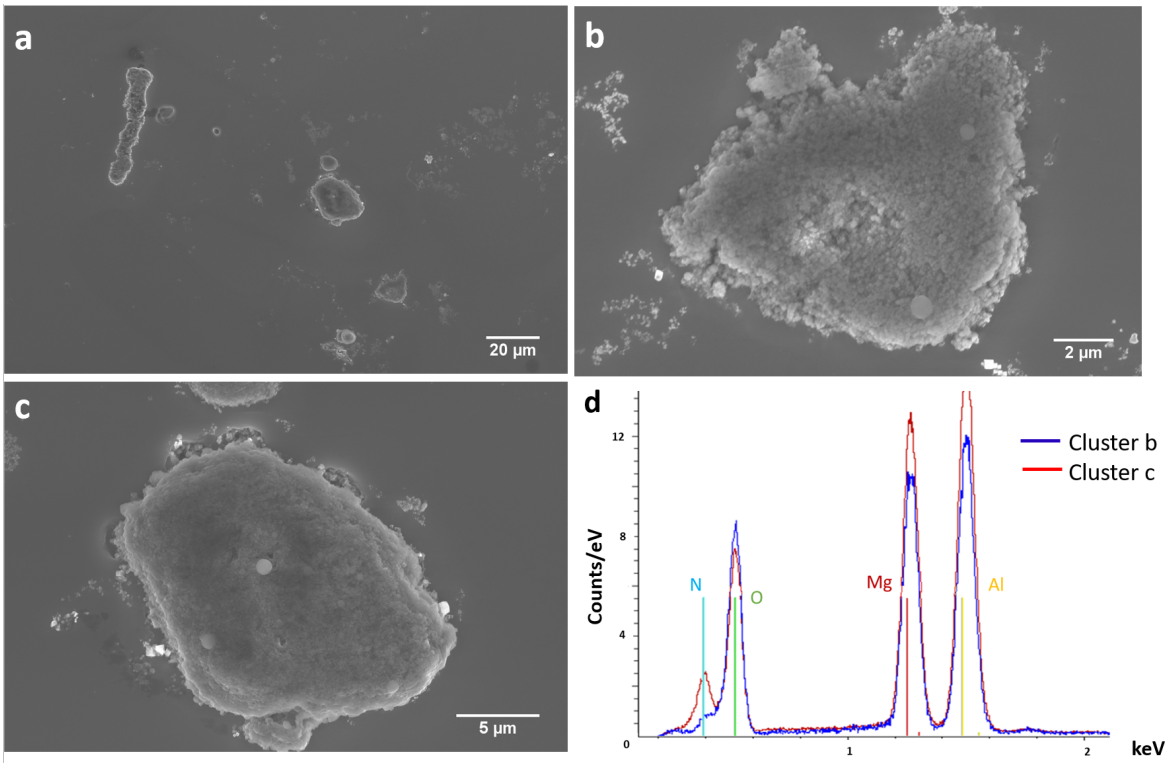

Figure 3.5 – SEM micrographs of Mg + Al_2O_3 sample evidence an inhomogeneous dispersion of Al_2O_3 particles (a) and a strong particles agglomeration (b and c). A chemical analysis (d) confirms the presence of Al_2O_3 particles in both clusters.

In addition, some square-shape particles have been observed (Figure 3.7 (a)). Since the initial Al_2O_3 particles have an spherical shape, a chemical analysis of these square particles has been performed and confirms the presence of MgO (Figure 3.7 (b))). It confirms that a chemical reaction has taken place during ultrasound assisted casting and magnesium has reacted with the Al_2O_3 particles. MgO, aluminum and $MgAl_2O_4$ are formed according to the following reactions [133]:

$$3\ Mg + Al_2O_3 \rightarrow 3\ MgO + 2\ Al$$

$$3\ Mg + 2\ Al_2O_3 \rightarrow 3\ MgOAl_2O_4 + 2\ Al$$

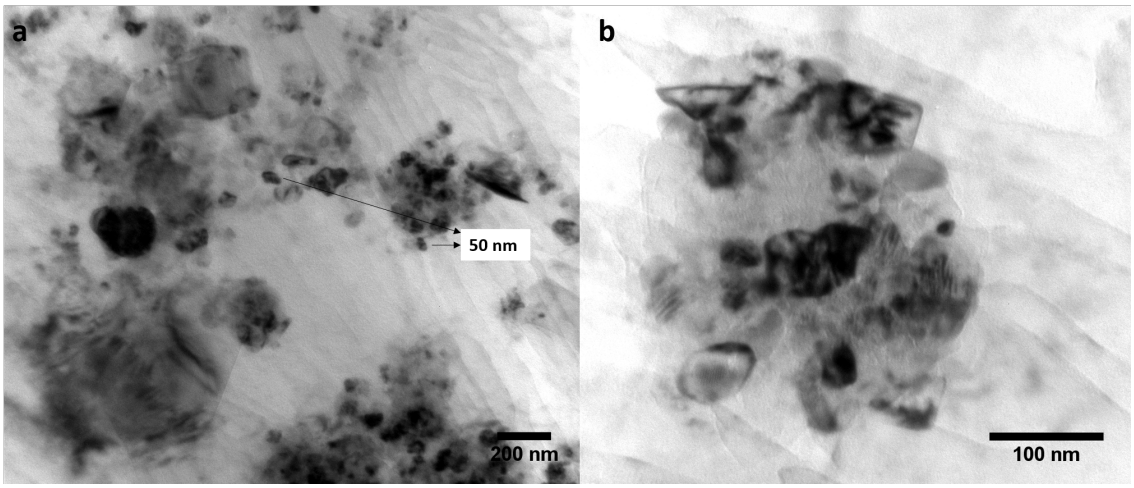

Figure 3.6 – Bright field TEM micrographs of Mg + Al_2O_3 sample evidence clustering of Al_2O_3 particles.

These observations clearly confirm that Al_2O_3 is unstable in magnesium.

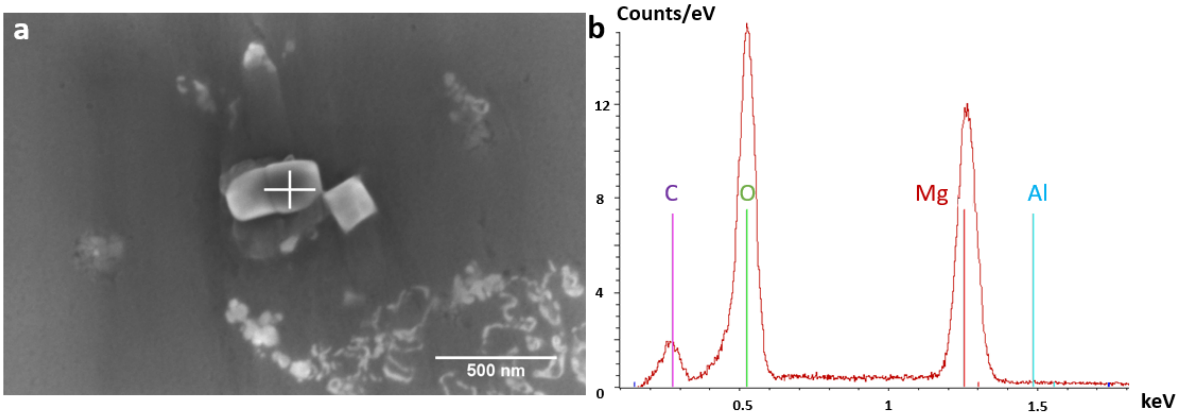

Figure 3.7 – EDS analysis performed at the white cross location in the SEM micrograph (a) of Mg + Al_2O_3 sample shows the presence of MgO (b).

In addition to the 2D observations using SEM and TEM, 3D observations have been carried out using synchrotron X-ray microtomography. The results indicate the presence of porosities and clustering in the Mg + Al_2O_3 sample, as it can be seen in the 2D slices extracted from the tomographic reconstructed volume (Figure 3.8). Clusters with sizes ranging from 50 to 90 μm are observed. The strong clustering is due to the fact that smaller particles are more likely to form clusters due to their higher surface energy.

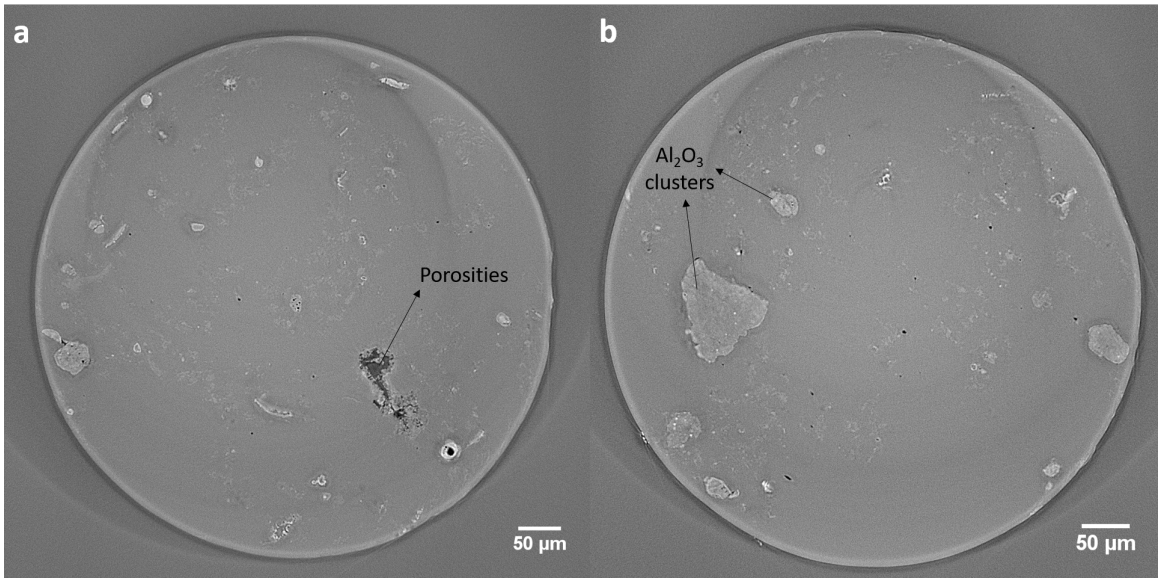

Figure 3.8 – 2D slices from synchrotron X-ray microtomography evidence the presence of some porosities (a) (dark regions) and large Al_2O_3 clustering (b) (white regions). The pixel size used in the synchrotron X-ray micromography is 0.55 μm.

- **Mg + MgO**

Similarly to Mg + Al_2O_3, Mg + MgO have also shown a heterogeneous dispersion of the reinforcement in the magnesium matrix (Figure 3.9). MgO square-shape

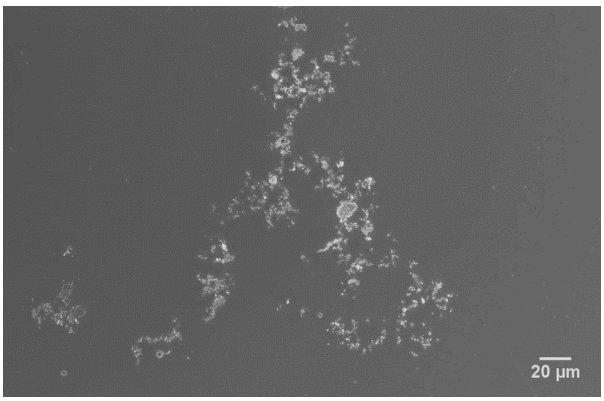

Figure 3.9 – SEM micrograph of Mg + MgO samples confirms an inhomogeneous dispersion of MgO particles.

particles have been formed during ultrasound assisted casting as it can be observed in Figure 3.10 (a and b). The sample examined by synchrotron X-ray microtomography did not show the presence of any MgO particle due to the presence of a huge porosity in the center of the sample, reducing then the area where MgO particles can be visualized.

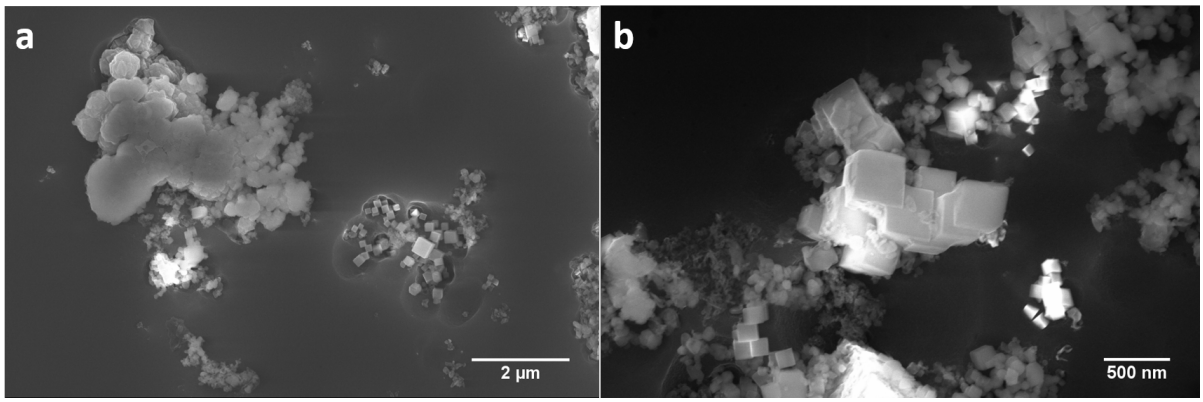

Figure 3.10 – SEM micrographs of Mg + MgO samples show a strong particle agglomeration (a). MgO square-shape particles have been formed during ultrasound assisted casting (a and b).

The results from synchrotron X-ray microtomography are inconclusive for Mg + MgO samples. Unfortunately it was not possible to perform additional analysis.

- **Mg + Y_2O_3**

As for the previous nanocomposites, Mg + Y_2O_3 have shown a heterogeneous dispersion of Y_2O_3 particles and particle agglomeration (Figure 3.11). Some large spher-

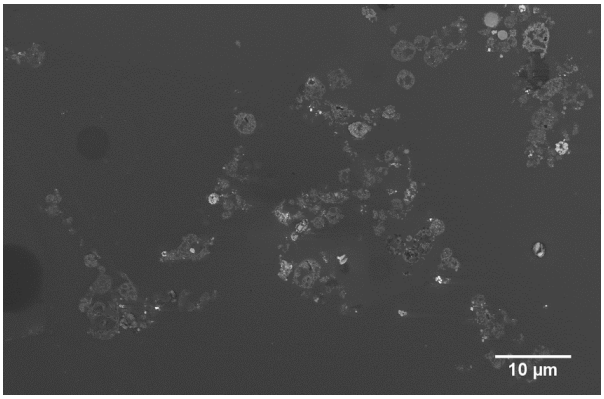

Figure 3.11 – SEM micrograph of Mg + Y_2O_3 sample evidences an inhomogeneous dispersion of Y_2O_3 particles.

ical Y_2O_3 particles can also be seen in Figure 3.12 (a and b). Y_2O_3 is more stable than Al_2O_3 and MgO: no MgO square-shape particles could be observed. Additionally, 2D slices extracted from the 3D reconstruction of the synchrotron X-ray microtomography scans are presented in Figure 3.13: no porosities were observed and the particle dispersion seems to be more homogeneous than the one observed in the previous samples (less clustering).

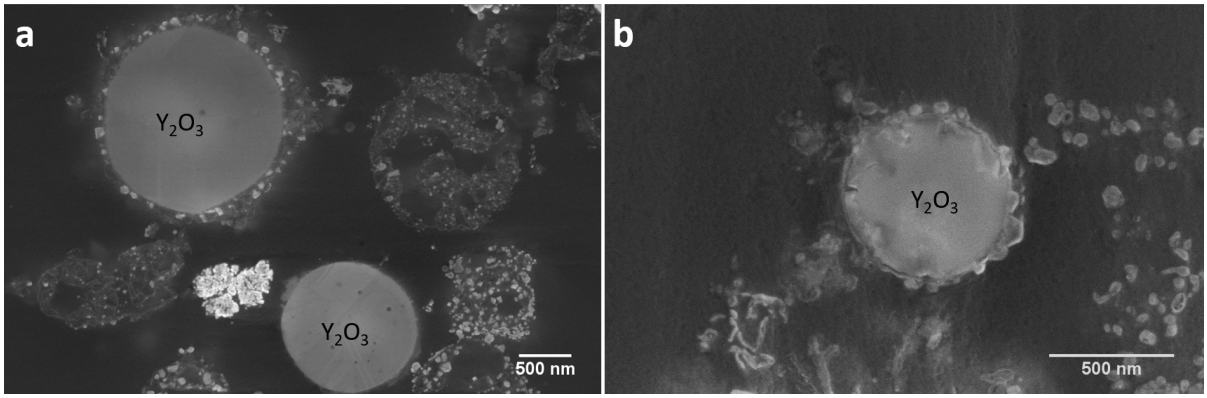

Figure 3.12 – SEM micrographs of Mg + Y_2O_3 sample show a strong particle agglomeration (a and b). Some large spherical Y_2O_3 particles can also be seen in (b and c).

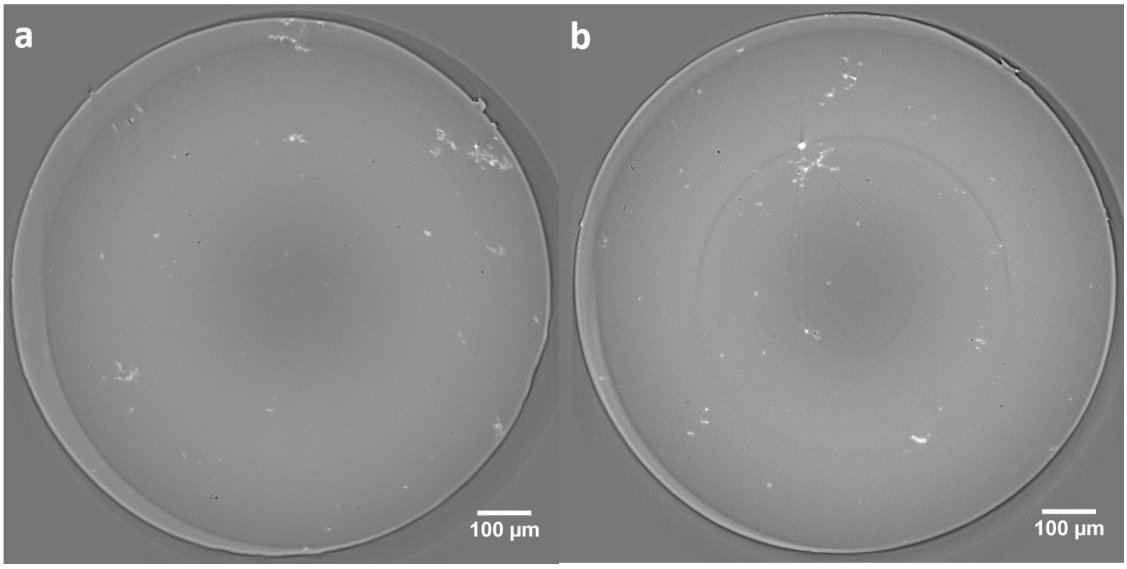

Figure 3.13 – 2D slices from synchrotron X-ray microtomography shows a quite homogeneous dispersion of Y_2O_3 particles (white regions) and a dense material (no porosities could be seen).

3.1.4 Mechanical properties

Microstructural characterization has already shown a heterogeneous dispersion of reinforcement and particle agglomeration for the three composites fabricated by ultrasound assisted casting. In addition, micro hardness and compression testing have been performed in order to measure any strengthening effect in the composites. Vickers micro hardness experiments have not shown any significant strengthening between pure magnesium and the composites and these results will not be presented. The specifications about the compression tests are presented in Section 2.3.1.

Figure 3.14 shows the true stress vs. true strain response for pure magnesium,

Mg + Al_2O_3, Mg + MgO and Mg + Y_2O_3 obtained from compression testing. Pure

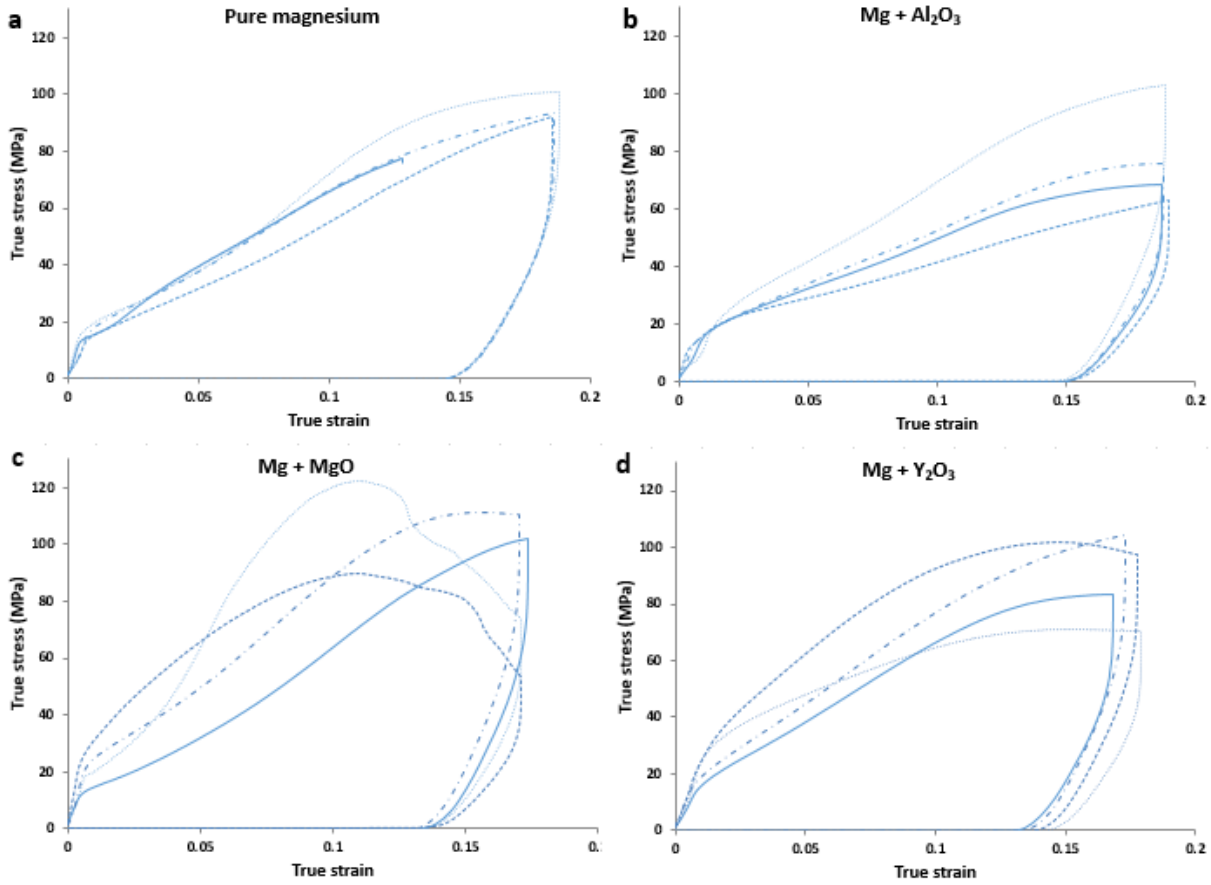

Figure 3.14 – True stress vs. true strain response for samples fabricated by ultrasound assisted casting: pure magnesium (a), Mg + Al_2O_3 (b), Mg + MgO (c) and Mg + Y_2O_3 (d).

magnesium specimens have shown a reasonable reproducible behavior, however, the same was not observed for the nanocomposites. Many factors can be responsible for such disparities in the mechanical response: coarse grain size, different crystal orientation, heterogeneous particle dispersion and the presence of porosities.

The small cross section of the compression specimens (3.14 mm^2) can contain only a single grain for such coarse grains: it has already been mentioned that the grains were larger than 1 mm. As magnesium has a strong anisotropic mechanical behavior, the crystal orientation can strongly affect the mechanical response. For a polycrystalline material with fine grains this effect is averaged, but in the present case, the coarse microstructure along with the small size of the compression specimen renders the crystal orientation effect important.

Moreover, the heterogeneous dispersion of the reinforcement particles, as evi-

denced by the microstructural characterization, can also induce a large scattering in the mechanical responses under compression. It is more likely that each specimen do not contain the same volume fraction of particles and consequently do not react the same manner under compression. Additionally, the porosity observed in the microtomography, especially in Mg + Al_2O_3, can also alter the mechanical response. Considering the fact that processing defects play a very important role in the mechanical response and can hinder the role of particles, it seems difficult to draw conclusions based on the curves of Figure 3.14.

To conclude, it is extremely difficult to identify the factors acting for each compression specimens. The compression tests cannot be conclusive whether there is a strengthening effect or not.

3.1.5 Suitability

The microstructural and mechanical characterizations performed on the composites prepared by ultrasound assisted casting have shown a heterogeneous dispersion of reinforcement particles. Even the addition of very small Al_2O_3 particles (36 nm) have presented strong clustering with cluster sizes larger than 40 μm (Figure 3.8). Such clustering and heterogeneous dispersion make the use of ultrasound assisted casting impossible for the elaboration of the "*model*" nanocomposite with the expected parameters (fixed volume fraction, particle size, minimum porosity, etc).

The homogeneous dispersion of reinforcement particles is extremely important especially when the objective is to perform microcompression testing for which the volume of material is limited. The compression tests at a macroscale have already shown a large dispersion of the mechanical response of the composites fabricated by ultrasound assisted casting. Figure 3.15 shows a microcolumn fabrication close to a cluster of particles on a Mg + Y_2O_3 sample fabricated by ultrasound assisted casting. Milling a single crystal of only a single phase produces a smooth surface, however, a rough surface is observed when the milled material contains particles, impurities or even when the grain orientation changes (see Figure 3.15). It is possible to observe that as the milling goes deeper, the particle cluster is still visible in the region where the material is removed. In this column, the Y_2O_3 particles will most probably be concentrated in the top of the column (indicated by a white arrow in Figure 3.15 (b) and (c)). This big cluster will act as a large Y_2O_3

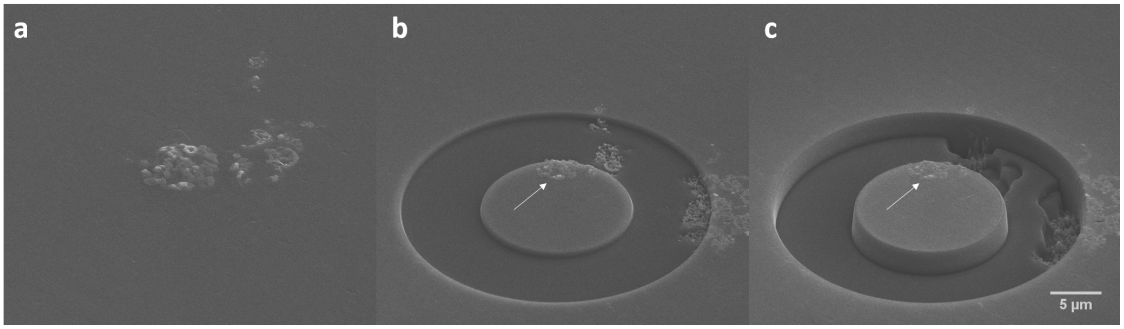

Figure 3.15 – Microcolumn FIB milling close to a cluster of particles (a) on a Mg + Y_2O_3 sample fabricated by ultrasound assisted casting. Milling a single crystal of only a single phase produces a smooth surface, however, as soon as particles, a different grain orientation or another impurity are present, a rough surface is observed. In this example, going deeper in the milling, it is still possible to observe the particle cluster in the region where the material is removed. In this column, the Y_2O_3 particles will most probably be concentrated in the top of the column (white arrow in b and c).

particle. In addition, the presence of wide regions without reinforcements observed in all the composites makes it difficult to confirm that the volume fraction of reinforcement is equivalent between two different columns of the same material. At this point, it is impossible to use the composites fabricated by ultrasound assisted casting as "*model*" nanocomposites.

It is important to precise that good results are presented in the literature [6, 88, 89] for nanocomposites fabricated by the ultrasound assisted casting technique and homogeneous dispersion of the reinforcement particles are obtained. In the present study, the samples elaborated by ultrasound assisted casting have been processed in the framework of the Exomet project and it was not possible to perform a deeper investigation of the processing parameters in order to improve the homogeneity, which is a crucial aspect as demonstrated previously. Table 3.3 correlates the results obtained by ultrasound assisted

Table 3.3 – Requirements for the "*model*" nanocomposite and the results obtained using ultrasound assisted casting.

Requirements	**Ultrasound assisted casting**
Coarse grains	✓
Particle dispersion	x
Particle stability	x

casting and the requirements for the "*model*" nanocomposite: particle dispersion and particle stability are not fulfilled. Thus, another processing technique will be considered

in order to elaborate the "*model*" nanocomposites, namely the friction stir processing.

3.2 Friction stir processing

Friction stir processing (FSP) technique has been tested for the preparation of the "*model*" nanocomposites. FSP is a novel solid state processing technique based on the same principles of friction stir welding (FSW) (see FSP in Section 1.3.1). The main difference between both techniques is the existence of a joint between two plates in FSW. It is usually applied to modify the microstructure of the material: grain refinement, homogenization of the microstructure of cast materials (reducing porosity and defects), precipitation and texture modification.

In the present study, FSP has been applied for the fabrication of magnesium based nanocomposites reinforced with Y_2O_3 particles. The details about the elaboration process and processing parameters will be presented as well as their influence on the final microstructure. To conclude, the viability of using the nanocomposites fabricated by FSP as "*model*" nanocomposite for this study will be discussed, as for ultrasound assisted casting.

3.2.1 Materials

Magnesium matrix nanocomposites were elaborated from 99.95 % purity magnesium plates (from Magnesium Elektron) and Y_2O_3 powder. The detailed chemical composition of the magnesium plates provided by the supplier is shown in Table 3.4. The original Y_2O_3 powder has a mean diameter of 3.5 μm [79]. The morphology of the Y_2O_3 powder is presented in Figure 3.16. The advantages of working with Y_2O_3 is its high thermal stability, which is one of the requirements for the "*model*" nanocomposite. Due to the large difference between the atomic number (Z) of Y_2O_3 (Z = 20.4) and Mg (Z = 12), Y_2O_3 presents a good contrast with respect to the magnesium matrix on the 3D tomographic images.

Table 3.4 – Chemical composition of magnesium plates used in this study.

Element	**Quantity (weight %)**
Mg	Balance
Al	<0.005
Cu	<0.005
Fe	<0.005
Mn	<0.02
Ni	<0.005
Si	<0.01

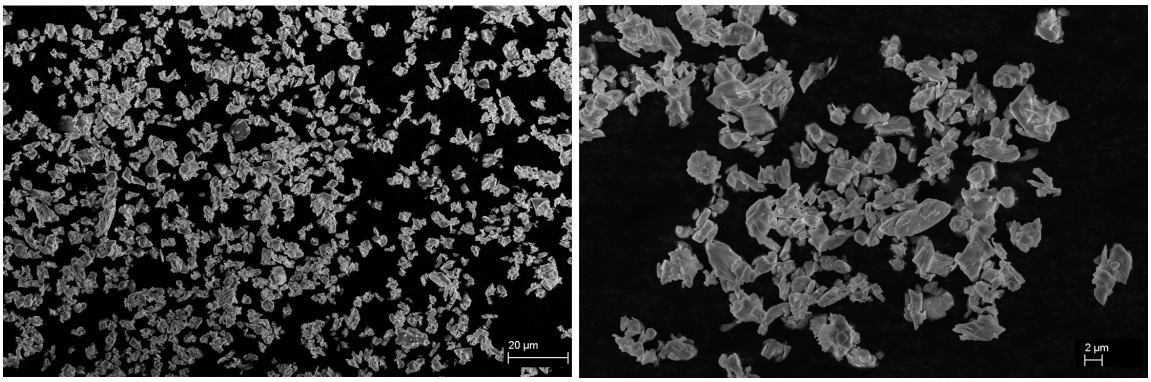

Figure 3.16 – SEM micrographs of the original Y_2O_3 powder used for FSP.

3.2.2 Optimization of processing parameters

FSP is performed in a machine similar to a milling machine, where a rotating tool is mounted. In the present case, the workpiece is an as-rolled magnesium plate with the following dimensions 3 mm x 250 mm x 48 mm (thickness x length x width). A linear groove (1 mm x 220 mm x 2 mm, depth x length x width) designed to receive the Y_2O_3 powder is machined on its surface along its length. The cavity is located in the central axis of the processing zone. The Y_2O_3 powder (around 0.5 g) is placed in the cavity and compacted. The groove is then covered with a 0.5 mm thick magnesium plate (same composition as the workpiece) in order to avoid powder loss during the process. The experiment set up is shown in Figure 3.17. The two plates were tightly fixed to the backing plate with two clamps (Figure 3.18 (a)). The 80 mm thick backing plate and the two clamps are both made of high carbon steel. The clamps provide a rigid fixing, ensuring the tight fitting of the thin magnesium plate with the 3 mm thick plate.

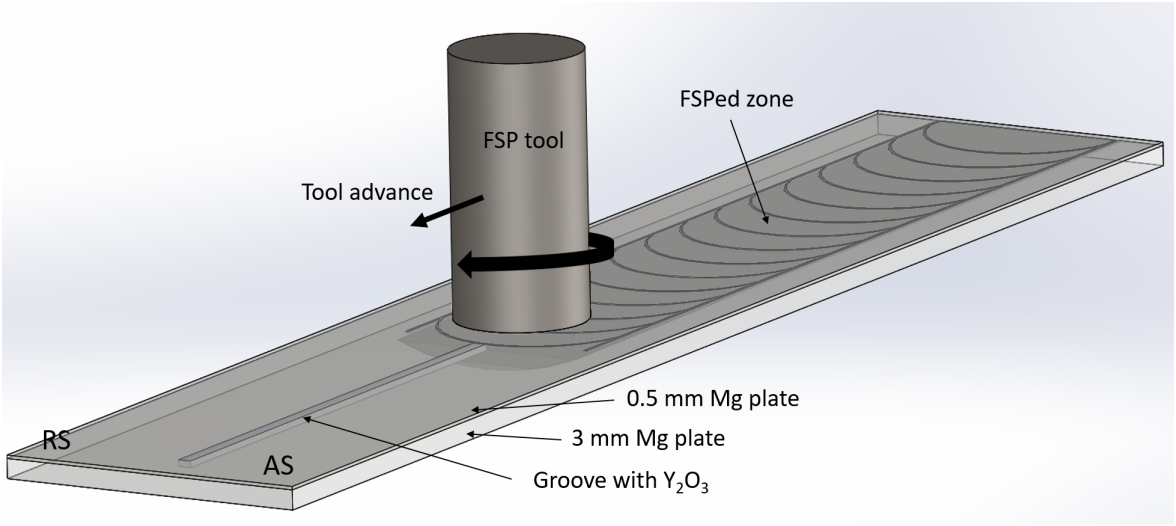

Figure 3.17 – Schematic diagram of the friction stir processing set up. A thin magnesium plate covers the groove filled with Y_2O_3 powder in order to avoid powder loss. The rotating tool penetrates on the material and advance following the center axis. The rotation of the tool favors material mixing. The advancing side (AS) corresponds to the side where the rotational tool movement is in the same direction as the advancing movement, while the retreating side (RS) is the opposite side.

The experiment was installed in a tank fulfilled with cutting oil in order to ensure the cooling of the backing plate and magnesium plates as it can be seen in Figure 3.18 (b). Friction stir processing was performed under displacement control using a HERMLE milling machine. The FSP tool was made of steel and it was tilted backwards by 1°. The tool has a 20 mm diameter scrolled shoulder and a 6 mm diameter pin (Figure 3.19). The M6 threaded Triflat pin (three sides of a hexagon inscribed in the circle of the pin) is 2 mm long [134].

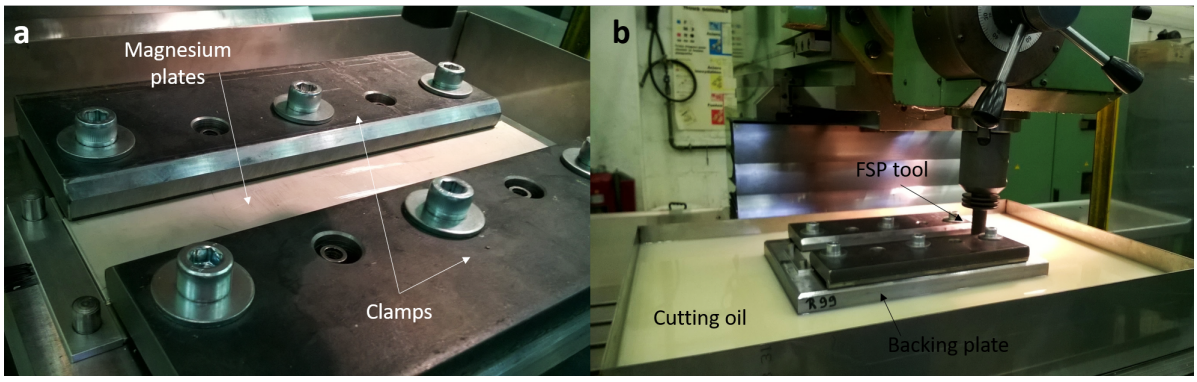

Figure 3.18 – The two magnesium plates are tightly fixed to the backing plate with two clamps (a). The experiment was installed in a tank fulfilled with cutting oil in order to ensure the cooling of the backing plate and magnesium plates (b).

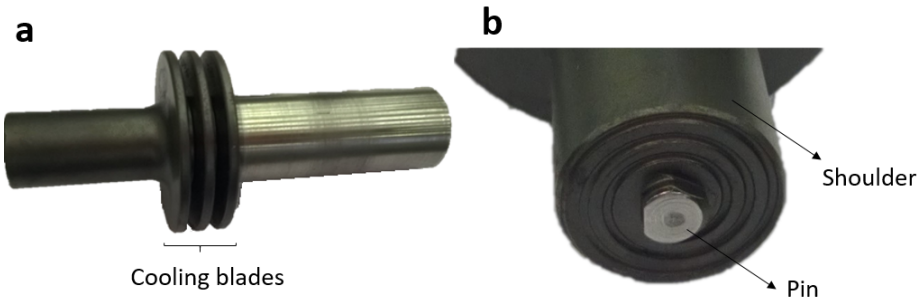

Figure 3.19 – Friction stir processing tool (a) and zoom on the shoulder (20 mm-diameter) and pin (6 mm-diameter) of the tool (b).

Three series of FSP passes were carried out successively on each sample. Each series comprises a first pass on the center axis (corresponding to the axis were the cavity fulfilled with Y_2O_3 powder is located), a second pass shifted by 1.5 mm from the center axis on the advancing side and a third pass shifted by 1.5 mm from the center axis on the retreating side (Figure 3.17). The advancing side (AS) corresponds to the side where the rotational tool movement is in the same direction as the advancing movement, while the retreating side (RS) is the opposite side. The tool displacement was parallel to the rolling direction of the magnesium sheets. The large number of passes (3x3) has been chosen since, according to the literature, the increase of the number of passes reduces the clustering of reinforcements [135, 136] and improves the homogenization [135, 136, 83].

According to Askari [137], the final microstructure and particle distributions are highly dependent on process parameters, as rotational speed, advancing speed and tool geometry. Thus, different parameters were tested as presented in Table 3.5. Pure magnesium reference samples were prepared using only the two magnesium plates, without any powder cavity.

3.2.3 Microstructural characterization

The microstructure of each pair of samples (Mg and Mg+Y_2O_3) elaborated with the same processing parameters will be analyzed. The influence of the Y_2O_3 particles on the microstructure will be investigated: grain size and particle dispersion.

The microstructural characterization has been performed in the stirred zone of the FSPed samples. Figure 3.20 shows a macrograph of the transverse cross-section of one typical FSPed sample. The stirred zone (SZ) presents a basin shape morphology

Table 3.5 – Process parameters used for the fabrication of the friction stir processed samples: FSP Mg and FSP Mg + Y_2O_3.

Materials	**Advancing speed (mm/min)**	**Rotational speed (rpm)**	**Y_2O_3 particles weight (g)**
Mg	300	1500	-
Mg	500	1500	-
Mg	500	1000	-
Mg+Y_2O_3	300	1500	0.526
Mg+Y_2O_3	500	1500	0.457
Mg+Y_2O_3	500	1000	0.461

and is symmetric in both advancing (AS) and retreating (RS) sides. The stirred zone is composed of small equiaxed grains homogeneously distributed all over the nugget. It is difficult to identify a thermomechanically affected zone or heat affected zone in the present case. Table 3.6 shows the stirred zone area as a function of the processing parameters. The area is similar for all the FSPed samples.

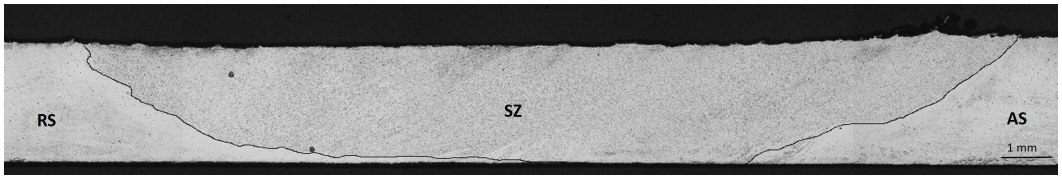

Figure 3.20 – Macrograph of the stirred zone (SZ) of a Mg+Y_2O_3 sample (processing parameters: rotational speed of 1500 rpm and advacing speed of 500 mm/min). AS and RS correspond to the advancing side and retreating side.

Table 3.6 – Stirred zone area for FSPed samples calculated from optical micrographs as represented in Figure 3.20.

Processing parameters	**Stirred zone area (mm^2)**	
	FSP Mg	FSP Mg + Y_2O_3
v=300 mm/min, ω=1500 rpm	33.5	40.3
v=500 mm/min, ω=1500 rpm	27.4	34.4
v=500 mm/min, ω=1000 rpm	31.2	36.1

The microstructural analysis of the samples have been performed using optical microscopy, scanning electron microscopy (SEM), transmission electron microscopy (TEM), laboratory tomography and synchrotron X-ray microtomography.

3.2.3.1 Influence of the FSP parameters on the grain size

The microstructure of the as-received magnesium plates used for the fabrication of the FSPed samples is presented in Figure 3.21. The mean grain size on the surface normal to ND, measured using the intercept method, is 50 μm (Figure 3.21 (b)). However, it was not possible to measure the grain size on the rolling direction due to the large amount of twinning (Figure 3.21 (a)).

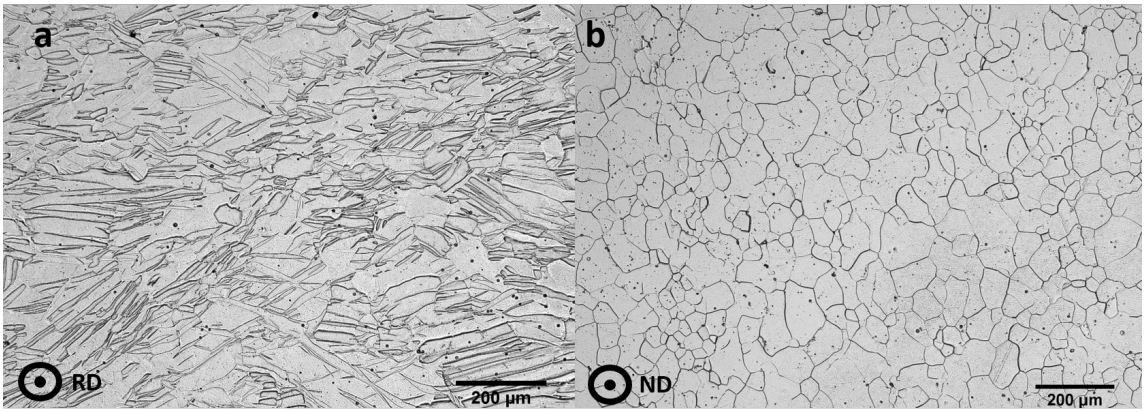

Figure 3.21 – Optical micrographs of the magnesium plates (99.95 %) used for FSP. The rolling direction (RD) (a) shows a large number of twins and the grain size could not be calculated. Therefore, the mean grain size measured using the intercept method on the surface normal (ND) is 50 μm(b).

Figure 3.22 shows optical micrographs of the FSPed samples elaborated under different processing conditions and Table 3.7 provides the grain size obtained for each FSPed sample. During FSP, a dynamic recrystallization takes place [138, 139] and the grain size is reduced from about 50 μm (in the as-received magnesium plates, Figure 3.21) to a mean grain size close to 10 μm. The micrographs confirm the microstructural changes along with the processing parameters. In the case of FSP Mg samples, the grain size is similar for the 3 samples. Therefore, it is possible to notice a small influence of the rotational speed on the grain size. The lower the rotational speed, the smaller the grain size. The mean grain size has been reduced when reducing the rotational speed from 1500 rpm to 1000 rpm. This grain size reduction is associated to a decrease of the maximum temperature as the rotational speed decreases: less frictional and deformation heat will be generated by the process [78].

With the addition of Y_2O_3 particles, however, the advancing speed seems to contribute to a grain size reduction. The highest advancing speed (500 mm/min) refines

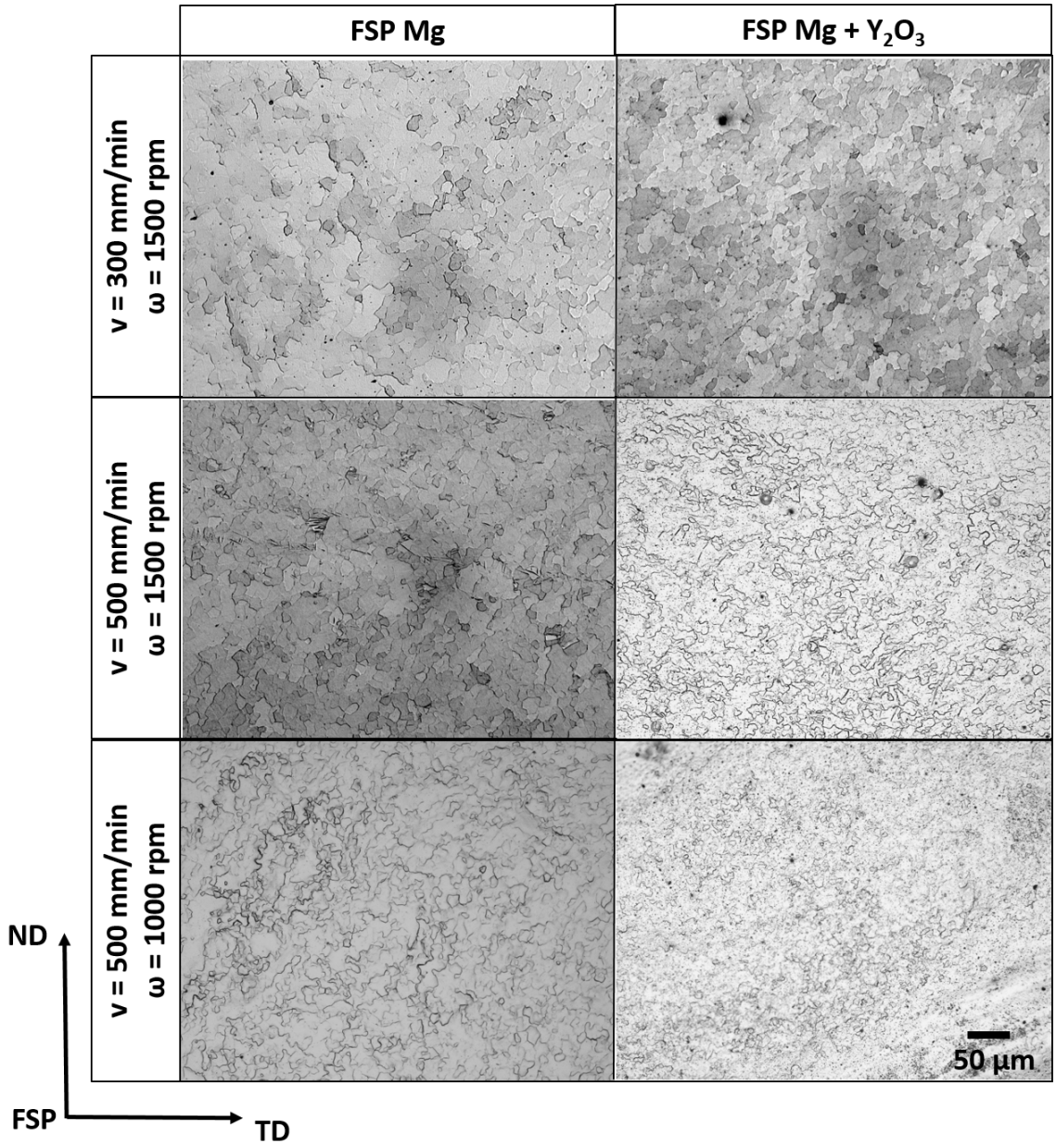

Figure 3.22 – Influence of the processing parameters and addition of Y_2O_3 particles on the microstructure of the FSPed samples.

the grain size. This observation is similar to the results obtained by Mertens *et al.* [72] when performing FSP of magnesium composites (AZ31B and AZ91D with carbon fibers): the higher advancing speed have fragmented the reinforcement into smaller fibers, resulting into a smaller grain size. Most probably in the present case, the advancing speed also affects the particle dispersion, since no effect has been observed in FSP Mg. The Y_2O_3 particle dispersion as well as the influence of the processing parameters on this dispersion will be discussed in the following section. The addition of Y_2O_3 particles does

Table 3.7 – Stirred zone area for FSPed samples calculated from optical micrographs as represented in Figure 3.20.

Processing parameters	**Grain size (μm)**	
	FSP Mg	FSP Mg + Y_2O_3
v=300 mm/min, ω=1500 rpm	10.8 ±0.98	10.7 ±0.94
v=500 mm/min, ω=1500 rpm	10.3 ±0.44	8.9 ±1.4
v=500 mm/min, ω=1000 rpm	9.8 ±0.86	8.9 ±1.4

not show a strong influence on the grain size due to the low volume fraction of particles that will be discussed in Section 3.2.3.2. A higher volume fraction of particles would lead to smaller grains in the FSP Mg+Y_2O_3 samples since the Y_2O_3 particle can restrain grain growth after recrystallization, during the cooling stage [140, 141].

3.2.3.2 Y_2O_3 particles volume fraction and dispersion

The volume fraction of the Y_2O_3 particles and their sizes have been measured and are summarized in Table 3.8 as a function of the processing parameters. SEM micrographs and synchrotron X-ray microtomography have been performed in order to measure the volume fraction. For synchrotron X-ray microtomography, 1200 images were recorded over 180° and the pixel size was 1.1 μm.

Table 3.8 – Characterization of the Y_2O_3 particles in the FSP Mg + Y_2O_3 samples. Surface fraction was obtained from SEM micrographs, while volume fraction and mean particle diameter from synchrotron X-ray microtomography. The mean particle diameter corresponds to the diameter of a sphere with the equivalent volume.

Processing parameters	**Surface fraction (%)**	**Volume fraction (%)**	**Mean particle diameter (μm)**
v=300 mm/min, ω=1500 rpm	0.54±0.12	0.88±0.32	2.5±0.06
v=500 mm/min, ω=1500 rpm	0.26±0.09	0.31±0.02	2.58±0.05
v=500 mm/min, ω=1000 rpm	0.73±0.16	0.72±0.14	2.41±0.02

The surface and volume fractions of Y_2O_3 particles (Table 3.8) seem to be influenced by the processing parameters: even if the same amount of Y_2O_3 powder have been introduced into the groove (see Table 3.5) before FSP, the volume fraction of particles

present in the three composites varies.

Considering at first the surface fraction, the sample elaborated using a higher advancing speed (500 mm/min) and lower rotational speed (1000 rpm) exhibits a higher surface fraction of Y_2O_3 particles (0.73 %). Once the advancing speed is reduced to 300 mm/min, the surface fraction is reduced to 0.54 %. Mertens *et al.* [72] have, similarly, obtained a lower volume fraction of reinforcements for FSPed samples elaborated with a lower advancing speed. The reason is that a lower advancing speed leads to a wider dispersion of the stirred zone due to the increase of the heat input, as it can be seen in Table 3.6. Even if the difference is weak (only 4 mm^2) between the two first samples, for such low volume fractions, it can already affect the surface fraction. In addition, powder loss during FSP can also contribute to the reduction of the volume fraction. The sample processed using a advancing speed of 500 mm/min and a rotational speed of 1500 rpm posses a stirred zone slightly smaller than the others (34.4 mm^2) even if the heat input should be higher due to the increase of the rotational speed. Additionally, this sample has shown the lower surface fraction of Y_2O_3, only 0.26 %. One reason could be powder loss during FSP. As presented in Section 3.2.2, a thin magnesium plate is used to cover the groove filled with Y_2O_3 in order to reduce the powder loss during processing. However, some powder loss was unavoidable. Most probably, for this processing conditions (500 mm/min and 1500 rpm), more Y_2O_3 powder has been lost during FSP.

The volume fraction of Y_2O_3 particles determined using synchrotron X-ray microtomography is different than the surface fraction obtained from SEM micrographs (Table 3.8). This result is usually expected for not completely spherical particles since with the surface analysis only a 2D information about the particles is available. The pixel size used for the microtomography analysis is 1.1 μm. Therefore, the high flux available using synchrotron radiation and the low noise observed in the microtomography allow the proper identification of particles with a diameter larger than 910 nm. A minimum of 2 pixels has been used for particle identification and the quantification has been performed using the particle volume calculated using marching cubes (algorithm for rendering isosurfaces in a volumetric data). As it can be seen in Figure 3.23, the Y_2O_3 particles have been fragmented during FSP and the size of some particles has been reduced from 3.5 μm to 200 nm. This fragmentation is due to the large plastic deformation that occurs during FSP. These smaller particles cannot be identified by synchrotron X-ray microtomograph, but SEM micrographs can identify them since magnifications ranging from 1400x to 3000x have been used.

The mean particle diameter determined from the microtomography results (Table 3.8) is close to 2.5 μm. This size is close to the original Y_2O_3 powder (3.5 μm) because mostly the larger particles will be detected by microtomography.

The volume fraction is lower for the samples elaborated using a higher advancing speed (500 mm/min), as it can be seen in Table 3.8. It confirms the assumptions from Section 3.2.3.1 that a higher advancing speed fragments the Y_2O_3 particles into smaller particles. In addition, Attallah *et al.* [130] have shown that higher rotational speed promotes more particle fragmentation. Even if it is not possible to identify the smaller particles using synchrotron X-ray microtomography, the sample fabricated using 500 mm/min (advancing speed) and 1500 rpm (rotational speed) should have the finer dispersion of Y_2O_3 particles.

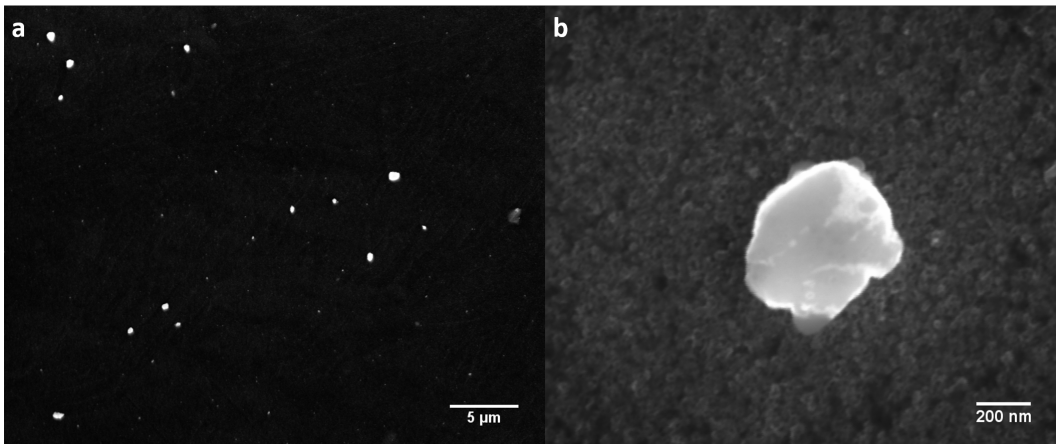

Figure 3.23 – SEM micrographs of FSP Mg + Y_2O_3 sample processed using an advancing speed of 500 mm/min and rotational speed of 1500 rpm. It is possible to observe the Y_2O_3 particles fragmentation (original Y_2O_3 size is 3.5 μm).

The importance of a homogeneous dispersion of the reinforcement phase has already been discussed in Section 3.1 and will be investigated hereafter. Figure 3.24 shows the 3-D reconstruction of the synchrotron X-ray microtomography performed on the FSP Mg + Y_2O_3 samples. It shows a homogeneous dispersion of Y_2O_3 particles all over the analyzed area. No large clusters or highly concentrated areas could be seen, differently from the observed for samples prepared using ultrasound assisted casting (see Figures 3.8 and 3.13). The high number of FSP passes (9 passes) contributes to this homogenization [79]. According to the literature [78, 142, 143], a more homogeneous and finer reinforcement distribution is generally observed at higher rotational speeds, but no difference has been observed in the 3-D reconstruction of synchrotron X-ray microtomography since the smaller Y_2O_3 particles are not identifiable.

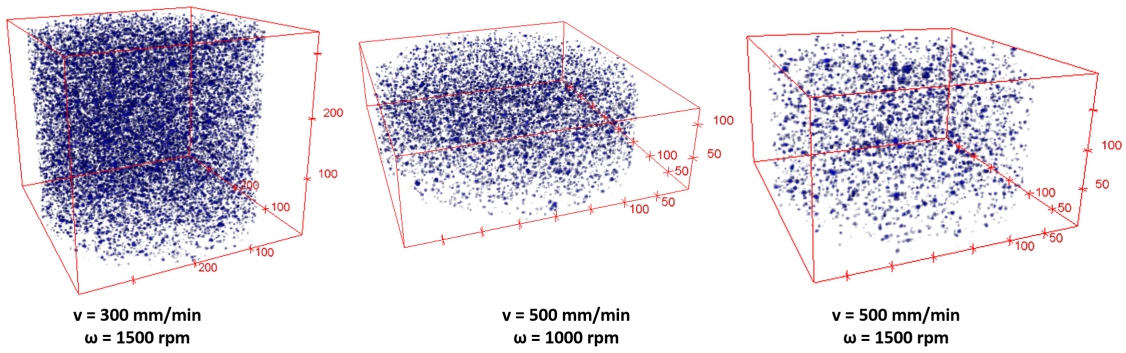

Figure 3.24 – 3-D reconstruction of the synchrotron X-ray microtomography performed on the FSP Mg + Y_2O_3 samples as a function of processing parameters. The volume fractions are presented in Table 3.8 and the scale is given in μm. The volume analyzed for each sample during microtomography was similar, but here different volumes are presented.

Complementary to the synchrotron X-ray microtomography, laboratory tomography have also been performed in the FSP Mg + Y_2O_3 samples. A pixel size of 500 nm has been used for the analysis, but the low flux available in the laboratory X-ray source along with the important noise observed in the tomographic analysis does not allow obtaining a better resolution than the synchrotron X-ray microtomography despite a smaller pixel size. The results obtained from laboratory tomography are not convenient for quantitative analysis, such as volume fraction, due to the important noise. However, information about the distribution of the large particles in the volume can still be obtained. An advantage of laboratory tomography is that the access is much easier, allowing the analysis of a more important number of samples.

For the laboratory tomography, cylindrical samples have been sampled from each FSP Mg + Y_2O_3 sample in the center of the stirred zone (center), closer to the retreating side (RS) and to the advancing side (AS) as shown in Figure 3.25. The objective is to observe if there is any heterogeneities on the Y_2O_3 particles dispersion along the stirred zone and the influence of the processing parameters on that dispersion. To do so, a qualitative analysis of the Y_2O_3 particles distribution has been performed in collaboration with the Institute of Mechanics, Materials and Civil Engineering of Université Catolique de Louvain (UCL) within an ongoing PhD work by Florent Hannard [144, 145, 146].

The nearest-neighbor distribution method has been used in order to investigate the Y_2O_3 particle dispersion. This method is called Dirichlet tessellation and uses the coordinates of the centroids of each particle to construct a network of polygon cells such that any point within the polygon is closer to the center of the enclosed particle than to

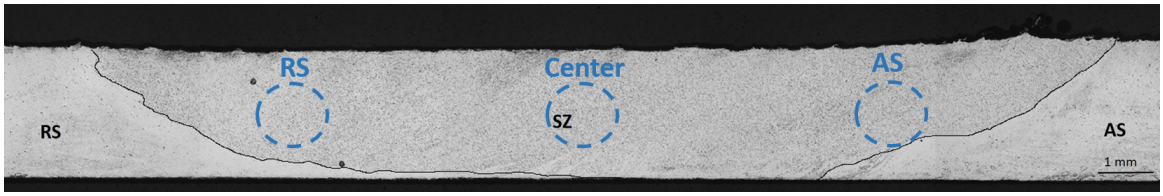

Figure 3.25 – Schematic of the sampling from FSP Mg + Y_2O_3 samples.

the centroid of any other particle [147, 148], as it can be seen in Figure 3.26. Further explanation about the Dirichlet tessellation method can be found in [147, 148, 149, 150].

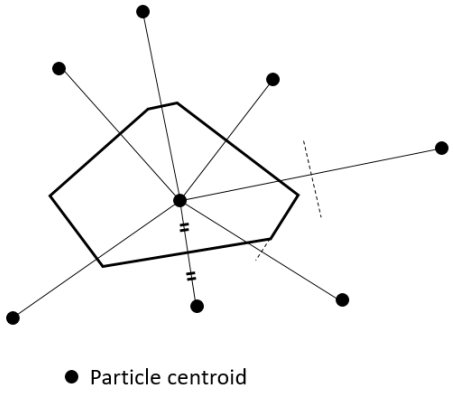

Figure 3.26 – Dirichlet polygon is constructed using the distance between the centroids of neighbor particles [150].

Figure 3.27 shows the distance between Y_2O_3 particles centroids from different regions of the stirred zone along with the influence of the processing parameters. The Y_2O_3 particles distribution seems to be more homogeneous for the sample fabricated using an advancing speed of 500 mm/min and rotational speed of 1500 rpm. A much wider distribution of nearest distances between the Y_2O_3 particles is observed when using a lower advancing speed (300 mm/min), especially closer to the retreating side. The mean distance between Y_2O_3 particles centroids is 19 μm for all processing conditions. In order to compare the homogeneity of particle distribution in the different FSP Mg + Y_2O_3 samples, the distances have been normalized by a factor $\rho^{-1/3}$, where ρ is the number of particles per unit volume [146]. The occurrence in the vertical axis is expressed in relation to the total number of particles in each zone AS, center and RS. Once the results are normalized, there are very few difference between different regions of the stirred zone and even between different processing parameters, even if a more homogeneous response is obtained for the sample fabricated using 500 mm/min and 1500 rpm. The mean normalized distance for all samples is 0.55. It indicates that the larger Y_2O_3 particles

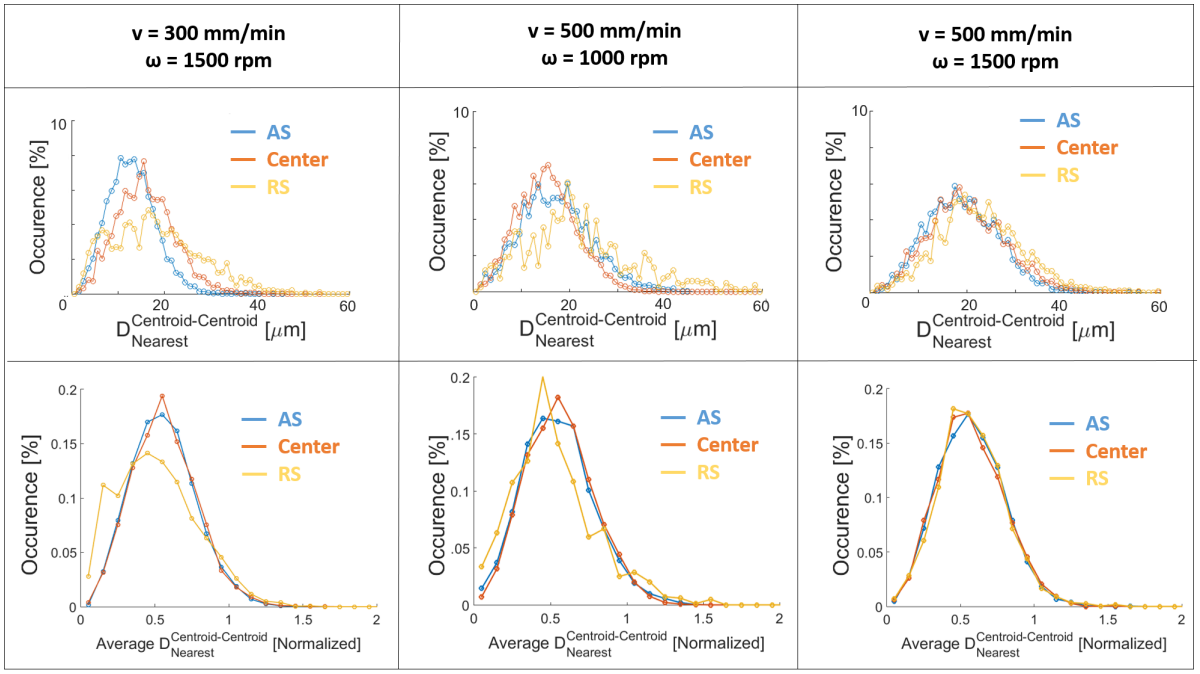

Figure 3.27 – The distance between Y_2O_3 particles centroids and the normalised distance have been calculated in different regions of the stirred zone based on the laboratory tomography performed on FSP Mg + Y_2O_3 samples (quantification performed in collaboration with Florent Hannard [144]).

(observed during laboratory tomography) are randomly distributed on the stirred zone for all the processing conditions. According to Chandrasekar [151, 146, 152], the expected normalized distance in a perfect random distribution of particles should be equal to 0.554. It indicates that the larger Y_2O_3 particles accessible considering the resolution have a distribution close to random for the three sets of processing parameters. The distribution remains random even for different regions of the stirred zone: advancing side, center and retreating side.

Based on the complete analysis of the Y_2O_3 particles dispersion, it would be preferable to use the samples fabricated using an advancing speed of 500 mm/min and a rotational speed of 1500 rpm. In order to confirm the choice for this sample, it is still necessary to evaluate the possibility to obtain coarse grains for the different samples.

3.2.4 Post processing annealing heat treatment

One of the requirements for the "*model*" nanocomposite is the presence of coarse grains for the fabrication of single crystalline microcolumns for microcompression testing.

The microstructural analysis given in the previous section has shown a mean grain size of 10 μm after FSP due to dynamic recrystallization, which does not provide the necessary volume to machine microcolumns as explained at the beginning of this Chapter.

An annealing heat treatment has then been carried out in order to obtain abnormal grain growth (AGG). At first, the study of the AGG has been performed using only FSP Mg samples and 500°C for 1 hour using a Nabertherm furnace. The samples were slowly cooled to room temperature inside the furnace. In order to prevent oxidation, the process took place under a constant argon flow. This annealing heat treatment promotes significant changes in the microstructure of the FSPed samples. Large grains with sizes of hundreds of microns were observed due to the AGG that promotes a discontinuous coarsening of the grain structure. It usually takes place in the surface of the stir zone and is also dependent of the processing parameters.

A significant AGG has been observed in the FSP Mg samples as shown in Figure 3.28. The processing parameters seems to have an influence on the AGG since a higher extent of larger grains has been observed for samples fabricated using an advancing speed of 500 mm/min. This result is in accordance with [130] who showed that lower-to-intermediate advancing speeds reduce the AGG.

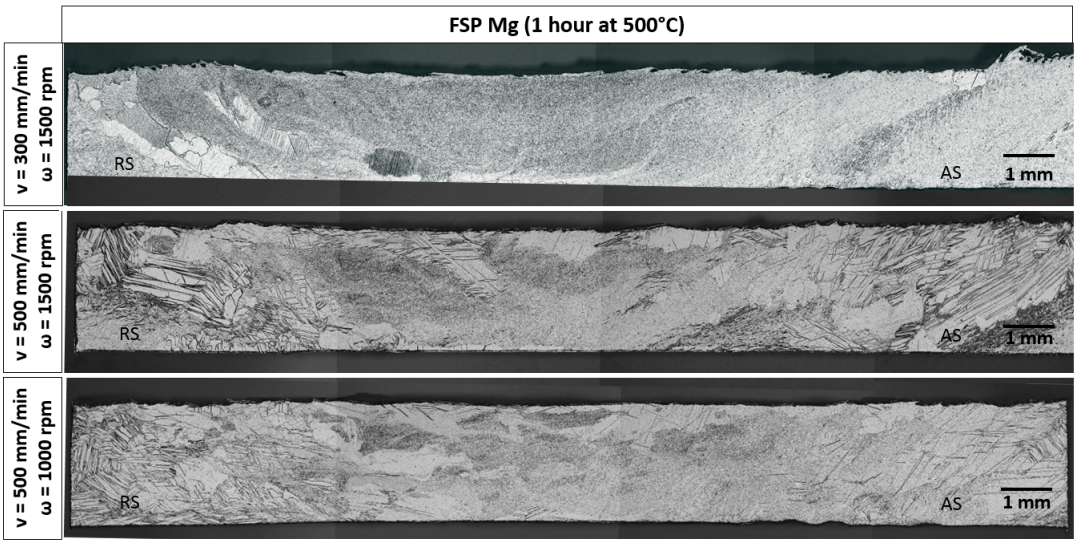

Figure 3.28 – Optical micrographs showing the influence of the processing parameters on the extent of AGG for FSP Mg samples.

The annealing heat treatment has then been carried out on the FSP Mg + Y_2O_3 samples at 500°C for 3 hours. Figure 3.29 shows the influence of the processing parameters on the AGG for the FSP Mg + Y_2O_3 samples. Similarly to that observed for FSP Mg,

a higher extent of AGG is present when an advancing speed of 500 mm/min is used. The extent of abnormal grain growth was larger in the sample prepared using the higher advancing speed (500 mm/min) with the higher rotational speed (1500 rpm). Again, this leads to the selection of this ideal processing parameters set.

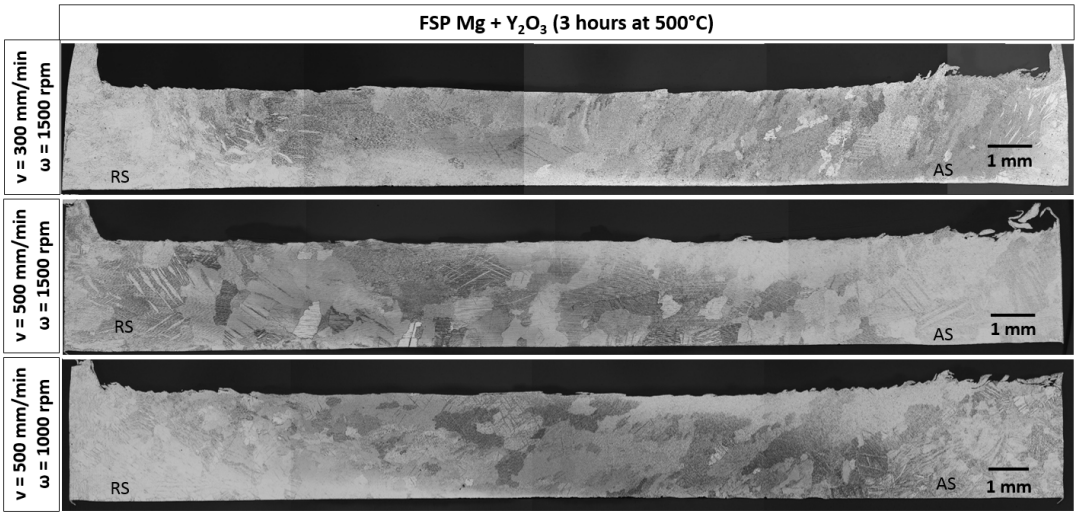

Figure 3.29 – Optical micrographs showing the influence of the processing parameters on the extent of AGG for FSP Mg + Y_2O_3 samples.

As shown in Figure 3.22, the presence Y_2O_3 particles refines the grain size for higher advancing speeds (500 mm/min). When the grain size decreases, the pressure generated by the driving force for grain growth will exceed the particle pinning pressure, leading then to AGG [130]. According to Humphreys *et al.* [153], abnormal grain growth becomes impossible for a mean grain size (D_M) of

$$D_M = \frac{2d_{particle}}{3f_v} \tag{3.1}$$

where $d_{particle}$ is the mean particle diameter (considering spherical particles) and f_v is the volume fraction of particles. The lower the volume fraction, the larger the minimum grain size for abnormal grain growth. It explains why the extent of abnormal grain growth was larger in the sample with the lower surface fraction of particles (0.26 %), prepared using the following processing parameters: 500 mm/min and 1500 rpm. Figure 3.30 shows optical micrographs of the sample, confirming the presence of grains larger than 1 mm after annealing treatment.

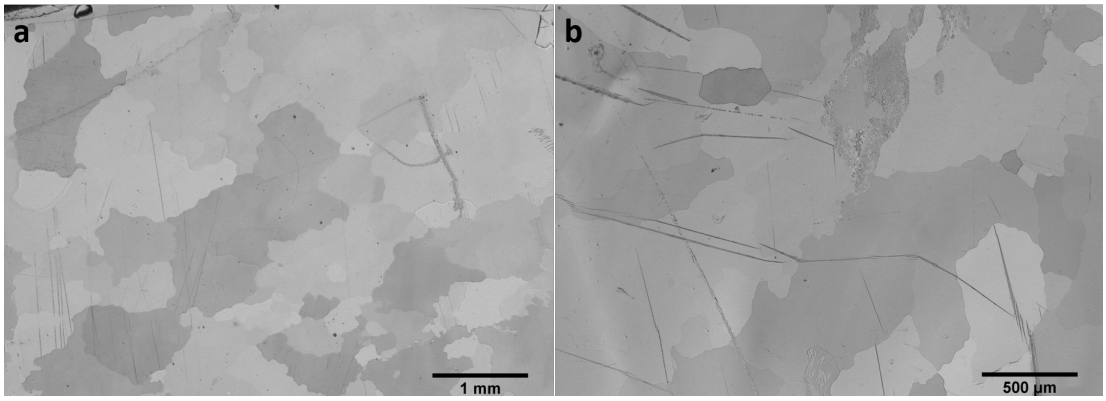

Figure 3.30 – Optical micrographs of a FSP Mg + Y_2O_3 sample processed using an advancing speed of 500 mm/min and rotational speed of 1500 rpm after annealing treatment. Grains larger than 1 mm could be observed due to AGG. It is possible to observe some twins (b) that traverse these large grains.

3.2.5 Suitability

The microstructural characterization performed on the FSPed samples has shown a homogeneous dispersion of Y_2O_3 particles for the different processing parameters tested. The initially 3.5 μm size Y_2O_3 particles have been fragmented during FSP and their size has been reduced in some cases to some hundreds of nanometers (according to SEM analysis). FSP promotes dynamic recrystallization, leading to small grain sizes (around 10 μm). A subsequent annealing heat treatment that favors AGG had however enable the achievement of coarse grain sizes. Table 3.9 correlates the results obtained from the microstructural characterization of FSPed samples and the requirements for the "*model*" nanocomposite. All the requirements have been fulfilled.

Table 3.9 – Requirements for the "*model*" nanocomposite and the results obtained for FSPed samples.

Requirements	**FSP**
Coarse grains	✓
Particle dispersion	✓
Particle stability	✓

Even if all the requirements have been fulfilled for the "*model*" nanocomposite, one of the FSP Mg + Y_2O_3 samples needs to be selected in order to perform a deeper microstructural characterization prior to the micromechanical investigation. Considering the particle dispersion, a homogeneous dispersion of finer particles should be preferable for

the micromechanical investigations. It will ensure the presence of Y_2O_3 particles inside one microcolumn. The literature [130, 72, 78, 142, 143] as well as the results obtained during the preliminary microstructural characterization indicate that a higher rotational speed along with a higher advancing speed leads to a more homogeneous and finer distribution of reinforcements. This points to the FSP Mg + Y_2O_3 sample fabricated using an advancing speed of 500 mm/min and rotational speed of 1500 rpm. Additionally, the larger extent of AGG grain growth has been observed for this sample. Thus, this sample is chosen as the "*model*" nanocomposite.

3.2.5.1 Drawbacks

A drawback of the friction stir processing technique was that a good reproductibility was not observed between different samples prepared under the same set of processing parameters. The volume fraction of Y_2O_3 particles has been found to be up to three times higher in other samples elaborated under the same processing parameters. As it has already been mentioned, a powder loss was observed during FSP and is the most probable cause for such discrepancy between the different samples. It implies that

Figure 3.31 – Optical micrographs of a FSP Mg + Y_2O_3 fabricated using the same processing parameters as the "*model*" nanocomposite. It was not possible to reproduce the AGG observed in Figure 3.30.

the AGG grain cannot take place with such volume fraction of particles as it can be seen in Figure 3.31. Therefore, since a very low amount of material is required for the micro-compression testing, it was still possible to use the sample fabricated at 500 mm/min and 1500 rpm as the "*model*" nanocomposite.

3.3 Characterization of the "model" nanocomposite

The selection of the "*model*" FSP Mg + Y_2O_3 sample has been discussed in the previous Section 3.2. A deeper microstructural characterization will now be performed using TEM and synchrotron X-ray nanoholotomography in order to obtain the 3-D dispersion of the reinforcement particles at higher resolution. Since SEM micrographs (Figure 3.23) have shown particle fragmentation during FSP, a microstructural analysis at higher resolution needs to be performed.

3.3.1 TEM analysis

TEM analysis have been performed in lamellas sampled at 1 mm from the top surface in normal sections of the stirred zone and prepared using electropolishing (further details are given in Section 2.5.1). TEM micrographs have revealed an uniform distribution of particles and the presence of three different sizes of Y_2O_3 particles, which is consistent with what was observed in copper nanocomposites by Avettand-Fènoël *et al.* [79] when working with the same Y_2O_3 particles. A first group of Y_2O_3 particles remains with the original micrometer size: agglomerates larger than 1.5 μm can be seen in Figure 3.32 (a and b). Intermediate Y_2O_3 particles (usually agglomerates of smaller particles) with sizes between 100 and 300 nm can be seen in Figure 3.32 (c and d). A large number of small isolated Y_2O_3 particles that are inferior to 50 nm can also be observed (Figure 3.32 (e and f)).

3.3.2 Synchrotron X-ray nanoholotomography

Considering the resolution limitations of both laboratory tomography and synchrotron X-ray microtomography, it was necessary to use synchrotron X-ray nanoholotomography. This high resolution technique enables the investigation of the 3-D distribution of even the smaller Y_2O_3 particles (Figure 3.33). Different pixel sizes have been used (25, 50 and 120 nm) and the smallest one allows the imaging of the small Y_2O_3 particles observed in TEM. As for the Dirichlet analysis presented earlier (Section 3.2.3.2), the quantitative analysis of the 3-D tomographic scans has been performed in collaboration with the Institute of Mechanics, Materials and Civil Engineering of Université Catolique

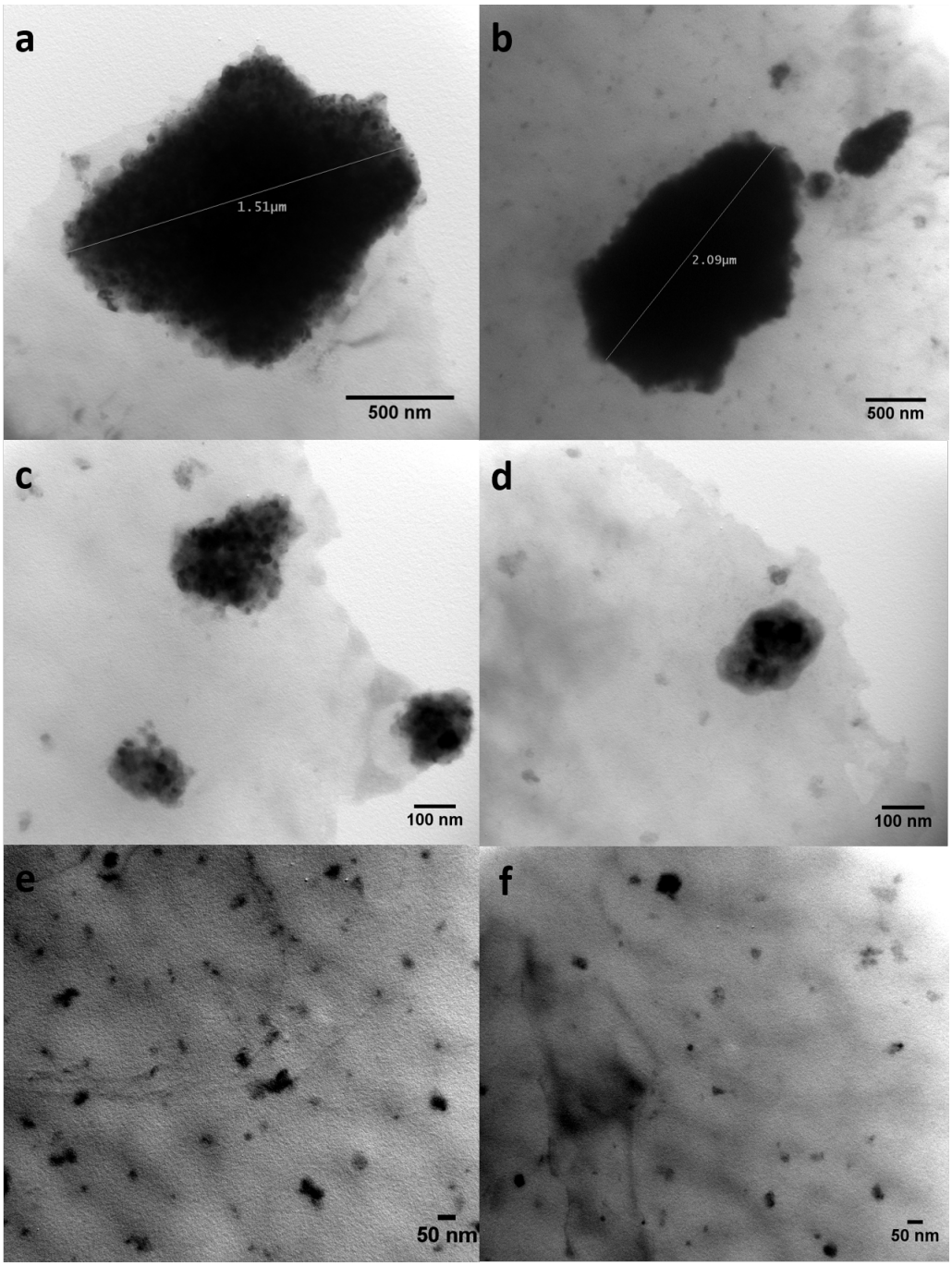

Figure 3.32 – TEM micrographs of the "*model*" nanocomposite. Three different sizes of Y_2O_3 particles have been observed: original micrometer size (a and b), hundreds of nanometers-intermediate size (c and d) and small nanometer size (e and f).

de Louvain (UCL) using matlab routines developped by Florent Hannard [144, 145, 146].

Dirichlet tesselation

Figure 3.34 presents a 3-D reconstruction of the centroids of each particle ob-

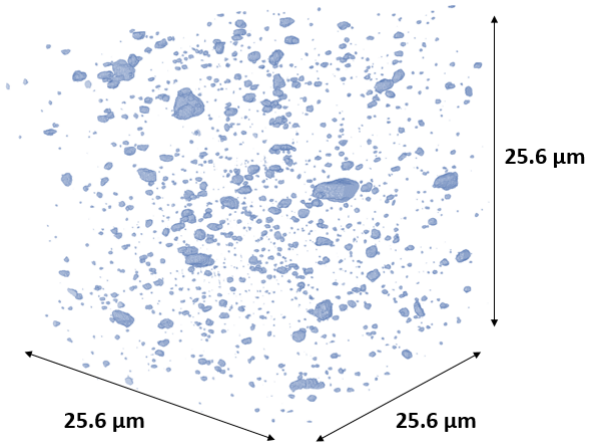

Figure 3.33 – 3-D reconstruction of the synchrotron X-ray nanoholotomography performed in the "*model*" nanocomposite using a voxel size of 25 nm.

served in the nanoholotomography of the "*model*" nanocomposite. Particles centroids seem to be well dispersed in the entire volume and just based on the 3-D reconstruction, it is not possible to observe clustering. Thus, a quantitative analysis using the nearest-neighbor distribution method (or Dirichlet tessellation, detailed in Section 3.2.3.2) is performed by measuring the distances between centroids of all particles, as represented in Figure 3.35. The double peak is usually a signature of clustering. The highest occurrence

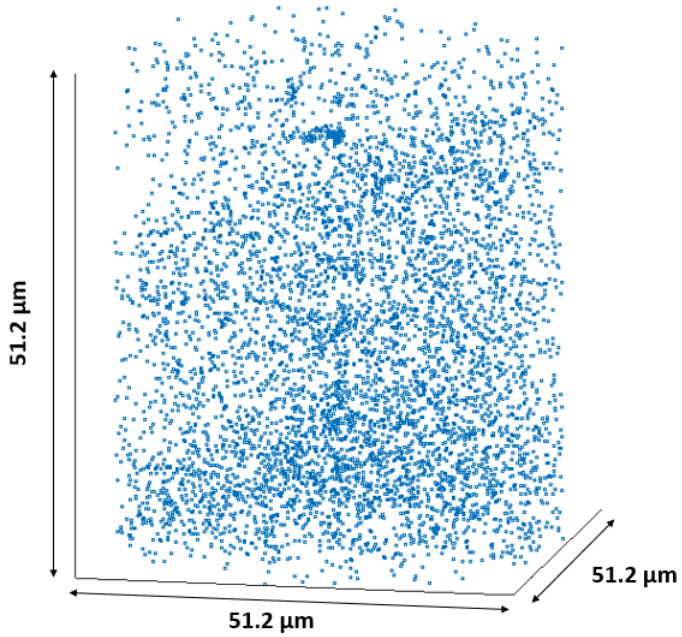

Figure 3.34 – 3-D distribution of the particle centroids based on the 3-D reconstruction of the synchrotron X-ray nanoholotomography performed in the "*model*" nanocomposite using a voxel size of 25 nm.

peak evidences that a large number of particles centroids are spaced 1.3 μm from each other. The lowest occurrence peak shows that a certain number of particles are very close to each other, with a mean distance of 125 nm. These ones correspond to the clusters of particles and might be a residue of the large 3.5 μm-sized Y_2O_3 particles broken at the last FSP pass. The particles that have been broken during the first FSP passes are expected to have their fragments already dispersed at the subsequent FSP passes.

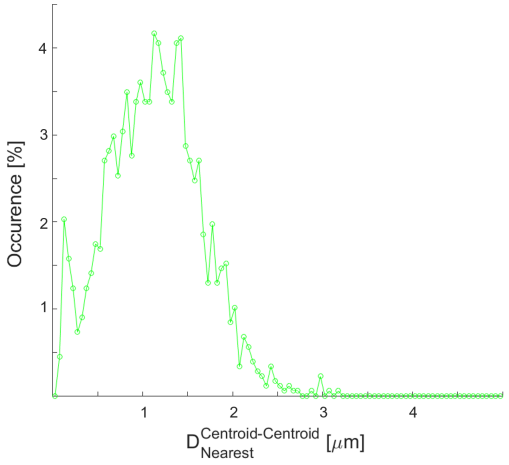

Figure 3.35 – The nearest distance between the Y_2O_3 particles centroids has been quantified from the synchrotron X-ray nanoholotomography performed at the highest resolution (25 nm).

In order to verify the clustering, the Y_2O_3 particles distribution has been analyzed using the grid count analysis [150]. In this method, the entire sample field is meshed with squares having a volume $1/\lambda$, where λ is the average volume centroid density. Figure 3.36 (a) shows the grid count analysis of the Y_2O_3 particles dispersion, where the difference in probability represents the deviation from the expected frequencies for a random distribution (Poisson‘s distribution). The sinusoidal shape of the curve for the "*model*" nanocomposite is very similar to what is obtained for a ideal clustered simulated distribution as represented in Figure 3.36 (b) [150]. This confirms the clustered aspect of the distribution.

Finite body tesselation

Since the Dirichlet tessellation has identified the presence of Y_2O_3 particles clusters, the finite body tessellation method has been applied in order to characterize and quantify these clusters. In this method, a network of cells is constructed from the interfaces of each particle in such a way that every point within a cell is closer to the corresponding particle than to any other [147] (Figure 3.37). According to the literature

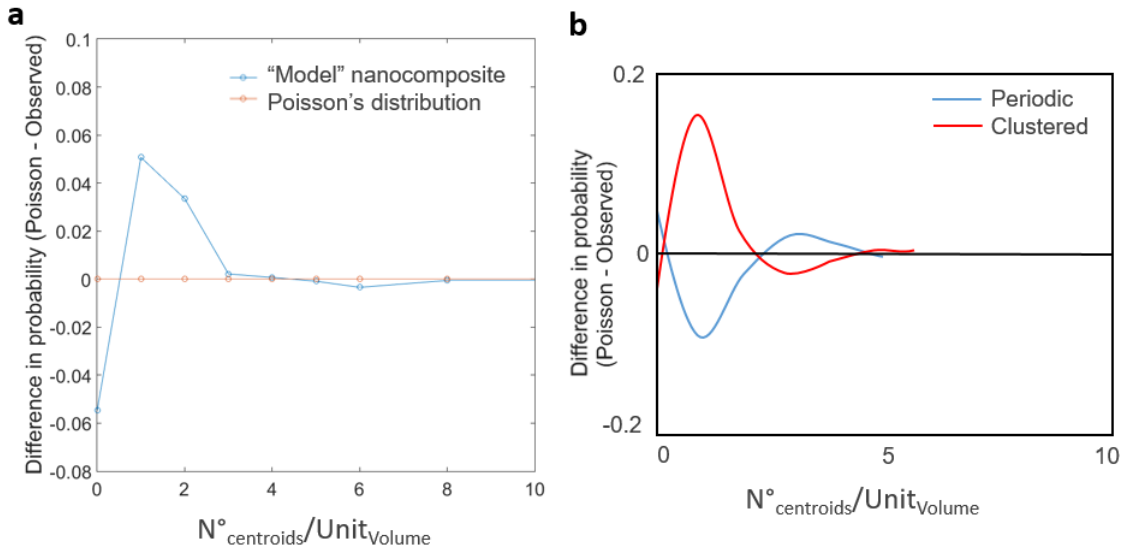

Figure 3.36 – Grid count analysis of the Y_2O_3 particles dispersion (a) identify a slighly clusterised behavior when compared to Burger's studies [150] on periodic and clustered distributions (b).

[147], finite body tessellation is more physically representative of local distribution as it uses the true distance between the particles.

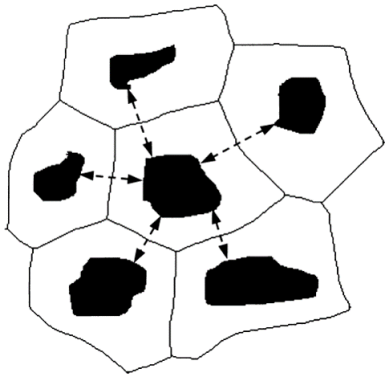

Figure 3.37 – The finite body tessellation cell is constructed using the distances between the interfaces of neighboring particles [147]. This is the true distance between particles.

The neighbors of a Y_2O_3 particle are considered as the particles whose finite body tessellation cell shares one facet with the cell of the corresponding particle. The analysis of the clusters in the "*model*" nanocomposite requires the distinction of cluster and isolated Y_2O_3 particles. As proposed by Achon [154], a cluster will be defined based on the occurrence of a clustering distance ($D_{clustering}$). A certain particle will belong to a cluster if it is distant from all its near-neighbors, identified during the finite body tesselation, by a distance inferior to a $D_{clustering}$. Figure 3.38 (a) shows a plot of the number of

clusters for a given diameter. The number of clusters increases with the increasing of the $D_{clustering}$ until a certain point where the number of clusters starts to decrease. This decreasing is due to the coalescence of clusters for a large $D_{clustering}$. The $D_{clustering}$ for the "*model*" nanocomposite corresponds to the distance where the maximum number of clusters has been identified: 1.375 μm. The same method is also performed using a random distribution of particles in order to determine a minimum cluster size, the minimum number of Y_2O_3 particles to consider as a cluster [146].

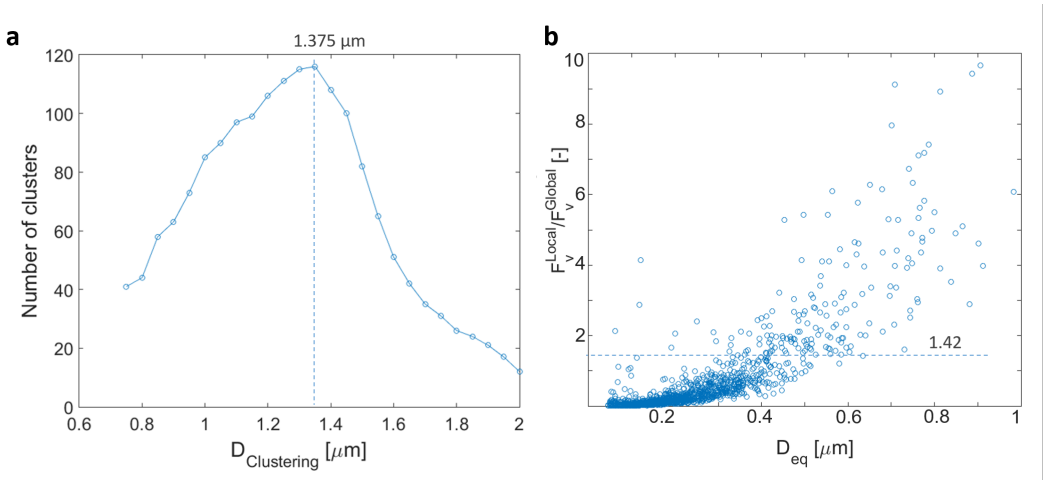

Figure 3.38 – Analysis proposed by Achon [154] for the calculation of the $D_{clustering}$ (a) and the equivalent particle diameter as a function of the volume fraction (b).

A mean cluster size of 8.03 particles and a mean cluster volume of (3.93 μm)^3 have been estimated from the finite body tessellation. The mean local volume fraction of Y_2O_3 particles (f_v^{global}), obtained by the ratio of the particle volume by the volume of its associated cell (finite body tessellation cell), is 0.33 %. This value is similar to the ones obtained during the Y_2O_3 particle dispersion in Table 3.8: surface and volume fractions of 0.26 and 0.31 %, respectively. It was expected that the volume fraction of Y_2O_3 particles would be higher when analyzing the nanoholotomography data since even the small particles with a diameter of 50 nm could be identified. However, it is important to recall here that only a very small volume is analyzed using the nanoholotomography (field of view of 45 μm) and small variations of the volume fraction would be observed experimentally. Additionally, the mean local volume fraction of Y_2O_3 particles belonging to clusters ($f_v^{clusters} = 0.47$ %) is higher than for isolated particles ($f_v^{isolated} = 0.11$ %). Thus, considering the mean ratio $f_v^{clusters}/f_v^{global}$ for particles inside clusters as 1.42 (0.47/0.33) and the graphic in Figure 3.38(b), the Y_2O_3 particles with a diameter larger than 500 nm are inside clusters. It supports the observations from the Dirichlet tessellation: large

Y_2O_3 particles that have been fragmented at the last FSP passes are still close together. It has also been observed that 61 % of the particles (in volume) are inside clusters.

Size distribution

From the graphic in Figure 3.39, it is possible to observe a large number of small particles: 90 % of the Y_2O_3 particles are smaller than 400 nm. These smaller particles, however, only contribute to 13 % of the volume fraction of particles. The mean particle equivalent diameter (D_{eq}), which corresponds to the diameter of a sphere with a volume equivalent to the particle, is 430 nm (calculated using the number of particles).

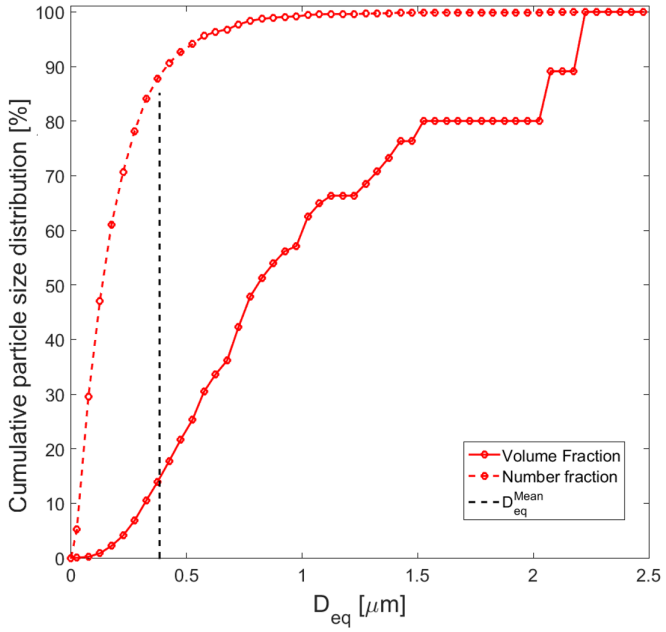

Figure 3.39 – Cumulative particle size distribution in volume and number fraction. 90 % of the particles are smaller than 400 nm.

Table 3.10 summarizes the main characteristics of the "*model*" nanocomposite.

3.3.3 Conclusion

The "*model*" nanocomposite has successfully been fabricated by FSP. The chosen processing parameters have induced fragmentation of Y_2O_3 particles and have enable a relatively homogeneous distribution of Y_2O_3 particles with a small clustering. The uniform dispersion of Y_2O_3 particles inside the nanocomposite has then been confirmed using high

Table 3.10 – Characteristics of the "*model*" nanocomposite.

Mean particle diameter		430 nm
Mean volume fraction	Global f_v^{global}	0.33 %
	Particles within clusters $f_v^{clusters}$	0.47 %
	Isolated particles $f_v^{isolated}$	0.11 %
Volume fraction of Y_2O_3 particles	Within clusters	61 %
	Outside clusters	39 %
Mean cluster volume		$(3.93\ \mu m)^3$
Mean cluster size		8.03 particles
Mean interparticle spacing		1.3 μm

resolution techniques (TEM and synchrotron X-ray nanoholotomography).

The mean distance between Y_2O_3 particles has been identified as 1.3 μm, which is delicate for the fabrication of microcolumns smaller than 1 μm (mid-height diameter). Since the microcolumns have been fabricated prior to the nanoholotomography analysis, the minimum mid-height diameter of the columns studied using microcompression testing is 2 μm as presented in Chapter 2. It corresponds to a column volume of 18.8 μm^3, which is smaller than the mean cluster volume of 61 μm^3 identified in the finite body tessellation. Thus, the use of 2 μm columns becomes critical and will be further discussed in Section 4.2.

The next chapter (Chapter 4) will experimentally investigate the mechanical response of the "*model*" nanocomposite at the scale of the polycrystal in order to validate the strengthening effect of the Y_2O_3 particles at the macroscale and also at the scale of the single crystal.

Key points of Chapter 3

1. The requirements for the "*model*" nanocomposite that will be further investigated in the study of the mechanisms of plastic deformation in magnesium based nanocomposites have been specified: coarse grains, homogeneous reinforcement distribution and chemical stability of reinforcements.

2. Magnesium based composites have been elaborated using two different techniques: ultrasound assisted casting and friction stir processing, for comparison.

3. Several techniques have been used for the characterization of the composites, including: optical microscopy, SEM, TEM, EBSD and synchrotron X-ray microtomography and nanoholotomography.

4. Three different types of reinforcements (Al_2O_3, MgO and Y_2O_3) have been used on the composites fabricated by ultrasound assisted casting. The microstructural characterization of these composites have shown a strong particle agglomeration and highly heterogeneous particle distribution. Additionally, chemical reactions have occurred between the magnesium matrix and the reinforcement particles during processing. These composites were not suitable for use as the "*model*" nanocomposite.

5. Friction stir processing has been used for the reinforcement of magnesium with Y_2O_3 particles. Different processing conditions have been tested and they have all shown an uniform distribution of particles.

6. A thermal treatment has been performed on the FSPed samples in order to induce abnormal grain growth, since the grain size after FSP is inferior to 15 μm. Grains larger than 1 mm have been successfully generated.

7. The selected material for the "*model*" nanocomposite has been fabricated using an advancing speed of 500 mm/min and rotational speed of 1500 rpm.

8. High resolution 2D and 3D characterization of the "*model*" nanocomposite have shown a high number of small particles (90 % of the Y_2O_3 particles are inferior to 400 nm). Mean particle diameter and mean interparticle spacing are, respectively, 430 nm and 1.276 μm. Some clustering is observed, but most of the Y_2O_3 particles seems to be randomly dispersed.

CHAPTER 4

Experimental mechanical investigations

The present chapter presents a multiscale study of the mechanical behavior of magnesium based nanocomposites reinforced with Y_2O_3. As mentioned in the previous chapter (Chapter 3), the "*model*" nanocomposite chosen for the study has been prepared by FSP due to the good dispersion of Y_2O_3 particles achieved using this method and predisposition to abnormal grain growth. FSP pure magnesium (FSP Mg) and FSP nanocomposites (FSP Mg + Y_2O_3) samples fabricated using the same processing conditions (advancing speed of 500 mm/min and rotational speed of 1500 rpm) are compared in order to observe the direct influence of Y_2O_3 particles on the mechanical response.

The macroscale mechanical behavior has been studied by means of tensile testing and will be discussed in Section 4.1. In this case, different volume fraction of Y_2O_3 particles have been used and the polycrystalline mechanical behavior of the materials could be investigated. The single crystalline mechanical behavior has been investigated at microscale using microcompression testing and will be presented in Section 4.2. In addition, *in situ* TEM experiments have also been performed (Section 4.3).

4.1 Tensile testing

Tensile tests were performed at room temperature comparing FSP Mg and FSP Mg + Y_2O_3 samples in order to confirm that the addition of Y_2O_3 particles produces an improvement of the tensile properties. No annealing heat treatment that could induce grain growth was performed prior to mechanical testing.

4.1.1 Optimization of the fabrication method: milling machine or EDM

The tensile samples were extracted inside the stir zone of the FSPed samples (Figure 4.1) and fabricated using two different techniques: milling machining and electrical discharge machining (EDM). The specimens fabricated for each technique have a different shape, which is presented in Section 2.3.1. The sampling and machining of FSPed tensile samples are very delicate regarding the small volume of the FSPed zone and machining can lead to strong changes in the microstructure that can affect the mechanical response. The stress-strain curves obtained for each fabrication technique will be first presented individually and then compared in order to choose the ideal fabrication method.

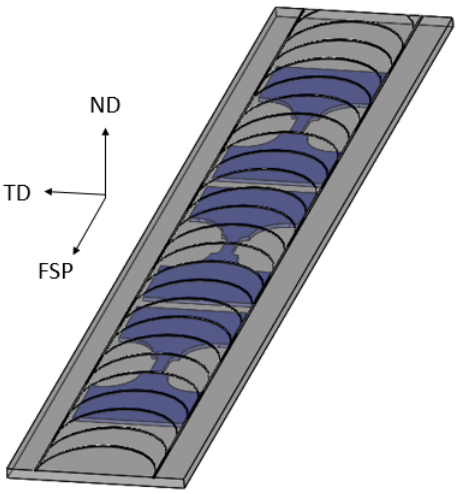

Figure 4.1 – Schematic of the sampling of tensile specimens in the stir zone of FSPed samples.

4.1.1.1 Milling machining

Tensile specimens fabricated by milling machining from FSP Mg and FSP Mg + Y_2O_3 (0.3 %) samples were compared. The FSP Mg + Y_2O_3 (0.3 %) corresponds to the "*model*" nanocomposite, which have a volume fraction of particles of 0.3 % (see Section 3.3).

Figure 4.2 shows the true stress vs. true strain curves for the tensile specimens fabricated by milling machining and Table 4.1 summarizes the resulting mechanical properties. The use of Y_2O_3 particles as reinforcement does not induce any strengthening

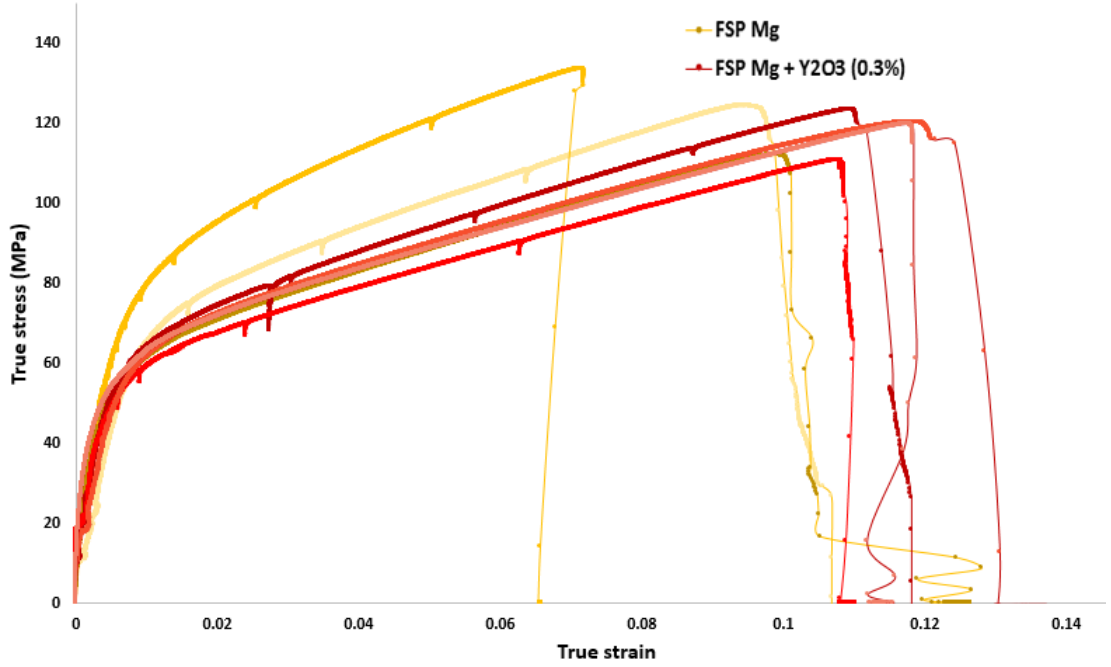

Figure 4.2 – True stress vs. true strain tensile loading curves for specimens prepared using milling machining. Initial engineering strain rate of 6.4×10^{-4} s^{-1}.

Table 4.1 – Mechanical properties of FSP Mg and FSP Mg + Y_2O_3 samples fabricated by milling machining.

Sample	**0.2 % Yield strength (MPa)**	**Ultimate tensile strength (MPa)**	**Ductility (%)**	**Strain hardening coefficient (MPa)**
Mg	86.1±9.3	122.7±7.2	9.1±1.2	623±71.7
Mg+Y_2O_3(0.3)	74.7±2.6	116.8±3.7	11.4±0.5	507.4±17.4

effect and the ductility seems to be superior in the case of FSP Mg + Y_2O_3 (0.3 %) samples. This result is inconsistent when compared to similar studies found in the literature for nanocomposites [3, 4]. These studies have all shown an increase of the yield stress and ultimate tensile stress with the addition of only 0.2 % (volume fraction) of Y_2O_3 particles. In addition, the ductility has been increased 72 % [4] and 276 % [3].

One explanation for the absence of strengthening could be the residual stresses after milling machining. Indeed this technique can induce a strong plastic deformation at the surface layer of the sample. For such thin samples (1 mm), the microstructure of almost the entire thickness can be altered during the process. This is critical especially for magnesium, that has such anisotropic mechanical behavior. In order to verify the results obtained for the specimens fabricated by milling machining, another technique was used

for specimen machining: electrical discharge machining (EDM).

4.1.1.2 EDM

The same samples (FSP Mg and FSP Mg + Y_2O_3 (0.3 %)) have been fabricated by EDM for comparison. The mechanical responses obtained from tensile test of these samples and the ones fabricated by milling machining are compared (Figure 4.3). The ductility of samples fabricated by EDM is 180 % higher than the one obtained for samples fabricated by milling machining. The strain hardening obtained for samples fabricated by milling machining is significantly higher (122 % for FSP Mg).

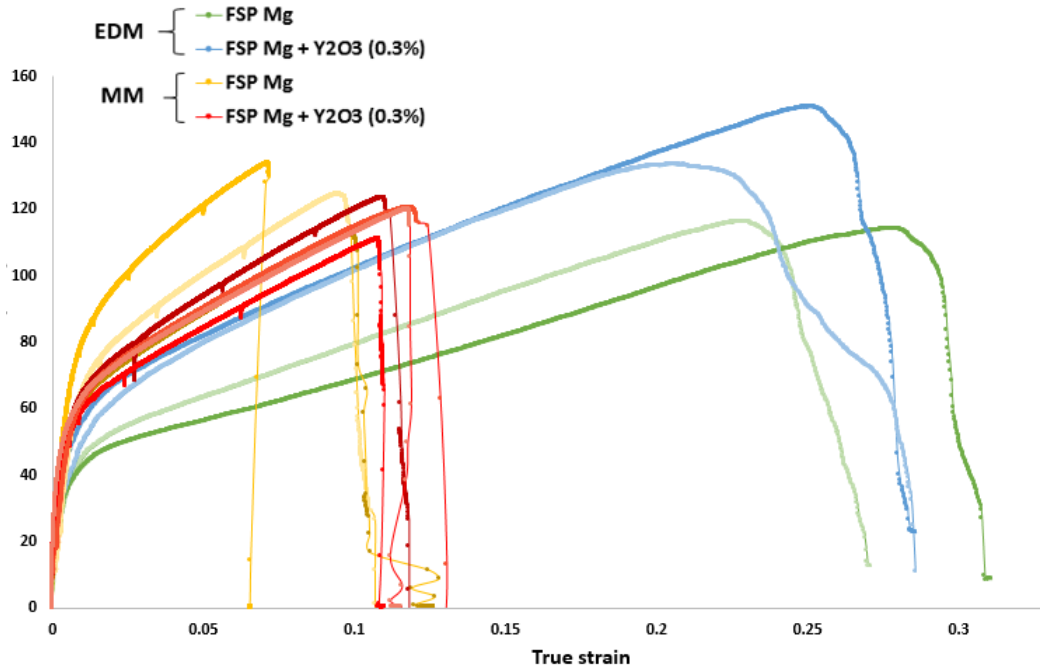

Figure 4.3 – True stress vs. true strain comparison for tensile specimens prepared using EDM and milling machinning.

4.1.1.3 Texture analysis and selection of the ideal fabrication method

Texture analysis were performed in order to understand the microstructural differences that could lead to the disparity of the mechanical response between samples fabricated by EDM and mechanical milling. Indeed, the mechanical behavior of magnesium is known to be strongly related to its texture. The stress-strain response when tensile twinning is favorable for a certain testing configuration (tensile stress along the

c-axis) will be completely different from the one obtained if tensile twinning would not be favorably oriented [155]. In order to study the texture obtained after FSP, it is first important to understand how the FSP affects the texture. Thus, a texture analysis of the as-received magnesium plates (base material for FSP) is presented in Figure 4.4. A strong fibre texture in the (0 0 0 2) pole figure can be observed: the basal planes are parallel to the rolling direction.

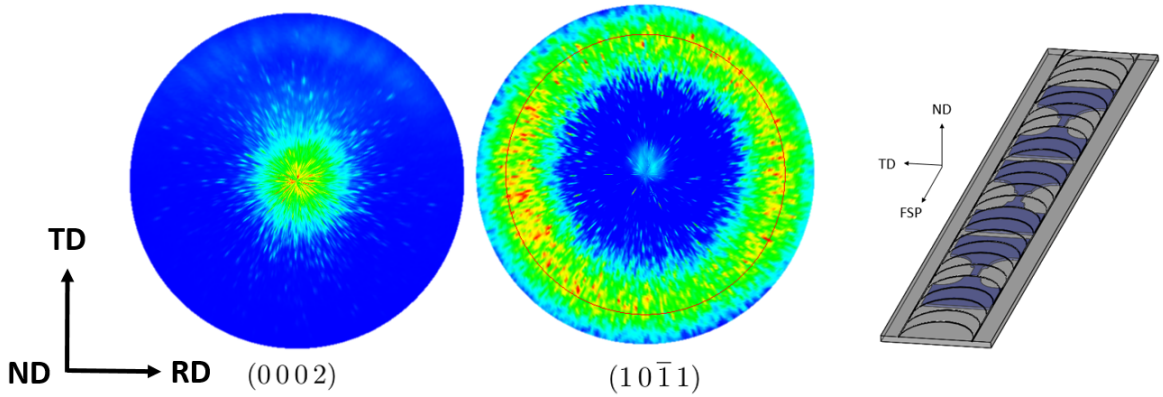

Figure 4.4 – (0 0 0 2) and (1 0 $\bar{1}$ 1) incomplete pole figures ($0° < \chi < 75°$) obtained by X-ray diffraction for the as-received magnesium plates.

The (0 0 0 2) and (1 0 $\bar{1}$ 1) pole figures of FSP Mg and FSP Mg + Y_2O_3 (0.3 %) fabricated by EDM and milling machining prior and after tensile testing are presented in Figure 4.5 and Figure 4.6, respectively. Focusing at first on the texture directly after FSP, it is noticeable in both cases a reduction of (0 0 0 2) texture presented in the as-received magnesium plates.

- the samples fabricated by EDM have shown a reorientation of the c-axis between 20 to 30° towards the FSP direction when compared to the base material (Figure 4.4). It is important to precise that an incomplete pole figure is obtained by X-ray diffraction since the upper limit of the angle χ measured is 75° and not 90° (see Section 2.7),
- this modification of the texture is also present in the samples fabricated by milling machining but with a much lower intensity (Figure 4.6). The most dominant orientation, in this case, shows a reorientation of the c-axis by 50° towards a direction that is 30° misoriented counterclockwise from the TD. The (1 0 $\bar{1}$ 1) is close to the ND.

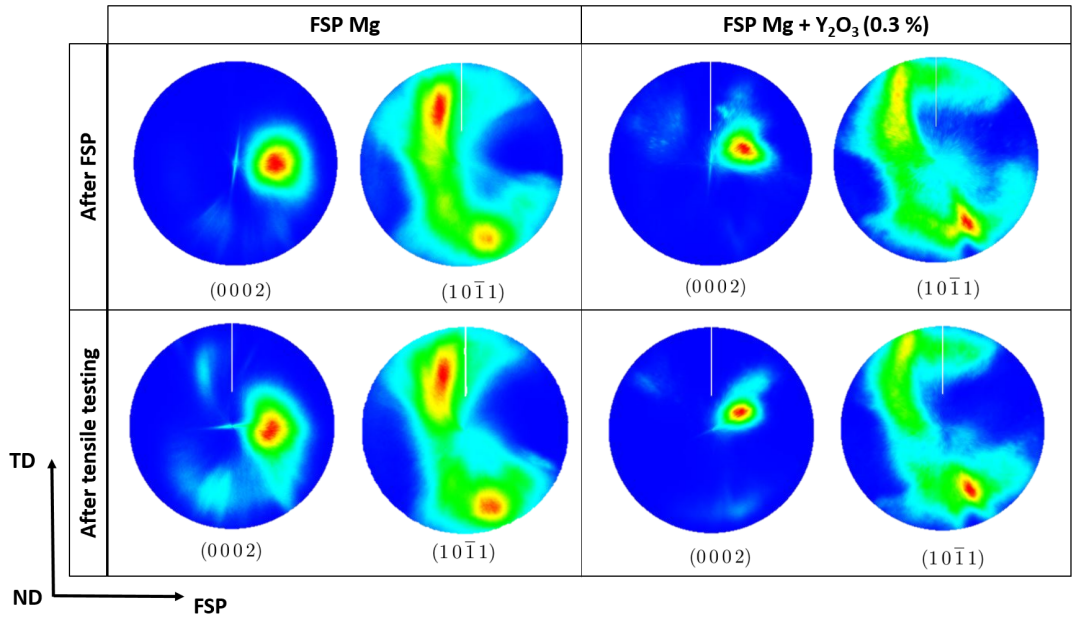

Figure 4.5 – (0 0 0 2) and (1 0 $\bar{1}$ 1) incomplete pole figures ($0° < \chi < 75°$) obtained by X-ray difraction of FSP Mg and FSP Mg + Y_2O_3 (0.3 %) samples fabricated by EDM prior and after tensile testing. FSP direction is the same as the rolling direction of the original plates. Tensile direction is parallel to FSP direction.

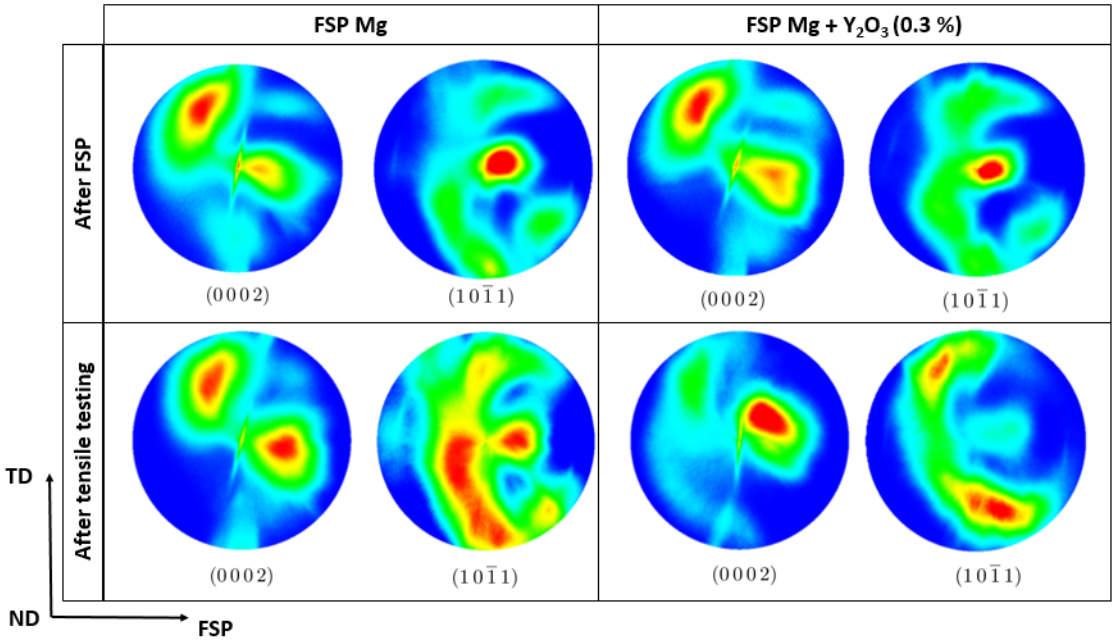

Figure 4.6 – (0 0 0 2) and (1 0 $\bar{1}$ 1) incomplete pole figures ($0° < \chi < 75°$) obtained by X-ray diffraction of FSP Mg and FSP Mg + Y_2O_3 (0.3 %) fabricated by milling machining prior and after tensile testing. FSP direction is the same as the rolling direction of the original plates. Tensile direction is parallel to FSP direction.

Tensile specimens fabricated by milling machining show a stronger texture close to the $[1\,0\,\bar{1}\,1]$ orientation (Figure 4.6), which is similar for both FSP Mg and FSP Mg + Y_2O_3 (0.3 %). It seems that the microstructure of the specimens has been modified during milling machining. In order to interpret the texture modification, the 3D Explorer software[1] has been used to measure the misorientation between the two most intense orientations in the pole figures of specimens fabricated by milling machining (Figure 4.6). A misorientation between 65° and 71° has been measured. This value is close to the misorientation obtained when $\{1\,0\,\bar{1}\,3\}$ compression twinning takes place in magnesium (64°) as mentioned in Section 1.2.3. Another phenomenon called double twin can also take place. With the application of further load, a region that has already been twinned can twin another time in order to better accommodate the deformation [16]. The second twin can propagate through the whole volume occupied by the first twin [16]. The misorientation of the double twins corresponds to the addition of the individual misorientation of each one of the twins. After a first $\{1\,0\,\bar{1}\,1\}$ twin in magnesium, six possible secondary twin variants exist and are described in Table 4.2. Twin of types 3 and 4 have a misorientation angle that is similar to the one measured on the pole figures. For timing constraints however it was not possible to further investigate these samples in order to determine whether $\{1\,0\,\bar{1}\,3\}$ compression twinning or double twinning takes place during fabrication by milling machining.

Table 4.2 – Misorientation between different double twins present in magnesium [16, 156] after a first $\{1\,0\,\bar{1}\,1\}$ compression twin.

Double twin variant	**Secondary twin plane**	**Twin direction**	**Misorientation**
Type 1	$(1\,0\,\bar{1}\,2)$	$[1\,\bar{2}\,1\,0]$	37.5°
Type 2	$(\bar{1}\,0\,1\,2)$	$[1\,\bar{2}\,1\,0]$	30.1°
Type 3	$(0\,\bar{1}\,1\,2)$	$[5\,\bar{9}\,4\,3]$	66.5°
	$(\bar{1}\,1\,0\,2)$	$[5\,\bar{9}\,4\,3]$	66.5°
Type 4	$(0\,1\,\bar{1}\,2)$	$[2\,\bar{4}\,2\,1]$	69.9°
	$(0\,\bar{1}\,0\,2)$	$[2\,\bar{4}\,2\,1]$	69.9°

[1] 3D Explore software from Rigaku is used to display reciprocal space maps and pole figures

Texture analysis has been performed on the surface normal of the tensile specimens. In order to investigate if milling machining has promoted microstructure modification in the entire tensile specimen or only on the specimen surface, texture analysis has also been performed at the mid-thickness of the tensile specimens (FSP Mg and FSP Mg + Y_2O_3 (0.3 %)). Prior to the texture analysis, a thickness of 0.5 mm (specimen thickness is 1 mm) has been removed using mechanical polishing. The texture analysis of these samples is presented in Figure 4.7. The texture is different from the one observed on

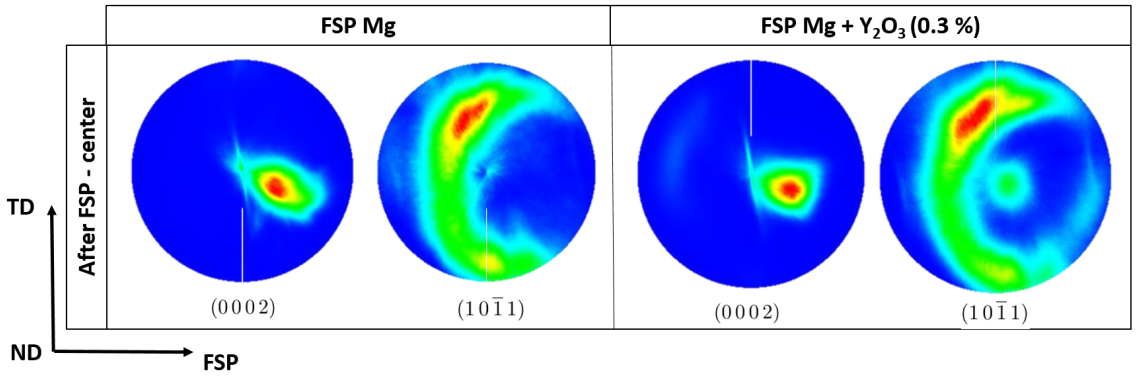

Figure 4.7 – (0 0 0 2) and (1 0 $\bar{1}$ 1) pole figures of FSP Mg and FSP Mg + Y_2O_3 (0.3 %) fabricated by milling machining prior to tensile testing (measurement at 0.5 mm from the specimen surface).

the surface of the samples fabricated by milling machining, but very similar to the texture obtained when preparing the specimens using EDM (Figure 4.5). It indicates that milling machining affects mostly the microstructure at the surface.

To summarize, the results obtained for the specimens fabricated by EDM seem to be more reliable since no microstructural modification has been observed. Results found in the literature support this hypothesis since texture comparable to the one obtained in EDM were reported. The *c*-axis should normally be oriented parallel to the FSP direction in hcp materials [157]. However, the texture obtained after FSP is much more complex and varies within the FSPed zone:

- Park *et al.* [158] and Xin *et al.* [159] have shown that the basal planes tend to align with the rotating tool following the material flow and forming an ellipsoid trace texture, as shown in Figure 4.8 (indicated as SZ center).
- The texture in the upper surface of the stirred zone is different [160] due to the material flow induced by the tool shoulder during FSP (Figure 4.9). This reorientation is in agreement to the one observed in the tensile specimens prepared by EDM.

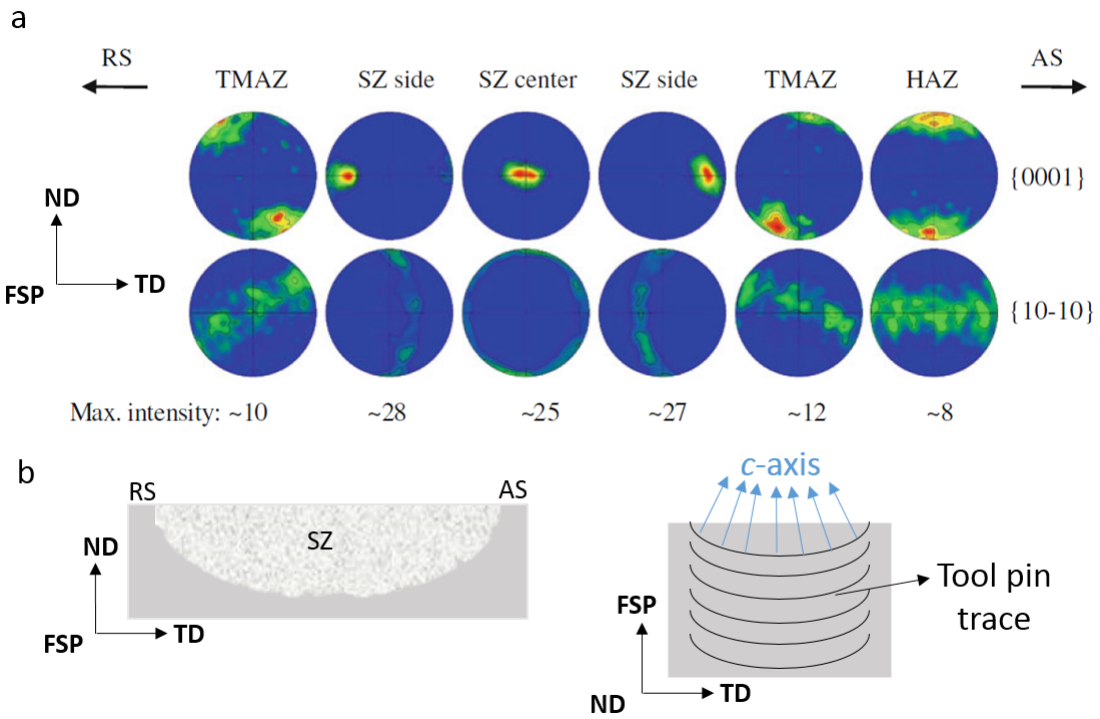

Figure 4.8 – $(0\,0\,0\,1)$ and $(1\,0\,\bar{1}\,0)$ pole figures of different regions in a FSPed AZ31 magnesium alloy show that the c-axis tends to be aligned to the FSP direction in the center of the stirred zone (SZ)[159] (a). Schematic illustration of the basal plane orientation (b) in the middle of the stirred zone in FSP magnesium, based on Park's studies [158]. TMAZ and HAZ correspond to the thermo-mechanically affected zone and heat affected zone, respectively.

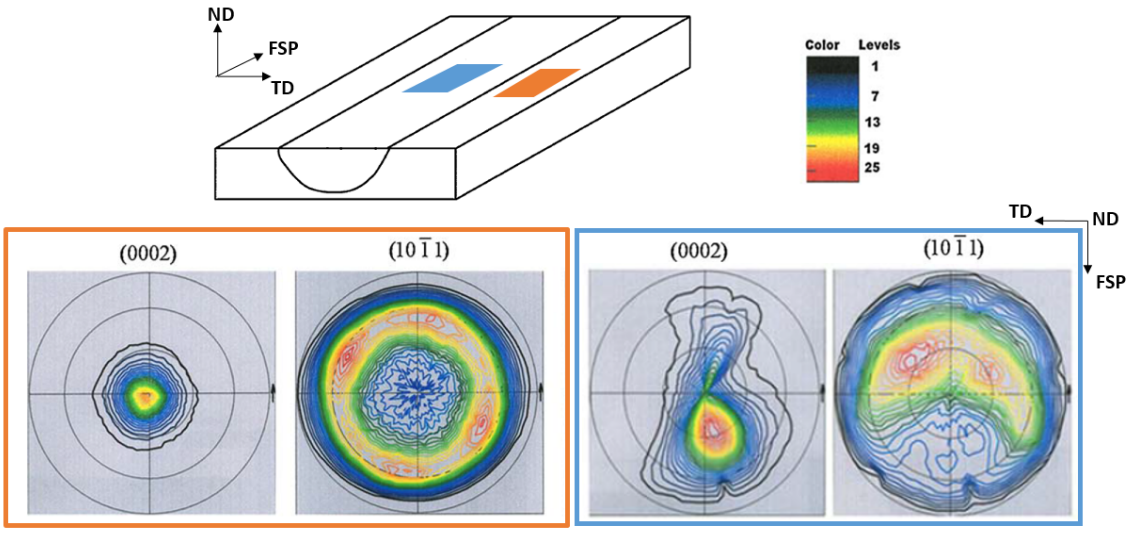

Figure 4.9 – $(0\,0\,0\,2)$ and $(1\,0\,\bar{1}\,1)$ pole figures showing the influence of the FSP on the texture of AZ31B magnesium alloy [160]. Orange and blue correpond to the base material and the stirred zone, respectively.

4.1.2 Macroscopic characterization of the nanocomposite

Knowing that EDM is the ideal fabrication method for the preparation of the tensile specimens, two additional volume fractions of Y_2O_3 particles (1.64 and 2.11 %) have been compared to the previous tested FSP Mg and FSP Mg + Y_2O_3 (0.3%). All the FSP Mg + Y_2O_3 samples have been fabricated under the exact same processing conditions. The objective is to check if the Y_2O_3 particles have a strengthening effect. Two tensile specimens were tested for each volume fraction. The surface fraction of Y_2O_3 particles was calculated based on SEM images analysis since this technique seems to give results closer to the volume fractions obtained by nanoholotomography as it has already been discussed in Chapter 3.

4.1.2.1 Tensile testing

Figure 4.10 shows the true stress vs. true strain curves for the tensile specimens prepared using EDM. The corresponding mechanical properties are presented in Table 4.3.

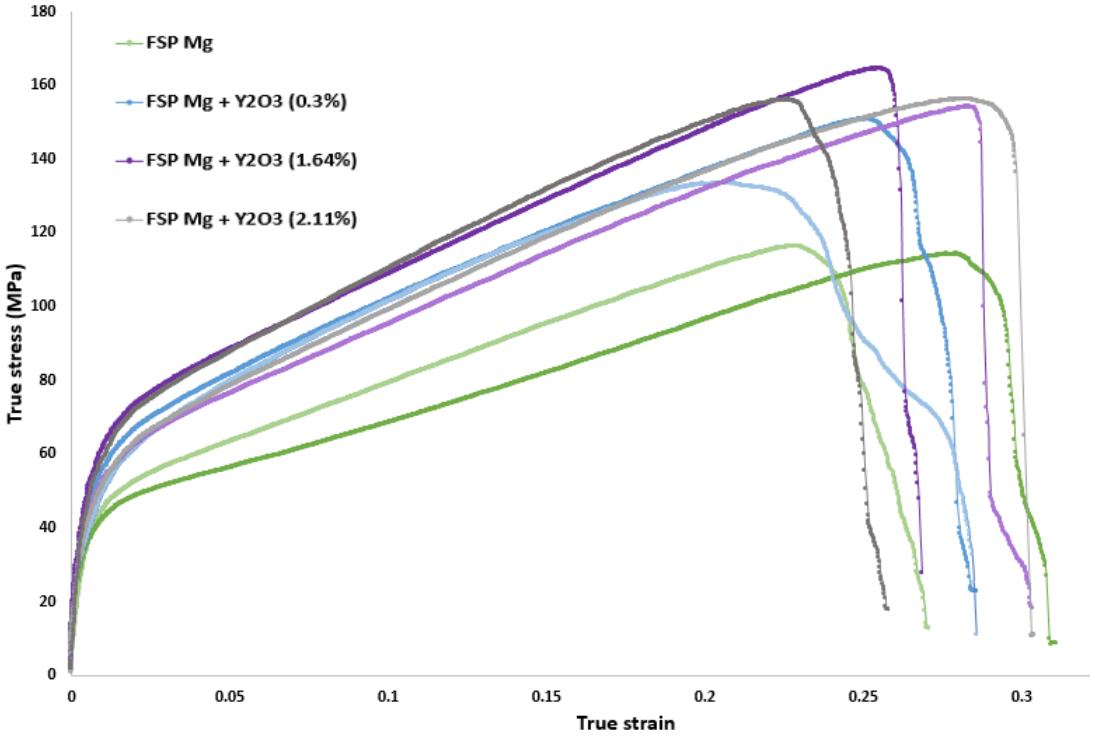

Figure 4.10 – True stress vs. true strain tensile loading curves for specimens prepared using EDM. Initial engineering strain rate of $4x10^{-4}$ s^{-1}.

An improvement of the ultimate tensile strength and yield strength was observed with the

Table 4.3 – Mechanical properties of FSP Mg and FSP Mg + Y_2O_3 samples fabricated by EDM.

Sample	0.2 % Yield strength (MPa)	Ultimate tensile strength (MPa)	Ductility (%)	Strain hardening coefficient (MPa)
Mg	52.4±2.5	115.2±1.1	28.8±1.9	279.5±41
Mg+Y_2O_3(0.3%)	68.7±1.8	142.1±8.6	28.3±0.1	425.8±43
Mg+Y_2O_3(1.64%)	72.4±5.5	159.2±5.2	28.5±1.8	382.5±36
Mg+Y_2O_3(2.11%)	71.4±4.5	156.1±0.1	27.9±2.2	425.4±20.5

addition of Y_2O_3 particles. The ductility is not affected by the addition of the particles. A higher strain hardening coefficient is also noticeable in the samples containing Y_2O_3 particles, which is in agreement with similar studies found in the literature [3, 4]. The increase of the strain hardening is better evidenced in the Kocks plot given in Figure 4.11, where the strain hardening coefficient ($\theta = d\sigma/d\varepsilon$) is plotted as a function of the stress level. The strain hardening coefficient decreases until an inflection point, which determines the critical stress. The increase of the ultimate tensile strength is directly related to the higher strain hardening observed in the FSP Mg + Y_2O_3 samples, which is confirmed by the increase of the strain hardening coefficient that describes the dislocation storage rate. Very low influence of the volume fraction of Y_2O_3 on the mechanical properties is observed.

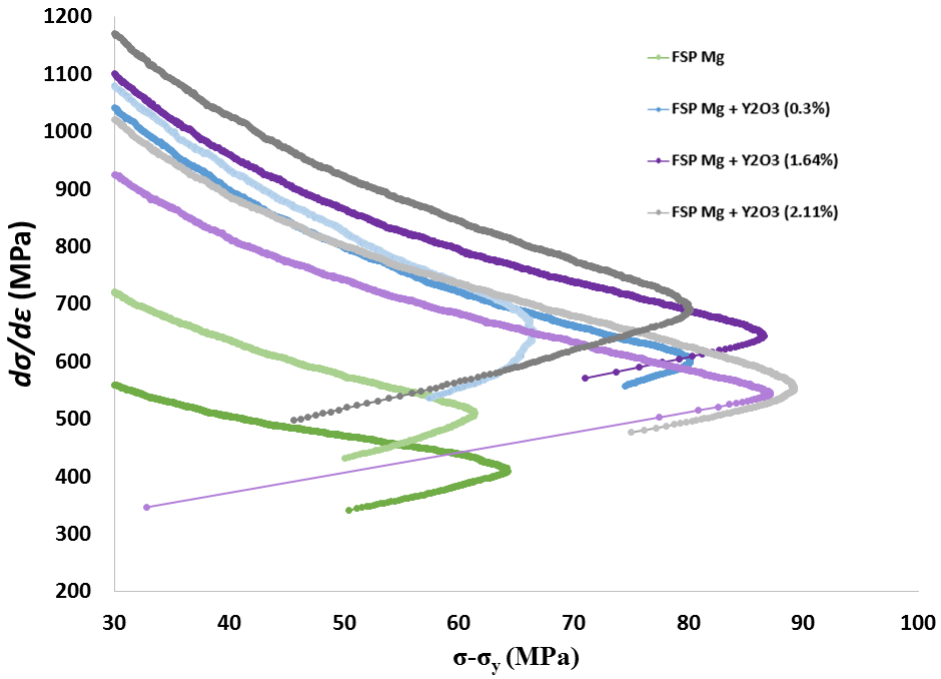

Figure 4.11 – Kocks plot for the FSP Mg and FSP Mg + Y_2O_3 samples fabricated by EDM.

In order to understand the strengthening observed with the addition of Y_2O_3 particles, the grain size has been measured on the surface normal of the tensile specimens (FSP Mg and FSP Mg + Y_2O_3 (0.3 %)) and are shown in Figure 4.12. The mean grain

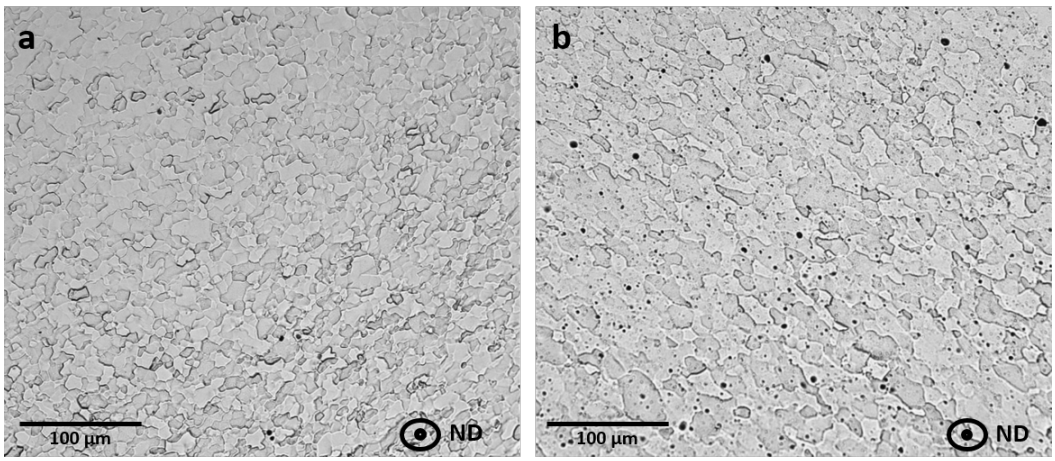

Figure 4.12 – Grain size measured on the surface normal (ND) of the tensile specimens fabricated by EDM: FSP Mg (a) and FSP Mg + Y_2O_3 (0.3 %) (b).

size of the FSP Mg and FSP Mg + Y_2O_3 (0.3 %) are 7.8±0.66 μm and 11.7±1.23 μm, respectively. The higher grain size in the FSP Mg + Y_2O_3 (0.3 %) indicates that the Hall-Petch strengthening is not the mechanism responsible for the strengthening observed. It can be concluded that the Y_2O_3 particles are contributing to the strengthening observed on the true stress vs. true strain curve (Figure 4.10).

Considering the texture, the incomplete pole figure from Figure 4.5 has not shown a significant modification of the texture after FSP with the addition of Y_2O_3 particles. The same is observed for higher volume fractions of particles, as seen in Figure 4.13. Additionally, the texture before and after tensile test remains similar. The same is however not observed for the samples prepared by milling machining (Figure 4.6): the texture is different after tensile testing, especially for FSP Mg + Y_2O_3 (0.3 %). The texture close to the $[1\,0\,\bar{1}\,1]$ orientation presented the $(1\,0\,\bar{1}\,1)$ incomplete pole figure prior to tensile testing is reduced in the FSP Mg + Y_2O_3 (0.3 %). It indicates that the presence of Y_2O_3 particles affects the deformation mechanisms at this new orientation developed during milling machining.

To summarize, a strengthening effect of the Y_2O_3 particles has been clearly evidenced at the macroscale.

- no significant change in the grain size with the addition of Y_2O_3 particles

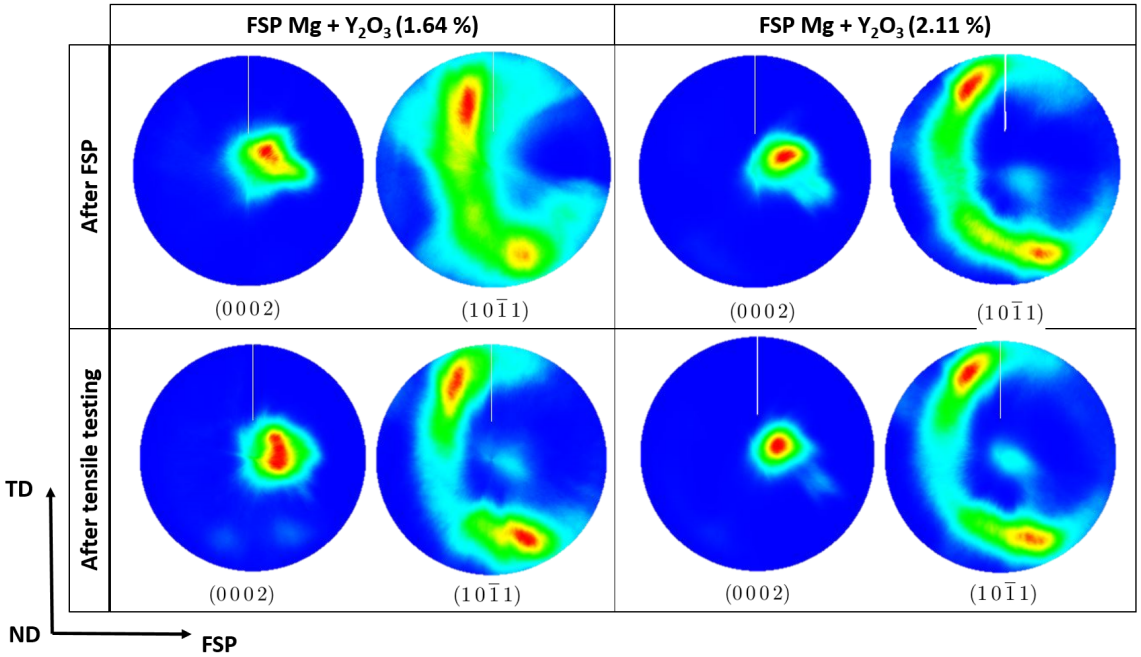

Figure 4.13 – (0 0 0 2) and (1 0 $\bar{1}$ 1) incomplete pole figures (0° < χ <75°) obtained by X-ray difraction of FSP Mg + Y_2O_3 (1.64 and 2.11 %) samples fabricated by EDM prior and after tensile testing. FSP direction is the same as the rolling direction of the original plates. Tensile direction is parallel to FSP direction.

- no modification of the texture by the Y_2O_3 particles
- Y_2O_3 particles seem to play a role when the stress is applied in specific orientations (Figure 4.6)

In order to isolate the strengthening mechanisms, the following section will focuses on the single crystalline plastic behavior of both FSP Mg and FSP Mg + Y_2O_3 (0.3 %) by means of microcompression testing.

4.2 Microcompressiong testing

In the present section, the plastic deformation behavior of magnesium single crystals with and without Y_2O_3 particles will be presented. The focus is on the orientation-dependent mechanisms of plastic deformation in relation with the particle strengthening effect. The stress-strain response has been obtained using microcompression. The mechanical response of FSP Mg and FSP Mg + Y_2O_3 (0.3 %) samples favorably oriented for basal slip and tensile twinning are compared. These configurations have been chosen

taking into consideration the fact that, at room temperature, magnesium deforms mainly by basal slip or twinning.

At the macroscopic scale, the tensile tests realized on polycrystals have shown a strengthening with a volume fraction of Y_2O_3 particles as low as 0.3 %. Samples with higher volume fractions (1.64 and 2.11%) of particles will not be investigated at the single crystal scale due to the impossibility to reproduce the abnormal grain growth when a higher fraction of particles is present.

As presented in Section 3.2, the Mg and Mg + Y_2O_3 (0.3 %) samples obtained by FSP are polycrystalline and a thermal treatment at 500°C for 3 hours was performed in order to induce abnormal grain growth. Samples with larger grains have been privileged since they facilitate the FIB machining of single crystalline microcolumns. EBSD analysis was performed prior to column machining by FIB in order to identify the grain orientation. Grains with specific orientations were selected after the calculation of the different Schmid factors associated to a compression oriented along the surface normal direction. The *post mortem* analysis of the deformed column was performed using: scanning electron microscopy (SEM), cross-sectioning electron backscattered diffraction (EBSD) and transmission electron microscopy (TEM) in order to characterize the slip and twin activity and dislocation/particles interactions.

In addition to the orientation-dependent plasticity mechanisms, size effects will also be investigated comparing columns with varying sizes. Columns with varying mid-height diameter (2, 5, 10 and 15 μm) have been fabricated. Each column will be identified according to its mid-height diameter (example, 2 μm columns). The size effects of pure magnesium single crystals have already been studied by G. S. Kim [2]. Kim's studies have shown a strong dependence between grain orientation and microcolumn size. The present results will be compared to the ones obtained by G. S. Kim and the influence of the Y_2O_3 particles on the size effects will also be discussed.

4.2.1 Columns favorably oriented for basal slip

The mechanical behavior of microcolumns favorably oriented for basal slip was studied. The ideal Schmid factor for activation of basal slip is 0.5 and corresponds to a misorientation angle of 45° between the normal to the basal plane and the loading axis. As the "*model*" nanocomposite is polycrystalline, it is extremely difficult to find a grain

with such a perfect orientation. However, according to Kelley *et al.* [161], even a slight misalignment of the *c*-axis with respect to the loading axis can lead to sufficient RSS to activate basal slip. In the present case, the misorientation angles will be consider for each column tested. The mechanical response of the microcolumns is then presented in terms of resolved shear stress (RSS) vs. true compression strain.

The mechanical response will first be presented according to column sizes. The different columns sizes studied are 2, 5, 10 and 15 μm for an optimal comparison with G. S. Kim [2]. Afterwards, the influence of the Y_2O_3 particles on the plastic deformation mechanisms will be discussed to emphasis the influence of the crystal orientation and size effect.

4.2.1.1 Column diameter: 2 μm

The RSS vs. true strain response of 15 columns of 2 μm diameter is presented in Figure 4.14. The stress increases until a strain burst occurs at a mean RSS of 15 MPa for both FSP Mg and FSP Mg + Y_2O_3 samples. SEM micrographs of the different deformed columns are shown in Figure 4.15. Table 4.4 details the Schmid factor and the misorientation angles with the slip plane and slip direction for each column tested.

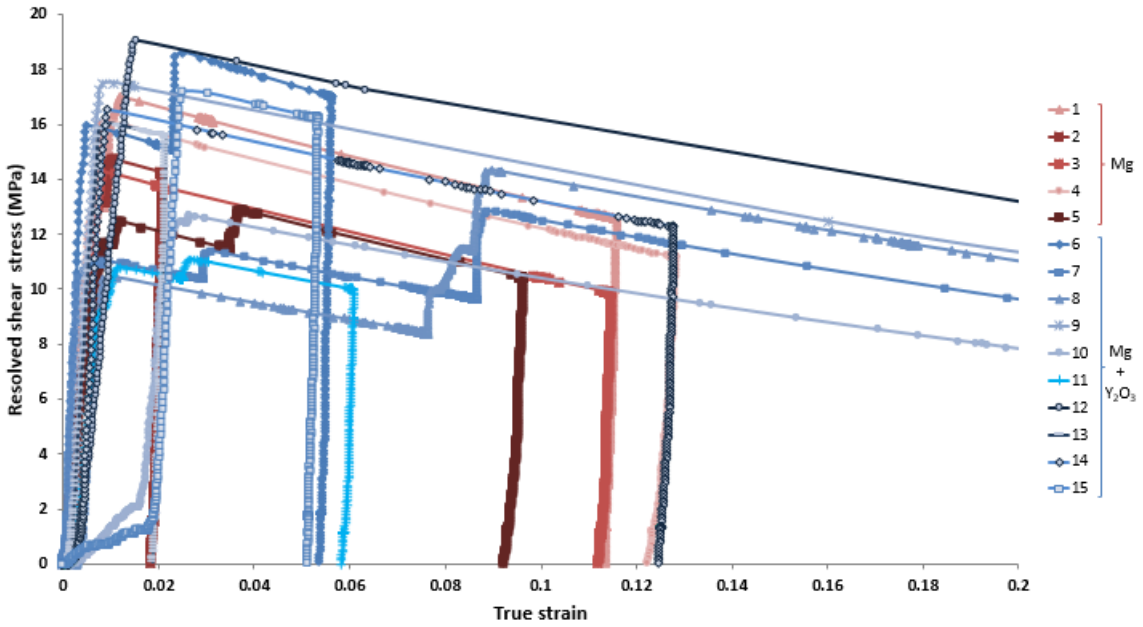

Figure 4.14 – RSS vs. true strain for 2 μm columns favorably oriented for basal slip. Red and blue curves correspond, respectively, to FSP Mg and FSP Mg + Y_2O_3 (0.3 %) samples.

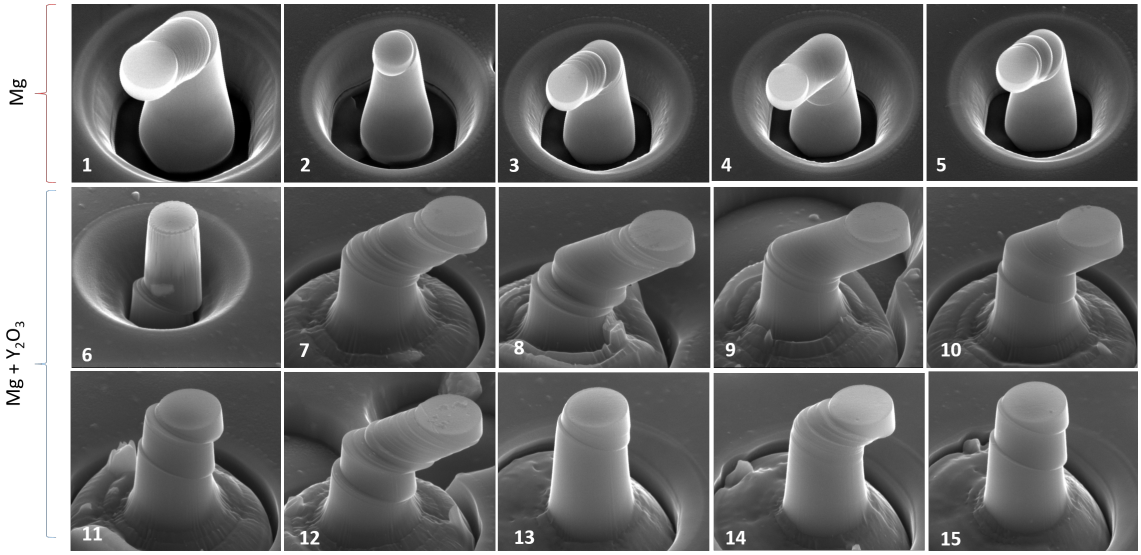

Figure 4.15 – SEM micrographs of the fifteen deformed 2 μm columns (graphic in Figure 4.14).

Table 4.4 – Schmid factor and misorientation angles of each 2 μm column tested for basal slip (only the highest Schmid factors are indicated).

Column	**1**	**2-5**	**6**	**7-12**	**13-15**
Materials	Mg	Mg	$Mg+Y_2O_3$	$Mg+Y_2O_3$	$Mg+Y_2O_3$
Loading axis	$[\bar{1}\bar{1}\,12\,\bar{1}\,50]$	$[\bar{4}\,5\,\bar{1}\,21]$	$[\bar{5}\,2\,3\,14]$	$[1\,2\,\bar{3}\,\bar{1}\bar{2}]$	$[\bar{1}\bar{1}\,7\,4\,41]$
Slip plane	$(0\,0\,0\,1)$	$(0\,0\,0\,1)$	$(0\,0\,0\,1)$	$(0\,0\,0\,1)$	$(0\,0\,0\,1)$
Angle with slip plane	13.65°	12.9°	18.24°	13.06°	13.92°
Slip direction	$[\bar{1}\,2\,\bar{1}\,0]$	$[\bar{1}\,2\,\bar{1}\,0]$	$[2\,\bar{1}\,\bar{1}\,0]$	$[1\,1\,\bar{2}\,0]$	$[2\,\bar{1}\,\bar{1}\,0]$
Angle with slip direction	77.57°	77.63°	71.76°	77°	76.1°
Schmid factor	0.21	0.21	0.3	0.22	0.23

The morphology of the column changes for every serration in strain in the RSS vs. true strain curve (Figure 4.14). Each burst in displacement corresponds to a slip step at the surface of the column. As an example, Figure 4.16 shows the RSS vs. true strain curve for column 11 (FSP Mg + Y_2O_3) and a SEM micrograph of the same column after deformation. The two prominent slip steps formed at the surface of the column are related to the two strain bursts observed on the RSS vs. true strain curve.

Although the maximum displacement is prescribed in the loading protocol, due to plastic instability and limited response of the nanoindentation, significantly larger total displacements are often achieved. This is shown in Figure 4.16 (Column 11), where a prescribed displacement of 4 % was set, but it is possible to observe that the actual true strain reached after the test is close to 6 %. The same behavior is observed in most

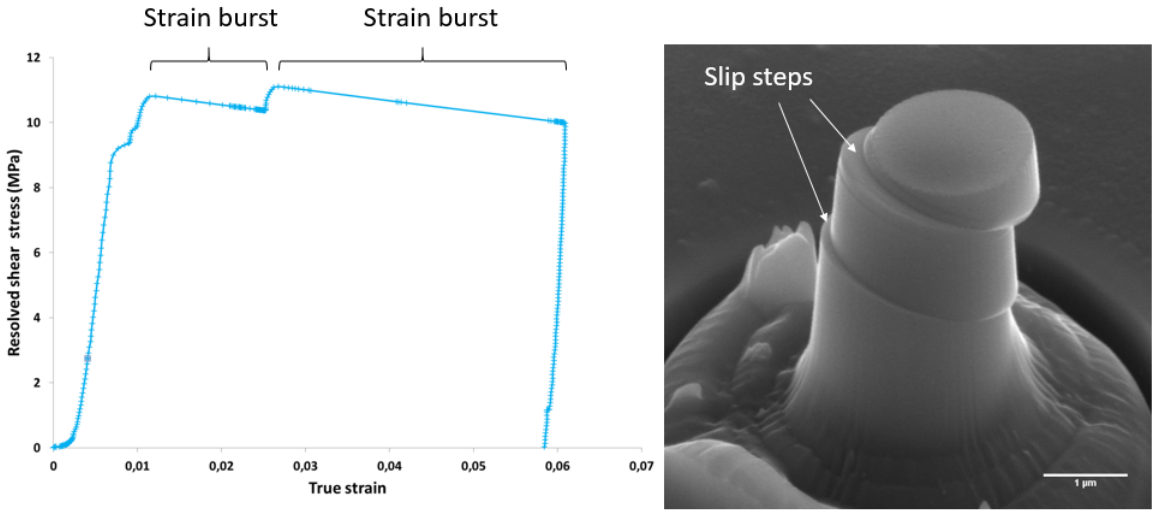

Figure 4.16 – Slip steps appear at the surface of the column for every strain burst in the RSS vs. true strain curve. In this example, column 11 (FSP Mg + Y_2O_3 (0.3 %)) from Figure 4.15 is presented.

microcolumns. The physical instabilities related to the material and instrument behavior during the testing lead to these larger displacements (further details in Section 2.3.2.1).

4.2.1.2 Column diameter: 5 μm

The RSS vs. true strain response of 11 columns of 5 μm diameter and the respective *post mortem* SEM micrographs are presented in Figure 4.17 and Figure 4.18, respectively. Table 4.5 details the Schmid factor and angles between the loading axis and the slip plane and between the loading axis and the slip direction for each column tested. The overall behavior is similar to the 2 μm columns: the stress increases until the strain burst occurs. The slip marks generated during the massive strain bursts are shown in Figure 4.19. A cross-sectioning of one column (Figure 4.20) evidences this massive basal slip. In this case, the strain bursts of the FSP Mg + Y_2O_3 seem to occur at a lower stress or equivalent lower strain. The mean critical stress for massive basal slip obtained from the RSS vs. true strain curves is close to 14 MPa for FSP Mg, but it is only 10 MPa for FSP Mg + Y_2O_3.

Another major difference between FSP Mg and FSP Mg + Y_2O_3 samples concerns the number of successive bursts, which is much larger for pure magnesium than for the nanoparticle reinforced material. These successive bursts are most probably related to pre-existing defects in the material. For the upcoming discussion, the critical resolved

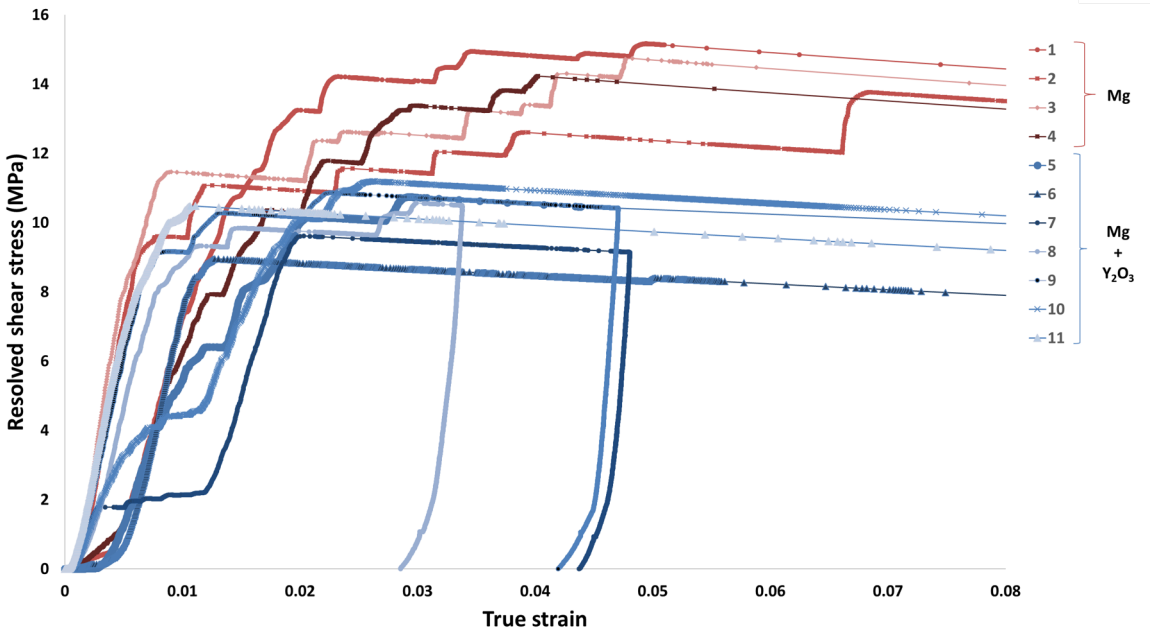

Figure 4.17 – RSS vs. true strain of 5 μm columns favorably oriented for basal slip. Red and blue curves correspond, respectively, to FSP Mg and FSP Mg + Y_2O_3 (0.3 %) samples.

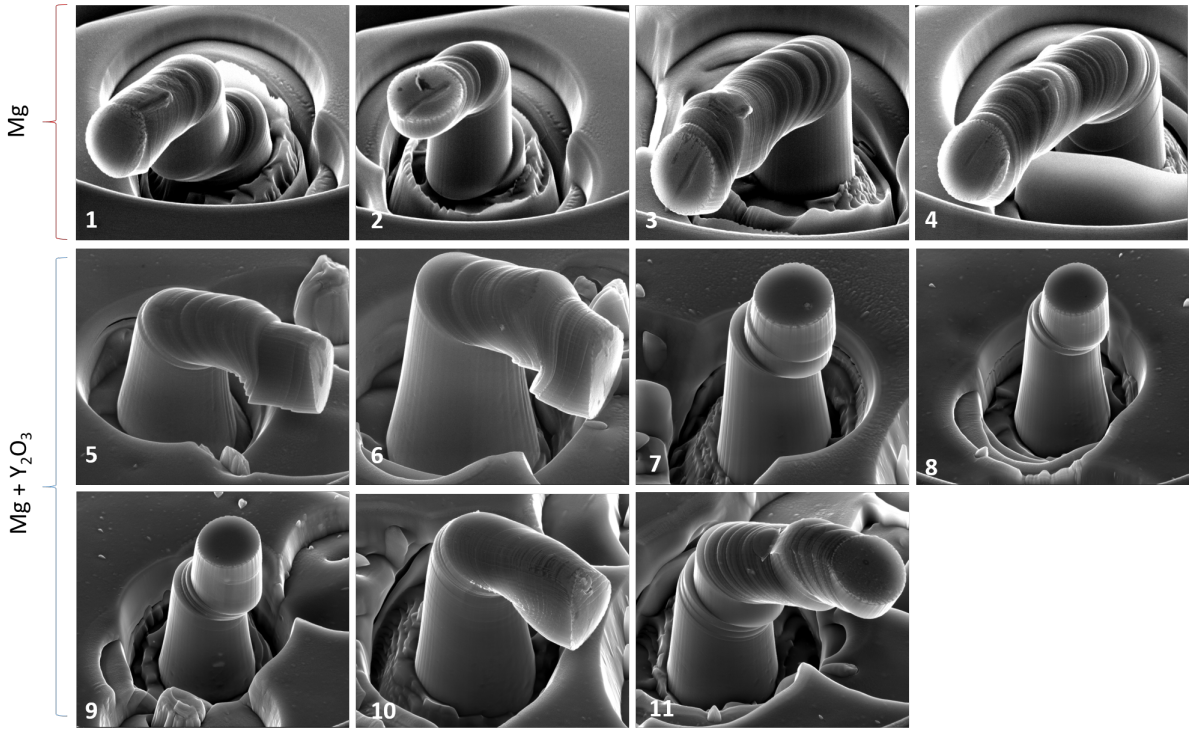

Figure 4.18 – SEM micrographs of the eleven deformed 5 μm columns (graphic from Figure 4.17).

shear stress (CRSS) will be considered at the stress when a first burst occurs and a critical burst shear stress (CBSS) will be considered at the stress when massive strain burst

occurs.

Table 4.5 – Schmid factor and orientation of each 5 μm column tested for basal slip (only the highest Schmid factors are indicated).

Column	**1-4**	**5-11**
Materials	Mg	Mg+Y_2O_3
Loading axis	$[\bar{1}\bar{1}\,12\,\bar{1}\,50]$	$[0\,1\,\bar{1}\,\bar{6}]$
Slip plane	$(0\,0\,0\,1)$	$(0\,0\,0\,1)$
Angle with slip plane	13.65°	9.9°
Slip direction	$[\bar{1}\,2\,\bar{1}\,0]$	$[\bar{1}\,2\,\bar{1}\,0]/[1\,1\,\bar{2}\,0]$
Angle with slip direction	77.57°	81.3°
Schmid factor	0.21	0.15

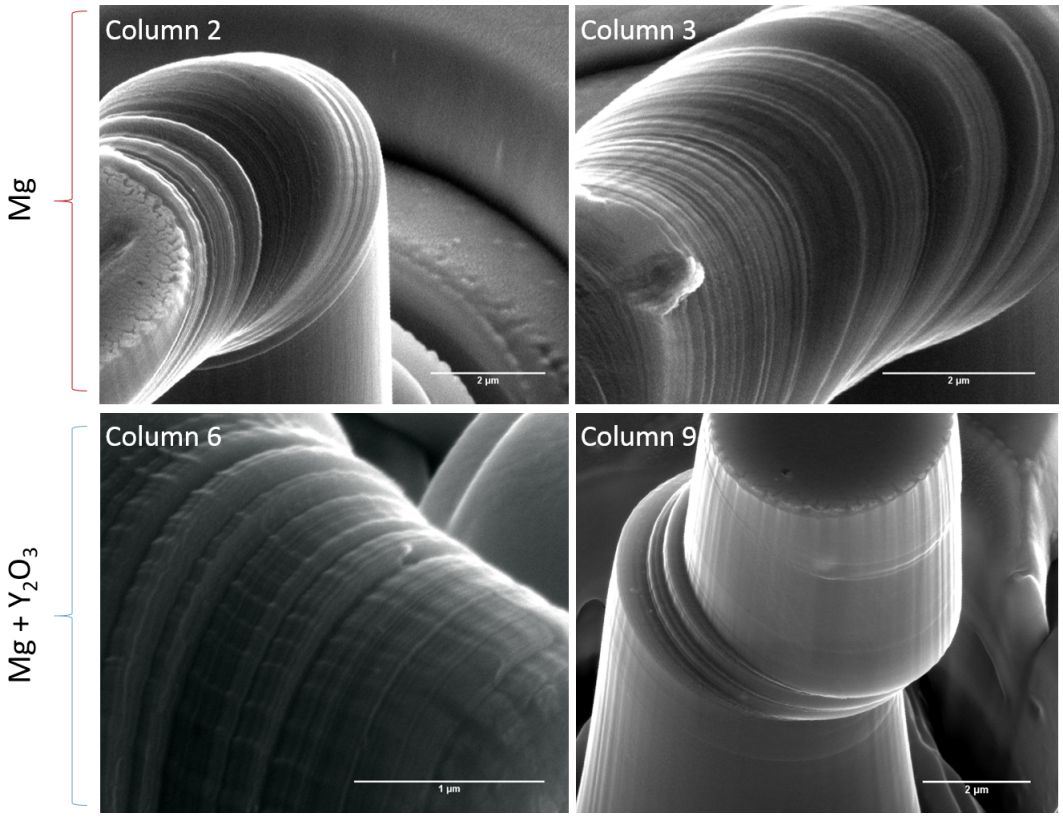

Figure 4.19 – SEM micrographs of the deformed columns revealing a massive basal slip (5 μm columns). Columns 2 and 3 correspond to FSP Mg, while columns 6 and 9 correspond to FSP Mg + Y_2O_3 (0.3 %) (Figure 4.18).

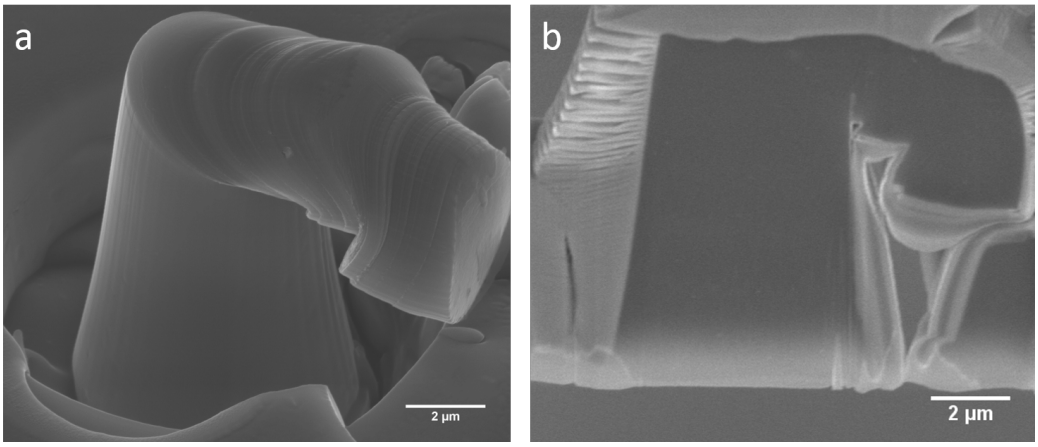

Figure 4.20 – SEM micrographs of FSP Mg + Y_2O_3 (0.3 %) after deformation (column 6 from Figure 4.17) before (a) and after (b) cross-sectioning detail the massive basal slip.

4.2.1.3 Column diameter: 10 μm

Only a few larger columns (10 and 15 μm columns) were fabricated due to practical issues that involve FIB milling time and milling depth (difficulty to obtain a single crystalline column), as discussed in Section 2.3.2.2.

Four microcolumns with a nominal diameter of 10 μm have been tested. The RSS vs. true strain and the respective *post mortem* SEM micrographs are presented in Figure 4.21 and Figure 4.22, respectively. Table 4.6 details the Schmid factor and angles between the loading axis and the slip plane and between the loading axis and the slip direction for each column tested.

Table 4.6 – Schmid factor and orientation of each 10 μm column tested for basal slip (only the highest Schmid factors are indicated).

Column	**1-2**	**3**	**4**
Materials	Mg	Mg+Y_2O_3	Mg+Y_2O_3
Loading axis	$[\bar{5}\,4\,1\,\bar{1}9]$	$[\bar{5}\,7\,\bar{2}\,\bar{1}1]$	$[\bar{4}\,6\,\bar{2}\,\bar{9}]$
Slip plane	$(0\,0\,0\,1)$	$(0\,0\,0\,1)$	$(0\,0\,0\,1)$
Angle with slip plane	14.3°	31.1°	32.03°
Slip direction	$[2\,\bar{1}\,\bar{1}\,0]$	$[\bar{1}\,2\,\bar{1}\,0]$	$[\bar{1}\,2\,\bar{1}\,0]$
Angle with slip direction	76.4°	59.81°	58.55°
Schmid factor	0.23	0.43	0.44

In this case, the behavior is different than what was observed for 2 and 5 μm

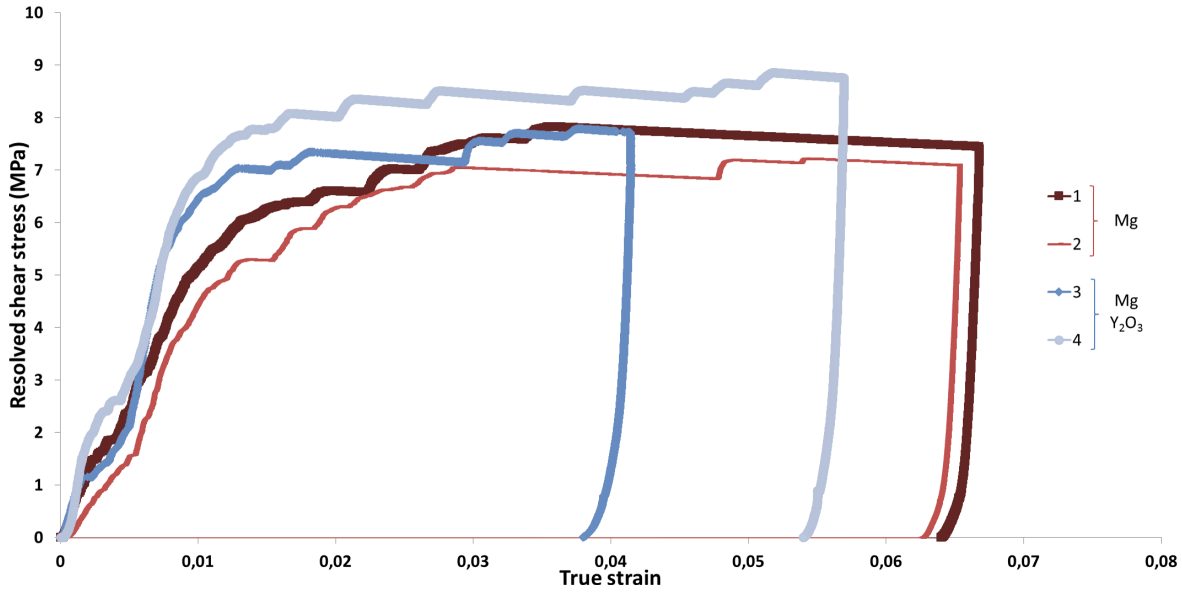

Figure 4.21 – RSS vs. true strain for 10 μm columns favorably oriented for basal slip. Red and blue curves correspond, respectively, to FSP Mg and FSP Mg + Y_2O_3 (0.3 %) samples.

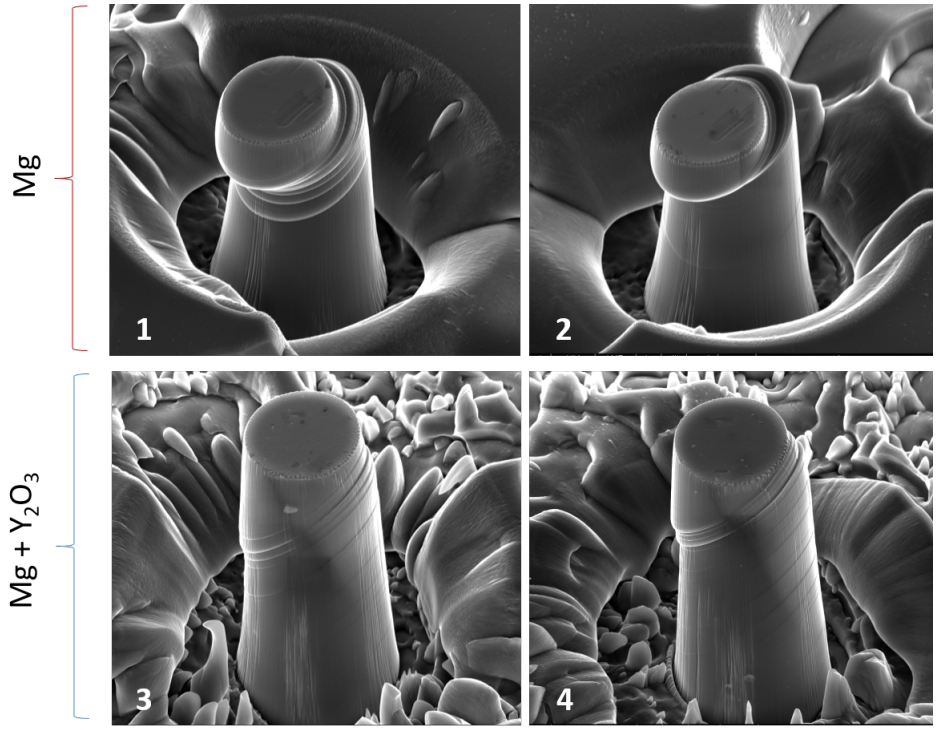

Figure 4.22 – SEM micrographs of the four deformed 10 μm columns (graphic in Figure 4.21).

columns: the mean CBSS is slightly higher for the FSP Mg + Y_2O_3 (8.3 MPa) in comparison to FSP Mg (7.5 MPa). The CRSS of FSP Mg + Y_2O_3 is also higher (7.5 MPa) when compared to the FSP Mg (5.95 MPa). The hardening observed after the plastic yield is higher in the samples containing particles. Note that the maximum strain achieved during

microcompression testing is lower than the obtained for 2 and 5 μm columns (Figure 4.14 and Figure 4.17, respectively) because of a smaller value for the maximum displacement set prior to testing.

4.2.1.4 Column diameter: 15 μm

A single 15 μm column machined in the FSP Mg + Y_2O_3 was tested using microcompression testing. The Schmid factor and the loading axis are 0.33 and $[\bar{6}\,8\,\bar{2}\,19]$, respectively. The angles between the loading axis and the slip plane $(0\,0\,0\,1)$ and between the loading axis and the slip direction $[\bar{1}\,2\,\bar{1}\,0]$ are 21.93° and 68.9°. The RSS vs. true strain and the SEM micrograph of the deformed column are shown in Figure 4.23. The stress increases up to 7.86 MPa (CBSS), when a slight strain burst can be observed before unloading. However, the yield stress is estimated at 18.4 MPa (CRSS of 6.07 MPa).

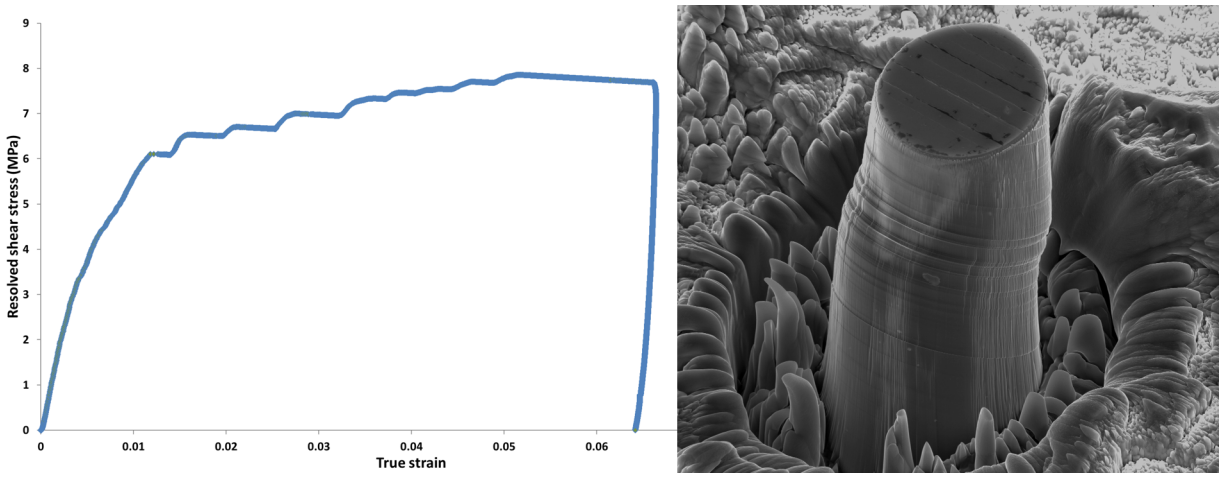

Figure 4.23 – RSS vs. true strain and SEM micrograph of a FSP Mg + Y_2O_3 (0.3 %) deformed 15 μm column favorably oriented for basal slip.

4.2.1.5 Effect of Y_2O_3 particles on basal slip

The RSS vs. true strain for all the columns favorably oriented for basal slip have shown very little strain hardening and massive strain burst was observed in most cases (especially for 2 and 5 μm columns). The critical burst shear stress (CBSS) and the critical resolved shear stress (CRSS) for activation of basal slip were estimated from RSS vs. true strain curves for different column sizes and material. Table 4.7 summarizes the CBSS and CRSS for activation of basal slip for FSP Mg and FSP Mg + Y_2O_3 for different column

sizes. The CBSS values were obtained experimentally taking the maximum value for the resolved shear stress prior to massive strain burst. In the present study, the discussion will focus only on the CBSS.

Table 4.7 – Experimentally obtained CBSS and CRSS for basal slip for different column sizes.

Material	**Critical burst shear stress (MPa)**			
	15 μm	10 μm	5 μm	2 μm
FSP Mg	-	7.53 ±0.3	14.48 ±0.48	15±1.24
FSP Mg+Y_2O_3	7.86	8.32 ±0.53	10.34 ±0.61	15.6 ±2.28
	Critical resolved shear stress (MPa)			
	15 μm	10 μm	5 μm	2 μm
FSP Mg	-	5.95±0.94	10.55±2.29	13.02±0.9
FSP Mg+Y_2O_3	6.07	7.5±0.53	9.14±1.31	14.35±3.5

Considering at first, 5 μm columns, it is noticeable that the CBSS for activation of basal slip is higher in the case of FSP Mg, when compared to the FSP Mg + Y_2O_3. One explanation can be that the nanocomposite presents a higher density of potentially mobile dislocations. The difference between the thermal expansion coefficient of the magnesium matrix and the Y_2O_3 reinforcement particles leads to the generation of geometrically necessary dislocations (GND) at the interface between the reinforcement and the matrix during cooling from higher temperatures (already explained in Section 1.4.3). These higher temperatures are achieved, in the present work, during FSP and during the thermal treatment (500°C). TEM experiments have shown a high concentration of dislocations at the interface between the magnesium and the Y_2O_3 particles (Figure 4.24). This phenomena was observed especially close to the largest particles with a mean diameter larger than 500 nm. *In situ* TEM experiments with thermal cycling have been performed in order to investigate the GND generation in the FSP Mg + Y_2O_3 and will be presented in Section 4.3.

The density of geometrically necessary dislocations generated by the difference in the coefficient of thermal expansion can be calculated using Equation 1.10. The coefficient of thermal expansion (α) of magnesium and Y_2O_3 are, respectively, 25 and 8.1 10^{-6} K^{-1}. According to the literature, the temperatures reached during FSP can vary between 60 to 95 % of the melting temperature of the matrix [162]. In the present study, the temperature was not measured. Thus, an intermediate temperature (0.75 T_{melt} of magnesium) was considered. It gives a ΔT of 392K between the FSP and the room temperature. The

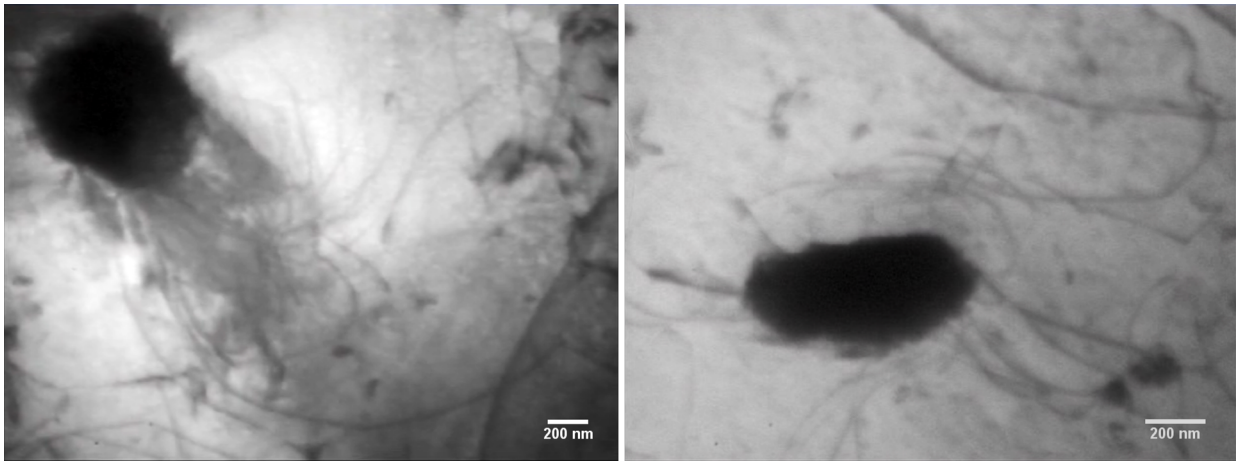

Figure 4.24 – TEM micrograph of the nanocomposite showing a higher concentration of dislocations at the interface between the Y_2O_3 particles and the magnesium matrix (LaB_6 Jeol JEM-2010 MET at 130 kV).

dislocation density introduced during FSP is then 1.9x10^{12} m^{-2}. As mentioned before, the thermal treatment can also lead to the generation of extra dislocations. The dislocation density generated during annealing heat treatment is 2.3x10^{12} m^{-2}. Table 4.8 details the parameters used for the calculations and the corresponding values of the estimated GND density (ρ) generated due to the coefficient of thermal expansion.

Table 4.8 – Contribution of coefficient of thermal expansion to GND generation in FSP Mg + Y_2O_3 (0.33%).

Contribution	$\Delta\alpha$ **(K)**	Δ**T (K)**	f_v **(%)**	d_p **(nm)**	ρ **(m^{-2})**
FSP	1.69 10^{-5}	392	0.33	430	1.9x10^{12}
Annealing treatment	1.69 10^{-5}	473	0.33	430	2.3x10^{12}
	Sum of contributions				4.22x10^{12} m^{-2}

Considering an initial dislocation density for magnesium single crystals ($\rho_\circ$) of 10^{10} m^{-2} and the GNDs generated during FSP and annealing treatment, the dislocation density in the FSP Mg + Y_2O_3 should be 4.23x10^{12} m^{-2} ($\rho_\circ$ + 4.22x10^{12} m^{-2}). In other words, the initial dislocation density is negligible and most of the dislocations present in the columns are GND induced by the Y_2O_3 particles during the FSP and the heat treatment. The real value should, however, differs from the one estimated since the annealing treatment can annihilate some dislocations generated during the FSP, but some dislocations might be trapped by the Y_2O_3 particles. Additionally, the equations used for

the calculation of the dislocation density considers a homogeneous size of particles. In reality, it is extremely difficult to obtain a nanocomposite material with an homogeneous size of reinforcement, due to clustering or particle fracture during incorporation to the matrix.

The decrease of the yield stress for activation of basal slip when a higher density of dislocations is present on the material contradicts the predictions of the continuum plasticity theory based on the Taylor hardening (Equation 1.11). Indeed, according to Taylor's model, an increase of the dislocation density in a material is accompanied by an increase of the stress needed for the dislocations to overcome the dislocation forest created from the interactions of dislocations. In the present case, the plasticity is mainly confined to parallel basal slip planes, the forest hardening is then negligible and the yield stress strongly depends on the initial mobile dislocation density.

The absence of a strong strengthening in FSP Mg + Y_2O_3 samples favorably oriented for basal slip indicates that the other strengthening mechanisms (load transfer, Orowan and Hall-Petch) described in Section 1.4 do not operate. The Hall-Petch strengthening is absent since single crystalline columns are used and the load transfer is negligible for such low amount of reinforcement (0.3 %) [92]. Considering a shear modulus of 16.5 GPa for magnesium and Equation 1.9, it is possible to obtain a contribution of 2.3 MPa from the Orowan effect in the FSP Mg + Y_2O_3. This value is almost negligible due to the large interparticle spacing (1.3 μm according to nanoholotomography). Additionally, the wide range of particle size can hinder the Orowan effect (mean diameter of 430 nm). Again, the equation that predicts the Orowan strengthening considers an homogeneous distribution of particles with almost the same size.

4.2.1.6 Effect of Y_2O_3 particles on the size dependent behavior

The CBSS values obtained from the RSS vs. true strain curves for the different columns sizes of the FSP Mg are presented in Table 4.9. A size effect can clearly be identified for FSP Mg in Table 4.9: the CBSS for 5 μm columns is much higher than the one for 10 μm columns. The size effects observed in pure magnesium micropillars have already be explained by the dislocation starvation theory [2]. At small scales, the mobile dislocations have a higher probability of annihilating at the free surfaces rather than multipling or being pinned by other dislocations [163]. When the starvation conditions are met, plasticity is accommodated by the nucleation and motion of new dislocations

Table 4.9 – Comparison between the experimentally calculated critical burst shear stress obtained in the present study and in Kim's study [2].

Material	**Critical burst shear stress (MPa)**			
	15 μm	10 μm	5 μm	2 μm
Mg [2]	-	7.8±0.25	13	23.4±2.8
FSP Mg	-	7.53±0.3	14.48±0.48	15±1.24
FSP Mg+Y_2O_3	7.86	8.32 ±0.53	10.34 ±0.61	15.6 ±2.28

instead of motion and interactions of existing dislocations.

These results obtained for FSP Mg were compared to the literature (Table 4.9): Kim [2] has studied the size effects of high purity magnesium (99.999%) using microcompression testing. According to his results, $[2\,\bar{1}\,\bar{1}\,2]$ oriented microcolumns (favorable for basal slip) have shown a strong size effect: the flow stress for 1 μm columns was four times greater than the flow stress of 10 μm columns. It is important to precise that G. S. Kim [2] has used a high purity magnesium single crystals and optimum orientations for his experiments, thus CBSS and CRSS have the same value.

The CBSS values obtained in both studies were similar for 5 and 10 μm columns (Table 4.9). A disparity was however observed for the 2 μm columns. One explanation for such disparity is the purity of the magnesium used: Kim [2] has used a 99.999% magnesium, while a 99.95% magnesium has been used in the present study. The presence of solute atoms can explain the difference in the RSS for 2 μm columns. A strain hardening of about 4 % could be observed for 10 μm column, both for FSP Mg and FSP Mg + Y_2O_3, whereas no strain hardening could be observed in high purity magnesium [2], as it can be seen in Figure 4.25.

Considering then the FSP Mg + Y_2O_3 samples, Table 4.9 shows a similar CBSS for 5, 10 and 15 μm columns indicating that the particles mitigate the size effects. One explanation is that the dislocation starvation mechanisms is not present in the nanocomposite and the plasticity is accommodated by the preexisting mobile dislocations. Plasticity is mainly confined to parallel basal slip planes, the forest hardening is negligible and the yield stress strongly depends on the initial dislocation density, which is higher in the nanocomposite. In other words, the yield stress in nanocomposites is no more related to

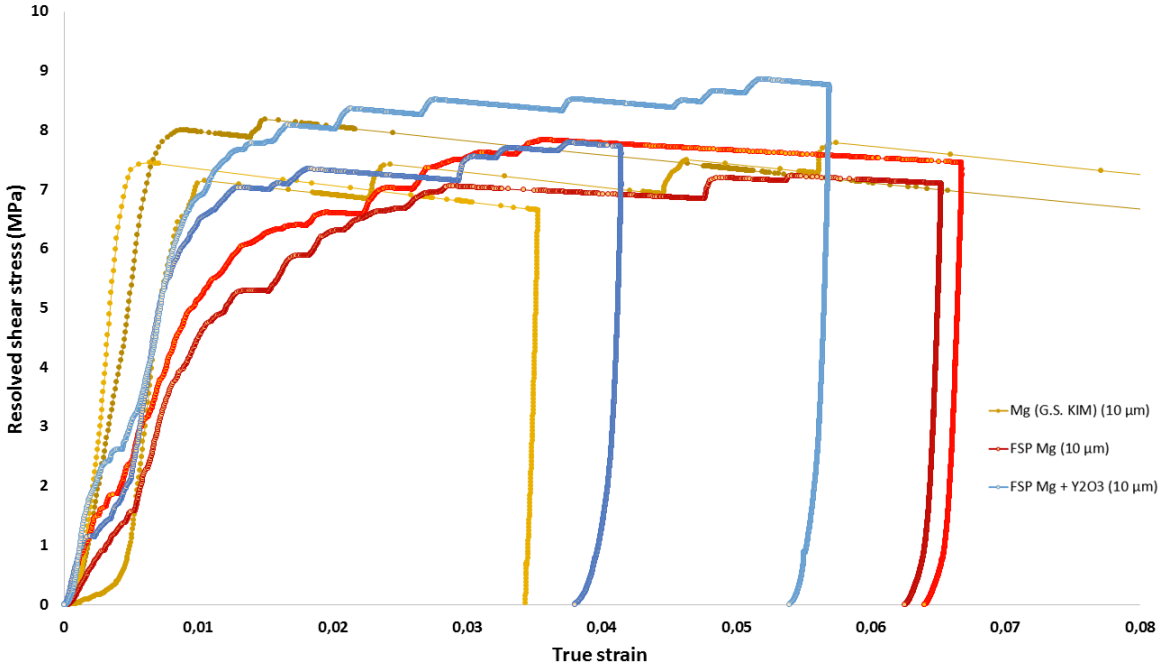

Figure 4.25 – RSS vs. true strain curves for 10 μm columns favorably oriented for basal slip evidences the strain hardening observed in the samples prepared in this study (99.95 % magnesium) in comparison to a higher purity magnesium (99.999 %) used in G. S. Kim's study [2].

the size effect but rather to the possibility to generate mobile dislocations.

The number of Y_2O_3 particles inside each FSP Mg + Y_2O_3 column can be estimated considering a volume fraction of 0.33 % and mean particle diameter of 430 nm, obtained from the nanoholotomography, and it is presented in Table 4.10. A significant number of particles is presented inside the 5, 10 and 15 μm microcolumns. However, the probability to have a comparable volume fraction of particles between two different 2 μm columns is reduced. This can explain the fact that the 2 μm columns of FSP Mg + Y_2O_3 have a plastic response comparable to FSP Mg. Additionally, the volume of a 2 μm column is smaller than the mean cluster volume of 61 μm^3, as mentioned in Section 3.3.

Table 4.10 – Estimation of the number of Y_2O_3 particles inside each column according to column size.

Column diameter	15 μm	10 μm	5 μm	2 μm
Column volume (μm^3)	$7.95x10^3$	$2.36x10^3$	$2.95x10^2$	$1.88x10^1$
Number of particles	630	187	23	1.5

To summarize, the size dependent RSS vs. true strain behavior for columns

favorably oriented for basal slip is presented in Figure 4.26. The 2 μm columns were not considered. The size effect is clearly observed in FSP Mg samples, but it is mitigated once magnesium is reinforced with Y_2O_3 particles.

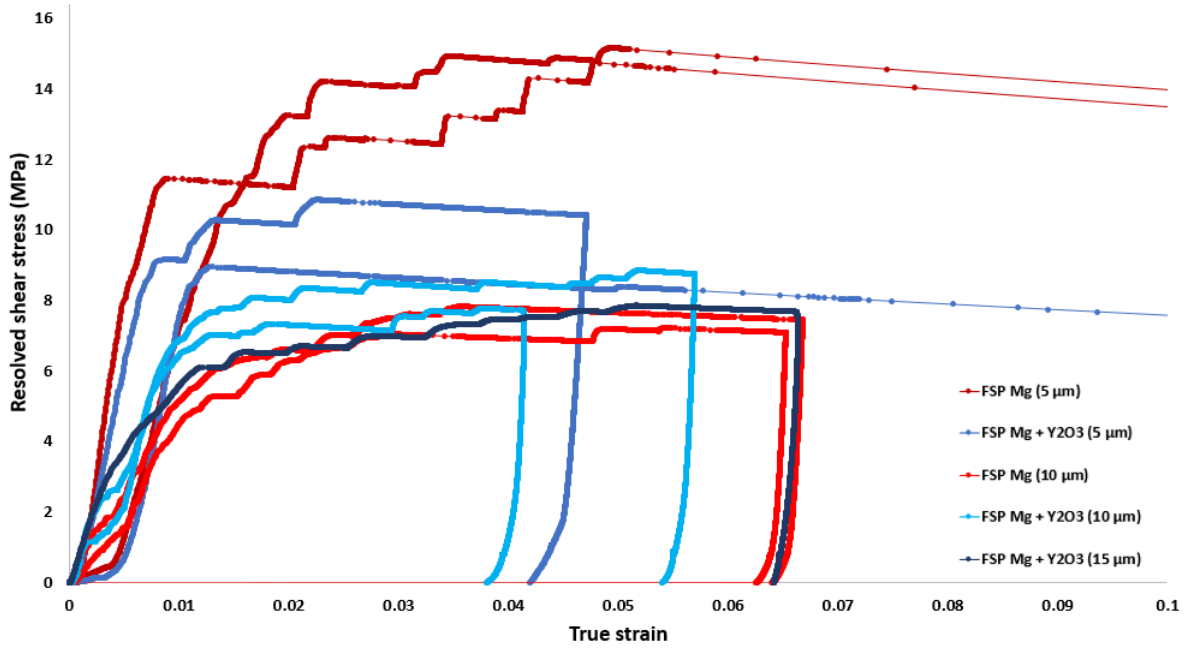

Figure 4.26 – Size dependent RSS vs. true strain behavior for columns favorably oriented for basal slip. A strong size effect is observed for pure magnesium, while no size effect is observed in the nanocomposite (FSP Mg + Y_2O_3 (0.3 %)).

4.2.2 Columns favorably oriented for twinning

Tensile twinning is activated when a tensile stress is applied along the *c*-axis or a compression stress is applied perpendicular to the *c*-axis (see Section 1.2.3). In the present study, the *c*-axis is oriented almost perpendicularly to the loading axis during microcompression testing. The Schmid factor for activation of tensile twinning for all the studied microcolumns was about 0.49. In this section, the mechanical response will be presented in terms of true stress vs. true strain and no RSS vs. true strain. Indeed, the representation of the mechanical results using a stress component resolved on a given slip or twin system is not suitable since the plastic deformation observed here is a combination of basal slip and twinning. The Schmid factor for activation of tensile twinning should first be considered until the nucleation, propagation and growth of twins. Once the twin has propagated and grown, the Schmid factor for activation of tensile twinning is no applicable due to a change in the orientation.

The mechanical behavior of microcolumns favorably oriented for tensile twinning has been studied comparing only 5 and 10 μm columns. The previous results have shown that, because of the low volume fraction of particles, the 2 μm columns of FSP Mg + Y_2O_3 behave as FSP Mg. Thus, 2 μm columns were not used for the study of tensile twinning. Additionally, 15 μm columns could not be fabricated as they require a much larger volume than the one required for 5 and 10 μm columns (see Figure 2.7). In the current case, it was not possible to find a grain large enough and with the appropriate orientation needed for the fabrication of such a microcolumn.

The mechanical response will first be presented according to column size. Then, the influence of the Y_2O_3 particles on tensile twinning will be discussed. To conclude, their influence on the size effects will be examined.

4.2.2.1 Column diameter: 5 μm

The true stress vs. true strain curves of 5 μm columns favorably oriented for tensile twinning are presented in Figure 4.27. The corresponding SEM micrographs of the deformed columns are shown in Figure 4.28. Table 4.11 details the Schmid factor and the misorientation angles with the slip plane and slip direction for each column tested. The stress increases until a first strain burst (Figure 4.29) occurs for both FSP Mg and FSP Mg + Y_2O_3. This first strain burst is related to unstable twin propagation, as it has already been mentionned by [2].

Table 4.11 – Schmid factor and orientation of each 5 μm column tested for tensile twinning (only the highest Schmid factors are indicated).

Column	**1-5**	**6-8**	**9-12**	**13-14**	**15**
Materials	Mg	Mg+Y_2O_3	Mg+Y_2O_3	Mg+Y_2O_3	Mg+Y_2O_3
Loading axis	$[\bar{3}\,35\,\overline{32}\,5]$	$[13\,\overline{15}\,2\,0]$	$[7\,\bar{8}\,1\,0]$	$[12\,\bar{1}\,\overline{11}\,0]$	$[\bar{1}\,18\,\overline{17}\,1]$
Twinning plane	$(0\,\bar{1}\,1\,2)$	$(\bar{1}\,1\,0\,2)/(1\,\bar{1}\,0\,2)$	$(\bar{1}\,1\,0\,2)/(1\,\bar{1}\,0\,2)$	$(1\,0\,\bar{1}\,2)/(\bar{1}\,0\,1\,2)$	$(0\,1\,\bar{1}\,2)$
Angle with twinning plane	39.06°	45°	47°	47°	43.8°
Twinning direction	$[0\,1\,\bar{1}\,1]$	$[1\,\bar{1}\,0\,1]/[\bar{1}\,1\,0\,1]$	$[1\,\bar{1}\,0\,1]/[\bar{1}\,1\,0\,1]$	$[\bar{1}\,0\,1\,1]/[1\,0\,\bar{1}\,1]$	$[0\,\bar{1}\,1\,1]$
Angle with twinning direction	51°	46°	43°	43°	46.3°
Schmid factor twinning	0.49	0.49	0.49	0.496	0.5
Slip plane	$(0\,0\,0\,1)$	$(0\,0\,0\,1)$	$(0\,0\,0\,1)$	$(0\,0\,0\,1)$	$(0\,0\,0\,1)$
Slip direction	$[\bar{1}\,2\,\bar{1}\,0]$	$\langle\bar{1}\,2\,\bar{1}\,0\rangle$	$\langle\bar{1}\,2\,\bar{1}\,0\rangle$	$\langle\bar{1}\,2\,\bar{1}\,0\rangle$	$[\bar{1}\,2\,\bar{1}\,0]$
Schmid factor basal slip	0.12	0	0	0	0.05

Figure 4.29 shows the early stage of the true stress vs. true strain curve. It is

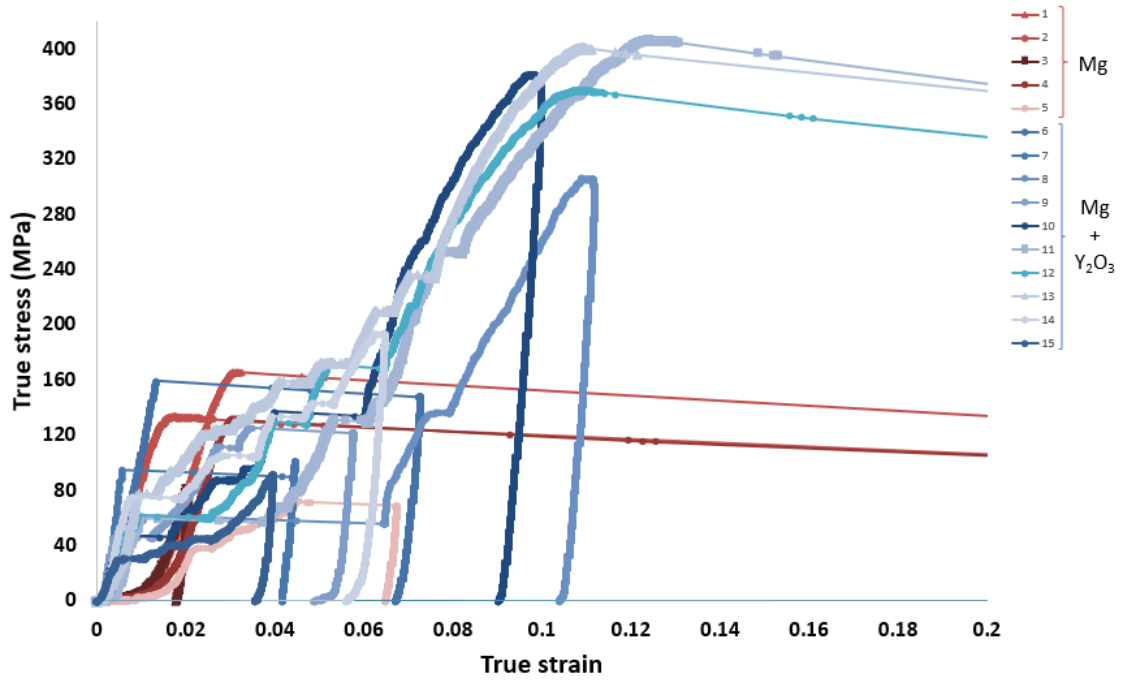

Figure 4.27 – True stress vs. true strain for 5 μm columns favorably oriented for tensile twinning. Red and blue curves correspond, respectively, to FSP Mg and FSP Mg + Y_2O_3 (0.3 %).

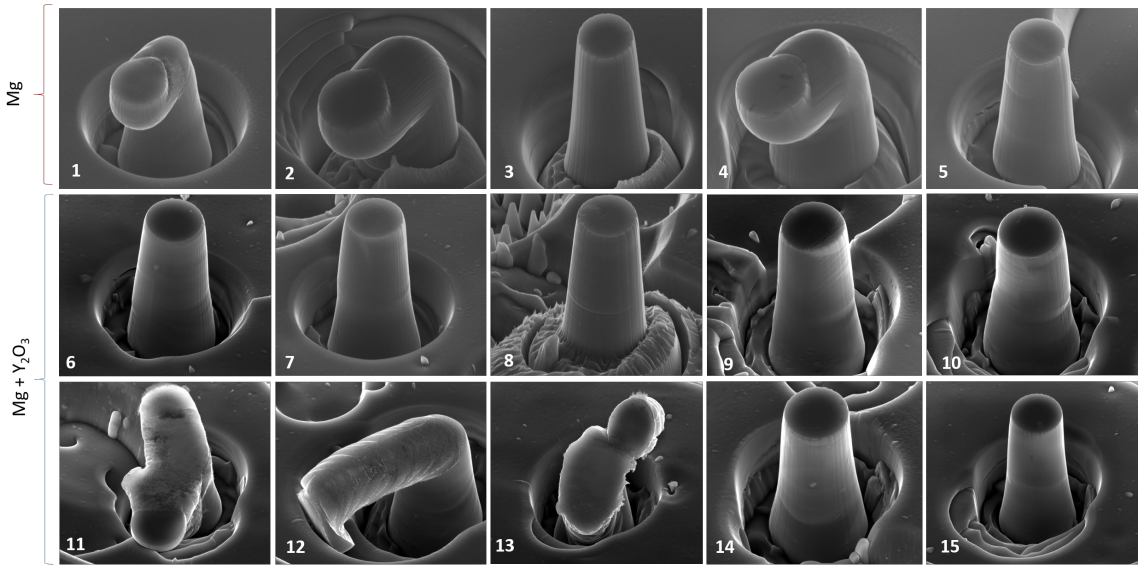

Figure 4.28 – SEM micrographs of the deformed 5 μm columns favorably oriented for twinning.

possible to notice that the twins nucleate more easily in the case of FSP Mg + Y_2O_3. The average stress for unstable twin propagation in FSP Mg and FSP Mg + Y_2O_3 are, respectively, 124.93±38.86 MPa and 75.47±34.32 MPa. The lower stress for FSP Mg + Y_2O_3 can be attributed to the presence of stress concentration close to the Y_2O_3 particles during compression, facilitating twin nucleation inside the nanocomposite.

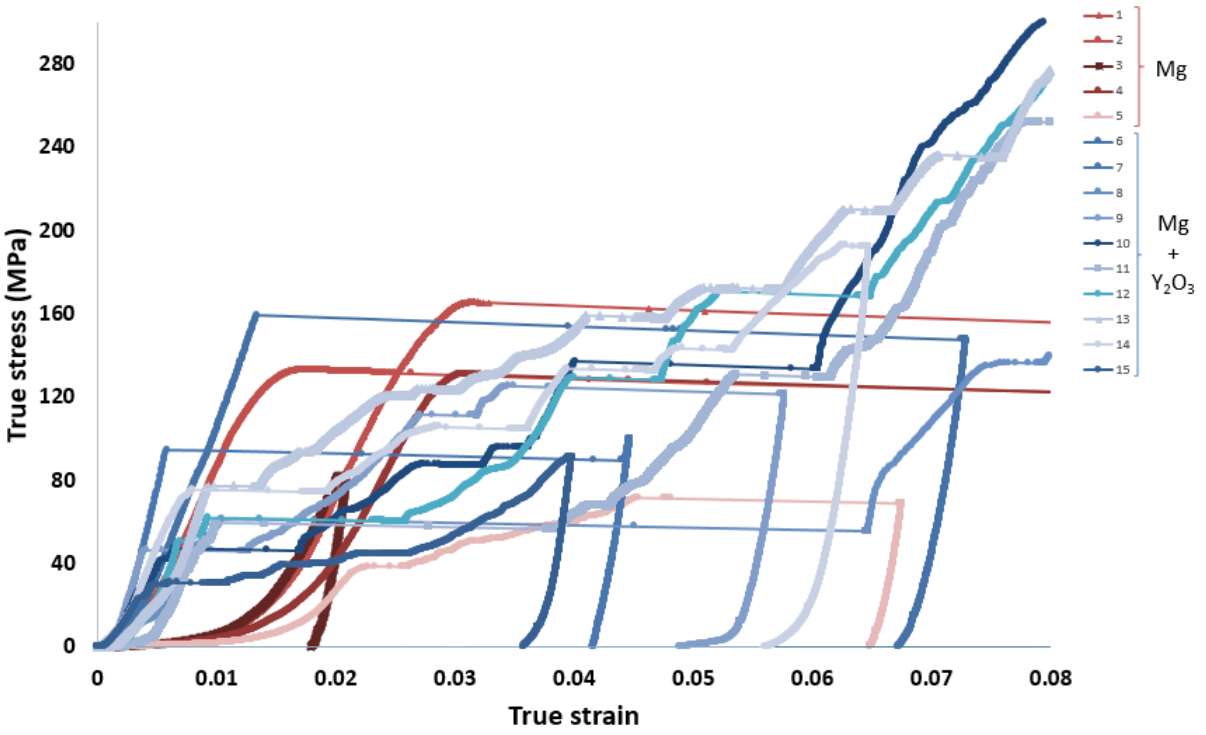

Figure 4.29 – Zoom at the early stage of deformation of the true stress vs. true strain curve from Figure 4.27 evidences that the twins nucleates easily in the FSP Mg + Y_2O_3 (0.3 %) samples (5 μm columns).

As it can be seen in Figure 4.29, unstable twin propagation occurs until a plastic strain of about 6 % for the FSP Mg + Y_2O_3 samples, a strain hardening is then observed and the applied stress increases until a second strain burst occurs at a stress close to 400 MPa (Figure 4.27). The longitudinal strain due to twinning shear can be calculated by the following expression [2]:

$$\varepsilon = f_{v,twin} m \gamma \tag{4.1}$$

where $f_{v,twin}$ is the volume fraction of the twin, m is the Schmid factor (0.49 for the studied orientations) and γ is the twinning shear for tensile twinning in magnesium (0.129 according to [45]). If the twin has propagated through the entire column, it would lead to a strain of 6.321 %. Thus, it is clear that the entire column has been twinned once the strain hardening takes place. This hardening after twinning is a consequence of the new crystal orientation after twinning. Indeed, tensile twinning promotes a reorientation of the twinned region of about 86° (see Section 1.2.3) so that the c-axis becomes almost parallel to the loading axis, which is not favorable neither for basal slip nor for twinning. For this orientation (close to [0 0 0 1] direction), the pyramidal $\pi 2$ slip system is the only slip system with a non-zero Schmid factor. This slip system has a $< c + a >$ Burgers vector. The deformation is then supposed to be accommodated by the six equivalent pyramidal

$\pi 2$ slip systems in this orientation. Deformation twinning is also a possible mechanism of deformation for this orientation [1]. However, P. G. Partridge [14] has shown that the $\pi 3$ twinning system is not easily activated during [0 0 0 1] compression of magnesium. It can be concluded that the activation and multiplication of $< c+a >$ dislocations is responsible for the strain hardening observed in the true stress vs. true strain curves (Figure 4.27).

Figure 4.27 shows a massive strain burst after hardening at a deformation of about 12 %, which appears once the applied stress overcomes the forest of dislocations. Figure 4.30 shows the SEM micrographs of column 8 (FSP Mg + Y_2O_3) and the cor-

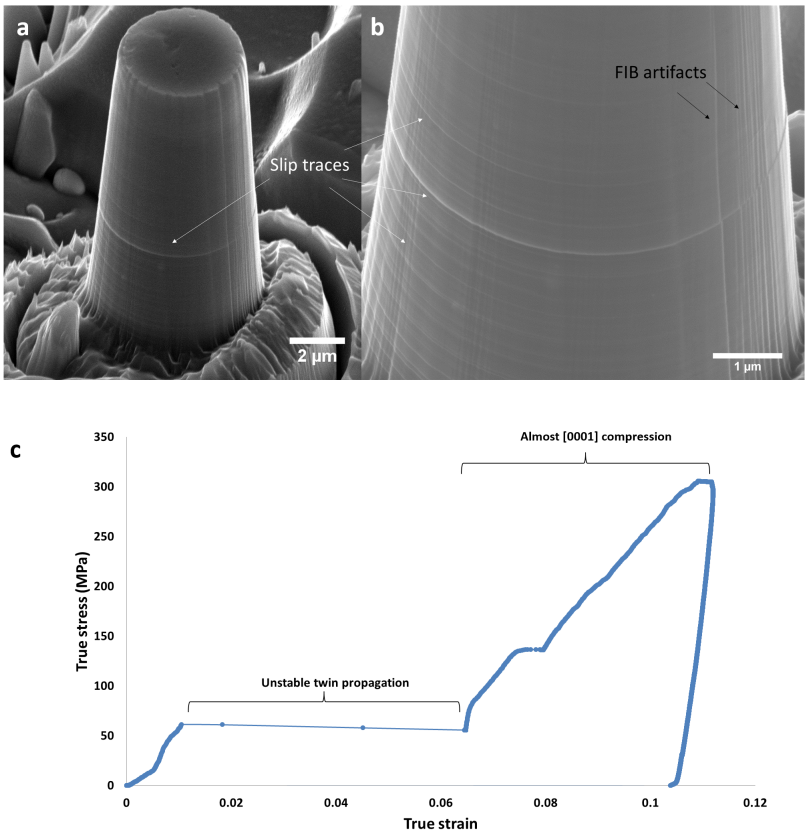

Figure 4.30 – SEM micrographs (a and b) of column 8 ((FSP Mg + Y_2O_3 (0.3%)) from Figure 4.28 evidence the slip traces (white arrows) on the surface of the microcolumn. In the twinned region, the basal plane is almost perpendicular to the loading axis. The black arrows indicate the FIB artifacts: straight lines in the same direction as the ion beam during FIB milling. True strain vs. true stress response (c): the first strain burst is due to unstable twin propagation.

responding loading curve. It is possible to observe the slip traces at the surface of the column, almost perpendicular to the loading direction. Further loading of the column would induce massive basal slip.

Twinning analysis

FIB cross sectioning followed by EBSD analysis of some deformed columns was performed in order to confirm if tensile twin has occurred and to investigate the twin morphology. The method used for cross sectioning EBSD is presented in Section 2.4.2. Figure 4.31(a) shows a SEM micrograph of the lamella extracted from column 1 (FSP Mg) in Figure 4.28. The corresponding EBSD orientation mapping is shown in Figure 4.31(b). The EBSD mapping is superposed to image quality as the grayscale component. It is possible to notice a single twin in the column. Figure 4.32 presents the misorientation profile between the parent crystal and the twin. The crystal was reoriented by 85.8° in the twinned region, which corresponds to the misorientation angle expected when tensile twinning occurs. The twin has probably nucleated at the top of the microcolumns, at the interface with the indenter due to the stress concentration below the flat punch. It is possible to observe a region that remains with the orientation of the parent crystal at the top right of the column. Massive basal slip has occurred in the twinned region of the crystal.

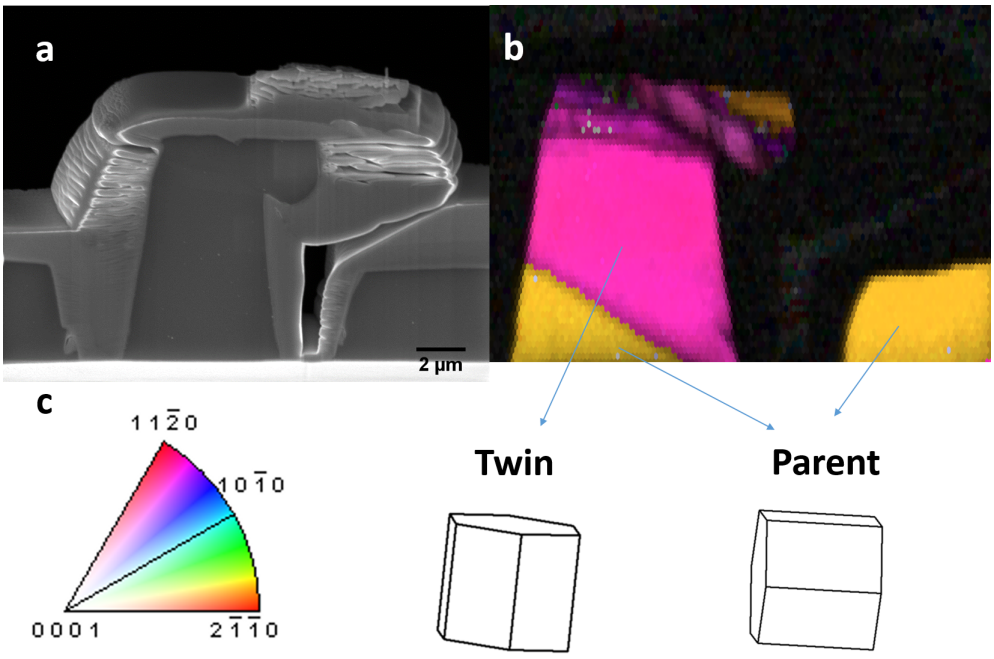

Figure 4.31 – SEM micrograph of a lamela extracted from the column 1 (FSP Mg 5 μm column) from Figure 4.28(a) and the corresponding EBSD orientation mapping (b) along with the parent and twin orientation. The color coded map is presented in (c).

It was not possible to obtain an EBSD map of the cross sectioning of a 5 μm column of FSP Mg before massive basal slip. Since the columns are single crystals, there

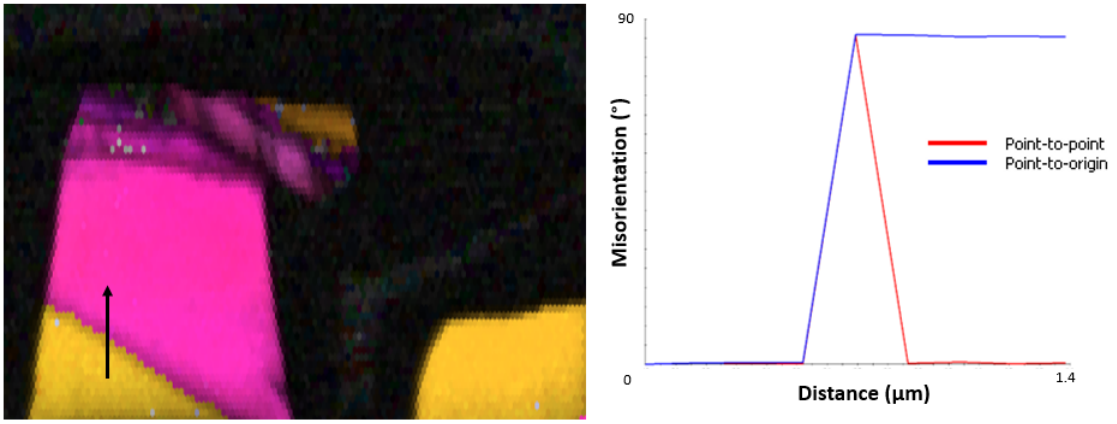

Figure 4.32 – The misorientation profile between the parent crystal and the twin (black arrow) evidences the nucleation of a tensile twin, misorientation of 85.8° (for column 1 - FSP Mg 5 μm column).

are no obstacles for twin propagation. The twin nucleates and propagates almost through the entire column and once the critical stress is reached, basal slip will be activated. The columns of FSP Mg had their test stopped either during the earliest stages of twin nucleation/propagation and most probably the twin was removed during the cross sectioning. A lamella of just 2-2,5 μm thickness is removed for the cross sectioning EBSD. It is possible that the twinned region was cut off during FIB milling (the preparation of the lamellas for cross sectioning EBSD is detailed in Section 2.4.2).

Similar characterizations of twinning activity have been performed for FSP Mg + Y_2O_3 samples. Figure 4.33(a) shows a lamella extracted from the columns 6 from Figure 4.28. The EBSD mapping given in Figure 4.33(b) indicates that almost the entire column has been twinned during compression. Again, tensile twinning has been confirmed, with a misorientation between the parent crystal and the twin of 87.6°. Additionally, Figure 4.33(c) shows an orientation deviation map, which gives the deviation from each point in the column with respect to the average orientation of the grain. This evidences a heterogeneous misorientation distribution inside the twinned zone.

Figure 4.34 presents the EBSD mapping of column 8 (FSP Mg + Y_2O_3) from Figure 4.28. Again the entire column seems to be twinned after testing, but reveals a strongly heterogeneous orientation spread, consistent with the nucleation of multiple twins of the same variant. The misorientation map from Figure 4.34(c) shows a misorientation band in the neighboring of the two Y_2O_3 particles.

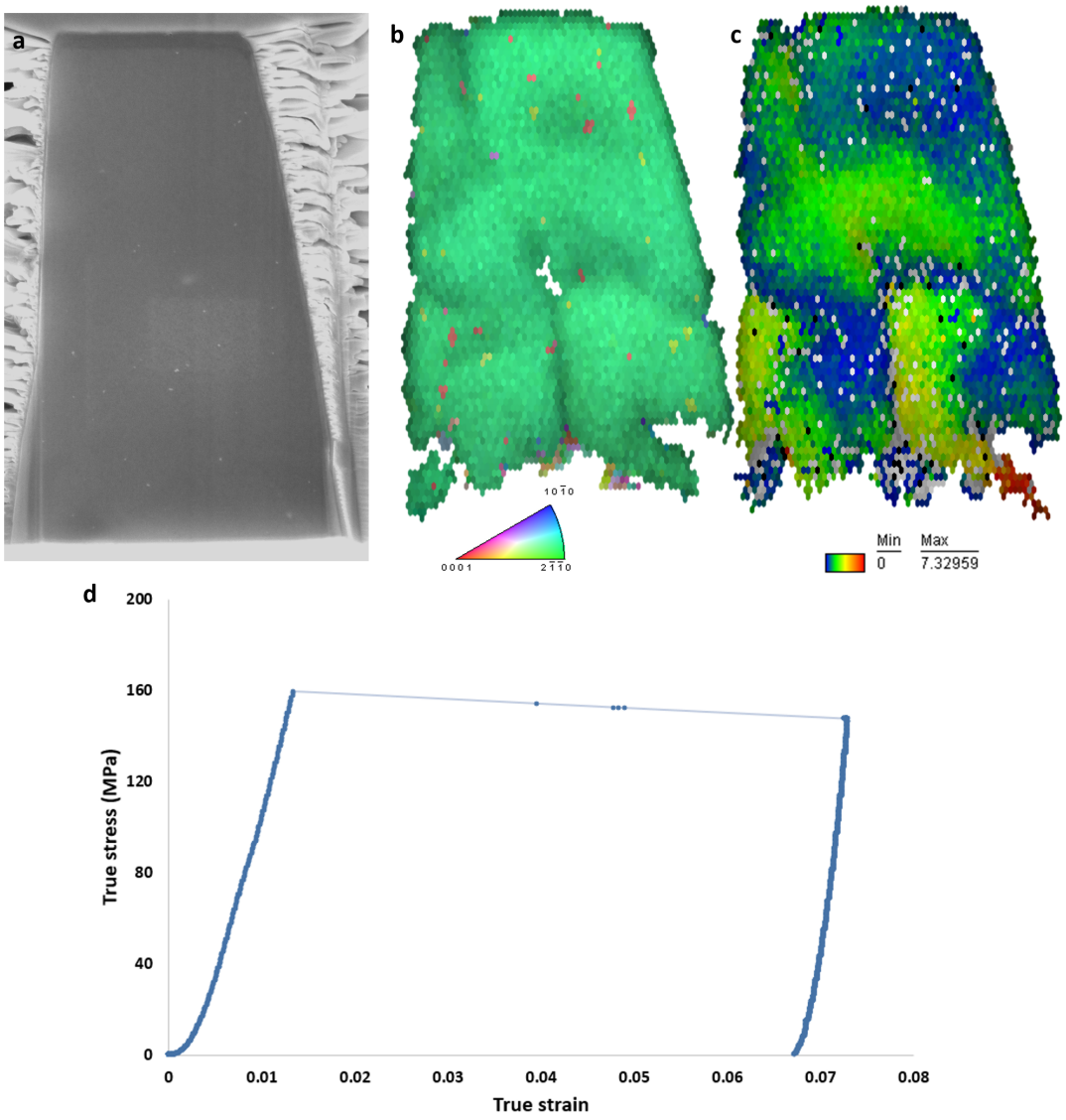

Figure 4.33 – SEM micrograph of a lamela extracted from the column 6 (FSP Mg + Y_2O_3 (0.3 %)) from Figure 4.28(a) and the corresponding EBSD orientation mapping (b), where OIM software image quality is used as grayscale component. In (c), the orientation deviation map reveals the misorientation inside the twin due to the heterogeneous microstructure of the nanocomposite. In (d), the true stress vs. true strain curve: the test has been stopped after twin propagation and before basal slip.

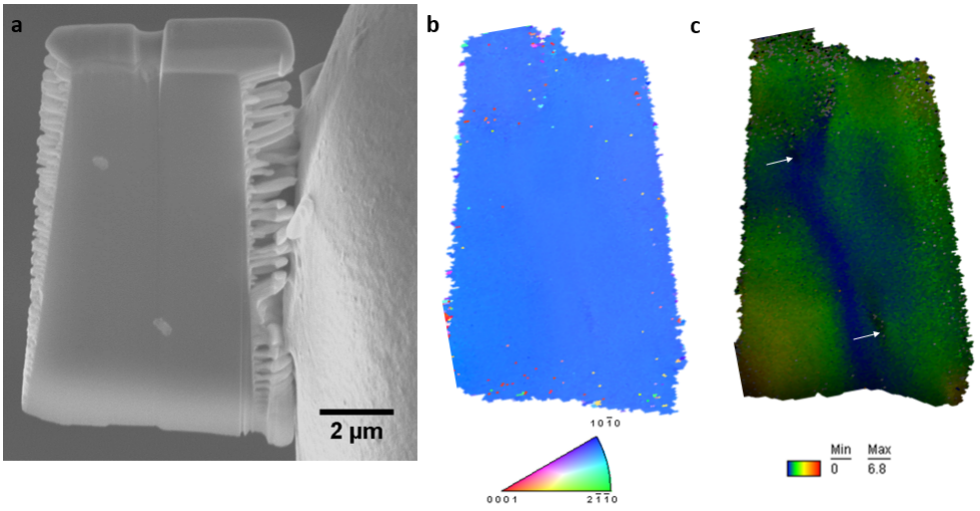

Figure 4.34 – SEM micrograph of a lamela extracted from column 8 (FSP Mg + Y_2O_3 (0.3 %)) from Figure 4.28(a) and the corresponding EBSD orientation mapping (b) showing that the entire columns has been twinned. The orientation deviation map presented in (c) put into evidence a deformation band in the neighboring of the Y_2O_3 particles (white arrows).

4.2.2.2 Column diameter: 10 μm

The plastic behavior of 10 μm columns favorably oriented for tensile twinning was also studied. The true stress vs. true strain curves of seven microcolumns are presented in Figure 4.35. The corresponding SEM micrographs of the deformed columns are shown in Figure 4.36. Table 4.12 details the Schmid factor and the misorientation angles with the slip plane and slip direction for each column tested. As previously observed for 5

Table 4.12 – Schmid factor and orientation of each 10 μm column tested for tensile twinning (only the highest Schmid factors are indicated).

Column	1-2	3	4	5	6	7
Materials	Mg	Mg	Mg+Y_2O_3	Mg+Y_2O_3	Mg+Y_2O_3	Mg+Y_2O_3
Loading axis	$[\bar{3}\,35\,\overline{32}\,5]$	$[13\,\overline{14}\,1\,1]$	$[13\,\overline{15}\,2\,0]$	$[7\,\bar{8}\,1\,0]$	$[\bar{1}\,23\,\overline{22}\,2]$	$[7\,\bar{8}\,1\,0]$
Twinning plane	$(0\,\bar{1}\,1\,2)$	$(1\,\bar{1}\,0\,2)$	$(\bar{1}\,1\,0\,2)/(1\,\bar{1}\,0\,2)$	$(\bar{1}\,1\,0\,2)/(1\,\bar{1}\,0\,2)$	$(0\,1\,\bar{1}\,2)$	$(\bar{1}\,1\,0\,2)/(1\,\bar{1}\,0\,2)$
Angle with twinning plane	39.06°	43°	45°	47°	42°	47°
Twinning direction	$[0\,1\,\bar{1}\,1]$	$[\bar{1}\,1\,0\,1]$	$[1\,\bar{1}\,0\,1]/[\bar{1}\,1\,0\,1]$	$[1\,\bar{1}\,0\,1]/[\bar{1}\,1\,0\,1]$	$[0\,\bar{1}\,1\,1]$	$[1\,\bar{1}\,0\,1]/[\bar{1}\,1\,0\,1]$
Angle with twinning direction	51°	47.2°	46°	43°	48°	43°
Schmid factor twinning	0.49	0.497	0.49	0.49	0.497	0.49
Slip plane	$(0\,0\,0\,1)$	$(0\,0\,0\,1)$	$(0\,0\,0\,1)$	$(0\,0\,0\,1)$	$(0\,0\,0\,1)$	$(0\,0\,0\,1)$
Slip direction	$[\bar{1}\,2\,\bar{1}\,0]$	$[\bar{1}\,2\,\bar{1}\,0]$	$\langle\bar{1}\,2\,\bar{1}\,0\rangle$	$\langle\bar{1}\,2\,\bar{1}\,0\rangle$	$[\bar{1}\,2\,\bar{1}\,0]/[1\,1\,\bar{2}\,0]$	$\langle\bar{1}\,2\,\bar{1}\,0\rangle$
Schmid factor basal slip	0.12	0.06	0	0	0.07	0

μm columns, the twins seems to nucleate at a lower stress level in the FSP Mg + Y_2O_3 than in FSP Mg. A strain hardening is observed after a deformation of 6 % in both FSP

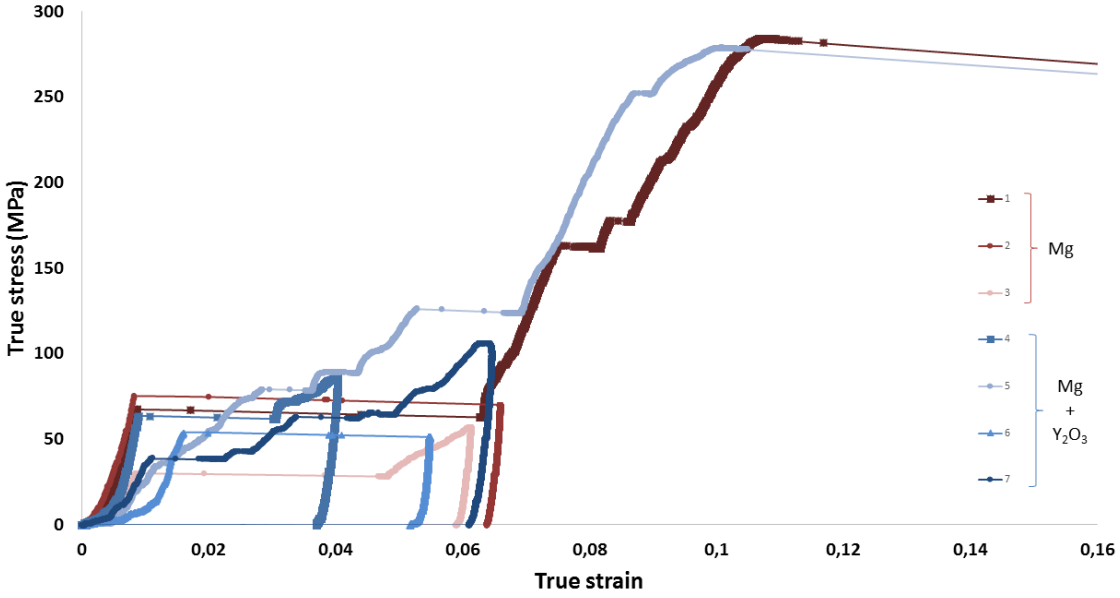

Figure 4.35 – True stress vs. true strain for 10 μm columns favorably oriented for tensile twinning. Red and blue curves correspond, respectively, to FSP Mg and FSP Mg + Y_2O_3 (0.3 %) samples.

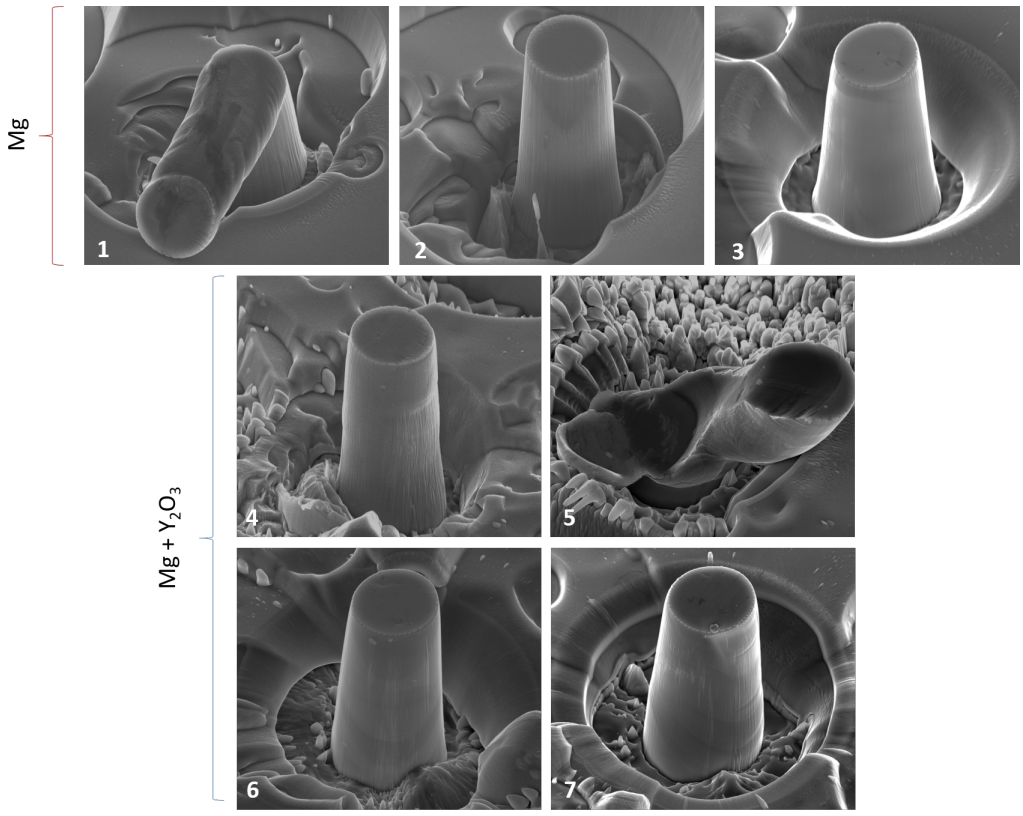

Figure 4.36 – SEM micrographs of the deformed 10 μm columns favorably oriented for twinning.

Mg and FSP Mg + Y_2O_3 followed by a massive basal slip at a stress level of 280 MPa.

Twinning analysis

Cross-sectioning EBSD of column 3 in the Figure 4.36 shows the presence of two twins in a FSP Mg column (Figure 4.37). Both twins seem to nucleate at the top of the

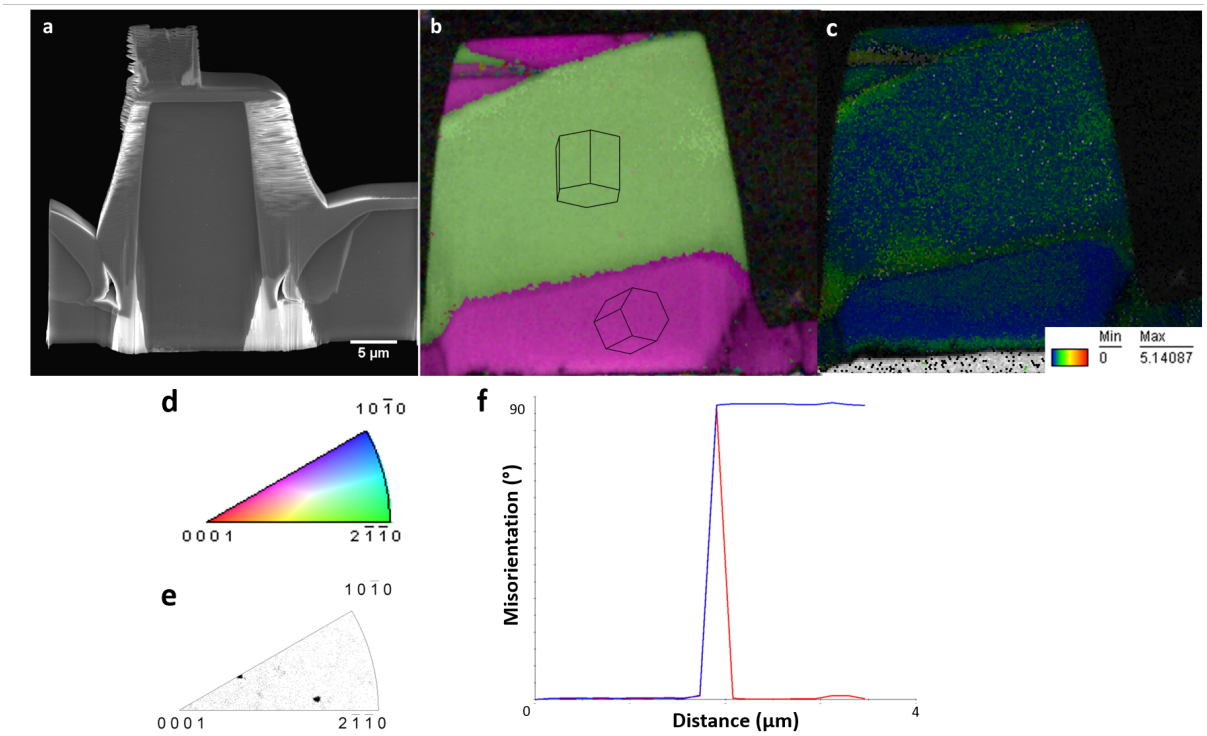

Figure 4.37 – SEM micrograph of a lamela extracted from a FSP Mg column with 10μm diameter (column 3 from Figure 4.36) (a) and the corresponding EBSD orientation mapping (b). The EBSD map is superposed to the image quality as grayscale component. The orientation deviation map (c) evidence a higher misorientation only at the twin boundary. The color coded map type and the [0 0 1] inverse pole figure for magnesium are shown in (d) and (e), respectively. The misorientation profile between the parent crystal and the twin (f) evidences a misorientation of 87.8°.

column. As it was already mentioned for columns with 5 μm diameter, twins nucleate at the stress concentration zones. In column 3, one twin seems to have stopped the other. Yu *et al.* [164] have studied the twin-twin interactions in magnesium. Their studies have shown that when one twin try to cross another and when the applied loading favors the growth of both twins, one twin cannot transmit into the other across a twin boundary. These results are in agreement with the observations of column 3 (Figure 4.37). A misorientation of 87.8° between the parent crystal and the twin is measured in Figure 4.37(e). The orientation deviation map present in Figure 4.37 (c) evidences a higher misorientation only at the twin boundary. Comparing to the 5 μm columns in Figure 4.33 for a FSP Mg

+ Y_2O_3 sample, which have shown a heterogeneous misorientation, twinning in FSP Mg is much more homogeneous.

Figure 4.38 and 4.39 show the cross sectioning EBSD of a FSP Mg + Y_2O_3 column (Column 4 from Figure 4.36). It is possible to identify the presence of several

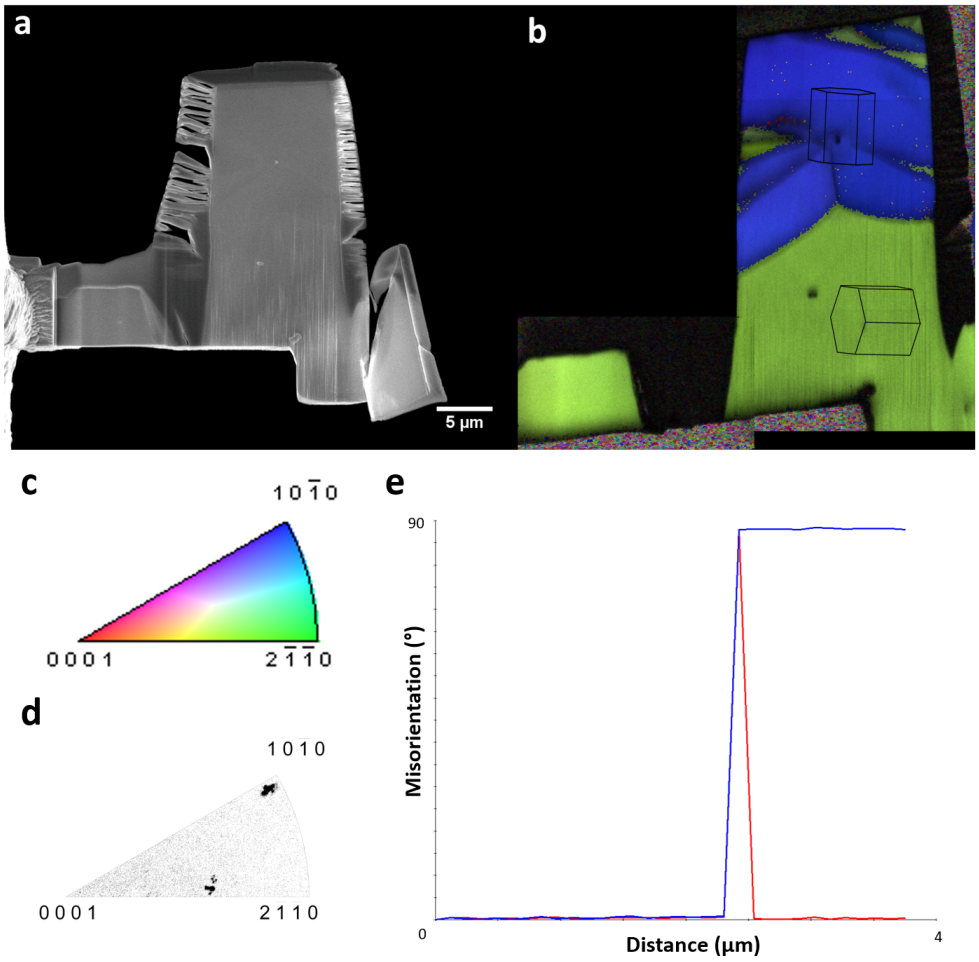

Figure 4.38 – SEM micrograph of a FSP Mg + Y_2O_3 (0.3 %) lamela extracted from column 4 (Figure 4.36 - 10 μm diameter) (a) and the corresponding EBSD orientation mapping (b). The EBSD map is superposed to the image quality as grayscale component. The color coded map type and the [0 0 1] inverse pole figure for magnesium are shown in (c) and (d), respectively. The misorientation profile between the parent crystal and the twin (e) evidences a misorientation of 88.5°.

twins. Most probably, multiple twins nucleate at the interface with the Y_2O_3 particles where the stress is concentrated. The twins will grow until they reach an obstacle (particle, another twin or the surface). Then, new twins will nucleate in order to accommodate the applied strain. A misorientation of 88.5° between the parent crystal and the twin is measured in Figure 4.38(e).

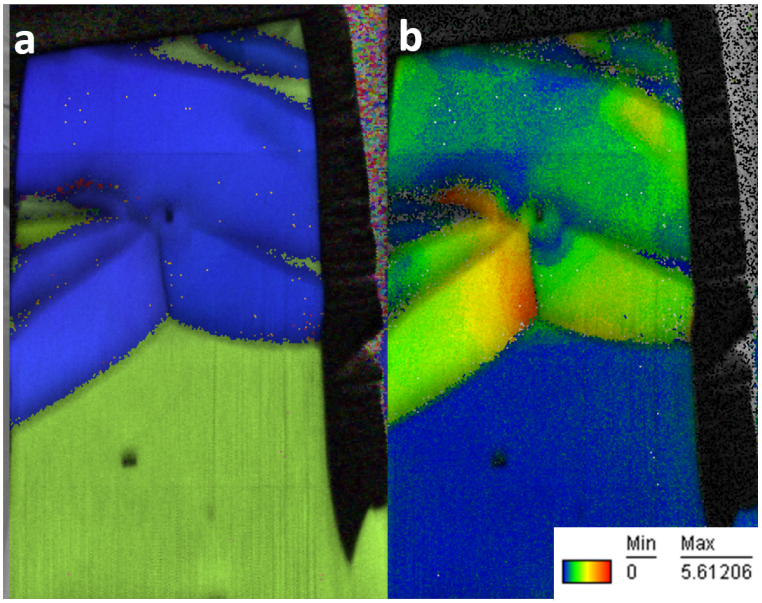

Figure 4.39 – Cross-sectioning EBSD of a FSP Mg + Y_2O_3 (0.3 %) column (column 4 from Figure 4.36 - 10 μm diameter) (a), using OIM software confidence index as grayscale component. The orientation deviation map (b) evidence a heterogeneous misorientation inside the twinned region.

4.2.2.3 Effect of Y_2O_3 particles on tensile twinning

The true stress vs. true strain curves for both FSP Mg and FSP Mg + Y_2O_3 have shown a first strain burst that is related to the unstable twin propagation. The stress required for twin propagation is lower in the FSP Mg + Y_2O_3 since the heterogeneous microstructure will generate stress concentrations close to the Y_2O_3 particles.

The cross-sectioning EBSD have evidenced the nucleation of the twins at the top of the column for FSP Mg samples. This behavior is expected due to the stress concentration between the indenter tip and the column. A maximum of two twins have been observed per column. FSP Mg + Y_2O_3 samples behave differently and multiple twins seems to have nucleated at the interface with the Y_2O_3 particles (Figure 4.38). The particles seems to affect the deformation mechanisms taking place at columns favorably oriented for tensile twinning. The twin nucleation stress and morphology are affected by the presence of Y_2O_3 particles.

The orientation deviation map from the EBSD orientation mapping have shown a higher misorientation concentrated at the twin boundary in FSP Mg (Figure 4.37 (c)). However, a much more heterogeneous distribution of the misorientation has been observed

in FSP Mg + Y_2O_3 samples. Even when the column has been entirely twinned (example in Figure 4.33 and Figure 4.34), a misorientation distribution can be observed especially close to the Y_2O_3 particles. As an example, Figure 4.33 (d) shows the true stress vs. true strain curve of a 5 μm FSP Mg + Y_2O_3 column. The test has been stopped just after twin propagation and a misorientation distribution is observed as seen in Figure 4.33. It indicates that this misorientation is not related to the strain hardening stage, when further loading is applied on the twinned region, but most probably to the presence of multiple twins.

The presence of multiple twins in the FSP Mg + Y_2O_3 can also be correlated to the true stress vs. true strain curve, which shows multiple strain bursts. The twin will propagate until it finds an obstacle (typically a Y_2O_3 particle or another twin). Then, the stress increases until another twin nucleates and again stops. The multiple steps observed on the curve correspond to the twins propagation. Figure 4.40 shows the true stress vs. true strain curve for a 10 μm FSP Mg + Y_2O_3 column and the corresponding cross-sectioning EBSD (image quality gives the grayscale component).

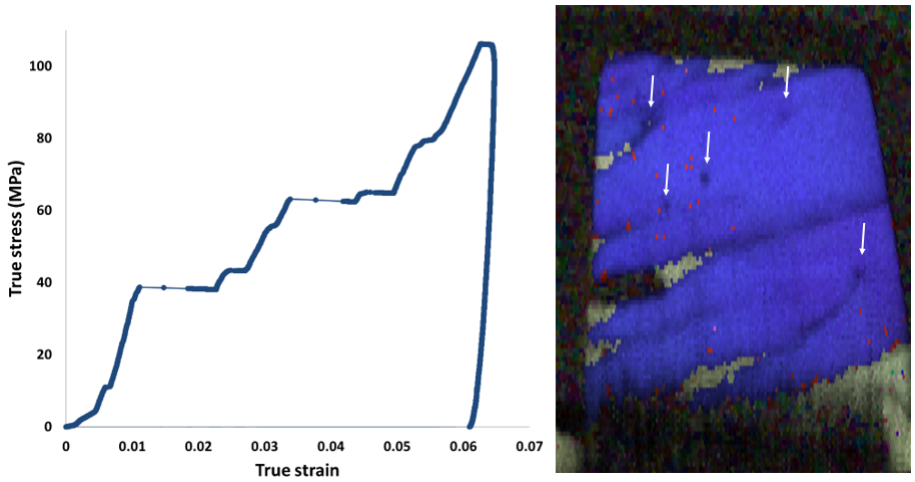

Figure 4.40 – True stress vs. true strain curve for a 10 μm FSP Mg + Y_2O_3 (0.3 %) column and the corresponding cross-sectioning EBSD (OIM software image quality gives the grayscale component). The multiple steps observed on the curve are related to the multiple twins nucleated inside the column. The white arrows indicate the Y_2O_3 particles.

4.2.2.4 Size dependent behavior

Figures 4.27 and 4.35 show the true stress vs. true strain response for all the columns tested for tensile twinning. Table 4.13 summarizes all the information

Table 4.13 – Summary of the orientation of each column tested for tensile twinning and the corresponding stresses obtained from the true stress vs. true strain curves.

5 µm column

Column	1	2	3	4	5	6	7	8	9	10	11	12	13	14	15
Material	Mg					$Mg+Y_2O_3$									
Initial orientation of the compression axis (t_{parent})	[-3 35 -32 -5]					[13 -15 2 0]			[7 -8 1 0]			[12 -1 -11 0]		[-1 1 8 -17 1]	
Schmid factor (twinning)	0.49	0.49	0.49	0.49	0.49	0.49	0.49	0.49	0.49	0.49	0.49	0.49	0.496	0.496	0.5
Schmid factor (basal slip)	0.12	0.12	0.12	0.12	0.12	0	0	0	0	0	0	0	0	0	0.05
True stress (first burst) (MPa)	165	133		130	71.7	157.4	94.68	60.61	46.4	46.3	60	62	76.8	75	
RSS (twinning) (MPa)	80.85	65.17	No burst	63.70	35.13	77.13	46.39	29.70	22.74	22.69	29.40	30.38	38.09	37.20	No burst
RSS (basal slip) (MPa)	19.8	15.96		15.6	8.604	0	0	0	0	0	0	0	0	0	
Angle t_{parent} with [0001] (°)	82.1	82.1	82.1	82.1	82.1	89.99	89.99	89.99	89.99	89.99	89.99	89.99	89.99	89.99	86.93
Angle t_{twin} with [0001] (°)	3.9	3.9	3.9	3.9	3.9	3.99	3.99	3.99	3.99	3.99	3.99	3.99	3.99	3.99	3.99
SS (basal slip) (MPa) in the tw	11.20	9.03		8.82	4.87	10.93	6.57	4.21	3.22	3.21	4.16	4.30	5.33	5.21	

10 µm column

Column	1	2	3	4	5	6	7
Material	Mg	Mg	Mg	$Mg+Y_2O_3$	$Mg+Y_2O_3$	$Mg+Y_2O_3$	$Mg+Y_2O_3$
Initial orientation of the compression axis (t_{parent})	[-3 35 -32 -5]		[13 -14 1 1]	[13 -15 2 0]	[7 -8 1 0]	[-1 23 -22 2]	[7 -8 1 0]
Schmid factor (twinning)	0.49	0.49	0.497	0.49	0.49	0.497	0.49
Schmid factor (basal slip)	0.12	0.12	0.06	0	0	0.07	0
True stress (first burst) (MPa)	64.5	72.89	28.75	63.64	79.21	53.03	38.28
RSS (twinning) (MPa)	31.61	35.72	14.29	31.18	38.81	26.36	18.76
RSS (basal slip) (MPa)	7.74	8.7468	1.725	0	0	3.7121	0
Angle t_{parent} with [0001] (°)	82.1	82.1	86	89.99	89.99	85.23	89.99
Angle t_{twin} with [0001] (°)	3.9	3.9	0	3.99	3.99	0.77	3.99
RSS (basal slip) (MPa) in the twin	4.38	4.95	0.00	4.42	5.50	0.71	2.66

obtained from the curves and the orientation of each columns tested for tensile twinning, including initial orientation, the corresponding Schmid factors and misalignment.

Table 4.14 shows the RSS for unstable twinning propagation during the first strain burst. A strong size effect is observed in FSP Mg: a factor two is observed between 5 and 10 μm columns. With the addition of the Y_2O_3 particles, this size effect is strongly reduced similarly to what has been observed for columns favorably oriented for basal slip.

Table 4.14 – Mean resolved shear stress for twinning during the first strain burst.

Material	**Resolved shear stress for twinning (MPa)**	
	10 μm	5 μm
FSP Mg	27.21±8.61	61.21±13.04
FSP Mg+Y_2O_3 (0.3 %)	28.78±6.22	37.08±16.82

Deformation mechanisms after twinning

After a first massive strain burst, a strain hardening has been observed for both FSP Mg (10 μm columns) and FSP Mg + Y_2O_3 (5 and 10 μm columns). This strain hardening is compatible with a compression direction aligned to the *c*-axis. As mentioned, the *c*-axis in the twinned region is almost parallel to the loading axis once tensile twinning has occurred. This hardening stage corresponds to the activation of the pyramidal slip systems, which generate a large amount of forest dislocations that limit the basal glide.

In the case of the 5 and 10 μm columns of FSP Mg, the different shape for the true stress vs. true strain curve indicates a different mechanism (Figure 4.41):

- 5 μm columns have shown a single strain burst at a stress level of 124.93±38.86 MPa. As already mentioned, if the entire column has been twinned it would lead to an axial compression strain of 6.321%. Since the true strain observed is superior to 12%, twinning alone could not accommodate the entire cumulated strain. Thus, basal slip has also occurred and this is consistent with the SEM micrographs of the deformed columns, where massive basal slip can clearly be observed (Figure 4.28).
- 10 μm columns have shown a first strain burst of about 6% amplitude at a stress level

of 56.7±25.1 MPa. This amount of plastic strain indicates that the entire column has been twinned after the initial strain burst. Then, another plastic mechanism takes place, corresponding to the hardening stage observed on the curve. Basal dislocations are finally activated when the compression stress level reaches 282 MPa. Note that the hardening related to the activation of pyramidal slip system has been observed for 2 columns (1 and 3) and that it is a common behavior observed in the case of compression direction aligned with the c vector [2].

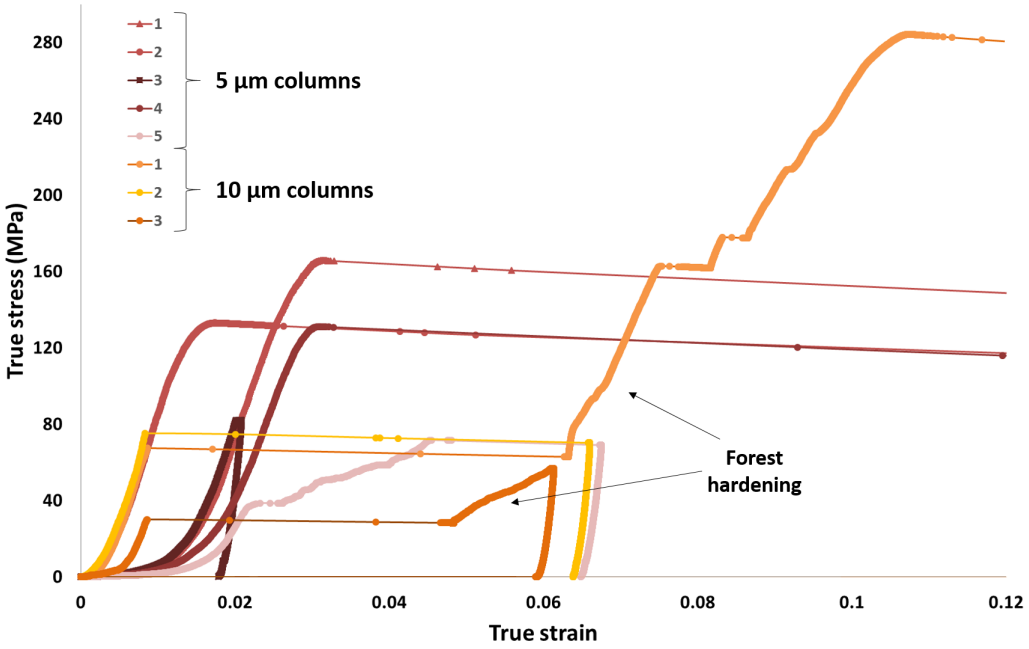

Figure 4.41 – True stress vs. true strain curve comparing 5 and 10 μm FSP Mg columns.

Thus, in order to explain this different behavior, it is necessary to discuss the orientation of the column. Although, attention has been made in order to fabricate microcolumns with an orientation as close to the $[1\,0\,\bar{1}\,0]$ as possible, some misalignment is unavoidable when working with polycrystalline materials. Table 4.13 shows that the Schmid factor for basal slip is non zero at the initial orientation for FSP Mg columns. It means that tensile twinning and basal slip are competing at the beginning of the test.

The resolved shear stress on the basal plane when the first strain burst occurs (Table 4.13) can be compared to the CBSS values from Table 4.7:

- In **5 μm columns:** the RSS on the basal plane for columns 1, 2 and 4 are superior to the CBSS value from Table 4.7 (14.48 MPa) and thus, basal slip should be activated.

However, Figure 4.31 shows that twinning has occurred. Basal slip has probably occurred only after twinning.

- In **10 μm columns:** the RSS on the basal plane for columns 1 and 2 are also superior to the CBSS value from Table 4.7 (7.53 MPa) and again basal slip should be activated. Similarly to the 5 μm columns, tensile twinned has been confirmed, in this case by the subsequent hardening stage (column 1) that can only be related to the activation of pyramidal slip and by the absence of slip steps on the surface of column 2.

This behavior can be explained by the fact that twinning has already occurred at the beginning of the test even before the first burst, which is related only to the unstable twin propagation. The twinned zone developed inside the column can already influence the basal slip even if it is occupying only a small fraction of the microcolumn.

Based on the assumption that twinning starts first, once it occurs, Table 4.13 shows that the c-axis is not completely aligned with the [0 0 0 1] direction in the twinned region of the column: a misalignement close to 3.9° is observed. The resolved shear stress on the basal plane in the twinned region can be estimated using the misalignement angle (α) and the applied stress by the following equation [2]:

$$RSS = \sigma cos\alpha cos(90 - \alpha) \tag{4.2}$$

which can be simplified as

$$RSS = \frac{\sigma sin(2\alpha)}{2} \tag{4.3}$$

Using Equation 4.3, it is possible to estimate the resolved shear stress on the basal plane when the first burst occurs. These results are presented in Table 4.13 and show that massive basal slip has been activated in the 5 μm columns when the RSS for basal slip was superior to 8.82 MPa. Due to the size effect, the RSS for basal slip in the 10 μm columns are much lower (around 4.5-5 MPa) and massive basal slip does not occurs. It is important to precise that it is not possible to compare the RSS for basal slip in the twinned region to the critical values obtained from the experiments performed on columns favorably oriented for basal slip (Section 4.2.1) because the dislocation structure is completely different once twinning has occurred. This was evidenced by G. S. Kim [2], who has shown a dislocation microstructure during massive basal slip within the twin that is completely different to the one observed in the case of $[2\,\bar{1}\,\bar{1}\,2]$ compression (Schmid

factor for basal slip 0.45). It is also known that twinning has the potential to increase the density of potentially mobile dislocations, however, it is still unclear if it would lead to a hardening of softening of the material. The current results would indicate a softening, but further tests should be performed for confirmation.

The same does not occurs for 5 μm columns of FSP Mg + Y_2O_3. The Schmid factor for basal slip at the initial orientation of the crystal is almost zero for all columns.

Deformation mechanism after strain hardening

After strain hardening, a massive basal slip is observed once the shear stress for basal slip overcome the strength corresponding to the forest dislocations developed on the pyramidal systems. The stress values reached in 5 μm column are close to 400 MPa (for the FSP Mg + Y_2O_3 samples only). For 10 μm columns, the stress levels are similar for FSP Mg and FSP Mg + Y_2O_3: 280 MPa. The resolved shear stress on the basal plane in the twinned region has been calculated when the second strain burst occurs (Table 4.15). These values are much higher than the ones obtained for the CBSS (Table 4.7) when basal slip operates alone.

Table 4.15 – Resolved shear stress on the basal plane in the twinning during second strain burst.

Column	**11**	**12**	**13**	**1**	**5**
Material	Mg+Y_2O_3	Mg+Y_2O_3	Mg+Y_2O_3	Mg	Mg+Y_2O_3
Column size	5 μm	5 μm	5 μm	10 μm	10 μm
True stress (second burst) (MPa)	405.6	370.17	400.51	283.74	278.63
Angle t_{twin} with [0 0 0 1] (°)	3.99	3.99	3.99	3.9	3.99
RSS (basal slip)(MPa) in the twin	28.15	25.69	27.8	19.25	19.34

Interestingly, a size effect can clearly be observed for FSP Mg + Y_2O_3. Such size effect during uniaxial microcompression along the *c*-axis of pure magnesium single crystals has already been observed using microcompression testing [1, 2]. Both studies have shown a clear size effect for pure magnesium. Kim's studies [2] have shown massive basal slip for stress values of 495 MPa (5 μm columns) and 417 MPa (10 μm columns). In the present case, it is not possible to observe this size effect in the FSP Mg samples, since no hardening has been observed for the 5 μm columns. Figure 4.42 compares the results

from the literature [2] and evidences the size dependent behavior of FSP Mg + Y_2O_3 samples once the twin has propagated and grown. The discrepancy between the values obtained by G. S. Kim and the present study comes from the misalignment between the c-axis and the loading axis. In the present case, a misalignment of about 3.9° (Table 4.13) is responsible for the lower stress values obtained for activation of basal slip.

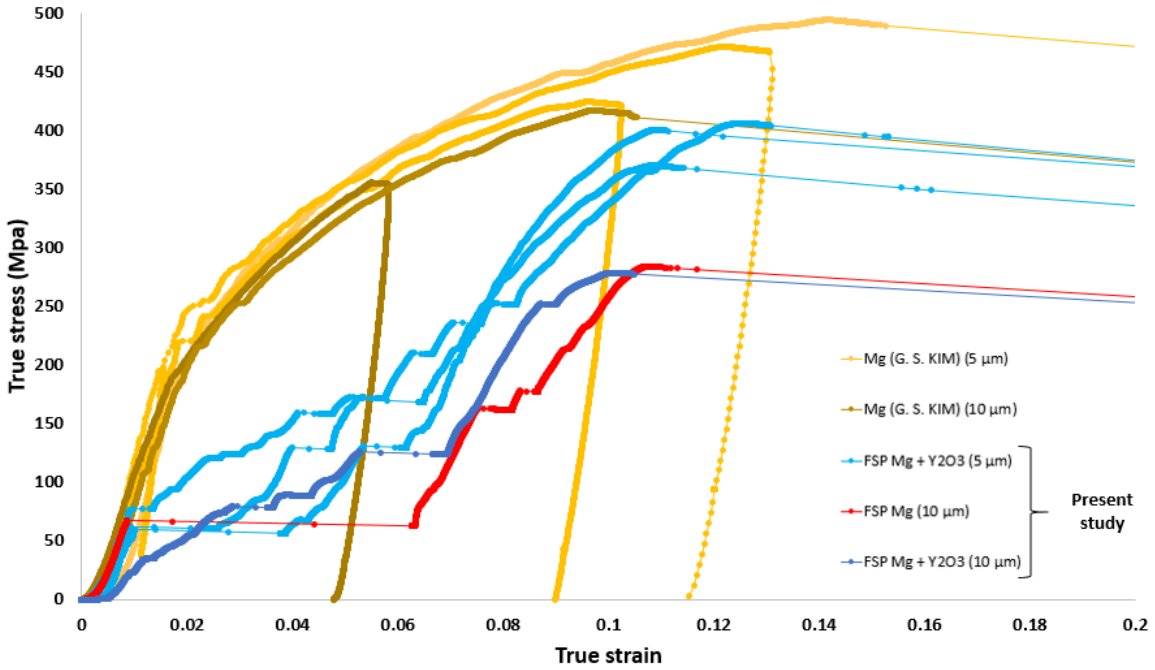

Figure 4.42 – Size dependent true stress vs. true strain response of FSP samples favorably oriented for tensile twinning in comparison with high purity magnesium [2] compressed along [0 0 0 1] direction. Once the twin has propagated and grown, strain hardening is similar to the case of [0 0 0 1] compression. A size effect is clearly observed for the second strain burst.

In the previous section (Section 4.2.1), it was mentioned that the addition of Y_2O_3 particles had mitigated the size effect observed in FSP Mg when basal slip is the active deformation mode. The reason was that the yield stress was no more related to the size effect but rather to the possibility to generate mobile dislocations. In the present case, the activation and multiplication of $< c + a >$ dislocations during hardening lead to an increase of the critical stress for basal slip. These $< c + a >$ dislocations will interact with the initial dislocations present in the material (especially in FSP Mg + Y_2O_3). Wang *et al.* [165] have studied the interactions between dislocations and twin in magnesium AZ31 alloys. They have shown a high density of $< c + a >$ dislocations inside the tensile twins. These $< c + a >$ dislocations have shorter length aligned with the $< a >$ direction and a longer non-rectilinear segments on the non-basal planes [165]. These $< c + a >$ dislocations will interact with the preexisting dislocations and increase

the dislocation interaction (dislocation forest). As a consequence, the strengthening of the material due to the interaction of dislocations (forest hardening) applies and the size effect reappears. The effect of the Y_2O_3 particles and the twin boundaries becomes negligible and the strengthening is mainly controlled by the forest dislocations. Behavior of FSP Mg + Y_2O_3 and FSP Mg are then similar.

In summary, the Y_2O_3 particles have changed the mechanisms of plastic deformation (multiple twinning) and reduced the size effects normally observed in magnesium during twinning. However, these size effects reappear once forest hardening becomes too important and the effect of the particles is negligible.

4.2.3 Comparison between basal slip and twinning

Figure 4.43 summarizes the results obtained during microcompression testing.

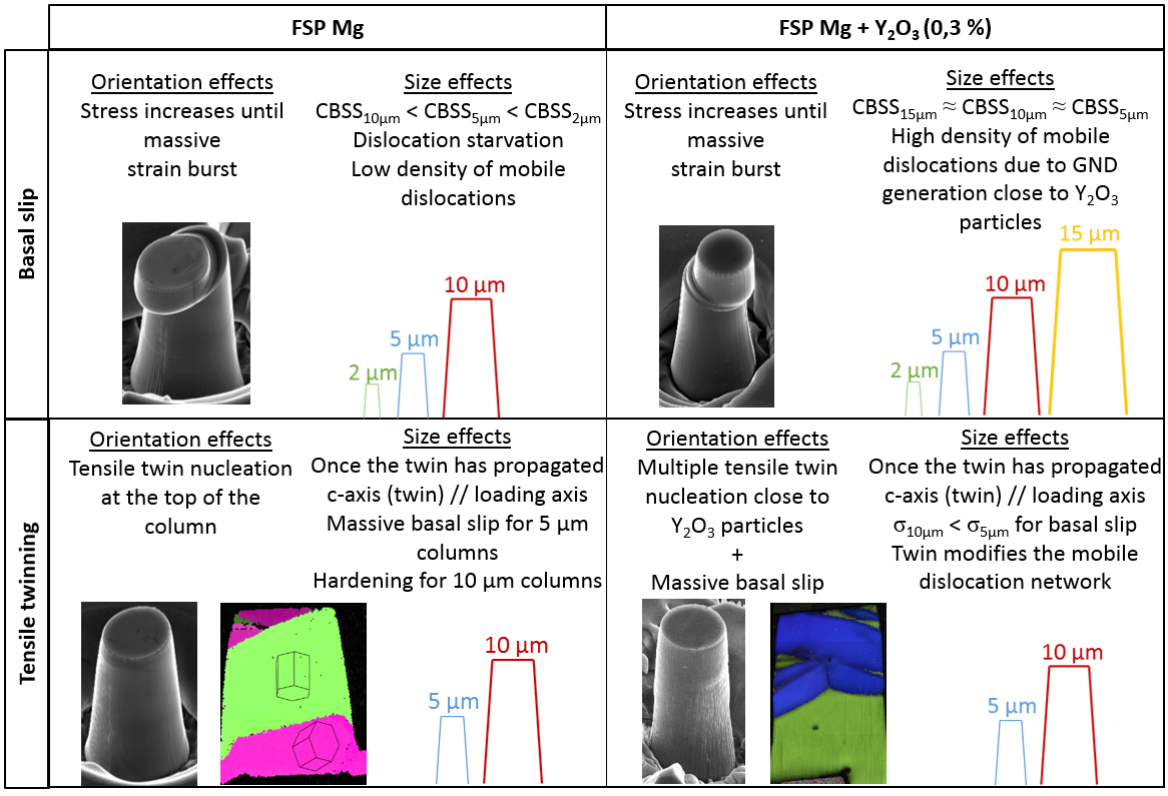

Figure 4.43 – Summary of the results obtained during microcompression testing of columns favorably oriented for basal slip and tensile twinning and a comparison between pure magnesium and the nanocomposite.

It is difficult to clearly identify a strengthening effect of the particles at small scale, espe-

cially when such a low volume fraction of particles (0.3 %) is present in the nanocomposite. Differently from the strengthening observed macroscopically, no clear strengthening effect is observed in microcolumns when dislocation glides operates. Indeed, the Y_2O_3 particles mitigate the size effects commonly observed when performing small scale mechanical testing on magnesium. The Y_2O_3 particles seem to affect the twin nucleation stress: twins nucleate much easily in the FSP Mg + Y_2O_3 samples due to the stress concentration close to the particles. The twin morphology is also modified for orientations favorable for tensile twinning with the presence of multiple twins that seem to be nucleated at the interface with the Y_2O_3 particles. The size effects usually observed for orientations favorable for twinning were also reduced.

4.3 *In situ* transmission electron microscope

In nanocomposites, reinforcement particles play three major roles:

(a) they pin grain boundaries and induce Hall-Petch strengthening,

(b) they act as obstacles for dislocations and induce Orowan strengthening,

(c) they increase the total dislocation density by generating GNDs.

In situ TEM experiments using thermal cycling and tensile testing were performed in order to investigate these possible strengthening mechanisms (b and c) in FSP Mg + Y_2O_3 (2.11 %) samples. No annealing heat treatment has been performed on the nanocomposite used for the *in situ* tests. TEM lamellas have been sampled at 1 mm depth from the top surface in normal sections of the stirred zone and prepared using electropolishing (further details in Section 2.5.1). The *in situ* TEM experiments have been performed at CEMES laboratory within the METSA network by Frédéric Mompiou.

4.3.1 Orowan strengthening

In situ TEM tensile testing and thermal cycling have been performed in order to observe a possible interaction between the Y_2O_3 particles and the dislocations in the FSP Mg + Y_2O_3 samples. The Orowan strengthening has already been presented in Section 1.4.2.

Figure 4.44 shows different steps during the thermal cycling of one FSP Mg +

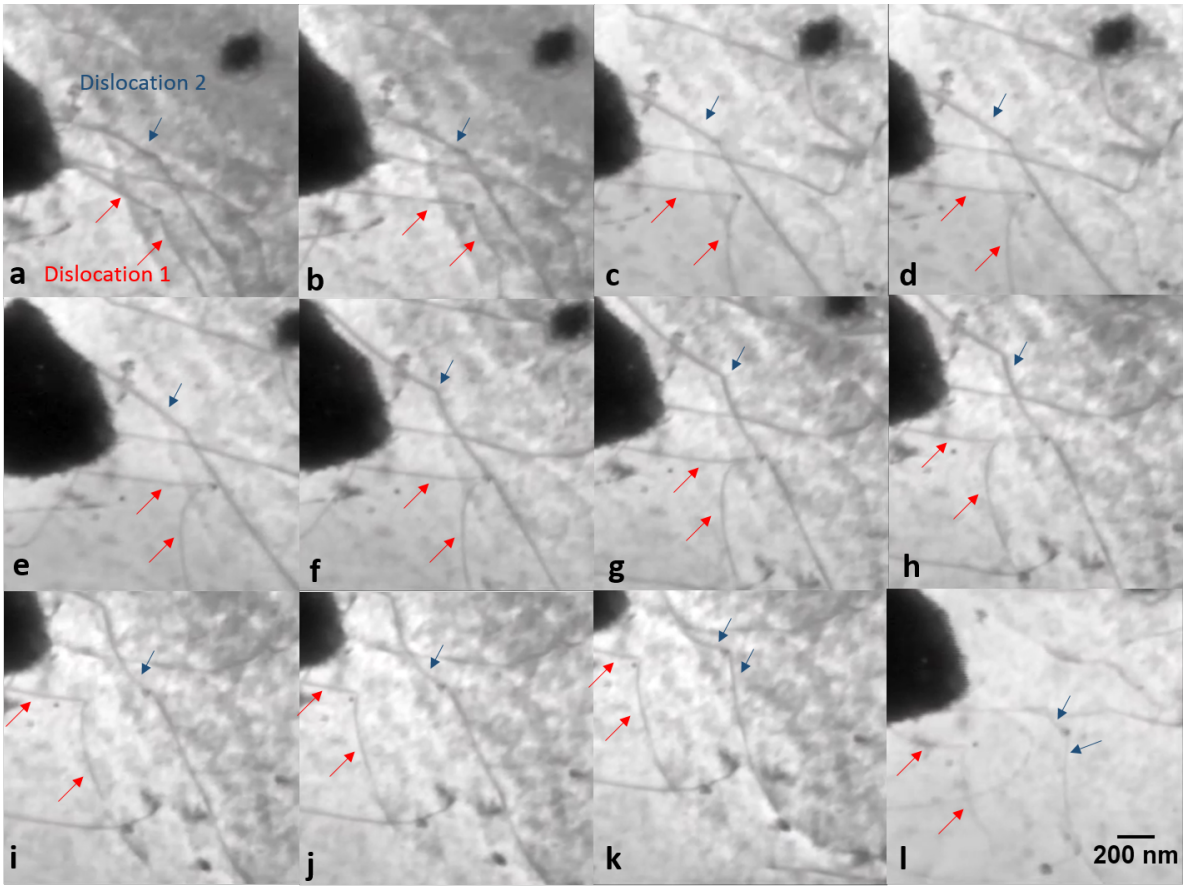

Figure 4.44 – TEM micrographs showing the different steps during thermal cycling (heating until 350°C). Dislocation bowing by particles can be observed. From (a) to (f), dislocation 1 bows around a Y_2O_3 particle until the formation of a jog (g) that remains once the dislocation has bypassed the Y_2O_3 particle (h). Once dislocation 1 has bypassed the Y_2O_3 particle, dislocation 2 meet the same particle and bows around it ((i) to (l)).

Y_2O_3 sample, where 2 dislocations are indicated by arrows (a)-(k), heating from 200 to 350°C, and (l) at 350°C. At first, dislocation 1 meets a Y_2O_3 particle and seems to be pinned by this particle (Figure 4.44(a-f)). This dislocation will cross slip and bypass the Y_2O_3 particle. In Figure 4.44(g), it is possible to observe the formation of a jog. This jog remains once the dislocation has cross-slipped and passed the particle, Figure 4.44(h-i). Dislocation 1 meets then another Y_2O_3 particle and the same process is repeated. Once the dislocation 1 has escaped the first Y_2O_3 particle, dislocation 2 starts bowing around the same particle indicating that the two dislocations lie in the exact same glide plane (Figure 4.44(i) to (l)).

According to Hull and Bacon [5], jogs can be formed by the movement of dislocations through impenetrable obstacles. Figure 4.45 schematically represent the Hirsch

mechanism when a predominantly edge dislocation moves through an obstacle. This

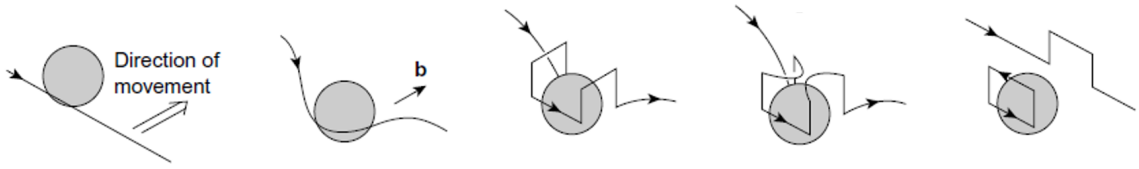

Figure 4.45 – Edge dislocation moving through impenetrable obstacles by cross slip [5, 166]. The Burgers vector is denoted by **b**.

mechanism involves the cross slip of screw segments so the dislocation can bypass the obstacle [5]. Cross slip occurs three times and one prismatic loop is left near the particle. Superjogs are produced in this cross slip process. This superjog is glissile in this configuration. This mechanism could be occurring in the Figure 4.44. The dislocations bow around Y_2O_3 particles, however, no loop could be observed once the dislocation has bypassed the particle. Additionally, a jog is formed once the dislocation has passed the particle. Thus, Orowan mechanism does not occurs in the current case. In Figure 4.44, no prismatic loop could be observed once the dislocation has bypassed the Y_2O_3 particle probably because of the small size of the Y_2O_3 particle.

The jogs in pure edge dislocations do not affect the subsequent glide of the dislocation according to Hull *et al.* [5]. Figure 4.46 schematically represent the formation of a jog when two edge dislocations intercept each other. The jog formed is perpendicular

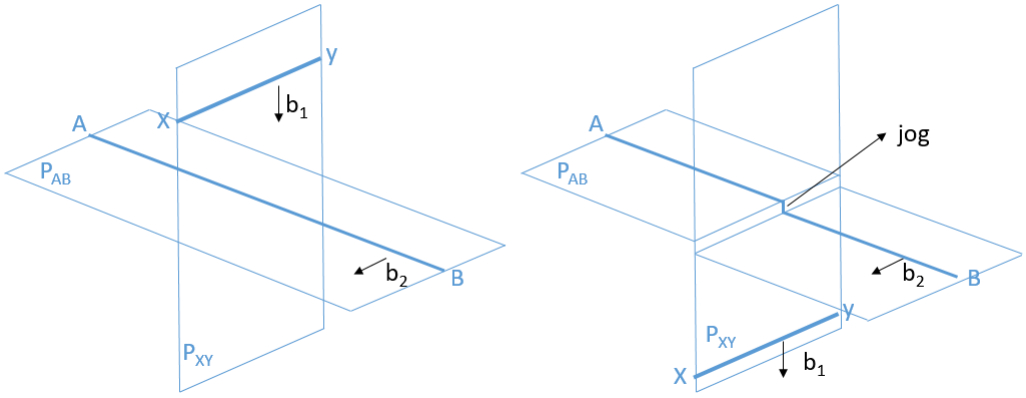

Figure 4.46 – Schematic of the formation of a jog when two edge dislocations intersept each other (inspired from [5]).

to its Burgers vector $\mathbf{b}_2$ and correspond then to an edge dislocation. The slip plane P_{AB} defined by the dislocation AB has a step on it, but the Burgers vector is at all times in

the slip plane [5]. Consequently, the jog will glide with the dislocation. However, this affirmation is true for face-centered cubic (CFC) metals, where P_{XY} and P_{AB} belong to the same family of planes ($\{1\,1\,1\}$, for example). In the case of hexagonal close-packed metals, as magnesium, the same does not occurs. If P_{AB} correspond to the basal plane, P_{XY} can correspond to the pyramidal $\pi 2$ plane, for example. It is well known that the glide of dislocations on the basal plane of hcp metals is much easier than in the other planes. Thus, the bowing of segments of dislocations present between jogs is due to the difference on the glide between dislocations on the basal plane and other planes.

The jogs observed in dislocations in other regions of the material, as in Figure 4.48, are most probably originally formed during an interaction between this dislocation and a Y_2O_3 particle.

Figure 4.47 shows TEM micrographs of different steps of the *in situ* tensile testing. A black dot (red arrow) in Figure 4.47 (a) seems to correspond to a Y_2O_3 particle that interacts with a dislocation. Further load (Figure 4.47 (b)) induces dislocation bowing and the black dot size is reduced, which signify that it does not correspond to a Y_2O_3 particle. In Figure 4.48, it is also possible to observe several dislocations bowing probably due to dislocation/dislocation interactions.

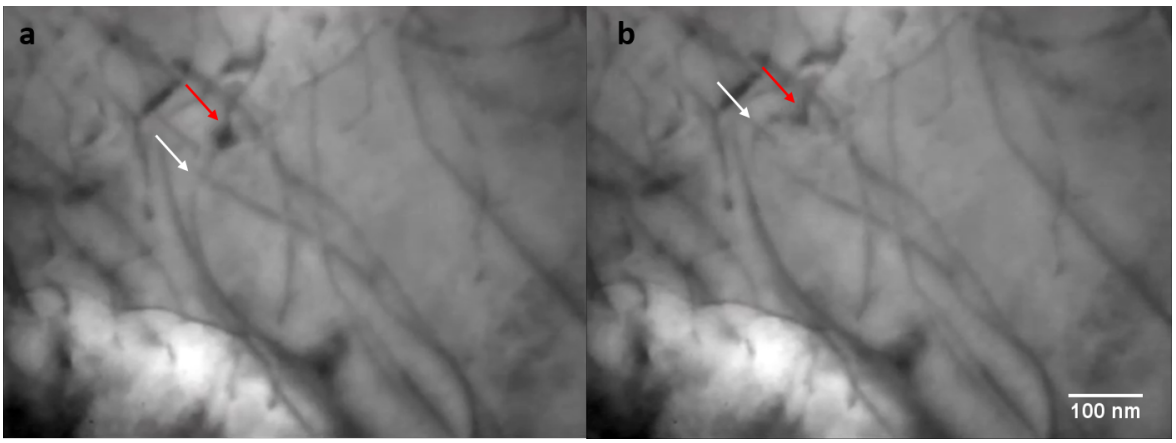

Figure 4.47 – TEM micrographs showing different steps of the *in situ* tensile testing. It is difficult to distinguish a Y_2O_3 particle from dislocation interactions in some cases. In (a), the dislocation (white arrow) seems to bow around a Y_2O_3 particle (red arow). However, further load (b) shows the dislocation moving and that the black dot size (red arrow) is reduced. Thus, what seemed to be a Y_2O_3 particle is actually just the interaction between two dislocations.

This high density of dislocations observed in this thin foil that lead to a strong dislocation/dislocation interaction have been most probably introduced during sample preparation. Magnesium being very ductile, the preparation of TEM foils is then delicate

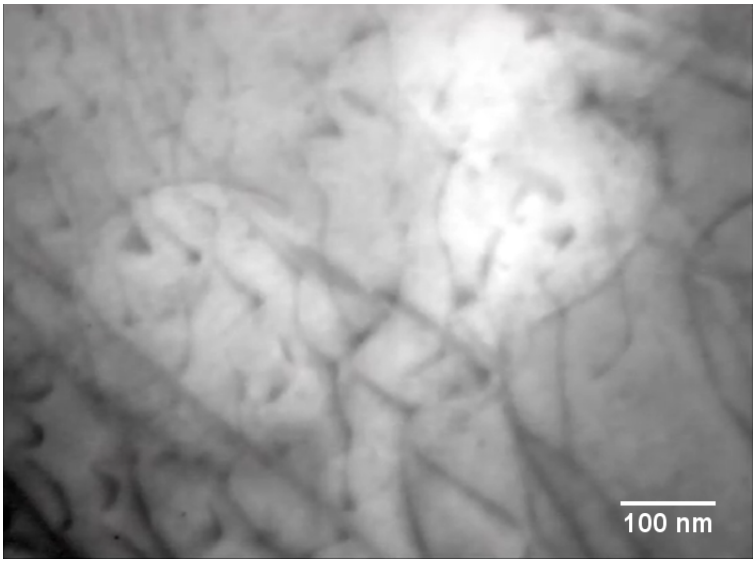

Figure 4.48 – TEM micrograph a high number of dislocations and dislocation/dislocation interactions. Similarly to Figure 4.47, dislocation bowing due to dislocation/dislocation interactions. The black dots that seems to be Y_2O_3 particles are just due the interaction between two dislocations.

and a high number of dislocations can be introduced during TEM foils preparation and handling. Additionally, during *in situ* tensile testing, it is not possible to observe the entire sample. With such high resolution technique as the TEM, it is necessary to focus on small regions where the stress would be concentrated during tensile testing. Ideally, when performing electropolishing of TEM samples, a circular hole should be introduced at the center of the lamella. In the lamellas elaborated in the present study, the hole introduced during electropolishing had a moon-shape geometry. This would lead to stress concentration on the sharpen ends of the hole. This regions are however the most plastically deformed and lots of dislocations are presented. Thus, the stress during tensile testing will be concentrated in these highly deformed regions, making it difficult to observe the interactions between the dislocations and the Y_2O_3 particles.

4.3.2 GND generation

Thermal cycling experiments can help to evidence GND generation in FSP Mg + Y_2O_3 samples. Section 4.2 have shown that the higher density of mobile dislocations present in the FSP Mg + Y_2O_3 sample avoids the size effects usually observed when performing microcompression testing in magnesium (for orientations favorably oriented for basal slip). It has also been mentioned that a high density of dislocations has been

observed closer to the bigger Y_2O_3 particles (Figure 4.24).

The GNDs generation mechanism in nanocomposites was first proposed by Arsenault *et al.* [103, 96, 100, 167]. Arsenault's studies were based on Al-SiC composites for which the difference between the thermal expansion coefficient of the aluminum matrix and the SiC is about 10:1. His thermal cycling studies were performed *in situ* in a high voltage electron microscope (HVEM) and have shown a strong GND generation close to SiC. The dislocation density measured in the composite was 2.5 times larger than in the base aluminum matrix. Thermal cycling was performed with a maximum temperature of 800 K ($\Delta T = 505$ K). In the present study, a similar experiment has been made in order to verify the GND generation close to the Y_2O_3 particles.

Thermal cycling has been performed using a TEM heating holder. The sample is heated *in situ* to 400°C, maintained for several minutes at this temperature and then cooled down to room temperature. Figure 4.49 shows the dislocation emission at the interface with a Y_2O_3 particle when increasing the temperature until 350°C. Additionally,

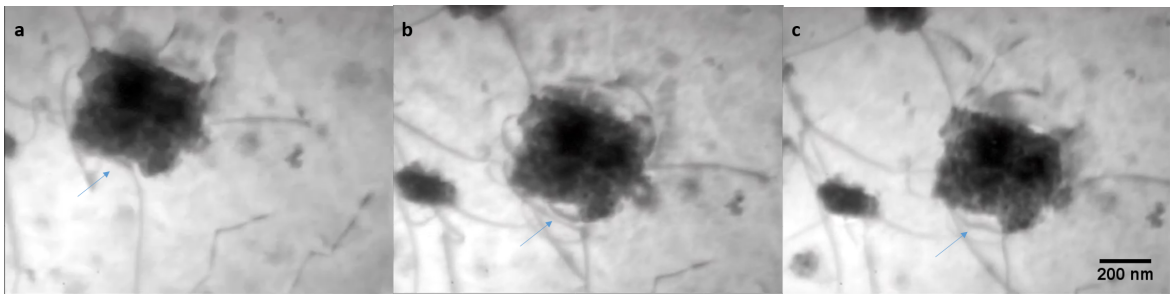

Figure 4.49 – TEM micrographs showing different steps of the thermal cycling experiment performed until 350°C. The blue arrow indicates the dislocation generation from the Y_2O_3 particle.

in Figure 4.50(a), dislocations seem to be emitted at the interface of a Y_2O_3 particle. The dislocation extinction conditions have shown that most of the dislocations generated in Figure 4.50(b) are essentially $< a >$ dislocations. In other regions of the foils, it was also observed a higher density of $< a >$ dislocations (Figure 4.51). The GND generation in the vicinity of the Y_2O_3 particles is not so clearly observed as in the experiments performed by Arsenault *et al.* [96, 167]. One of the reasons can be the lower difference between the coefficient of thermal expansion in the present study (3:1). Additionally, the thermal cycling in the present work has been performed at a maximum temperature of 400°C, while Arsenault's studies have reached temperatures closer to 500°C. A higher temperature could not have been used in the present *in situ* experiments because magnesium is highly inflammable. Another reason is that, in the present case, some Y_2O_3 particles are much

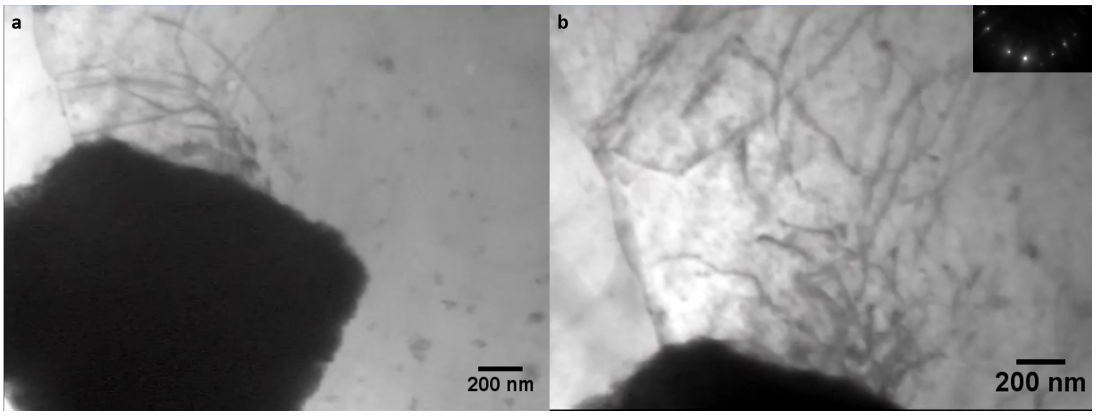

Figure 4.50 – Dislocations seems to be generated at the interface with the Y_2O_3 particles during thermal cycling (a). In (b), another zoom of the same region. Most of the dislocations in (b) are $< a >$ dislocations and have been identified using the dislocation extiction condition.

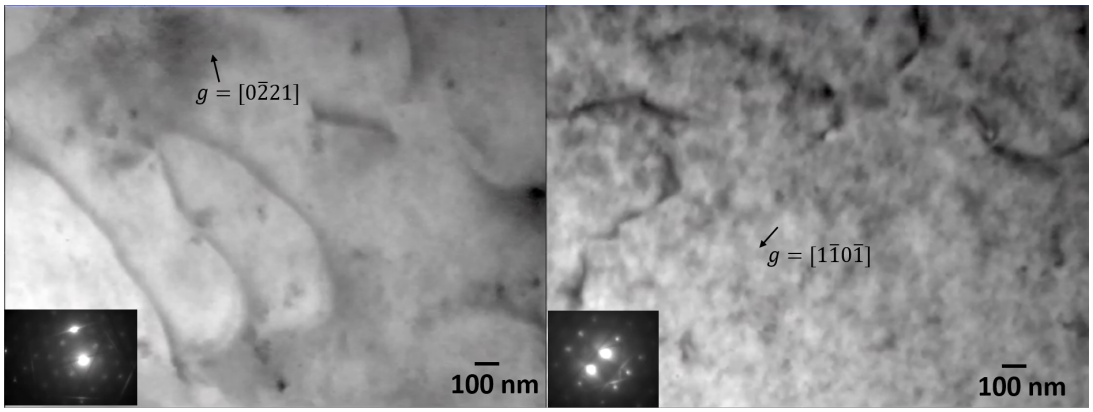

Figure 4.51 – A high density of $< a >$ dislocations have been observed in the FSP Mg + Y_2O_3 sample.

larger than the TEM foil thickness, which is usually close to 150-200 nm, resulting in a large free surface (Figure 4.52 (b)). In the experiment performed by Arsenault [103], TEM foils have been prepared using ion milling and the surface of the foil would have less roughness (Figure 4.52 (a)). In the present study, the TEM foils have been prepared using mechanical thinning (grinding) and electrochemical polishing. The magnesium matrix being softer than the Y_2O_3 particles, it is removed easily during grinding, and it is also easily etched during electrochemical polishing. The surface topography of bulk sample after mechanical grinding has been confirmed by SPM nanoindentation imaging, which is a technique similar to AFM, that uses nanoindentation to reconstruct the 3D topography. Figures 4.52 obtained using Berkovich (c) and cube-corner (d) indenters confirm that Y_2O_3 particles emerge at the surface).

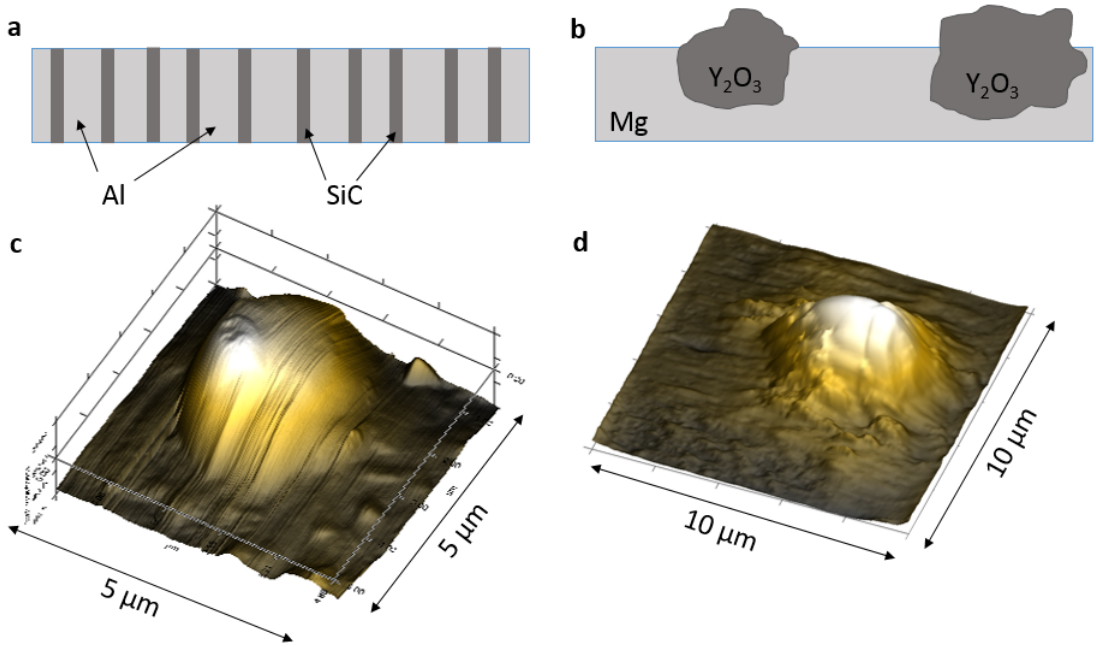

Figure 4.52 – Schmematic of the TEM foil of aluminum/SiC composites used during Arsenault's studies [103] in (a) and the one from the present study (b). In the present study, the Y_2O_3 particles have an important fraction of their volume outside the TEM foils as it can be seen in the 3D topography images (c and d) obtained by SPM nanoindentation imaging (courtesy of Hysitron).

In addition to the GND generation, the dislocation annihilation, which also occurs when performing the annealing heat treatment on the "*model*" nanocomposite, has also been investigated. With the increase of the temperature, it is possible to observe the relaxation of the material with the movement of the preexisting dislocations. Figure 4.53 shows different steps of the thermal cycling process. At room temperature (Figure 4.53(a)), it is possible to observe a dislocation pile up close to a grain boundary (region A) and several Y_2O_3 particles (black points). With the increase of the temperature until 400°C (Figure 4.53(b-e)), the dislocations start moving and their number is considerably reduced due to thermal annihilation. However, in Figure 4.53(f), a high number of dislocations is still present because the Y_2O_3 particles act as pinning points for dislocation movement (region B).

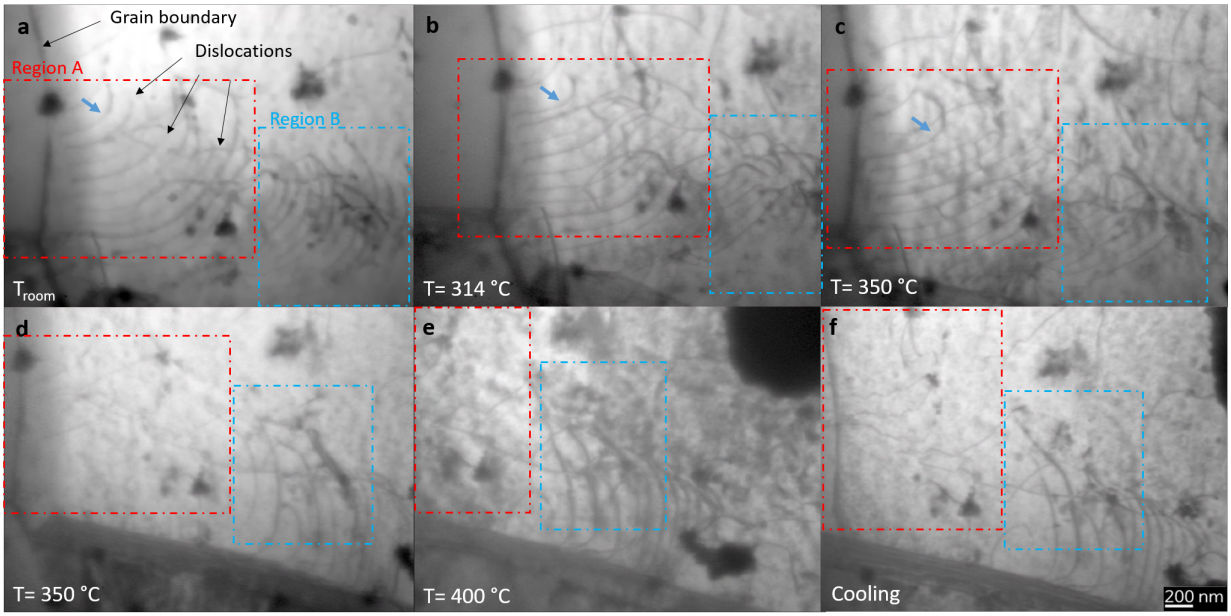

Figure 4.53 – TEM micrographs showing different steps of the thermal cycling experiment. At room temperature (a), a dislocation pile up is observed close to a grain boundary. With the increase of the temperature until 400°C (b-e), the dislocations start moving and their number is reduced. The blue arrow evidences the movement of one dislocation. However, the Y_2O_3 particles act as pinning points for dislocation movement (f).

4.4 Conclusion

A summary of all the experimental tests that have been performed and the samples used are presented in Table 4.16. Attempt has been made to identify the contribution of the different strengthening mechanisms described in Section 1.4. From the tensile tests performed on polycrystalline samples, it was shown that the addition of Y_2O_3 particles does not affect much the grain size for such low volume fraction of particles (0.3%) nor the texture. However, these particles seem to have an strengthening effect since a significant increase of the mechanical properties has been observed (Table 4.3). TEM experiments have shown a higher number of dislocations close to the Y_2O_3 particles in the nanocomposite due to the difference in the coefficient of thermal expansion. Since no thermal treatment has been performed on the tensile specimens, the effect of dislocation hardening should be even higher and can have a strong contribution to the strengthening of the nanocomposite.

Microcompression testing performed on FSP Mg+Y_2O_3 samples favorably oriented for basal slip have shown a reduction of the size effects usually observed in magne-

Table 4.16 – Summary of all the tests that have been performed and the samples used.

	Macrotensile testing		**Microcompression testing**		***In situ* TEM**
Strengthening mechanisms studied	Hall-Petch Orowan GND generation Load transfer		Orowan GND generation Load transfer		Orowan GND generation
Thermal treatment	X		3 h 500°C		X
Samples	Mg	Mg+Y_2O_3	Mg	Mg+Y_2O_3	Mg+Y_2O_3
f_v Y_2O_3 (%)	0	0.3, 1.64, 2.11	0	0.3	0.3
Grain size (μm)	7.8	11.8	Single crystal		11.8
Dislocation density (m^{-2})	High		Low ($\rho_\circ$)	$\rho_\circ$+4.22x10^{12}	High
Texture	Similar with and without Y_2O_3		X		X
Yield point (MPa)	52	70.8±1.42			
Orientation			Basal slip and tensile twinning		
Size effects			Basal slip and tensile twinning		

sium with the addition of Y_2O_3 particles (CBSS in Table 4.7). Additionally, no significant strengthening has been observed for these columns. In the case of 10 μm columns,

a slightly difference in the CBSS between FSP Mg and FSP Mg+Y_2O_3 would suggest that particles could play a role in the strengthening. This indicates a particle strengthening effect when approaching the size of a bulk material. Considering this tendency, one could expect that the difference between the CBSS in the 15 μm should be much higher, unfortunately, no 15 μm columns of FSP Mg has been tested.

This is confirmed by *in situ* TEM experiments, which have shown the interaction of the dislocations with the Y_2O_3 particles. These interaction dislocation/particles also contributes to the strengthening of the nanocomposite.

As a conclusion, the strengthening observed in the "*model*" nanocomposite is probably related to the forest hardening and to the interactions between the Y_2O_3 particles and the dislocations.

Key points of Chapter 4

1. A volume fraction of Y_2O_3 particles as low as 0.3 % has shown a strengthening effect for FSP Mg + Y_2O_3 samples during tensile testing of polycrystalline samples.

2. FSP Mg and FSP Mg + Y_2O_3 (0.3 %) single crystalline samples have been compared by means of microcompression testing.

3. Microcolumns favorably oriented for basal slip and tensile twinning have been tested. The results indicate that Y_2O_3 particles have a strong influence on the mechanisms of plastic deformation for magnesium based nanocomposites favorably oriented for basal slip and tensile twinning.

4. No clear strengthening effect has been observed when dislocation glide operates (CRSS for basal slip in FSP Mg + Y_2O_3 is lower than in FSP Mg) and the Y_2O_3 particles mitigate the size effects commonly observed at small scale mechanical testing of pure magnesium. The yield stress in nanocomposites is no more related to the size effect but rather to the possibility to generate mobile dislocations.

5. Y_2O_3 particles also affect the twin nucleation stress and twin morphology for orientations favorable for tensile twinning. Multiple twins seem to have nucleated at the interface with the Y_2O_3 particles, which is a stress concentration zone. In FSP Mg, twinning will most likely nucleate at the top of the column (contact with the indenter) and a maximum of two twin has been observed.

6. *In situ* TEM experiments with thermal cycling have shown a higher dislocation density closer to the Y_2O_3 particles. These results support the theory that geometrically necessary dislocations are generated due to the difference between the thermal expansion coefficient of magnesium and Y_2O_3. It explains the higher density of mobile dislocations in the nanocomposite.

Conclusion and perspectives

The plastic behavior of a "*model*" magnesium single and polycrystal strengthened by oxide dispersed particles has been studied in the present work. The first objective was to elaborate a "*model*" nanocomposite that fulfill all the requirements for a multiscale study, which are:

- good dispersion of the particles
- coarse grains
- particle stability

Several processing techniques have been considered as well as different reinforcement materials. Finally, magnesium based nanocomposites strengthened by Y_2O_3 particles were successfully elaborated using friction stir processing (FSP). Microstructural characterization have confirmed an uniform dispersion of Y_2O_3 particles. High resolution 2- and 3-D techniques such as laboratory tomography, synchrotron X-ray nanoholotomography and TEM were applied in order to characterize the "*model*" nanocomposite.

A multiscale mechanical study of both FSP Mg + Y_2O_3 and FSP Mg fabricated using the same processing parameters has been performed. At the millimeter scale, tensile tests on polycrystalline samples have shown a strengthening effect in the nanocomposite even when a small volume fraction of Y_2O_3 particles has been used (0.3 %). These tests lead us to conclude that the strengthening was neither due to grain size effect nor to texture modification by the particles. Further investigation at the scale of the single crystal have been done. At this micrometer scale, the mechanical behavior of the single crystal was studied by means of microcompression testing of microcolumns elaborated by focused ion beam. Magnesium deforms mainly by basal slip or twinning at room temperature. Thus, the orientation dependent mechanisms of plastic deformation have

been studied for two orientations: one favorable for basal slip and a second one which promotes twinning deformation. Both orientations are tested on the two samples: FSP Mg and FSP Mg + Y_2O_3.

For columns favorably oriented for basal slip, the results have shown a weak strengthening effect when dislocation glide operates. The presence of Y_2O_3 particles has also mitigated the size effect usually observed at small scale magnesium single crystals and usually explained by the dislocation starvation theory. One explanation is that the dislocation starvation mechanisms is not present in the nanocomposite and the plasticity is accommodated by the preexisting mobile dislocations. Plasticity being mainly confined to parallel basal slip planes, the forest hardening is negligible and the yield stress strongly depends on the initial dislocation density, which is higher in the nanocomposite. In other words, the yield stress in nanocomposites is no more related to the size effect but rather to the possibility to generate mobile dislocations.

In the case of tensile twinning, the Y_2O_3 particles seem to affect the twin nucleation stress and twin morphology. The particles have changed the mechanisms of plastic deformation, with the presence of multiple twins in the nanocomposite. The reason is the heterogeneous structure due to the presence of Y_2O_3 particles. It creates stress concentration zones close to the particles and consequently twin nucleation. The Y_2O_3 particles have also slightly reduced the size effects in tensile twinning.

The investigation of the single crystalline behavior helps on the understanding of the macroscopic behavior. The slight difference in the CBSS for 10 μm columns with the addition of Y_2O_3 particles lead to the interpretation that there is a strengthening due to the presence of particles. In order to confirm this theory, elaboration of single crystals with a higher volume fraction of particles is necessary.

Perspectives for future studies

3D Discrete Dislocation Dynamics

The mechanisms of plastic deformation of magnesium single crystals have already been studied by comparing experimental microcompression testing with numerical simulations using 3D discrete dislocations dynamics [2] and orientations for which dislo-

cation glide operates. In the present work, a preliminary study has been performed in collaboration with H. J. Chang, using the Tridis code modified for polycristalline and polyphase materials. A cylindrical microcolumn with 10 μm-diameter and 25 μm-height have been used and a volume fraction of 0.1 % of square-shaped reinforcement particles (diameter 250 nm) has been introduced in the microcolumn. During uniaxial compression (Figure 4.54), it is possible to observe the formation of the shear bands corresponding to intense basal slip activity. Further work need to be done in order to reproduce the exper-

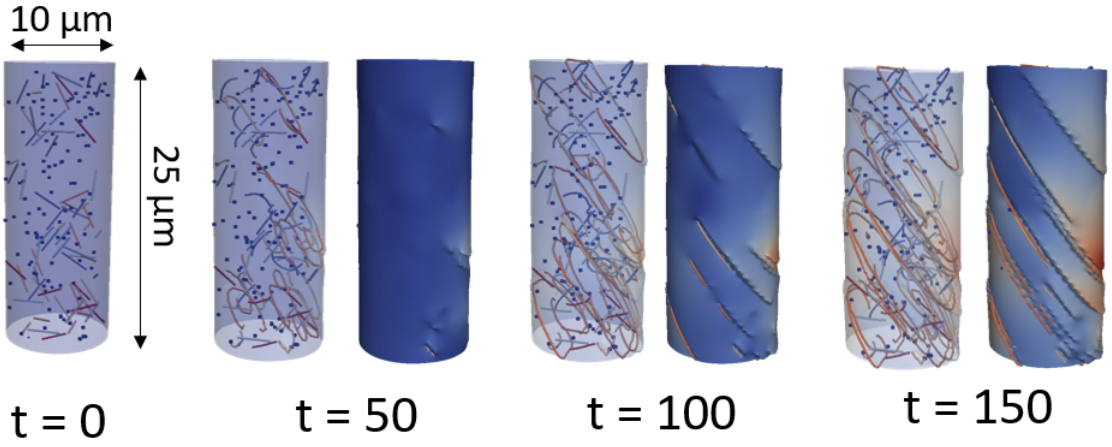

Figure 4.54 – 3D discrete dislocations dynamics simulations showing the formation of shear bands corresponding to intense basal slip when performing uniaxial compression of a cylindrical microcolumn with a volume fraction of square-shaped reinforcement particles of 0.1 %.

imental behavior observed in the present study. Namely, forest interaction mechanisms between $< a >$ and $< c + a >$ dislocations need to be accounted for. Such a reaction is not correctly reproduced in TRIDIS for which the junctions are just a superposition of two dislocation lines. Only a nodal code could be precisely take care of this as recently proposed by [168, 169]. A perspective of this work would be to use the nodal code NUMODIS developed in collaboration with CEA Saclay. Work has been started in this direction.

In situ EBSD and microcompression testing

Microcompression of microcolumns favorably oriented for tensile twinning in Section 4.2.2 has shown that the presence of Y_2O_3 particles change the twin morphology with the nucleation of multiple twins. These twins seem to have nucleated at the interface with the Y_2O_3 particles due to the stress concentration in this region. In order to confirm

the nucleation of the twins in the vicinity of the Y_2O_3 particles, it would be necessary to perform *in situ* EBSD and microcompression testing. Interrupted microcompression testing could be performed using an *in situ* nanoindenter and EBSD scans would be obtained during each interruption. An attempt to perform such a delicate *in situ* test has been done during this study. Square-shaped microcolumns have been machined by FIB milling as shown in Figure 4.55 (a) with the presence of a Y_2O_3 particle on the analyzed surface. Figure 4.55 (b) shows the position of the e-beam, *in situ* indenter and EBSD detector with respect to the microcolumn. Unfortunately, experimental issues with EBSD, which include shadowing and surface damage, have made impracticable the realization of the *in situ* test.

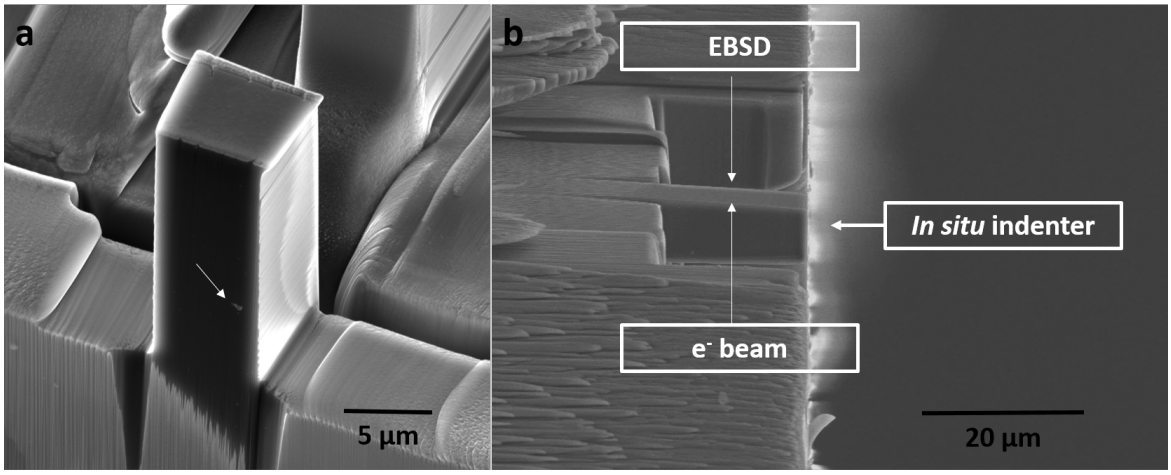

Figure 4.55 – SEM micrographs of square-shaped microcolumn prepared for *in situ* EBSD. In (a), it is possible to observe a Y_2O_3 particle (white arrow) on the surface of interest. In (b), a schematic of the experiment with the position of the e-beam, *in situ* indenter and EBSD detector.

In situ TEM testing

It has been mentioned in Section 4.3 that only a small region of the TEM foil has been observed when performing the *in situ* TEM testing. Additionally to these experiments, attempt has been made in order to perform *in situ* TEM tensile testing on a microtensile specimen with dimensions of 1 μm (width) x 2-4 μm (length). This work has been performed in collaboration with H. Idrissi from Université Catolique de Louvain and EMAT (Electron Microscopy for Materials Science), University of Antwerp. The experiments have been performed using a special microelectromechanical system device called Push-to-Pull, whose schematics is presented in Figure 4.56 [170]. Four

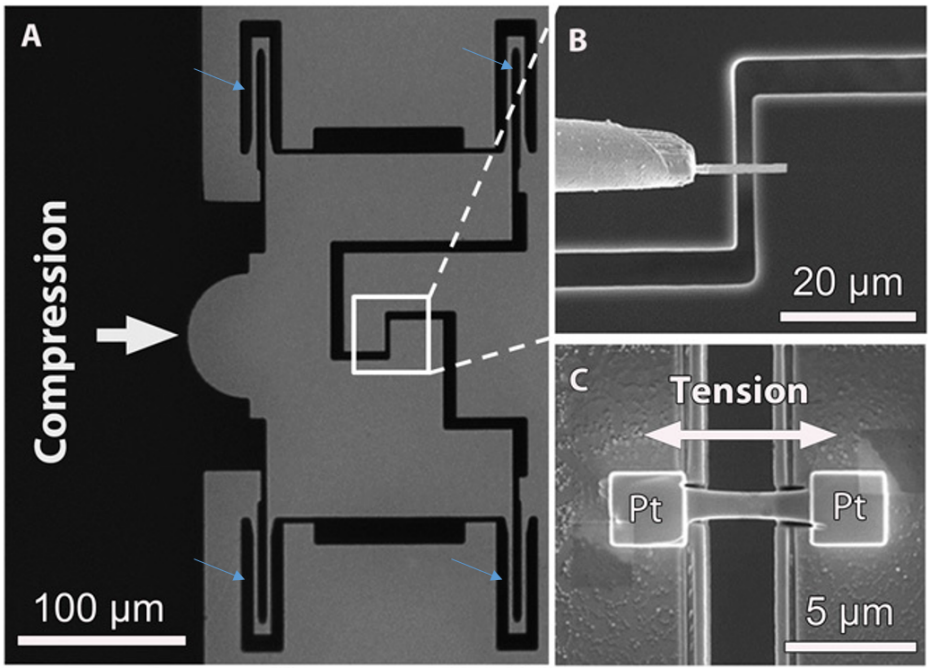

Figure 4.56 – Schematic of the Push-to-Pull device used for *in situ* TEM tensile experiments (A). The compression force applied on the semicircular end of the device is converted in uniaxial tensile load on the middle gap where the tensile specimen is placed (B and C). SEM micrographs in B and C show the transfer of a FIB foil onto the device and the mounting of the foil in the middle gap using platinum deposition, respectively [170].

identical springs are distributed symmetrically at the corners of the device (blue arrows in Figure 4.56 (a)) in such a way that when a compression force is applied on the semicircular end of the device, it is converted in uniaxial tensile load on the middle gap where the tensile specimen is placed. The compression force is applied using a diamond flat punch indenter in the PI95 TEM PicoIndenter from Hysitron Inc. in a load-controlled compression mode.

Some images of test performed on the "*model*" nanocomposite are presented in Figure 4.57. Unfortunately, the diffraction conditions did not provide a good contrast and dislocations are barely visible. To improve this, a specific reflection should be selected with a high F^2. The intensity of the diffracted beam is proportional to $|F_{(hkil)}|^2$. Table 4.17 presents the most important reflections in the case of magnesium and the corresponding intensity of the diffracted beam. These values were calculated using the JEMS software. EBSD measurements were performed before extracting a TEM lamella in order to chose a grain whose orientation will allow to have such a reflection. Due to time constrains, it was not possible to perform the experiment with this new TEM sample.

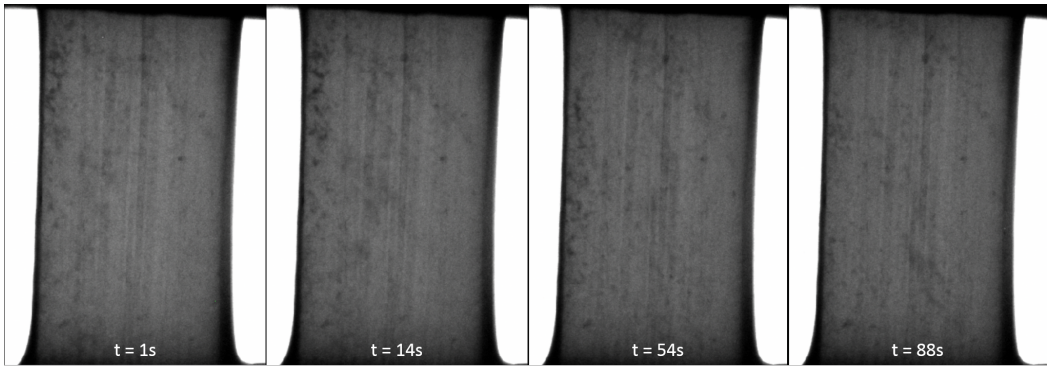

Figure 4.57 – TEM micrographs taken during *in situ* TEM tensile testing of the "*model*" nanocomposite (load controlled 150 μN).

Table 4.17 – Intensity of the diffraction spots for different reflections calculated using the structure factor equation.

(hkil)	Intensity	***(hkil)***	Intensity	***(hkil)***	Intensity	***(hkil)***	Intensity
$(0\,0\,0\,0)$	-	$(1\,1\,\bar{2}\,0)$	151	$(0\,0\,0\,4)$	24	$(2\,1\,\bar{3}\,1)$	91
$(1\,0\,\bar{1}\,0)$	252	$(1\,0\,\bar{1}\,3)$	167	$(2\,0\,\bar{2}\,2)$	29	$(1\,1\,\bar{2}\,4)$	56
$(0\,0\,0\,2)$	272	$(2\,0\,\bar{2}\,0)$	23	$(1\,0\,\bar{1}\,4)$	25		
$(1\,0\,\bar{1}\,1)$	1000	$(1\,1\,\bar{2}\,2)$	171	$(2\,0\,\bar{2}\,3)$	55		
$(1\,0\,\bar{1}\,2)$	137	$(2\,0\,\bar{2}\,1)$	121	$(2\,1\,\bar{3}\,0)$	16		

"Model" nanocomposite

As mentioned in Section 3.3, three groups of sizes have been observed in the current "*model*" nanocomposite: large micrometer-sized particles, intermediate sizes varying from 100-300 nm and particles smaller than 50 nm. A better control of the particle size distribution to obtain a monodisperse distribution of particles would lead to a better understanding of the particle influence since most of the strengthening theories consider only one size of reinforcement. Furthermore, the volume fraction of Y_2O_3 particles was not sufficient for the 10 μm column to fully account for the hardening effect. Elaboration of microcolumns with a higher volume fraction of particles is hence necessary.

Bibliography

[1] E. Lilleodden. Microcompression study of Mg (0 0 0 1) single crystal. *Scripta Materialia*, 62(8):532–535, 2010.

[2] G. S. Kim. *Small volume investigation of slip and twinning in magnesium single crystals*. PhD thesis, Université de Grenoble, 2011.

[3] S. F. Hassan and M. Gupta. Development and characterization of ductile Mg/Y_2o_3 nanocomposites. *Transactions of the ASME*, 129:462–467, 2007.

[4] S. F. Hassan. Effect of primary processing techniques on the microstructure and mechanical properties of nano-Y_2O_3 reinforced magnesium nanocomposites. *Materials Science and Engineering A*, 528:5484–5490, 2011.

[5] D. Hull and D. J. Bacon. *Introduction to dislocations*. Elsevier, fifth edition edition, 2011.

[6] A. Erman, J. Groza, X. Li, H. Choi, and G. Cao. Nanoparticle effects in cast Mg-1% SiC nano-composites. *Materials science & engineering A*, 558:39–43, 2012.

[7] M. Pozuelo, Y. W. Chang, and J. M. Yang. Effect of diamondoids on the microstructure and mechanical behavior of nanostructured Mg-matrix nanocomposites. *Materials scinece & engineering A*, 633:200–208, 2015.

[8] H. Ferkel and B. L. Mordike. Magnesium strengthned by SiC nanoparticles. *Materials science & engineering A*, 298:193–199, 2001.

[9] E. Alam, S. Han, Q. B. Nguyen, A. M. S. Hamouda, and M. Gupta. Development of new magnesium based alloys and their nanocomposites. *Journal of alloys and compounds*, 509:8522–8529, 2011.

[10] L. Chen, J. Xu, H. Choi, M. Pozuelo, X. Ma, S. Bhowmick, and J. Yang. Processing and properties of magnesium containing a dense uniform dispersion of nanoparticles. *Nature*, 528:539–543, 2015.

[11] G. E. Dieter. *Materials science and engineering series: Mechanical metallurgy*. 1976.

[12] G. I. Taylor. Plastic strain in metals. *Journal of the institute of metals*, 62:307–324, 1938.

[13] R. von Mises. Mechanik der plastischen Formänderung von Kristallen. *Zeitschrift für Angewandte Mathematik und Mechanik / Journal of applied mathematics and mechanics*, 8:161–185, 1928.

[14] P. G. Partridge. The crystallography and deformation modes of hexagonal close-packed metals. *Metallurgical reviews*, pages 169–194, 1967.

[15] B. Beausir, L. S. Tóth, and K. W. Neale. Ideal orientations and persistence characteristics of hexagonal close packed crystals in simple shear. *Acta materialia*, 55:2695–2705, 2007.

[16] M. Forget. *Laminage asymétrique de l'alliage de magnésium AZ31*. PhD thesis, Université de Grenoble, 2013.

[17] G. Thomas and M. J. Goringe. *Transmission electron microscopy of materials*. 1979.

[18] H. Yoshinaga and R. Horiuchi. On the nonbasal slip in magnesium crystals. *Transactions of the Japan Institute of Metals*, 5:14–21, 1963.

[19] H. Yoshinaga and R. Horiuchi. Deformation mechanisms in magnesium single crystals compressed in the direction parallel to hexagonal axis. *Transactions of the Japan Institute of Metals*, 4:1–8, 1963.

[20] E. C. Burke and W. R. Hibbard. Plastic deformation of magnesium single crystals. *Transactions of the Metallurgical Society of AIME*, 1952.

[21] H. Conrad and W. D. Robertson. Effect of temperature on the flow stress and strain hardening coefficient of magnesium single crystals. *Transactions AIME*, 209:503–512, 1957.

[22] M. Z. Bian and K. S. Shin. Twin interactions in magnesium single crystal. *Magnesium Technology and their Applications*, 2009.

[23] P. W. Bakarian and C. H. Mathewson. Slip and twinning in magnesium single crystals at elevated temperature. *AIME Transactions*, 152:226–254, 1943.

[24] E. Schmid. Beiträge zur Physik und Metallographie des Magnesiums. *Berichte der Bunsengesellschaft für physikalische Chemie*, 37(8-9):447–459, 1931.

[25] R. E. Reed-Hill and W. D. Robertson. Deformation of magnesium single crystals by non basal slip. *Transactions of AIME*, 209:496–502, 1957.

[26] P. W. Flynn, J. Mote, and J. E. Dorn. *AIME Transactions*, 221:1148, 1961.

[27] X. Y. Liu, J. B. Adams, F. Ercolessi, and J. A. Moriarty. EAM potential for magnesium from quantum mechanical forces. *Modelling and Simulation in Materials Science and Engineering*, 4(3):293, 1996.

[28] D. Y. Sun, M. I. Mendelev, C. A. Kudin, T. Haxhimali, M. Asta, J. J. Hoyt, A. Karma, and D. J. Srolovitz. Crystal-melt interfacial free energies in hcp metals: a molecular dynamics study in Mg. *Physical Review B*, 73:024116, 2006.

[29] A. Staroselsky and L. Anand. A constitutive model for hcp materials deforming by slip and twinning: application to magnesium alloy AZ31B. *International Journal of Plasticity*, 2003.

[30] R. E. Reed-Hill and W. D. Robertson. Pyramidal slip in magnesium. *The Metallurgical Society of AIME*, 212:256–259, 1958.

[31] W. J. McG. Tegart. Independent slip systems and ductility of hexagonal polycrystals. *Philosophical Magazine*, 9:339–341, 1964.

[32] T. Obara, H. Yoshinaga, and S. Morozumi. $\{1\,1\,2\,2\}\,\langle 1\,1\,2\,3\rangle$ slip system in magnesium. *Acta metallurgica*, 21:845–853, 1974.

[33] Z. Wu and W. A. Curtin. The origins of high hardening and low ductility in magnesium. *Nature*, 526:62–67, 2015.

[34] Z. Wu and W. A. Curtin. Intrinsic structural transitions of the pyramidal I $< c+a >$ dislocation in magnesium. *Scripta Materialia*, 116:104–107, 2016.

[35] M. D. Nave and M. R. Barnett. Microstructures and textures of pure magnesium deformed in plane-strain compression. *Scripta materialia*, 51:881–885, 2004.

[36] H. Yoshinaga and R. Horiuchi. On the flow stress of alpha solid solution Mg-Li alloy single crystals. *Transactions of the Japan Institute of Metals*, 4:134–141, 1963.

[37] J. Koike, Y. Sato, and D. Ando. Origin of the anomalous $\{1\,0\,\bar{1}\,2\}$ twinning during tensile deformation of Mg alloy sheet. *Materials transactions*, 49:2792–2800, 2008.

[38] P. D. Wu, X. Q. Guo, H. Qiao, and D. J. Lloyd. A constitutive model of twin nucleation, propagation and growth in magnesium crystals. *Materials Science & Engineering A*, 625:140–145, 2014.

[39] M. A. Gharghouri, G. C. Weatherly, J. D. Emburgy, and J. Root. Study of the mechanical properties of Mg-7.7at.%al by *in situ* neutron diffraction. *Philosophical magazine*, 79:1671–1695, 1999.

[40] S. Godet, L. Jiang, A. A. Luo, and J. J. Jonas. Use of Schmid factors to select extension twin variants in extruded magnesium alloy tubes. *Scripta materialia*, 55:1055–1058, 2006.

[41] I. J. Beyerlein, L. Capolungo, P. E. Marshall, R. J. McCabe, and C. N. Tomé. Statistical analyses of deformation twinning in magnesium. *Philosophical magazine*, 90:2161–2190, 2010.

[42] J. J. Jonas, S. Mu, T. Al-Samman, G. Gottstein, L. Jiang, and E. Martin. The role of strain accommodation during the variant selection of primary twins in magnesium. *Acta Materialia*, 59:2046–2056, 2011.

[43] I. J. Beyerlein and C. N. Tomé. A probabilistic twin nucleation model for HCP polycrystalline metals. *Proceedings of the Royal Society A*, 466:2517–2544, 2010.

[44] C. Bettles and M. Barnett. *Advances in wrought magnesium alloys: fundamentals of processing, properties and applications*. Woodhead Publications in Materials, 2012.

[45] M. H. Yoo. Slip, twinning and fracture in hexagonal close-packed metals. *Metallurgical transactions A*, 12A:409–418, 1981.

[46] J. E. Hack, R. A. Page, and G. R. Leverant. Tensile and fatigue behavior of aluminum oxide fiber reinforced magnesium composites: part I. fiber fraction and orientation. *Metallurgical transactions A*, 15A:1389–1396, 1984.

[47] J. Schröder and K. U. Kainer. Magnesium-base hybrid composites prepared by liquid infiltration. *Materials Science and Engineering*, A135:33–36, 1991.

[48] K. Purazrang, P. Abachi, and K. U. Kainer. Investigation of the mechanical behavior of magnesium composites. *Composites*, 25(4):296–302, 1993.

[49] D. J. Lloyd. Particle reinforced aluminum and magnesium matrix composites. *International Materials Reviews*, 39:1–23, 1994.

[50] A. R. Vaidya and J. J. Lewandowski. Effects of SiCp size and volume fraction on the high cycle fatigue behavior of AZ91D magnesium alloy composites. *Materials Science & Engineering A*, 220:85–92, 1996.

[51] S. C. Tjong. Novel nanoparticle-reinforced metal matrix composites with enhanced mechanical properties. *Advanced Engineering Materials*, 9(8):639–652, 2007.

[52] R. Casati and M. Vedani. Metal matrix composites reinforced by nano-particles - a review. *Metals*, 4:65–83, 2014.

[53] W. L. E. Wong and M. Gupta. Effect of hybrid length scales (micro + nano) of SiC reinforcement on the properties of magnesium. *Solid State Phenomena*, 111:91–94, 2006.

[54] S. R. Agnew and O. Duygulu. Plastic anisotropy and the role of non-basal slip in magnesium alloy AZ31B. *International Journal of Plasticity*, 21:1161–1193, 2005.

[55] S. F. Hassan and M. Gupta. Enhancing physical and mechanical properties of Mg using nanosized Al_2O_3 particulates as reinforcement. *Metallurgical and materials transactions A*, 36A:2253–2258, 2005.

[56] S. F. Hassan and M. Gupta. Development of nano-Y_2O_3 containing magnesium nanocomposites using solidification processing. *Journal of Alloys and Compounds*, 429:176–183, 2007.

[57] Googlescholar.

[58] H. A. Katzman. Fibre coatings for the fabrication of graphite-reinforced magnesium composites. *Journal of Materials Science*, 22:144–148, 1987.

[59] J. T. Evans. Fracture and subcritical crack growth in alumina-fibre/magnesium composites. *Acta Metallurgica*, 34(10):2075–2083, 1986.

[60] J. F. Mason, C. M. Warwick, P. J. Smith, J. A. Charles, and T. W. Clyne. Magnesium-lithium alloys in metal matrix composites - A preliminary report. *Journal of Materials Science*, 24:3934–3946, 1989.

[61] E. G. Wolff, B. K. Min, and M. H. Kural. Thermal cycling of a unidirectional graphite-magnesium composite. *Journal of Materials Science*, 20:1141–1149, 1985.

[62] S. Fox, H. Flower, and D. West. TEM characterisation of fibre-matrix interactions in light alloy MMC containing alumina fibres. *Elsevier Science Publishers*, pages 243–245, 1990.

[63] M. Gupta, L. Lu, M. O. Lai, and K. H. Lee. Microstructure and mechanical properties of elemental and reinforced magnesium synthesized using a fluxless liquid-phase process. *Material Research Bulletin*, 34(8):1201–1214, 1999.

[64] F. U. Rehman, S. Fox, H. M. Flower, and D. R. F. West. Fibre/matrix interactions in magnesium-based composites containing alumina fibres. *Journal of Materials Science*, 29:1636–1645, 1994.

[65] S. F. Hassan and M. Gupta. Development of high performance magnesium nanocomposites using nano-Al_2O_3 as reinforcement. *Materials science & Engineering A*, 392:163–168, 2005.

[66] W. W. Leong Eugene and M. Gupta. Simultaneously improving strength and ductility of magnesium using nano-size SiC particulates and microwaves. *Advanced engineering materials*, 8:735–740, 2006.

[67] C. Y. H. Lim, D. K. Leo, J. J. S. Ang, and M. Gupta. Wear of magnesium composites reinforced with nano-sized alumina particulates. *Wear*, 259:620–625, 2005.

[68] C. Mayencourt and R. Schaller. Mechanical-stress relaxation in magnesium-based composites. *Materials Science and Engineering A*, 325:286–291, 2002.

[69] B. L. Mordike and P. Lukác. Interfaces in magnesium-based composites. *Surface and Interface analysis*, 31:682–691, 2001.

[70] S. C. Sharma, B. Anand, and M. Krishna. Evaluation of sliding wear behavior of feldspar particle-reinforced magnesium alloy composites. *Wear*, 241:33–40, 2000.

[71] H. Fukuda, K. Kondoh, J. Umeda, and B. Fugetsu. Fabrication of magnesium based composites reinforced with carbon nanotubes having superior mechanical properties. *Materials Chemistry and Physics*, 127:451–458, 2011.

[72] A. Merterns, A. Simar, J. Adrien, E. Maire, H.-M. Montrieux, F. Delannay, and J. Lecomte-Beckers. Influence of fibre distribution and grain size on the mechanical

behavior of friction stir processed Mg-C composites. *Materials characterization*, 107:125–133, 2015.

[73] Y. Chen, Y. B. Guo, M. Gupta, and V. P. W. Shim. Dynamic tensile response of magnesium nanocomposites and the effect of nanoparticles. *Materials scinece & engineering A*, 582:359–367, 2013.

[74] C. Zhang, W. Li, and W. Xue. Microstructures and mechanical properties of carbon tubes reinforced AZ91D magnesium matrix composites prepared by squeeze casting. *The Minerals, Metals and Materials Society*, pages 1463–1470, 2013.

[75] J. Jayakumar, B. K. Raghunath, and T. H. Rao. Recent development and challenges in synthesis of magnesium matrix nano composites - a review. *International Journal of Latest Research in Science and Technology*, 1:164–171, 2012.

[76] N. Saheb, Z. Iqbal, A. Khalil, A. S. Hakeem, N. A. Aqeeli, T. Laoui, A. Al-Qutub, and R. Kirchner. Spark plasma sintering of metals and metal matrix nanocomposites: a review. *Journal of Nanomaterials*, pages 1–13, 2012.

[77] J. Liu, C. Suryanarayana, D. Ghosh, G. Subhash, and L. An. Synthesis of Mg-Al_2O_3 nanocomposites by mechanical alloying. *Journal of alloys and compounds*, 563:165–170, 2013.

[78] A. Simar and M.-N. Avettand-Fènöel. Friction stir processing for architectured materials. unpublished.

[79] M.-N. Avettand-Fènöel, A. Simar, R. Shabadi, R. Taillard, and B. de Meester. Characterization of oxide disperion strengthened copper based materials developed by friction stir processing. *Materials and Design 60*, pages 343–357, 2014.

[80] M. Yang, C. Xu, C. Wu, K. Li, Y. J. Chao, and L. An. Fabrication of AA6061/Al_2O_3 nanoceramic particle reinforced composite coating by using friction stir processing. *Journal of materials science*, 45:4431–4438, 2010.

[81] R. S. Mishra, Z. Y. Ma, and I. Charit. Friction stir processing: a novel technique for fabrication of surface composite. *Materials scinece & engineering A*, 341:307–310, 2003.

[82] B. Zahmatkesh and M. H. Enayati. A novel approach for development of surface nanocomposite by friction stir processing. *Materials scinece & engineering A*, 527:6734–6740, 2010.

[83] C. J. Lee, J. C. Huang, and P. J. Hsieh. Mg based nano-composites fabricated by friction stir processing. *Scripta Materialia*, 54:1415–1420, 2006.

[84] G. Faraji and P. Asadi. Characterization of AZ91/alumina nanocomposite produced by FSP. *Materials science & engineering A*, 528:2431–2440, 2011.

[85] X. Li, Y. Yang, and X. Chen. Ultrasonic-assisted fabrication of metal matrix nanocomposites. *Journal of materials science*, 39:3211–3212, 2004.

[86] K. S. Suslick, Y. Didenko, M. M. Fang, T. Hyeon, K. J. Kolbeck, W. B. McNamara, M. M. Mdleleni, and M. Wong. Acoustic cavitation and its chemical consequences. *Philosophical transactions of the Royal Society of London A: mathematical, physical and engineering science*, 357:335–353, 1999.

[87] Y. Tsunekawa, H. Suzuki, and Y. Genma. Application of ultrasonic vibration to in situ mmc process by electromagnetic melt stirring. *Materials & Design*, 22:467–472, 2001.

[88] Z. Wang, X. Wang, Y. Zhao, and W. Du. SiC nanoparticles reinforced magnesium matrix composites fabricated by ultrasonic method. *Transactions of Nonferrous Metals Society of China*, 20:s1029–s1032, 2010.

[89] G. Cao, H. Choi, J. Oportus, H. KOnishi, and X. Li. Study on tensile properties and microstructure of cast AZ91D/AlN nanocomposites. *Materials scinece & engineering A*, 494:127–131, 2008.

[90] S. Jayalakshmi and M. Gupta. *Metallic Amourphous Alloy Reinforcements in Light Metals Matrices*. SpringerBriefs in Materials, 2015.

[91] N. Ramakrishnan. An analytical study on strengthening of particulate reinforced metal matrix composites. *Acta Materialia*, 44(1):69–77, 1996.

[92] A. Sanaty-Zadeh. Comparison between current models for the strength of particulate-reinforced metal matrix nanocomposites with emphasis on consideration of Hall-Petch effect. *Materials Science and Engineering A*, 531:112–118, 2012.

[93] G. E. Dieter and D. Bacon. *Mechanical Metallurgy SI Metric Edition*. 1988.

[94] Z. Zhang and D. L. Chen. Consideration of Orowan strengthening effect in particulate-reinforced metal matrix nanocomposites: A model for predicting their yield strength. *Scripta Materialia*, 54:1321–1326, 2006.

[95] H. Dieringa. Properties of magnesium alloys reinforced with nanoparticles and carbon nanotubes: a review. *Journal of Materials Science*, 46:289–306, 2011.

[96] R. J. Arsenault and N. Shi. Dislocation generation due to differences between the coefficient of thermal expansion. *Materials Science & Engineering*, 81:175–187, 1986.

[97] R. Casati. *Aluminum matrix composites reinforced with alumina nanoparticles*. Springer, 2016.

[98] M. Kouzeli and A. Mortensen. Size dependent strengthening in particle reinforced aluminum. *Acta Materialia*, 2002.

[99] C. Kim, I. Sohn, M. Nezafati, J. B. Ferguson, B. F. Schultz, Z. Bajestani-Gohari, P. K. Rohatgi, and K. Cho. Prediction models for the yield strength of particle-reinforced unimodal pure magnesium (Mg) metal matrix nanocomposites (MMNCs). *Journal of Materials Science*, 48:4191–4204, 2013.

[100] M. Taya and R. J. Arsenault. *Metal Matrix Composites - Thermomechanical behavior*. •, 1989.

[101] J. Fan, J. Zhang, H. Chen, and Z. Jin. *Advances in heterogeneous material mechanics*. DEStech publisher, 2011.

[102] K. T. Ramesh. *Nanomaterials - Mechanis and Mechanisms*. Springer, 2009.

[103] R. J. Arsenault. The strengthening of aluminum alloy 6061 by fiber and platelet silicon carbide. *Materials Science & Engineering*, 64:171–181, 1984.

[104] C. S. Goh, J. Wei, L. C. Lee, and M. Gupta. Properties and deformation behavior of Mg-Y_2O_3 nanocomposites. *Acta Materialia*, 55:5115–5121, 2007.

[105] D. Hull and T. W. Clyne. *An introduction to composite materials*. Cambridge University Press, 2nd edition edition, 1996.

[106] Z. Zhang and D. L. Chen. Contribution of Orowan strengthening effect in particulate-reinforced metal matrix composites. *Materials Science & Engineering A*, 483-484:148–152, 2008.

[107] S. F. Hassan, M. J. Tan, and M. Gupta. High-temperature tensile properties of Mg/Al_2o_3 nanocomposite. *Materials Science & Engineering A*, 486:56–62, 2008.

[108] K. S. Tun and M. Gupta. Effect of heating rate during hybrid microwave sintering on the tensile properties of magnesium and Mg/Y_2o_3 nanocomposite. *Journal of Alloys and Compouds*, 466:140–145, 2008.

[109] J. Hütsch and E. T. Lilleodden. The influence of focused-ion beam preparation technique on microcompression investigations: Lathe vs. annular milling. *Scripta Materialia*, 77:49–51, 2014.

[110] W. C. Oliver and G. M. Pharr. An improved technique for determining hardness and elastic-modulus using load and displacement sensing indentation experiments. *Journal of Materials Research*, 7(6):1564–1583, 1992.

[111] W. C. Oliver and G. M. Pharr. Measurement of hardness and elastic modulus by instrumented indentation: advances in understanding and refinements to methodology. *Journal of Materials Research*, 19(1):3–20, 2004.

[112] M. D. Uchic, D. M. Dimiduk, J. N. Florando, and W. D. Nix. Sample dimensions influence strength and crystal plasticity. *Science*, 305:986–989, 2004.

[113] L. Reimer. *Transmission Electron Microscopy: physics of image formation and microanalysis*. Springer, 2013.

[114] M. Karlík and B. Jouffrey. Étude des métaux par microscopie électronique en transmission (MET) - Microscope, échantillons et diffraction. *Techniques de l'ingénieur*, m4134:1–16, 2008.

[115] D. B. Williams and C. B. Carter. *Transmission Electron Microscopy: a textbook for materials science - Diffraction II*. •, 1996.

[116] D. B. Williams and C. B. Carter. *Transmission Electron Microscopy: a textbook for materials science*. Springer, 1996.

[117] E. F. Rauch and M. Véron. Coupled microstructural observations and local texture measurements with an automated crystallographic orientation mapping tool attached to a TEM. *Materialwissenschaft und Werkstofftechnik*, 36(10):552–556, 2005.

[118] E. F. Rauch, M. Véron, J. Portillo, D. Bultreys, Y. Maniette, and S. Nicolopoulos. Automatic crystal orientation and phase mapping in TEM by precession diffraction. *Microscopy and analysis*, 22(6):S5–S8, 2008.

[119] E. F. Rauch and M. Véron. Automatic crystal orientation and phase mapping in TEM. *Materials characterization*, 98:1–9, 2014.

[120] Crystallography Open Database. www.crystallography.net.

[121] NanoMEGAS. ASTAR: Automatic Crystal Orientation and Phase Mapping package for TEM.

[122] H. Nguyen-Thi, L. Salvo, R. H. Mathiesen, L. Arnberg, B. Billia, M. Suery, and G. Reinhart. On the interest of synchrotron X-ray imaging for the study of solidification in metallic alloys. *Comptes Rendus Physique*, 13:237–245, 2012.

[123] E. Maire, J.-Y. Buffière, L. Salvo, J. J. Blandin, W. Ludwig, and J. M. Létang. On the application of X-ray microtomography in the field of materials science. *Advanced engineering materials*, 3:539–546, 2001.

[124] E. N. Landis and D. T. Keane. X-ray microtomography. *Materials characterization*, 61:1305–1316, 2010.

[125] J. Baruchel, J.-Y. Buffière, P. Cloetens, M. di Michiel, E. Ferrié, W. Ludwig, E. Maire, and L. Salvo. Advances in synchrotron radiation microtomography. *Scripta Materialia*, 55:41–46, 2006.

[126] M. Langer, A. Pacureanu, H. Suhonen, Q. Grimal, P. Cloetens, and F. Peyrin. X-Ray nanotomography resolves the 3D human bone ultrastructure. *Plos One*, 7(8):1–7, 2012.

[127] K. A. A. Hassan, A. F. Norman, D. A. Price, and P. B. Prangnell. Stability of nugget zone grain structures in high strength Al-alloy friction stir welds during solution treatment. *Acta Materialia*, 51:1923–1936, 2003.

[128] C. Lin, T. Lui, and L. Chen. Correlation between microstructural stability and tensile properties of FSWed Al-Mg-Mn cast plate during subsequent thermal exposure. *Materials Transactions*, 52(8):1667–1673, 2011.

[129] E. Cerri. Effect of post-welding heat treatment on mechanical properties of double lap FSW joints in high strength aluminum alloys. *Metallurgical science and technology*, 29-1:32–39, 2011.

[130] M. M. Attallah and H. G. Salem. Friction stir welding parameters: a tool for controlling abnormal grain growth during subsequent heat treatment. *Materials Science and Engineering A*, 391:51–59, 2005.

[131] L. Katsarou, M. Mounib, W. Lefebvre, S. Vorozhtsov, M. Pavese, C. Badini, J. M. Molina-Aldareguia, C. C. Jimenez, M. T. P. Prado, and H. Dieringa. Microstructure, mechanical properties and creep of magnesium alloy Elektron21 reinforced with AlN nanoparticles by ultrasound-assisted stirring. *Materials Science & Engineering A*, 659:84–92, 2016.

[132] W. H. Sillekens, D. J. Jarvis, A. Vorozhtsov, V. Bojarevics, C. F. Badini, M. Pavese, S. Terzi, L. Salvo, L. Katsarou, and H. Dieringa. The ExoMet project: EU/ESA research on high-performance light-metal alloys and nanocomposites. *Metallurgical and Materials Transactions A*, 45:3349–3361, 2014.

[133] A. D. McLeod and C. M. Gabryel. Kinetics of the growth of spinel, mgal$_2$o$_4$, on alumina particulate in aluminum alloys containing magnesium. *Metallurgical Transactions A*, 23A:1279–1283, 1992.

[134] C. Jonckheere, B. de Meester, A. Denquin, and A. Simar. Torque, temperature and hardening precipitation evolution in dissimilar friction stir welds between 6061-T6 and 2014-T6 aluminum alloys. *Journal of Materials Processing Technology*, 213:826–837, 2013.

[135] D. Khayyamin, A. Mostafapour, and R. Keshmiri. The effect of process parameters on microstructural characteristics of AZ91/SiO_2 composite fabricated by FSP. *Materials Science and Engineering A*, 559:217–221, 2013.

[136] A. Shamsipur, S. F. Kashani-Bozorg, and A. Zarei-Hanzaki. The effects of friction-stir process parameters on the fabrication of Ti/SiC nano-composite surfaces. *Surface and Coatings Technology*, 206:1372–1381, 2011.

[137] B. London M. Mahoney K. V. Jata M. W. Mahoney R. S. Mishra S. L. Semiatin S. Askari, S. Silling and D. P. Field. Temperature distribution and resulting metal flow. *Friction stir welding and processing IV*, pages 43–54, 2001.

[138] K. V. Jata and S. L. Semiatin. Continuous dynamic recrystallization during friction stir processing of high strength aluminum alloys. *Scripta Materialia*, 43:743–749, 2000.

[139] P. L. Threadgill. Friction stir welding - the state of the art. *Buletin 678*, 1999.

[140] P. Asadi, M. K. Besharati Givi, K. Abrinia, M. Taherishargh, and R. Salekrostam. Effects of SiC particle size and process parameters on the microstructure and hard-

ness of AZ91/SiC composite layer fabricated by FSP. *Journal of Materials Engineering and Performance*, 20:1554–1562, 2011.

[141] M. Najafi, A. M. Nasiri, and A. H. Kokabi. Microstructure and hardness of friction stir processed AZ31 with SiC_p. *International Journal of Modern Physics B*, 22:2879–2885, 2008.

[142] S. Jana, R. S. Mishra, J. A. Baumann, and G. J. Grant. Effect of friction stir processing on microstructure and tensile properties of an investment cast Al-7Si-0.6Mg alloy. *Metallurgical and Materials Transactions A*, 41:2507–2521, 2010.

[143] Z. Y. Ma, S. R. Sharma, and R. S. Mishra. Effect of friction stir processing on the microstructure of cast A356 aluminum. *Materials Science and Engineering: A*, 433:269–278, 2006.

[144] F. Hannard. PhD thesis, Université Catolique de Louvain, ongoing.

[145] F. Hannard, T. Pardoen, E. Maire, C. Le Bourlot, R. Mokso, and A. Simar. Characterization and micromechanical modelling of microstructural heterogeneity effects on ductile fracture of 6xxx aluminium alloys. *Acta Materialia*, 103:558–572, 2016.

[146] F. Hannard, S. Castin, E. Maire, R. Mokso, T. Pardoen, and A. Simar. Ductilization of aluminum alloy 6056 by friction stir processing.

[147] J. Boselli, P. D. Pitcher, P. J. Gregson, and I. Sinclair. Secondary phase distribution analysis via finite body tessellation. *Journal of Microscopy*, 195:104–112, 1999.

[148] W. A. Spitzig, J. F. Kelly, and O. Richmond. Quantitative characterization of second-phase populations. *Metallography*, 18:235–261, 1985.

[149] Y. J. M. Brechet. Clusters, plasticity and damage: a missing link? *Materials Science and Engineering*, A175:63–69, 1994.

[150] G. Burger. *The effects of microstructural inhomogeneity on damage accumulation and fracture*. PhD thesis, McMaster University, 1986.

[151] S. Chandrasekar. Stochastic problems in physics and astronomy. *Reviews of Modern Physics*, 15:1–89, 1943.

[152] S. P. Gupta. *Solid state phase transformation*. Allied Publishers Private Limited, 2002.

[153] F. J. Humphreys and M. Hatherly. *Recrystallization and related annealing phenomena*. Elsevier, Oxford, second edition edition, 2004.

[154] P. Achon. *Comportement et ténacité d'alliages d'aluminium à haute résistance*. PhD thesis, Ecole des Mines de Paris, France, 1994.

[155] N. Stanford and M. R. Barnett. Effect of particles on the formation of deformation twins in a magnesium-based alloy. *Materials Science and Engineering A*, 2009.

[156] I. J. Beyerlein, J. Wang, M. R. Barnett, and C. N. Tome. Double twinning mechanisms in magnesium alloys via dissociation of lattice dislocations. *Proceedings of the Royal Society A*, 468:1496–1520, 2012.

[157] H. Kokawa, Y. S. Sato, and S. Mironov. Texture development during friction stir welding of magnesium alloys. *Materials Science Forum*, 702-703:43–47, 2012.

[158] S. H. C. Park, Y. S. Sato, and H. Kokawa. Basal plane texture and flow pattern in friction stir weld of a magnesium alloy. *Metallurgical and Materials Transactions A*, 34:987–994, 2003.

[159] R. Xin, B. Li, A. Liao, Z. Zhou, and Q. Liu. Correlation between texture variation and transverse tensile behavior of friction-stir-processed AZ31 Mg alloy. *Metallurgical and Materials Transactions A*, 2012.

[160] G. Bhargava, W. Yuan, S. S. Webb, and R. S. Mishra. Influence of texture on mechanical behavior of Friction-Stir-Processed magnesium alloy. *Metallurgical and Materials Transactions A*, 41A:13–17, 2010.

[161] E. Kelley and W. Hosford. The deformation characteristics of textured magnesium. *Transactions of the Metallurgical Society of AIME*, 242:654–661, 1968.

[162] T. R. McNelley, S. Swaminathan, and J. Q. Su. Recrystallization mechanisms during friction stir welding/processing of aluminum alloys. *Scripta Materialia*, 58:349–354, 2008.

[163] J. R. Greer and W. D. Nix. Nanoscale gold pillars strengthened through dislocation starvation. *Physical Review B*, 73:245410, 2006.

[164] Q. Yu, J. Wang, Y. Jiang, R. J. McCabe, N. Li, and C. N. Tomé. Twin-twin interactions in magnesium. *Acta Materialia*, 77:28–42, 2014.

[165] F. Wang and S. R. Agnew. Dislocation-twin inderactions in magnesium alloy AZ31. *Magnesium Technology 2015*, pages 139–144, 2015.

[166] P. B. Hirsch and F. J. Humphreys. Physics of Strength and Plasticity. *MIT Press*, page 189, 1969.

[167] M. Vogelsang, R. J. Arsenault, and M. Fisher. An *in situ* HVEM study of dislocation generation at Al/SiC interfaces in metal matrix composites. *Metallurgical Transactions A*, 17A:379–389, 1986.

[168] H. Fan, S. Aubry, A. Arsenlis, and J. A. El-Awady. Grain size effects on dislocation and twinning mediated plasticity in magnesium. *Scripta Materialia*, 112:50–53, 2016.

[169] H. Fan, Q. Wang, X. Tian, and J. A. El-Awady. Temperature effects on the mobility of pyramidal <c+a> dislocatios in magnesium. *Scripta Materialia*, 127:68–71, 2017.

[170] H. Idrissi, C. Bollinger, F. Boioli, D. Schryvers, and P. Cordier. Low-temperature plasticity of olivine revisited with *in situ* TEM nanomechanical testing. *Science Advances*, 2(3):1–6, 2016.

Résumé :

Le magnésium est le plus léger des métaux, ce qui lui confère un fort potentiel pour être utilisé dans des applications où l'allégement des structures est requis. Pour autant, sa résistance mécanique est très faible, et doit donc être augmentée afin de rivaliser avec d'autres métaux légers tels que l'aluminium ou le titane. Une solution consiste à renforcer le magnésium et ses alliages en introduisant des nanoparticules d'oxydes. De par sa structure cristalline hexagonale compacte, le magnésium présente des propriétés plastiques complexes telles qu'une très forte anisotropie plastique et une prédisposition au maclage. La compréhension de ces mécanismes de déformation est essentielle pour le développement de nanocomposites plus performants en vue d'une utilisation industrielle plus répandue. Dans ce travail, nous nous sommes intéressés à l'élaboration et à la caractérisation de nanocomposites de magnésium pur renforcés par des particules d'oxydes. Différentes techniques ont été testées pour l'élaboration des nanocomposites : la solidification assistée aux ultrasons et le procédé de friction malaxage. L'homogénéité de la dispersion des particules a été vérifiée en 2D par observations en microscopie électronique et également en 3D par tomographie aux rayons X. On montre ainsi que le procédé de friction malaxage permet d'obtenir une distribution homogène des particules, tout en réduisant leur taille. Des essais de traction ont permis de mettre en évidence une augmentation de la limité d'élasticité pour une fraction volumique aussi faible que 0.3 %. Afin d'isoler le rôle des particules de celui des joints de grains sur le comportement plastique du nanocomposite, nous avons réalisé des essais de micro-compression sur des micro-piliers monocristallins usinés par canon à ions focalisés (FIB) dans des échantillons ayant préalablement subis un traitement thermique favorisant la croissance anormale des grains. Différentes orientations cristallines et tailles de micro-piliers ont été testées en vue d'étudier l'influence des particules d'une part sur la plasticité dans le plan basal par mouvement de dislocations et d'autre part sur la déformation par maclage. Contre toute attente, les essais sur monocristaux favorablement orientés pour un glissement basal ne montrent pas l'effet durcissant observé macroscopiquement. Nous attribuons cet effet à la densité initiale de dislocations mobiles, plus importante dans les nanocomposites que dans le magnésium pur, du fait des concentrations de contraintes autour des particules. Ces densités initiales de dislocations mobiles tendent également à supprimer l'effet de taille classiquement observé dans le magnésium pur. Les particules modifient également le mécanisme de déformation par maclage en favorisant l'apparition simultanée de plusieurs macles dans le micro-pilier qui interagissent entre elles au cours de la déformation alors que les micro-piliers de magnésium pur présentent généralement une macle unique (dans certains cas deux) qui envahi tout le monocristal. Ces résultats constituent une contribution originale à la compréhension du rôle des nanoparticules dans la déformation plastique des monocristaux de nanocomposites à base de magnésium.

Abstract:

Magnesium is the lightest of all structural metals, which gives it a huge potential to be used in applications that require lightweighting. However, its strength needs to be increased in order to compete with other light metals such as aluminum and titanium. A solution is the reinforcement of magnesium and its alloys with the addition of oxide nanoparticles. The hexagonal close packed crystalline structure is responsible for the complex plasticity of magnesium, which is characterized by a very strong plastic anisotropy as well as a complex twinning activity. Understanding these deformation mechanisms is crucial for the development of more performant nanocomposites, allowing widespread industrial application. The present work focuses on the processing and characterization of magnesium based nanocomposites reinforced with oxide particles. Two different processing techniques have been compared: friction stir processing and ultrasound assisted casting. The homogeneity of the dispersion of the reinforcement particles has been verified in 2 and 3 dimensions using electron microscopy and X-ray tomography, respectively. Friction stir processing produces nanocomposites with a more homogeneous dispersion of particles, while reducing their size. Tensile tests have shown strengthening of magnesium with the addition of a volume fraction of only 0.3 % of reinforcement. An annealing heat treatment has then been performed in order to promote abnormal grain growth and single crystalline microcolumns for microcompression testing have been machined by focused ion beam (FIB). The purpose is to isolate the role of particles. The orientation dependent mechanism of deformation and the size effects have been studied in order to understand the influence of the reinforcement particles on the plasticity for orientations favorable for basal slip or tensile twinning. Differently from the strengthening observed macroscopically, no clear strengthening effect is observed on microcolumns when dislocation glide operates. The reason is the higher density of potentially mobile dislocations that is generated due to stress concentrations around the reinforcement particles. In addition, the size effects usually observed on pure magnesium have also been suppressed with the addition of particles. The reinforcement particles seem to affect the twin nucleation stress and twin morphology: particles induce the nucleation of multiple twins inside a microcolumn, whereas in pure magnesium, only one or two twins have been observed. These results provide relevant insights on the role of nanoparticles on the onset of plastic deformation, as well as size effect, in single crystalline magnesium nanocomposites.